UNIVERSITY OF
LEICESTER

The Accretion Discs of Transient X-ray Binaries

Alexander Eckersall

Supervisors:

Simon Vaughan & Graham Wynn

Thesis to be submitted for the degree of

Doctor of Philosophy

at the University of Leicester.

X-ray & Observational Astronomy Group

Department of Physics and Astronomy

University of Leicester

May 7, 2018

ABSTRACT

One of the larger questions within the study of X-ray Binaries currently concerns the geometry of the accretion disc during the so called 'hard state'. A model involving a truncated disc is often used to explain the properties of the hard state, but there is still disagreement on the extent to which it is necessary. Presented in this thesis are three studies related to this issue.

The first looks into the changes in the accretion geometry using an argument based around radiative efficiency. Periods of exponential decay before and after the soft- to hard-state transition are found. The e-folding times of these decays are measured and it is found that this value changes from $\sim$12 days in the soft state to $\sim$7 days in the hard state. This factor $\sim$2 change would be expected if there is a change from a radiatively efficient regime to a radiatively inefficient regimee.

The second concerns the treatment of absorption from the Interstellar Medium in studies of X-ray Binaries. Column densities for the most abundant elements are found and compared with previous results for a number of sources. Simulated data is also used to test the impact of using incorrect column densities and older X-ray absorption models on spectral analysis. It is found that the use of incorrect absorption parameters can have a large effect on the results of spectral fitting.

The third directly tests for the presence of a truncated disc by fitting a model to energy spectra from the *XMM-Newton*/EPIC-pn instrument. The model assumes the accretion disc extends down to r_{ISCO} at all times, and is fit to a large range of observations in both the hard and soft states. In the majority of cases there is no explicit need for a truncated disc in either the soft or hard state.

Acknowledgments

First of all a thank you to my supervisors Simon and Graham. It's safe to say this wouldn't have been at all possible without all your help. I appreciate you always finding the time to read through the various drafts of papers, or the chapters of this thesis, and making helpful comments. And also for the all the other advice you've given me on the work we've done the past four years. Thank you also for giving me the opportunity to attend conferences, I enjoyed the two times I got to visit ESAC in Madrid, and all the other smaller meetings I attended.

Secondly a thank you to everyone I have shared an office with the past four years: Klaas, Ben, Suzy, Sarah, Alex and Joe. It was always a welcoming and friendly place to come in to and work during the day. And thanks to everyone else in the department who has made studying at Leicester a fun and worthwhile experience. Be it people who I just saw around the department or at the daily tea break, or people who I had the more dubious honour of spending many a late night with in some of Leicesters more questionable establishments, thanks for being nice.

Finally a thanks to my parents for being supportive these past eight years of me being a student. Helping me with moving house every year and all the various other things you've done for me. Maybe I'll be able to stop sponging off you now. You never know.

Declaration

I hereby declare that no part of this thesis has been previously submitted to this or any other University as part of the requirement for a higher degree. The work herein was conducted by the undersigned except for contributions as acknowledged in the text.

Alexander Eckersall

May 7, 2018

List of Publications

A significant amount of work contained in this thesis is due to be or has already been published in the following papers:

Eckersall A. J., Vaughan, S., Wynn G. A., 2015, MNRAS, 450, 3410
Eckersall A. J., Vaughan, S., Wynn G. A., 2017a, MNRAS, 471, 1468
Eckersall A. J., Vaughan, S., Wynn G. A., 2017b, in prep.

Contents

List of Tables

List of Figures

1

Introduction

Since the discovery of the first Galactic black hole, Cygnus X-1, in 1964 observations of such systems have become a key component of many X-ray missions. Observations of Galactic black holes and their immediate environments can have implications for a wide range of other topics. For example, at the center of most galaxies lies a black hole whose mass and growth have been shown to be related to the properties of its galaxy, with the nature of the accretion flow likely a factor in how the large-scale processes in these galaxies are regulated. Whereas the regions closer to the black hole, where gravitational affects are at their strongest, provide a location to test theories of general relativity.

The focus of this thesis will be on a set of objects called X-ray Binaries. These contain much smaller black holes than at the center of galaxies. The smaller size means they operate on much smaller timescales than Galactic black holes and so evolve much faster. They therefore present an opportunity to study the behaviour of accretion flow on human accessible timescales. These

systems can show large changes in their observed properties from month to month or year to year, so it is possible to study how these systems evolve over these periods.

1.1 X-Ray Binaries

X-ray binaries (XRBs) comprise a black hole (BH) or neutron star (NS), often called the primary, that accretes gas from a secondary star (also called the companion, or donor). The secondary supplies mass which when transferred towards the primary can be accreted onto the central compact object. This generates bright emission across the entire electromagnetic spectrum, not just in X-rays. Strong, collimated, relativistic radio jets can also be produced (Fender et al., 2009).

XRBs can be divided into two sub-classes: low mass X-ray binaries (LMXBs) and high mass X-ray binaries (HMXBs). The distinction is based on the mass of the companion star, rather than the compact object itself. LMXBs will have a secondary star with a mass of $\lesssim 1.5\mathrm{M}_{\odot}$, while the donor in HMXB systems will generally be much more massive. In these HMXBs the mass transfer mechanism is often then through some fraction of the stellar wind from the massive star being captured by the compact object. LMXBs are often transient objects, showing clear outburst events separated by periods of low luminosity. These outbursts vary in length from source to source but are generally from a few months long to around a year. The time between outbursts also varies between sources, some having fairly frequent outbursts (one every couple of years) while others show much longer periods of low activity. HMXBs, on the other hand, are usually seen as persistent sources, having constantly high mass accretion rates.

In this thesis we concentrate on LMXBs with a black hole primary; these systems are powerful but transient sources of X-rays. They spend most of their time in quiescence, with very low luminosity in X-rays and other wavebands, interrupted by outbursts that usually last for weeks-months during which the X-ray luminosity can be comparable to the Eddington luminosity (see

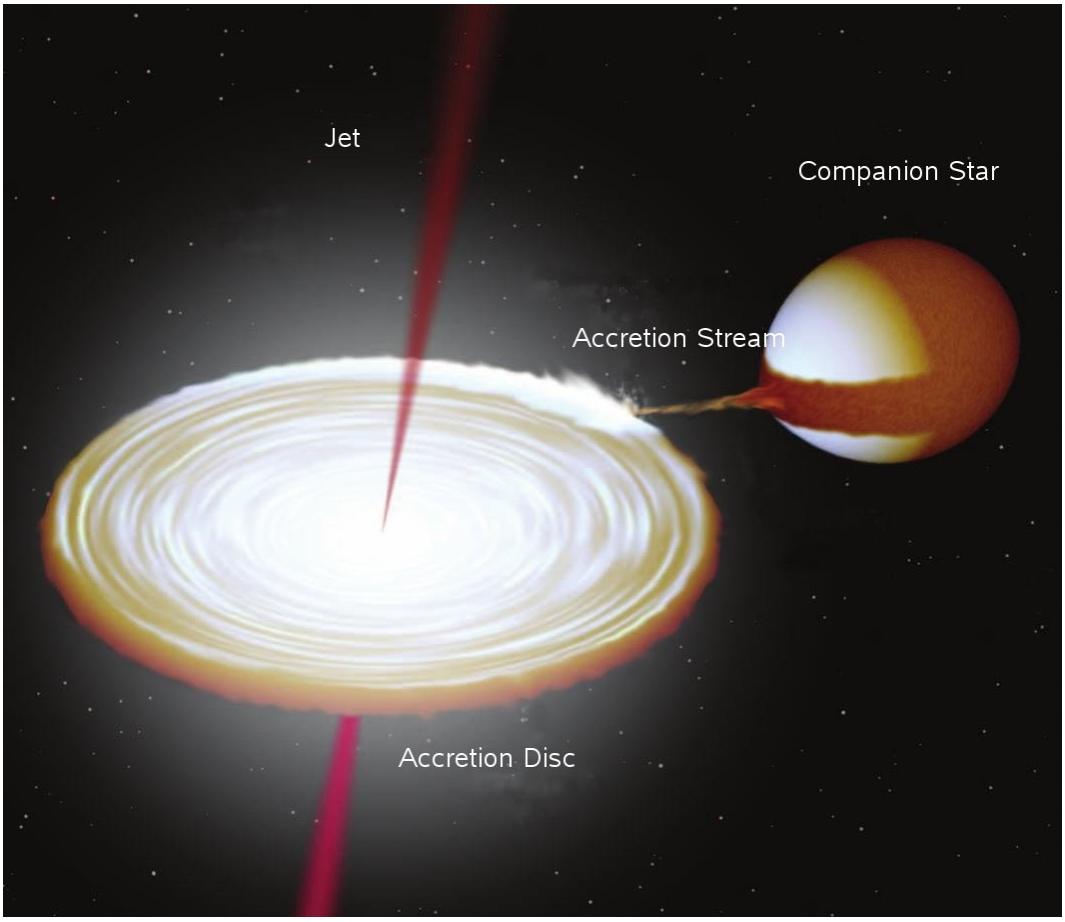

Figure 1.1: Artists impression of a low mass x-ray binary system. The system pictured is GX 339-4, with the relative masses and inclination taken from observational estimates of the properties of the system.

Section 1.1.3.) $L_{\rm Edd}$ ($\sim 10^{38} M_{BH}/{\rm M}_{\odot}$ erg s^{-1}) . Figure 1.1 shows what a LMXB system would possibly look like. An accretion disc is formed around the BH when the secondary fills its Roche lobe and material passes towards the BH (Shakura & Sunyaev, 1973; McClintock & Remillard, 2006; Done et al., 2007). The material in the accretion disc then spirals inwards losing potential energy and angular momentum while emitting large amounts of X-ray radiation.

Despite the frequency of double star systems there are only a few hundred luminous XRB systems in our Galaxy (Liu et al., 2007b). Fig 1.2 shows their distribution on the sky. Due to the nature of the stars in HMXBs (short lifespans) the distribution of these particular systems is different than those of LMXBs. Where LMXBs will be found in populations of older stellar systems in the central regions of the galaxy, HMXBs are mainly associated with star forming regions and so are

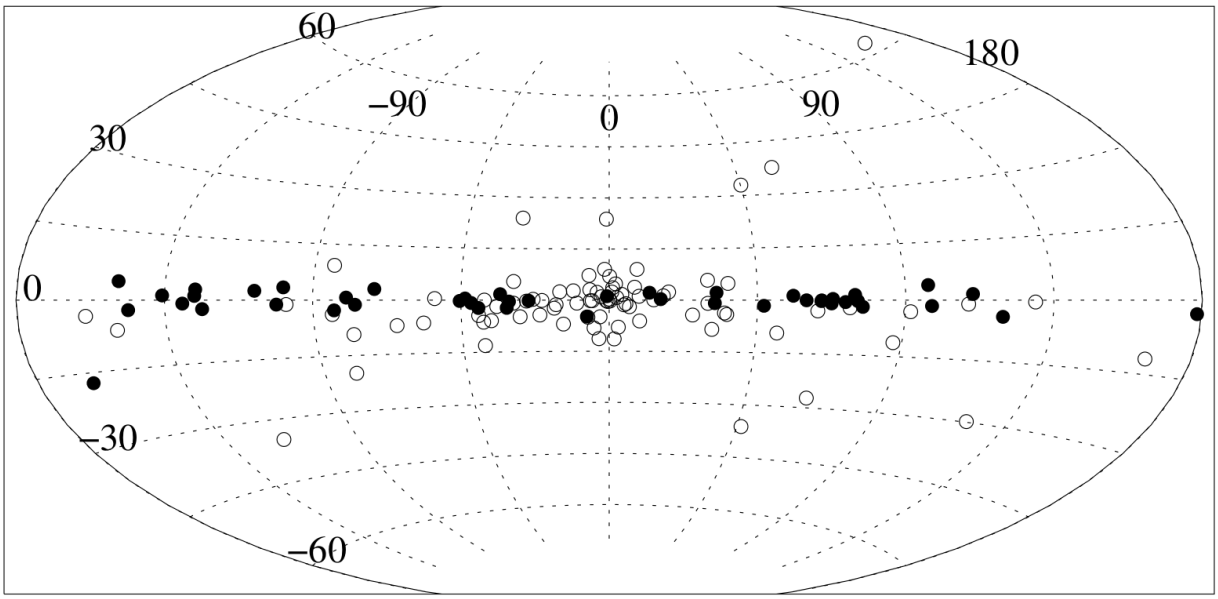

Figure 1.2: The distribution of HMXBs (filled circles) and LMXBs (open circles) in our Galaxy. There are a total of 138 systems shown, with 86 LMXBs and 52 HMXBs. This plot shows the key difference in the distribution of LMXBs and HMXBs, with the high-mass systems most spread along the Galactic Plane, and the heavy clustering of the low-mass systems in the Galactic Bulge (diagram from Grimm et al. 2002)

generally found close to the Galaxy's spiral arms (Grimm et al., 2002).

There are a number of direct and indirect observational methods to distinguish between BH and NS XRBs, many relying on the physical differences between the two objects creating tell-tale observational features. Neutron stars are less massive than black holes, having masses generally around $1.4\mathrm{M}_{\odot}$, while the mass of a black hole will be somewhere in the range of $3\mathrm{M}_{\odot}$ to $20\mathrm{M}_{\odot}$ (McClintock & Remillard, 2006). However, calculating the masses of individual objects is often difficult. Since, in these binary systems, both the compact object and the secondary will be rotating around their common center-of-mass, the velocity of each object can be found by the periodic oscillation in the Doppler shift. From this the radial velocity semi-amplitude can be found for each object, defined as $K = 2\pi a \sin(i)/P$, where a is the distance to the center of mass of the system, and i and P are the inclination and period of the system respectively, and where we have assumed a circular orbit.

In many cases K for the secondary can be measured. The mass function, $f(M)$, defined as,

$$f(M) = \frac{M_1^3 sin^3 i}{(M_1 + M_2)^2} = \frac{PK_1^3}{2\pi G}, \tag{1.1}$$

can then be used to help estimate the mass of the primary. While a and i might not be known, if an estimate of M_2 can be found, from its spectral type for example, then a limit can be derived for M_1.

While this is the most common way of measuring the masses of the compact objects, it is not the only way of distinguishing between BH and NS. Sometimes binary systems will show additional properties that can only be attributed to a NS, due to their solid surface and strong, consistent magnetic field, such as radio pulsations or irregular bursts (Strohmayer et al., 1996; Bildsten et al., 1997).

1.1.1 Properties of Black Holes

Stellar mass black holes ($M \sim 3 - 20\mathrm{M}_\odot$) are formed from the collapse of massive stars. When the stars energy sources are depleted the internal pressure is no longer sufficient to stop gravitational collapse. For less massive stars a white dwarf ($M \lesssim 1.4\mathrm{M}_\odot$) or neutron star ($1.4\mathrm{M}_\odot \lesssim M \lesssim 3\mathrm{M}_\odot$) will be the end result due to electron and neutron degeneracy pressure, respectively, stopping the collapse. For $M \gtrsim 3\mathrm{M}_\odot$ however, there is nothing to oppose gravity and a black hole is formed as the star collapses beyond its Schwarzschild radius.

The Schwarzschild radius of an object is the radius of a sphere such that, if the mass of the object was compressed to within the volume of this sphere then the escape velocity at the surface of the sphere would be equal to the speed of light. The value of the Schwarzschild radius is proportional to mass and is given by,

$$r_s = \frac{2GM}{c^2}. \tag{1.2}$$

The Schwarzschild radius for a $10\mathrm{M}_\odot$ black hole is about 30km .

1.1.2 Roche Lobe Overflow

The Roche potential in a binary system is given by,

$$\Phi_R(\boldsymbol{r}) = -\frac{GM_1}{|\boldsymbol{r} - \boldsymbol{r_1}|} - \frac{GM_2}{|\boldsymbol{r} - \boldsymbol{r_2}|} - \frac{1}{2}(\boldsymbol{\omega} \times (\boldsymbol{r} - \boldsymbol{r_c}))^2, \tag{1.3}$$

where M_1 and M_2 are the masses of the two objects, $\boldsymbol{r_1}$ and $\boldsymbol{r_2}$ are the positions of the two two objects, $\boldsymbol{r_c}$ is the position of the centre of mass of the system, and $\boldsymbol{\omega}$ is the angular velocity of the rotating frame. This describes the effective potential in a co-rotating frame of reference, which includes the gravity of each star and the rotation of the system.

Centered around the locations of the two objects, the black hole and the companion star in the case of LMXBs, are the Roche lobes. It is within these Roche lobes that matter is gravitationally bound to the respective object. The point where the two Roche lobes connect is the Lagrangian point L_1, representing a saddle point in the Roche potential. It is through this Lagrangian point that mass transfer can occur. The companion star can expand until it fills its Roche lobe. After that any further expansion will cause Roche lobe overflow as the material flows in the direction of decreasing potential, into the Roche lobe of the other object. The transferred mass then goes on to create an accretion disc.

There are four other Lagrangian points in a binary system, with L_2 and L_3 also corresponding to saddle points in the Roche potential, and with L_4 and L_5 as two minima. Figure 1.3 shows the

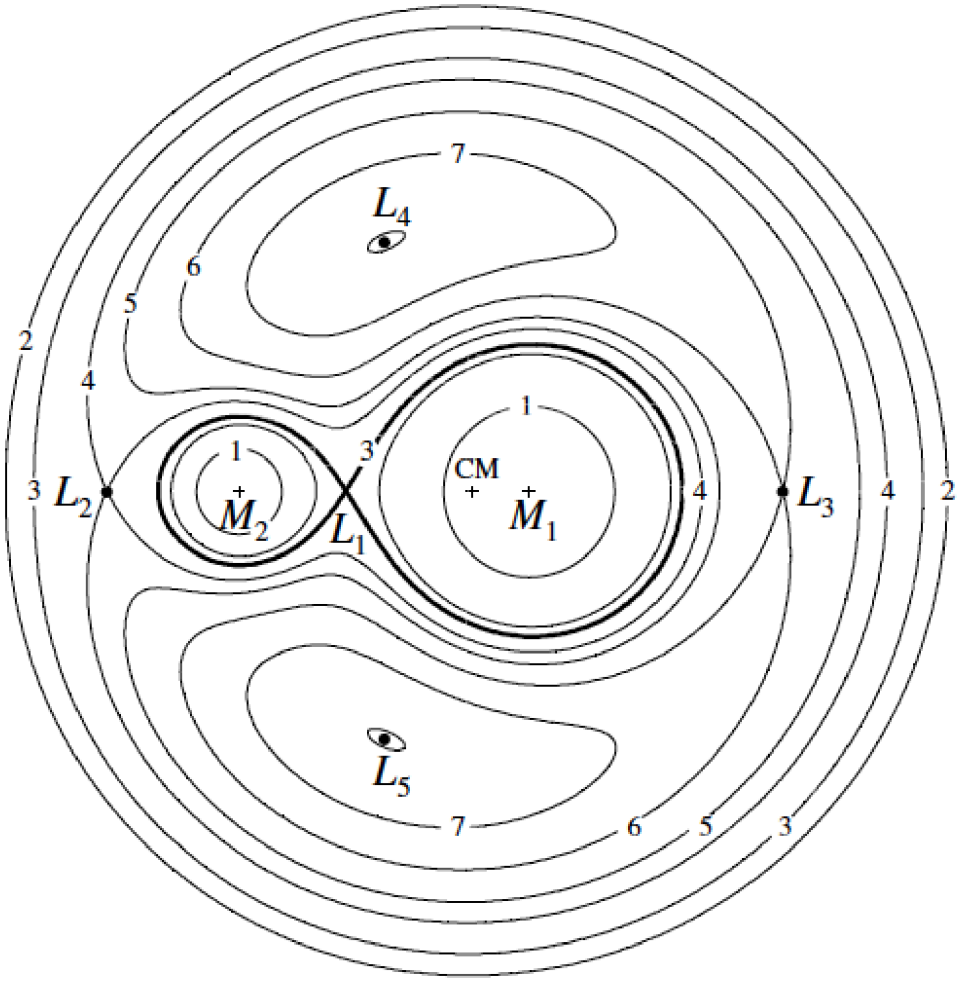

Figure 1.3: Diagram of the Lagrangian points and equipotential surfaces for the Roche potential in a binary system with mass ratio $M_2/M_1 = 0.25$. From Frank et al. (2002).

location of these.

1.1.3 Accretion

Accretion onto a compact object is a powerful source of radiant energy. The slow infall of mass onto the central object releases large amounts of gravitational potential energy. This material will not directly fall into the black hole due to its large angular momentum. Instead, mass passing through the Lagrange point will go into a nearly-circular orbit. As more mass is added the or-

bit becomes 'filled' (the material collides with more material passing that point) and begins to spread to different orbits and transfer angular momentum. This transfer of angular momentum is due to the magnetorotational instability (MRI; Balbus & Hawley 1998). This is a consequence of elements within a magnetised fluid acting like springs under tension, with displacements perpendicular to the magnetic field creating an attractive force proportional to the displacement. In an accretion disc, for example, if there are two masses, m_1 and m_2, orbiting around the central black hole at a certain radius and m_1 is allowed to orbit at a slightly smaller radius, it will have a slightly higher angular velocity. The attractive forces pull back on m_1 and drags m_2 forward. This causes m_1 to lose angular momentum due to the retarding torque, which then reduces its radius further. The opposite is true for m_2, which is now at a larger radius. With the displacement for each mass now larger, the torques also increase, resulting in the instability.

This process forms the accretion disc, a geometrically thin (the ratio between the height and radius of the disc $H/R << 1$), optically thick (on average a photon cannot pass through the disc without absorption) structure extending around the black hole.

A test mass of mass m a distance r from the center of the black hole of mass M will have gravitational potential energy,

$$E_{GR}(r) = -\frac{GMm}{r}. \tag{1.4}$$

When the mass travels from a large distance R_{out} to a distance R around the black hole ($R_{out} >> R$) it will change its gravitational energy by an amount,

$$\Delta E_{GR}(r) = \frac{GMm}{R}. \tag{1.5}$$

In a radiatively efficient accretion flow up to half of this amount is available to be radiated, the

other half is converted to kinetic energy. If material is being accreted onto the black hole at a rate $\dot{M}$ (e.g. in units of kg/s) then the luminosity produced is given by,

$$L_{acc} = \frac{1}{2}\frac{GM\dot{M}}{R}. \tag{1.6}$$

If the accreting matter radiates down to the Schwarzschild radius ($R = 2GM/c^2$) then $L_{acc} \approx \frac{1}{4}\dot{M}c^2$. To demonstrate the power of accretion the radiative efficiency η can be defined using,

$$L_{acc} = \eta\dot{M}c^2, \tag{1.7}$$

where c is the speed of light. A more detailed calculation shows that for a non-rotating black hole this efficiency is 5.7%, while a maximally rotating black hole can reach an efficiency of 32% (Thorne, 1974). To compare these values with other processes the efficiency of hydrogen to helium nuclear fusion is only 0.7%.

There is a theoretical maximum to the luminosity of an accretion disc, determined by the Eddington limit. This is the maximum luminosity that can be achieved before the inwards gravitational force is balanced with the outwards radiation pressure. In the approximation of spherical accretion of fully ionised hydrogen then balancing radiation pressure and gravity gives,

$$\frac{GMm_p}{r^2} = L_{Edd}\frac{\sigma_T}{4\pi cr^2}, \tag{1.8}$$

and after rearranging for L_{Edd},

$$L_{Edd} = \frac{4\pi GMm_p}{\sigma_T}, \tag{1.9}$$

where σ_T is the Thompson cross-section and m_p is the mass of a proton. This then leads to a corresponding limit on the mass accretion rate,

$$\dot{M}_{Edd} = \frac{L_{Edd}}{\eta c^2}. \tag{1.10}$$

1.1.4 Radiatively Inefficient Accretion

When mass accretion rate is high and the source is emitting at a high percentage of the Eddington Luminosity the disc will be the geometrically thin, optically thick structure described in the previous section. However, when the mass accretion rate is lower and the luminosity is well below the Eddington limit it is thought that there will be a change in the nature of the accretion disc (Esin et al., 1997; Done et al., 2007). This second class of accretion will be hotter than the relatively cool thin disc, as well as geometrically thicker and optically thin. One of the key features of these hot flows is the importance of energy advection.

The lower mass accretion rate creates a flow with a lower density, reducing the rate of particle collision which leads to less radiation. The reduced level of emission means less cooling and the disc remains hot. This starts a runaway effect as the hot gas expands under pressure lowering the density even further. The result of this process is a much thicker ($H \approx R$) accretion flow with lower radiative efficiency, with more energy trapped and carried with the flow (advected). This energy could be lost into the BH or used to energise radio jets. In this case the efficiency would be a function of the mass accretion rate, $\eta \sim \dot{M}$, in contrast to the radiatively efficient thin disc whose radiative efficiency is thought to be a constant. See e.g. Fender et al. (2003), Merloni et al. (2003), Körding et al. (2006) and Coriat et al. (2011) for further discussion of the link between X-ray and radio luminosities, accretion rate, and radiative efficiency.

A type of radiatively inefficient flow that is often used in the study of XRBs to help describe

certain observational properties is the Advection Dominated Accretion Flow (ADAF) (Narayan & Yi, 1995). There are two varieties of ADAFs for differing mass accretion rates. The first, at super-Eddington mass accretion rates, has a large optical depth which traps any incoming radiation within the inflowing gas, which is then advected into the central black hole. The second type of ADAF, and the one most relevant to the work in this thesis is one which occurs at very low mass accretion rates. These ADAFs are optically thin and have low densities meaning the energy liberated during the accretion process is stored within the gas as it is unable to cool efficiently. Compared to the efficient accretion presented in the previous section an ADAF will be much less luminous and create a spectrum with a wider energy distribution, produced by inverse-Compton emission.

1.2 Emission Processes

1.2.1 Black body

The emission of an optically thick medium, where the photons are in thermal equilibrium at a temperature T, will be a black body spectrum. This is a continuum process. The emission from a black body has an intensity described by Planck's law,

$$B_\nu(T) = \frac{2h\nu^3}{c^2}\frac{1}{exp(h\nu/kT) - 1}, \tag{1.11}$$

where h is Planck's constant and k is the Boltzmann constant.

The structure of an accretion disc can be seen as a series of annuli. Each of these annuli will have a local surface temperature $T_{eff}(R)$, where $T_{eff} \propto R^{-3/4}$ so temperature increases as the material approaches the compact object. The resulting emission is a sum of the black body spectrum for

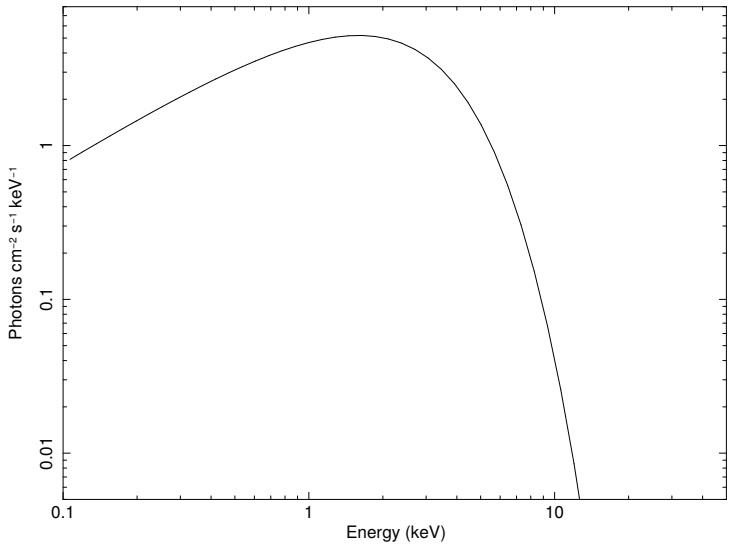

Figure 1.4: Plot showing an example of a black body spectrum. Created using the BBODY model, with temperature kT set at 1.0 keV.

each annulus, often referred to as a 'multi colour black body spectrum'. Black body emission from the disc would be radiatively efficient ($\eta \sim 0.1$, Shakura & Sunyaev 1973) and approximately constant with accretion rate.

The wavelength at which black body radiation peaks is entirely dependent on the temperature of the emitting region and is described by the Wien displacement law which states that,

$$\lambda_{max} = \frac{2.898 \times 10^{-3}}{T} mK, \tag{1.12}$$

1.2.2 Bremsstrahlung

Brehsstrahlung is the electromagnetic radiation produced due to the deceleration of electrons. The deceleration is caused by interactions with another charged particle, generally another electron or atomic nucleus, deflecting the path of the electron and reducing its kinetic energy. To preserve the conservation of energy a photon is emitted. The energy of the photon is dependent on the original

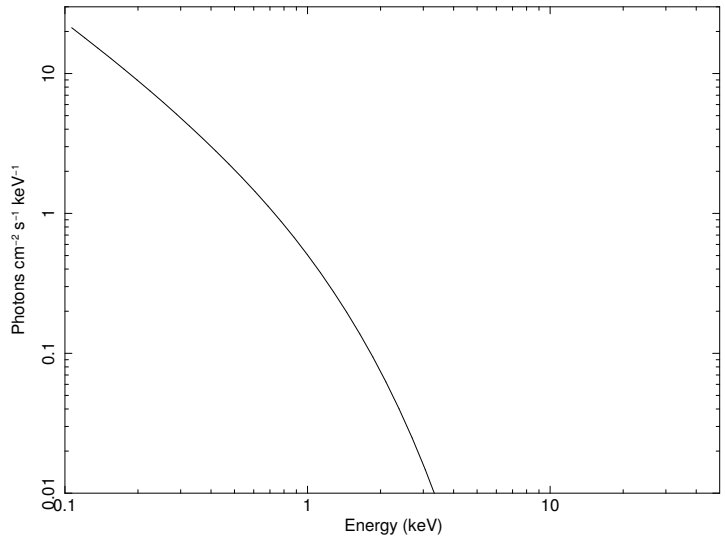

Figure 1.5: Plot showing an example of the spectrum produced by Bremsstrahlung emission. Created using the BREMSS model, with temperature kT set at 2.0 keV.

energy of the electron, if the energy before deceleration was high enough the resultant photon will be in the X-ray part of the electromagnetic spectrum. The resultant spectrum of Bremsstrahlung emission is continuous, with the peak becoming more intense and at higher frequencies as the energy of the electron increases. The total emission power density, integrated over all frequencies, is a function of the electron and ion densities, and the square root of the electron temperature.

1.2.3 Inverse-Compton

Inverse-Compton emission occurs due to the inelastic scattering between a photon and an electron. In this interaction the electron will transfer some of its energy to the photon. This process is important in an accretion disc as it can help to explain the presence of the power law component in the X-ray spectrum. The thin disc will produce black body spectrum, as described in Section 1.2.1. The photons produced in this way will then pass through a corona surrounding the disc. This corona represents active regions above and below the disc containing a population of non-thermal electrons. These relativistic electrons in this corona will then scatter the thermal photons to higher

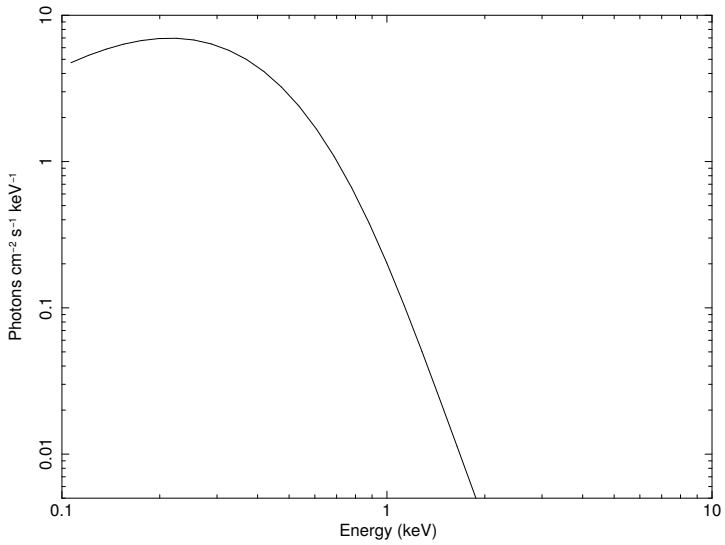

Figure 1.6: Plot showing an example of a spectrum produced by inverse-Compton emission. Created using the `COMPTT` model (Titarchuk, 1994). The input soft photon temperature is set at 0.1 keV, while the temperature of the plasma is set to 5.0 keV.

energies. The shape of the resulting spectrum will then be a power law with a lower limit at the energy of the unscattered thermal photons, and an upper limit determined by the energy of the relativistic electrons.

1.2.4 Synchrotron

Synchrotron radiation is due to the acceleration of relativistic electrons in a curved path or orbit. In an accretion disc synchrotron radiation would be produced when electrons spiral through magnetic fields. This is another potential origin of the hard X-ray emission, as the synchrotron radiation will have non-thermal power law spectra. The range of frequencies this power law emission can produce is extremely broad, reaching from radio all the way up to X-rays. The scattering of the photons produced this way by the electrons that emitted them (known as Synchrotron self-Compton radiation) can also produce even higher energy photons. Figure 1.7 shows an example of a model of Synchrotron emission. This model is a little different from the theoretical power law due to the distribution of electrons being an exponentially cut off power law.

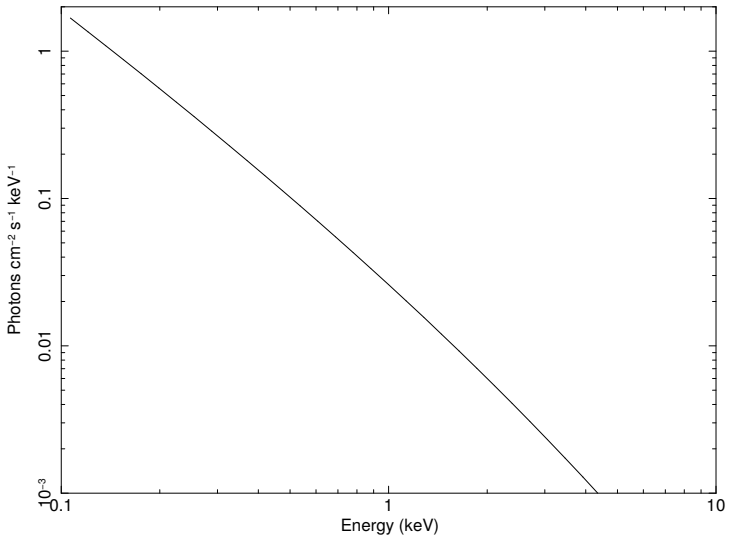

Figure 1.7: Plot showing an example of the spectrum produced by Synchrotron emission. Created using the `SRCUT` model (Reynolds & Keohane, 1998; Reynolds, 1999). The radio spectral index is set at 0.5, and the break frequency at 2.42×10^{17} Hz.

1.2.5 Line Emission

Line emission is the result of energy level transitions within atoms or molecules. When an electron in an excited ion drops from a higher energy state to a lower one a photon will be emitted. Since energy needs to be conserved the photon will have energy equal to the difference between the initial, higher energy state E_2 and the final, lower energy state E_1, i.e. $E_{photon} = E_2 - E_1 = h\nu$. So the frequency of the emitted photon is entirely dependent on the difference between the two energy levels.

For a given atom or molecule there will be a finite number of energy differences. Each transition will involve different energy levels so photons can be produced over a wide range of frequencies. This creates an emission spectrum, with each element producing a unique spectrum.

1.3 Outbursts

Low Mass X-ray Binaries spend most of their time in quiescence, with very low luminosity in X-rays and other wavebands. Occasionally though this will be interrupted by outbursts that usually last for weeks-months during which the X-ray luminosity can be comparable to the Eddington luminosity $L_{\rm Edd}$ ($\sim 10^{38} M_{BH}/{\rm M}_{\odot}$ erg s^{-1}). The mass transfer rate from the secondary will remain constant, so this large change in luminosity suggests there must be some change in the nature of the accretion flow during outbursts.

The observational signature of the beginning of one of these outbursts is the rapid increase in X-ray luminosity, rising by 2 or 3 orders of magnitude in a matter of days or weeks. This increase can be recorded by an All Sky Monitor (ASM), an X-ray telescope designed to track the count rates from known X-ray sources by taking measurements approximately once a day. Figure 1.8 shows the long term light curve for the LMXB GX 339-4 with data from the *RXTE*/ASM (see Chapter 2 for details) over a period of around 16 years. This shows clear outburst events lasting approximately a year separated by period of quiescence.

LMXB outbursts are thought to occur due to the increase in the mass accretion rate onto the compact object, with the reasons for the change in mass accretion rate being described by the Disc Instability Model (DIM; e.g. van Paradijs, 1996; King & Ritter, 1998; Lasota, 2001; Dubus et al., 2001).

In the quiescent state the accretion disc gas is mostly neutral and has a low viscosity. The rate at which mass is transferred from the secondary to the disc is typically larger than mass accretion rate through the disc onto the black hole, such that the disc mass and temperature increase over time. As the temperature approaches $\sim 10^4$ K hydrogen ionisation causes a dramatic change in the opacity of the gas within the disc that is associated with an increase in the disc viscosity. This triggers an increase in the accretion rate onto the primary, causing an outburst. As the mass

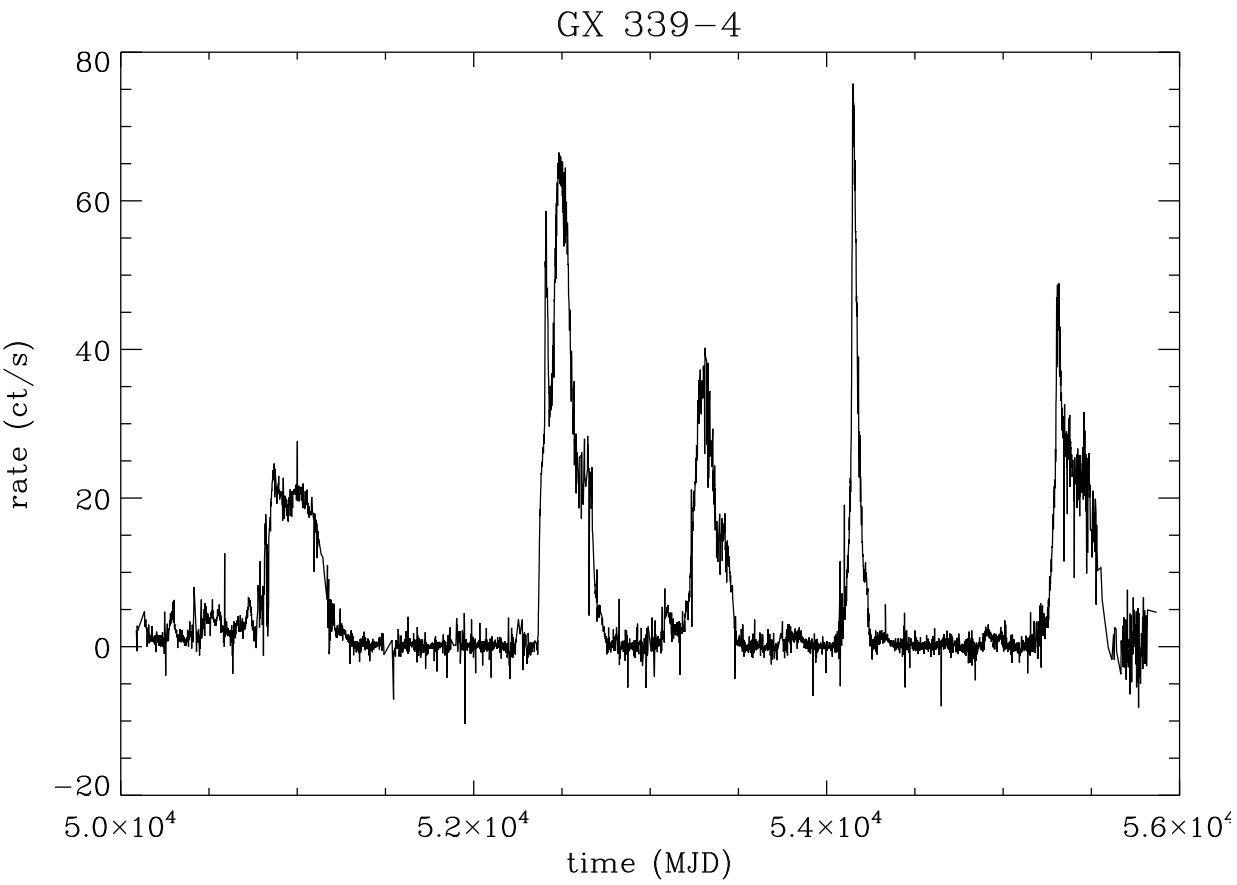

Figure 1.8: Light curve for the low mass black hole binary GX 339-4 using data from the *RXTE*/ASM.

accretion rate overtakes the mass transfer rate eventually the inner accretion disc will begin to empty. The disc then cools and returns to a low mass accretion rate state and the outburst ends.

This model well explains the observed behaviour of the dwarf novae (DN) sub-class of cataclysmic variables (CVs; white dwarf binary systems). The DIM's prediction of periods of outburst and quiescence matches the features of light curves from DN. Figure 1.9 demonstrates this behaviour. It shows the light curve from the dwarf nova SS Cyg and clearly shows the regular outbursts.

However, for neutron star and black hole systems the observations of outbursts show a different kind of behaviour to the white dwarf systems, particularly at the decaying stages of the outburst (Chen et al., 1997; Kuulkers, 1998; Jonker et al., 2010; Stiele et al., 2012; Tomsick et al., 2014). The decay of outbursts from these objects show an exponential decay in the luminosity (King &

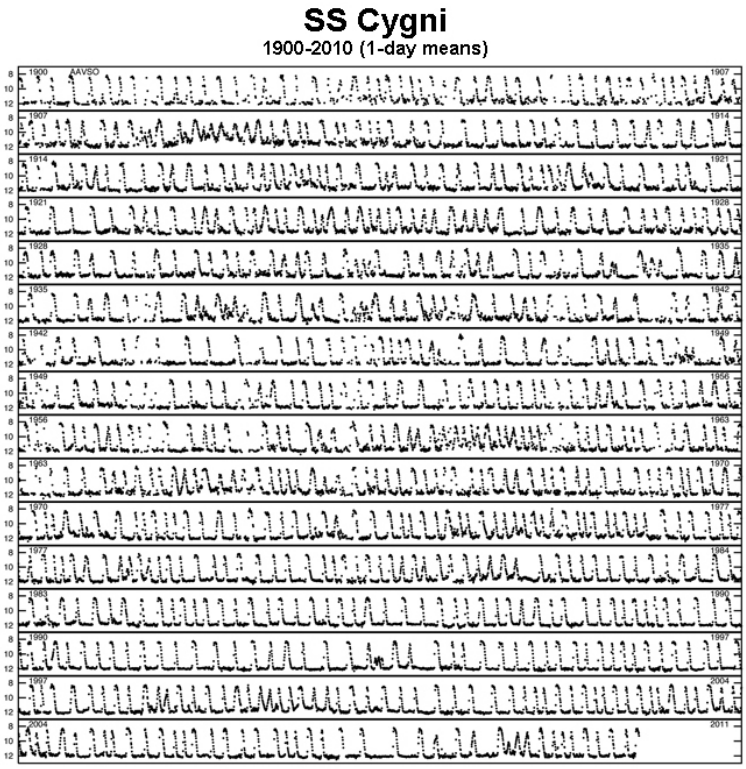

Figure 1.9: Light curve showing 300 days of data for the dwarf nova SS Cyg. It illustrates the periodic and uniform nature of outbursts from such objects. Figure courtesy of the AAVSO International Database (Kafka, 2018).

Ritter, 1998; Lasota, 2001; Dubus et al., 2001), so while the rising stages and the disc in quiescence can still be modelled by the DIM, there will be another factor present in the disc to explain these differences.During the outburst the disc (and related corona/jet) is a powerful source of X-rays. These X-rays irradiate the accretion disc and raise its temperature above that expected from viscous heating alone, keeping the disc in the hot, high viscosity phase. The mass transfer rate through the disc towards the primary is faster than mass transfer into the disc from the secondary, and over time the disc becomes depleted and the mass available to accrete will drop. This reduces the level of X-ray irradiation and allows the disc to return to its cool, low viscosity state. At this point the source returns to quiescence.

The timescales of these two instabilities (thermal and viscous) are different. When the disc becomes thermally unstable (small changes in temperature create further increases in temperature)

the timescale for growth is $t_{th} \sim \alpha^{-1} t_{dyn}$. While for the viscous instability (small changes in $\dot{M}$ generate larger increases in $\dot{M}$) the timescale is $t_{visc} \sim \alpha^{-1}(H/R)^{-2} t_{dyn}$. H is the vertical scale height of the disc, t_{dyn} is the dynamical (or orbital) timescale, and α is the Shakura-Sunyaev α parameter. For a thin disc the scale height H will be much smaller than R which makes it such than the thermal timescale is much faster than the viscous timescale, and the thermal instability can occur without much change in the amount of mass in the accretion disc at that particular radius. Whereas for a thick disc the timescales will be approximately equal and the disc can react to changes in temperature.

1.3.1 Spectral States

Within each outburst, XRBs usually show several distinct 'states' characterised by particular X-ray spectral and timing behaviour, but also correlated with other behaviour such as radio emission (e.g. Remillard & McClintock, 2006; Done et al., 2007; Belloni, 2010). The main two states are the 'soft' (sometimes also referred to as 'high' or 'thermal dominated') and 'hard' (alternatively 'low'), with intermediate states occurring during the transition between the two. The 'soft' and 'hard' terms refer to the different X-ray energies. Soft X-rays have lower energy, generally less than a few keV, while hard are higher energy, extending up to a few hundred keV.

Soft State

The soft state is generally seen at high luminosities near the peak of outbursts. In this state the X-ray spectrum is dominated by thermal emission from an optically thick accretion disc with a temperature $T_{\rm peak} \sim 1$ keV (Remillard & McClintock, 2006), and a weak, non-thermal tail of emission to higher energies. The X-ray emission is powered by a luminous, radiatively efficient accretion disc that is assumed to extend in to the innermost stable circular orbit ($r_{\rm ISCO} = 6r_g$ for a

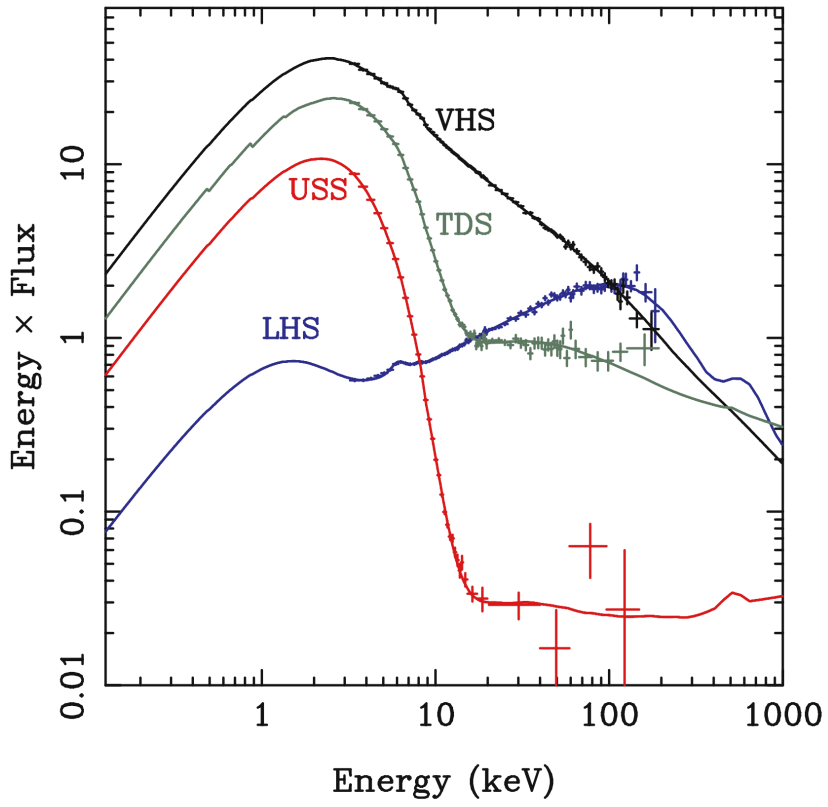

Figure 1.10: Four spectra from different states for the 2005 outburst of GRO J1655-40. The crosses represent data points, while the solid lines indicate the fitted model. From (Done et al., 2007).

non-rotating BH, where the gravitational radius is $r_g = GM/c^2$). The soft state shows only weak rapid X-ray variability and weak, if any, radio emission (Fender et al., 2009).

Figure 1.10 shows a sample of spectra from the 2005 outburst of the LMBHB GRO J1655-40. The grey line labelled TDS (for thermal dominated state) shows a typical soft state spectrum with the thermal black body component peaking at ~ 3 keV and a weak power-law contribution from ~ 10 keV onwards. The red line shows an example of the ultrasoft state (USS), an extreme variety of the soft state where the high energy tail is far weaker than usual.

Hard State

The hard state – always seen during the rise to outburst and decay to quiescence, and sometimes near outbursts peak – is characterised by an X-ray spectrum dominated by a non-thermal (power law) component, extending up to energies ~ 100 keV, with a much weaker, cooler thermal component ($T_{\rm peak} \lesssim 0.3$ keV) sometimes detectable at lower energies (Remillard & McClintock, 2006). The radio and timing properties are also different: the hard state shows strong, rapid X-ray variability (van der Klis, 2006; Belloni, 2010) and persistent (flat spectrum) radio emission (Fender et al., 2009). The source of the non-thermal emission is not fully understood but is often thought to be the result of either inverse-Compton scattering (of soft photons emitted from the accretion disc) in a corona of hot electrons above the disc (Haardt & Maraschi, 1993; Dove et al., 1997; Poutanen, 1998), or synchrotron and self-Compton emission produced in the base of the radio jet (Markoff et al., 2001, 2005).

In Figure 1.10 the blue line labelled LHS (for low hard state) shows an example of the spectrum produced during the hard state. The spectrum shows evidence of a weak black body component at $E \approx 1$ keV but is dominated by the power law component at higher energies (~ 100 keV).

Intermediate

The intermediate state is the name given the the period of outburst where the source rapidly transitions from the soft to the hard state (and vise versa). In the hard state (both rising and decaying) there is often little change in the spectra of the source so it is during the intermediate states where the majority of spectral evolution occurs. During the hard to soft transition the power law component will rapidly steepen and decrease in luminosity, while at the same time the black body component becomes dominant, leading to an overall softening of the spectrum. The rapid X-ray variability also undergoes large changes during this state, decreasing as the source enters the soft

state. The reverse process occurs during the soft to hard transition with the spectral and variability properties returning to almost exactly the same as the rising hard state (Belloni, 2010).

The intermediate state is also associated with a change in the jet behaviour and radio emission (Fender et al., 2009). In the hard to soft transition at least the radio emission becomes much more variable, with flare events being common during this phase, while the overall trend is a steady decline. Observations have also shown in certain cases mass ejection events related to these flares.

Quiescence

Despite the fact that most BHBs spend most of their time in quiescence, it is difficult to study them at these lowest luminosities due to observational constraints. This means, unfortunately, that the nature of the quiescent state and its relation to the soft and hard state are not well known. The quiescent state has shown evidence of having a softer spectrum than the hard state, but it is unknown if this actually the result of a change in the nature of the accretion. In the hard state the presence of the jet becomes increasingly important as luminosity decreases, so whether or not the jet still remains important in quiescence is one of the main unanswered questions.

1.3.2 Hardness Intensity Diagram

The way a source transitions through these different spectral states during an outburst can be shown visually through a hardness intensity diagram (HID), an example of which has been provided in Figure 1.11 for the 2002 outburst of the LMXB system GX 339-4.

Hardness is defined as the ratio between the flux of a hard and a soft energy band. For the example in Figure 1.11 these energy bands are $\approx 3-6$ keV for the soft band and $\approx 6-10$ keV for the hard. This hardness ratio is then plotted against the total count rate over the entire energy range

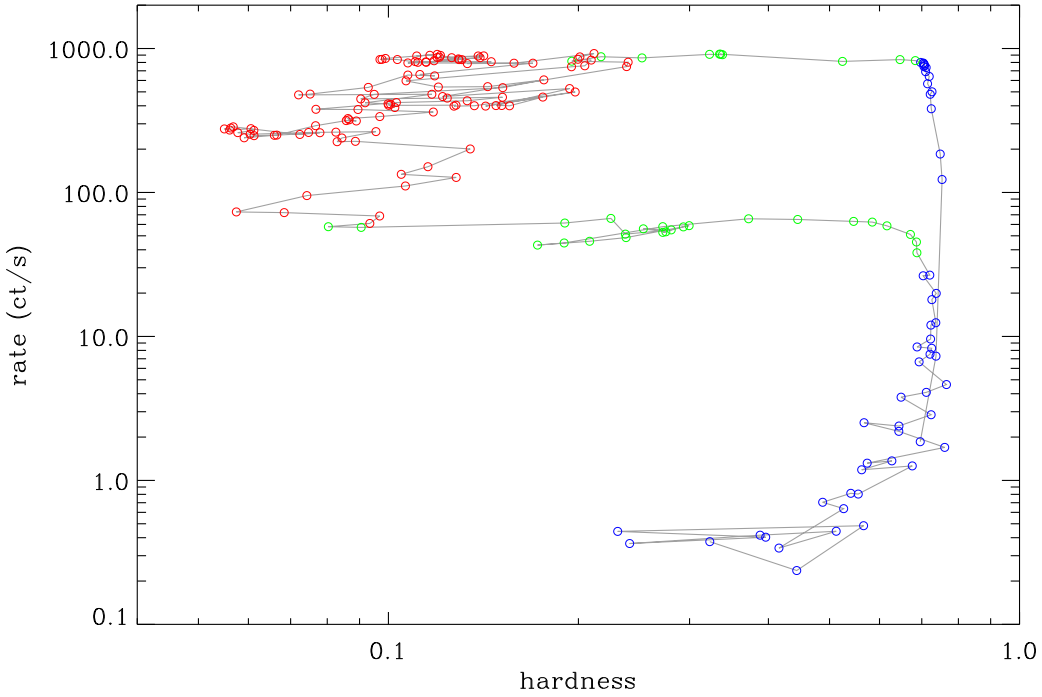

Figure 1.11: Hardness intensity diagram for the 2002 outburst of GX 339-4. The plot has been produced using data from the *RXTE*/PCA.

covered by both the soft and hard energy bands. So this shows which parts of the outburst are dominated by the soft thermal black body emission, and which parts are dominated by the hard power law emission.

The general shape of the HID is consistent for almost all black hole XRBs, forming a 'flag' shape. The source in quiescence will be in the hard state with a hardness close to one. When the outburst begins the X-ray luminosity rapidly increases with very little change in spectral shape, and therefore hardness, which produces the vertical rightmost side of the HID. At some luminosity (generally $10 - 50\%$ of L_{Edd}) the source will then suddenly transition over to the soft state, and the hardness quickly drops close to 0.1. Once fully in the soft state the hardness will vary but still stay at 0.1 as the source goes through periods of maxima, plateaus and finally a decay in the X-ray luminosity. At a luminosity of around 2% of L_{Edd} the transition back into the hard state will occur with little change in luminosity, forming the bottom of the HID. After the source fully

enters the hard state a final stage of decay back into quiescence completes the outburst cycle.

1.4 Disc Geometry

One of the current problems to solve in the study of XRBs is determining the exact nature of the mechanism that governs change in spectral states. It is clear that there must be some change to the accretion disc between the hard and soft states if we are to explain the distinct differences in the energy spectra, variability and radio emission, but it is the form of this change that has been the source of much debate.

1.4.1 The Truncated Disc Model

The most popular model used to explain the existence of the soft and hard states is one which involves a truncated disc (Esin et al., 1997; Poutanen et al., 1997). This allows for both states by letting the size of the disc change as a function of the mass accretion rate. Figure 1.12 demonstrates this effect visually. If we refer back to Figure 1.10 we can match each spectral state to a point in the cycle of the truncated disc model. At low luminosities the standard (optically thick, geometrically thin) disc will be truncated at a large distance from the central BH, with a hot, optically thin flow with relatively few photons from the disc illuminating this inner flow. The small number of seed photons from the disc entering the hot flow means that these is little Compton cooling of the electrons which produces the high energy emission peaking at $\sim$ 100keV (the blue spectrum in Figure 1.10). During an outburst, as the mass accretion rate starts to increase, the standard disc will slowly move inwards providing the hot inner flow with more cool seed photons. Eventually the hot inner flow will condense back into a standard disc. The switch from the hard state to the soft state then occurs at this point, with the emergence of an inner disc. This then produces the types of spectra seen as the red and green spectra in Figure 1.10, as the disc dominates

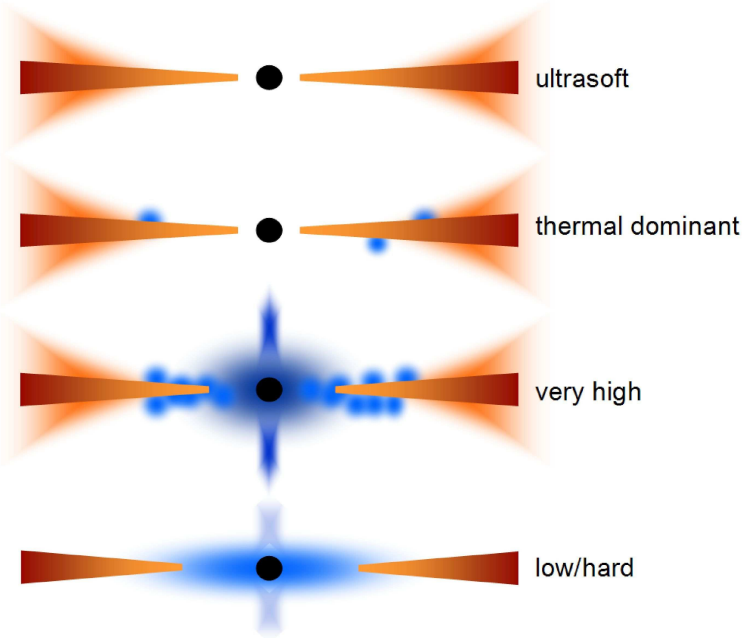

Figure 1.12: Cartoon demonstrating the geometry of the truncated disc model. From Done et al. (2007).

the total emission with only a small contribution from active regions around the disc forming a steep high-energy tail.

This model has been used to great success to explain a large number of the observed features of XRBs, and it is generally agreed that the disc truncates during quiescence (Tomsick et al., 2009). However, there are claims that certain hard state observations can be fit with a disc requiring no truncation prompting discussion on the extent to which the truncated disc model can be used to explain state changes.

1.4.2 The Inner Radius

For a standard accretion disc around a non-spinning BH the inner radius extends down the the innermost stable orbit, r_{ISCO}, which is located at $6R_g$. For a spinning BH this value will change

as a function of the dimensionless spin parameter a. For prograde orbits, when the spin of the BH is aligned with the rotation of the disc material a is positive and r_{ISCO} can decrease to a minimum of $1.23R_g$. Whereas for negative spins, retrograde orbits, the location of the innermost stable orbit increase up to a maximum of $9R_g$.

Given that the truncated disc model expects the inner radius of the disc to not be located at r_{ISCO} during the hard state, and is instead truncated at a radius r_{in} (where in this case $r_{in} >> r_{ISCO}$), it then becomes important to be able to measure this inner radius to ascertain the feasibility of the model. This is generally done in two different ways using X-ray spectra: through the fitting of the iron Kα line, or through the measurement of r_{in} using disc models.

Observations from accreting BH systems often show evidence of an interaction between emissions originating close to the black hole (from the power-law component) and the accretion disc. These interactions imprint additional features on the observed spectrum. These features include iron Kα line emission at 6.4keV and a flattering of the spectrum above 10 keV - the so called Compton hump - originating from Compton scattering of photons by cool electrons. The most relevant of these two in this work is that of the Fe-K emission which affects the observed spectrum in the $6 - 8$ keV range. This emission is thought to mostly emanate from the inner regions of the disc close to the BH so the properties of the line emission are affected by relativistic effects. For a non-relativistic disc the observed spectrum of the iron line would take a symmetric double peaked profile due to the blue- and red-shifting of the line from the approaching and receding sides of the disc respectively. The effects of special and general relatively modify the emission further. Relativistic beaming of the emitted radiation strengthens the blue peak, while the effects of the transverse Doppler effect and gravitational redshifting displace the entire line profile to lower energies. The end result is the sum of the effects on each radius within the disc, with the smallest radii producing the broadest spectrum. This means the width of the iron line can probe the inner radius of the disc; a heavily truncated disc would produce much narrower features than one which extends down to r_{ISCO} all other things being equal (e.g.the pattern and illumination and ionisation

state of the disc), so fitting the iron line using a model of this 'reflection' component can provide an estimate of r_{in}. Popular relativistic reflection models used for this purpose include `REFLIONX` (Ross & Fabian, 2005) and `RELXILL` (García et al., 2014).

Disc models attempt to determine the location of r_{in} by first measuring the temperature at the innermost regions of the disc. Using the Stefan-Boltzmann relation, $L \propto aT^4$, a inserting the maximum temperature and its corresponding luminosity returns the radiative area of the inner disc as the maximum temperature will occur at the innermost regions. Many of the disc models make certain assumptions about the nature of the disc component which can raise issues when calculating values of r_{in}. For example, the colour correction fraction, f_{col}, is used to correct for deviations from the standard black body model due to the vertical structure of the disc and any absorption, scattering and re-emission that would occur in the disc atmosphere (Shimura & Takahara, 1995).

It is defined as the ratio of the colour temperature, T_C, and the effective temperature, T_{eff}. This value is mostly assumed to be fixed at ~ 1.7 during both the soft and hard state, based on observations in the soft state and theoretical arguments. However, there have been studies investigating the use of f_{col} as an alternative to a truncated disc (Salvesen et al., 2013). In these studies they find that a increase in f_{col} as the source transitions into the hard state is a viable alternative to a receding disc component. Another issue, particularly in the hard state, is that of the effect from the Comptonised component. Rykoff et al. (2007) demonstrated that the choice of continuum model had an effect on the measured inner radius, as well as noting that heating via illumination of the disc from the harder X-rays will lead to inaccuracies in r_{in} estimates.

Most models agree that a disc extending all the way down to r_{ISCO} is likely to exist in the soft state, so it is observations in the hard state that prove the most valuable for both supporting and challenging the idea of disc truncation. One of the earlier challenges to the truncated disc model came from Miller et al. (2006b). There had been earlier works that had reported the presence of a

cool thermal component in hard state observations of Cygnus X-1 (Barr & van der Woerd, 1990; Balucinka & Hasinger, 1991; Ebisawa et al., 1996), but these were interpreted as possibly being due to accretion of its companions wind, not the presence of a disc. Miller et al. (2006b) present data from *XMM-Newton* for the system GX 339-4 and find that a standard cool accretion disc may extend down to a radius close to r_{ISCO}, and suggest that the region emitting the hard X-rays is the base of a jet. These results were countered in Done & Diaz Trigo (2010), who explained that the *XMM-Newton*/MOS data which was used in Miller et al. (2006b) is piled-up, and instead, use the simultaneous pn timing mode data (see Chapter 2 for details on instrumentation). With this data set they find a much narrower Fe line supporting a truncated disc.

In the years following those results there has been a wealth of spectral analyses of X-ray data, with no clear conclusion on the necessity of truncation during the bright hard state. Reis et al. (2010) presented results from both disc and iron line fitting of eight BH sources observed in the hard state by *XMM-Newton* and found that none of them showed strong evidence of truncation from either method, suggesting truncation only occurs below $\approx 10^{-3} L_{Edd}$. However the observations studied in this work have been analysed by various other authors who instead present evidence of a truncated disc (Done & Gierliński, 2006; Yamada et al., 2009; Done & Diaz Trigo, 2010; Kolehmainen et al., 2014). There is also the issue of the consistency between the two methods of measuring the inner disc radius. Kolehmainen et al. (2014) found that measuring r_{in} using disc emission and reflection lead to different results. They find that in some cases the disc emission suggests a lower truncation radius than the reflector, but warn that due to the relatively small contributions from the disc and reflector in the hard state there could be errors due to issues with instrument calibration. Recently, Steiner et al. (2017) presented another study of GX 339-4 data, with the key difference in their method being the consideration of the Comptonisation of the reflected emission, implemented in a photon-conserving, self-consistent manner. With the reflection being generally linked to the regions of highest Comptonisation this is likely an important feature, but is usually ignored. They find that their self-consistent model can produce a well fit spectrum with little truncation, and that, from photon-counting, a solution with large scale

truncation would require unrealistically high mass accretion rates.

There have been alternate models presented for the geometry of XRBs that do not require truncation during the bright hard state. Merloni & Fabian (2002) suggested a standard, thin disc which generates a magnetically dominated coronae, where the power of this coronae increases as the mass accretion rate decreases. Beloborodov (1999) considers a system in which the height of magnetic flares which feed the corona determines the state. During the hard state the emission of the hard X-rays would be beamed slightly, explaining the low reflection fractions. Liu et al. (2007a) investigated the possibility of an inner accretion disc within the ADAF, fed by the condensation of the ADAF due to Compton cooling by the soft photons from the optically thick disc. They find that this model would apply for the brighter stages of the hard state, down to a luminosity of $L/L_{Edd} \approx 0.001$. Begelman et al. (2015) use MRI theory to suggest that changes in spectral state could be due to changes in the relative strengths of two different MRI-active regions in the magnetically supported accretion disc. In their model the hard and intermediate states are due to the MRI being triggered in the hot corona, whereas in the soft state this region would not be active.

1.4.3 Quasi-Periodic Oscillations

As we have seen studies of spectral data alone can sometimes produce ambiguous or inconsistent results so Fourier analysis techniques are also often used as an alternative and complementary method to probe the inner regions of the accretion disc. These techniques are used to assess the variability properties of light curves from XRBs, with one of the most widely used techniques being the power spectrum. The power spectrum shows which frequencies contain the variability power, where in this case power is the magnitude of the time series Fourier transform squared. Power spectra from XRBs show a broad-band noise component, and often, sharp peaks known as quasi-periodic oscillation (QPOs).

QPOs have been observed in accreting systems of virtually all types, from Cataclysmic Variables up to Active Galactic Nuclei. They feature strong peaks that can be associated with accretion based timescales, although their exact origin is still unknown. QPOs in XRBs can be broadly split into two different groups: low frequency QPOs and high frequency QPOS. These groupings are based on the frequency range at which they are observed, with low frequency QPOs extending up to ≈ 50Hz (Casella et al., 2005; Motta et al., 2012), while high frequency QPOs are generally those above ≈ 100Hz (Strohmayer, 2001; Belloni et al., 2012). The low frequency QPOs can then be divided further into three sub-categories labelled as A, B and C. These three smaller groups are defined by features such as their centroid frequency and width, as well as the properties of the broad-band noise component. Type-A QPOs are broad ($\nu/\Delta\nu \leq 3$) and weak, with the central frequency between 6-8 Hz (Homan et al., 2001). Type-B have stronger and broader peaks with $\nu/\Delta\nu \geq 6$, located at either 6 Hz or 1-3 Hz (Motta et al., 2011b). Type-C QPOs also have strong, narrow peaks with $\nu/\Delta\nu \geq 10$. The frequency range in which Type-Cs are found in is much larger than the other two types though, with them being found between a few mHz and $\sim$10 Hz in the hard state, and extending up towards 30 Hz in the soft state (Motta et al., 2012). Figure 1.13 shows an example of types A, B and C QPOs and their differences.

Type A and B QPOs are fairly rare, meaning the majority of those observed fit into the type C group which have been found to exist in all states (Motta et al., 2012). To explain the origin of type C QPOS a model involving a truncated disc has been proposed and has provided some strong evidence in the case for the existence of truncation (Ingram et al., 2009). The basic picture of the geometry suggested in this model is that of a binary system with the binary axis and the BH spin axis misaligned. In this scenario the accretion disc will be aligned with the binary axis, while the hot inner flow will be aligned with the spin axis, creating a break at the disc inner radius. The type C QPOs then originate from the Lense-Thirring procession of a radially extended section of the hot inner flow. As the source transitions towards the soft state the disc inner radius decreases forcing the radius of the processing flow to also decrease leading to the creation of QPOs of a higher frequency seen in the soft state.

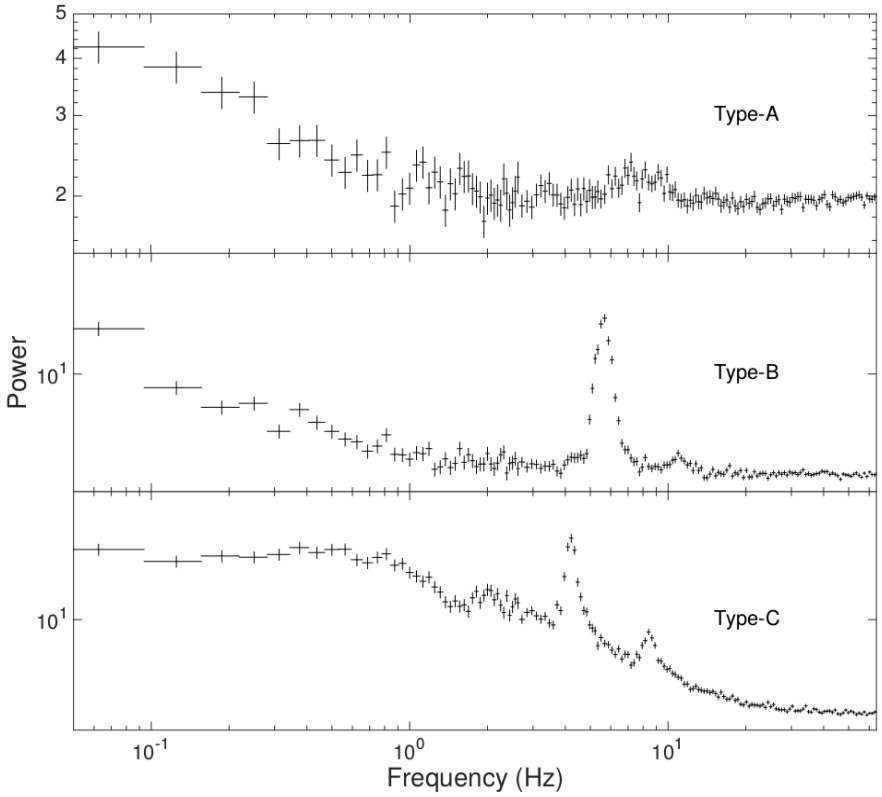

Figure 1.13: Power spectra from GX 339-4 to demonstrate the shape of type A, B and C low frequency QPOs. From (Motta et al., 2011a).

To explain the nature of the high frequency QPOs the relativistic procession model (RPM) was proposed (Stella & Vietri, 1998; Stella et al., 1998). This was originally just used to explain the existence of QPOs in NS systems but has since been broadened to include BH XRBs as well (Stella & Vietri, 1999; Motta et al., 2014). The assumption of this model is that three QPOs (the type C low frequency QPO and two high frequency QPOs) are associated with the strong-field general relativistic frequencies of particle motion close to r_{ISCO}. These frequencies are described by three relatively simple equations which connect the QPOs with the mass and spin of the BH. This model was fit to observations of the system GRO J1655-40 the only source which has had the three QPOs detected simultaneously, and found a mass consistent with that found from optical/NIR studies (Motta et al., 2014).

1.5 The Interstellar Medium

When observing X-ray binaries one more factor to take into consideration is absorption from the Interstellar Medium (ISM). The space between stars is not empty, and is instead filled with a mixture of gases and dust which together is called the ISM. The majority of the ISM is hydrogen ($\approx 90\%$), with a smaller percentage of helium ($\approx 10\%$) and a fractional amount of heavier elements created during thermonuclear fusion in stars and spread by stellar winds or supernova. Many analyses of the composition of the ISM have been performed in recent years since the launch of *XMM-Newton* and *Chandra* both of which are equipped with high resolution X-ray spectrometers. The results of these studies indicate the presence of a multi-phase ISM structure: a cold phase of a mixture of dust, molecules and mostly neutral gas at $< 10^4 K$, a warm phase of weakly ionised gases at $\sim 10^4 K$ and a more highly ionised hot phase at $\sim 10^6 K$. In order to observe systems of interest we have to look through this medium. This presents a source of error as the ISM will absorb or scatter the incoming X-rays, so it is important that we are able to understand and model the ISM accurately to apply the best corrections to observational data.

The ISM forms a disc in the place of our Galaxy (with diameter ≈ 30 kpc and thickness ≈ 0.7 kpc), and since many of known X-ray binaries are located close to Galactic center, it will have a large impact on observed spectra. The X-rays are absorbed through the photoelectric effect, where the total photoelectric absorption coefficient σ_{ISM} is defined as the sum of contributions from the three different phases,

$$\sigma_{ISM} = \sigma_{gas} + \sigma_{molecules} + \sigma_{grains}, \tag{1.13}$$

where σ_{ISM} is normalised to the total hydrogen number density N_H, which means that the observed X-ray spectrum of a source, after passing through the ISM, can be written as,

$$I_{obs}(E) = e^{-\sigma_{ISM}(E)N_H} I_{source}(E), \tag{1.14}$$

where the units of N_H are atoms cm^{-2} and I_{source} is simply the spectrum emitted from the source. When modelling absorption N_H is generally a fitted parameter, whereas σ_{ISM} is obtained by summing the photo-ionisation cross-sections of each of the atoms and ions that make up the ISM weighted by their abundances. The gas phase, for example, can be written as,

$$\sigma_{gas} = \sum_{Z,i} A_Z \times \ a_{Z,i} \times \ (1 - \beta_{Z,i}) \times \ \sigma_{Z,i}, \tag{1.15}$$

where $A_Z = N_Z/N_H$ is the abundance of element Z relative to hydrogen, $a_{Z,i} = N_{Z,i}/N_Z$ is the fraction of ions of element Z in the ith ionisation state, $\beta_{Z,i}$ is the fraction of ions in the other two phases (so $(1 - \beta_{Z,i})$ represents the fraction of ions in the gas phase), and finally $\sigma_{Z,i}$ is the total photo-ionisation cross-section of this ionisation state.

If we are to successfully model the features imprinted on a X-ray spectrum by the ISM then it becomes necessary to have both accurate cross-sections and an accurate value of N_H for any given target source. Two common methods of estimating the column density of hydrogen along the line-of-sight to a target system are by 21cm intensity mapping and the use of photoabsorption models.

1.5.1 21 cm Maps

The 21 cm line (also referred to as the hydrogen line or the HI line) refers to the electromagnetic radiation spectral line created by a change in energy state of neutral hydrogen atoms. In a neutral hydrogen atom the energy state when the proton and electron have parallel spins is slightly higher

than when the spins are anti-parallel. So when there is a change to an anti-parallel spin state a photon is produced with a wavelength of roughly 21 cm. Conducting radio surveys to measure the intensity of this emission allows a determination of the column density of the gas at any given location.

Two of the most commonly used 21 cm maps come from Dickey & Lockman (1990) and Kalberla et al. (2005). These can calculate a N_H estimate at any point on the sky based on a weighted averages of nearby measurements, typically within 1° of the target position. A more recent survey improving the 21 cm maps comes from Willingale et al. (2013) who use the X-ray afterglows from Gamma Ray Bursts to study the ISM. They add a correction to take into account the affect of molecular hydrogen, a significant contributor to galactic absorption. All three of these surveys suffer from the same weaknesses though in regards to their use in studying XRBs. The ISM does not only contain atomic or molecular hydrogen, but also atomic and ionised He, and metals. So the 21 cm maps can only work as a proxy for X-ray absorption. There is also the additional consideration of small-scale variations in the ISM, potentially from the source itself, that the 21 cm maps do not have the resolution to identify.

1.5.2 Photoabsorption Models

As a separate and complementary method to the 21 cm maps, X-ray high resolution spectroscopy has become a useful tool in studying the composition of the ISM. Data from grating spectrometers, such as the Reflection Grating Spectrograph (RGS) on *XMM-Newton* or the High Energy Transmission Grating Spectrometer (HETGS) on *Chandra* , pointed towards a bright X-ray source can be used to calculate elemental abundances and other useful features of the ISM in the study of XRBs. Due to the high penetrating power of the X-ray photons, direct measurements of absorption lines and edges can provide column densities for neutral and ionised species of various elements in both the gas and solid components of the ISM. Figure 1.15 shows an example of a

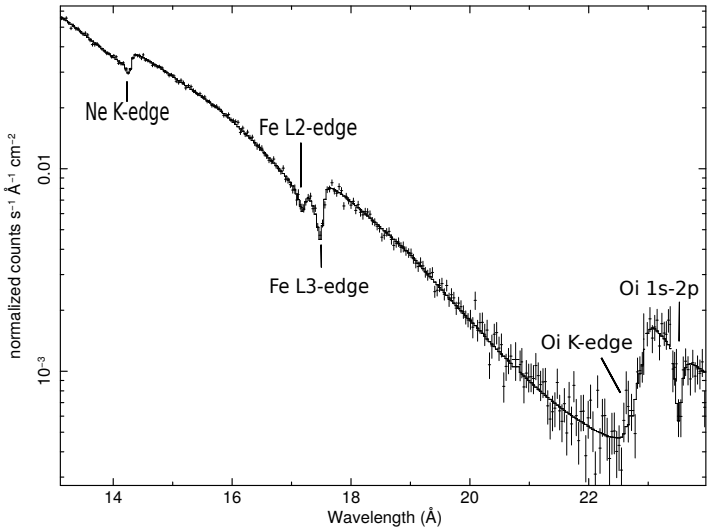

Figure 1.14: Simulated data from the *XMM-Newton* RGS instrument, assuming $N_H = 10^{22}$ cm^{-2}. Labels identify the key atomic features which can be resolved using data from grating spectrometers when fit with a photoabsorption model.

simulated *XMM-Newton* RGS spectrum labelled with atomic features from O, Ne and Fe. The simulated data represents a 5 ks observation assuming a hydrogen column density of $N_H = 10^{22}$ cm^{-2}, and that the relative abundances of the other elements is equal to that presented in Wilms et al. (2000) for the ISM.

Photoabsorption models are necessary to successfully trace the features of the ISM present in the grating spectrometer data. A variety of photoabsorption models have been used in the past. For example, `wabs`, which uses relatively simple photoelectric cross-section models from Morrison & McCammon (1983), solar abundances from Anders & Ebihara (1982) but had no contributions from ions, molecules and grains, and only allowed the column density of hydrogen as a free parameter. The model `Phabs` (Balucinska-Church & McCammon, 1992) remedied the latter issue, with adjustable abundancies for 17 elements. With revised cross-sections and abundances `TBabs` (Wilms et al., 2000) provided a further improvement, also including the effects of grains and H_2 molecules, but still only considered neutral atomic species. A recent model, `ISMabs` (Gatuzz et al., 2015), has the ability to also include ionised species and a database of the most accurate atomic data available for neutrally, single and doubly ionised species of 11 elements.

These models are compatible with X-ray spectral fitting software, and have already allowed a variety of studies to be performed on data from XRBs (e.g. Pinto et al. 2010, 2013; Gatuzz et al. 2013a, 2016).

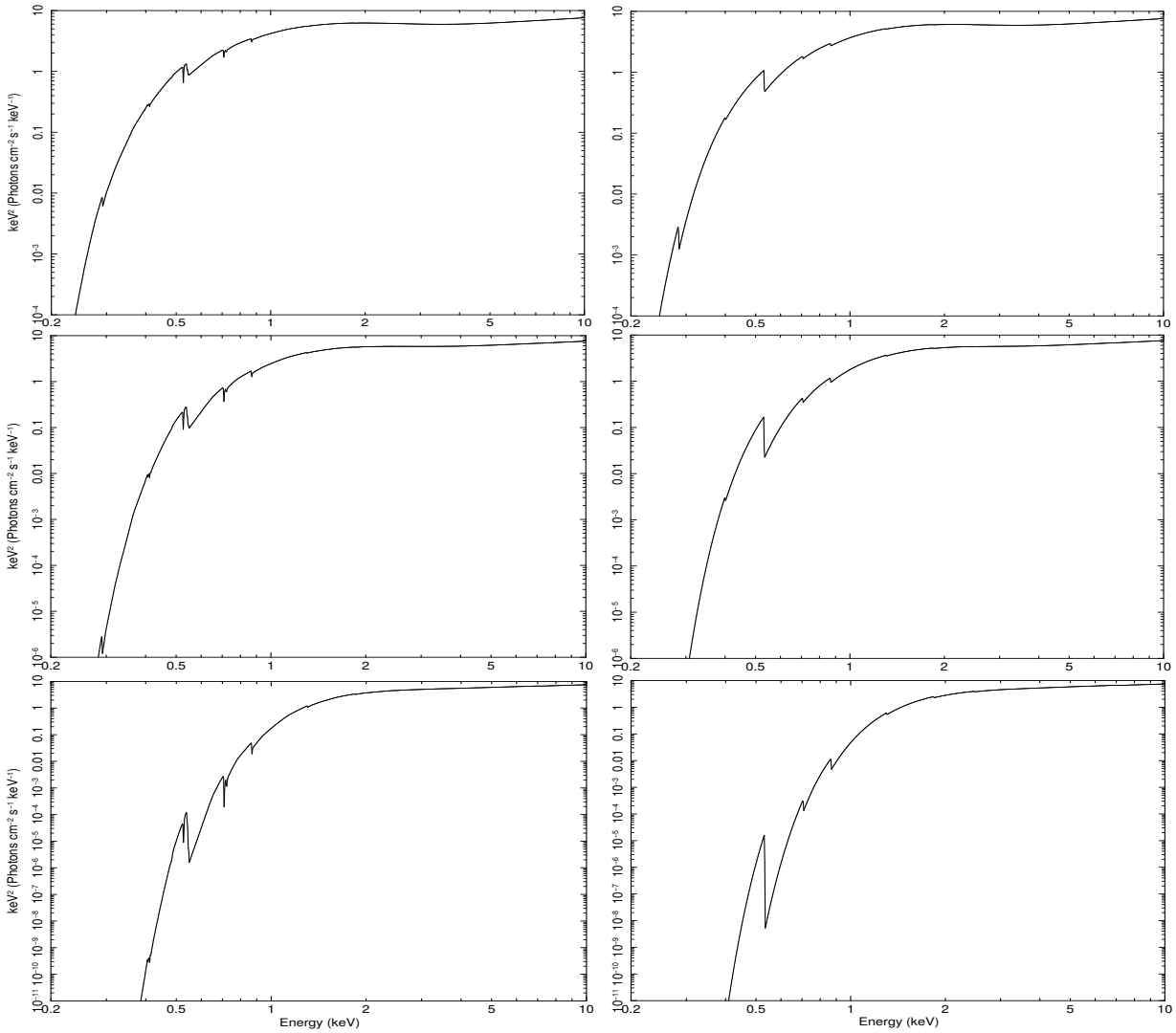

Figure 1.15: Plot to demonstrate the abilities of `ISMabs` and the difference between an older model (`WABS`). The left hand column is made with `ISMABS*(SIMPL*KERRBB)` at three different N_H values: 0.2×10^{22} cm^{-2} for the top plot, 0.5×10^{22} cm^{-2} in the middle, and 2.0×10^{22} cm^{-2} at the bottom. Continuum parameters are set at values typical for the hard state. The right hand column show the same model parameters but with `WABS` instead.

2

Instrumentation

2.1 Rossi X-ray Timing Explorer

The Rossi X-ray Timing Explorer (*RXTE*) was a satellite designed to observe transient X-ray astronomical sources such as black hole and neutron star binaries and X-ray pulsars. It was launched on 30th December 1995, and was active for 16 years when operations stopped on the 3rd January 2012. It was fitted with three separate instruments: the All-Sky Monitor (ASM), the Proportional Counter Array (PCA), and the High Energy X-ray Timing Experiment (HEXTE). Each instrument was designed with different energy ranges and resolutions, allowing them to serve different purposes. This thesis will be mostly concerned with data from the ASM and PCA instruments.

The ASM is a survey instrument which took measured count rates from known X-ray sources approximately once per day, allowing XRB systems to be monitored for outbursts. It consists of

three Scanning Shadow Cameras (SSC) with spatial resolution of 3×15 arcmin. The cameras can be rotated allowing 80% of the sky to be monitored for every 90 minute orbit. The instrument operates in the 1.5-12 keV band.

The PCA was a more sensitive instrument with a greater energy range which would be used to take more detailed measurements of a sources timing and spectral properties. There are five proportional counter units (PCUs) in the array, each with a collimator module giving a field of view of 1° FWHM. In total the collecting area is $\sim 6500 cm^2$. The PCA was a non-imaging instrument with an energy range of 2-60keV, an energy resolution of $< 18\%$ at 6 keV and a maximum time resolution of $1\mu s$. PCA could be operated in seven different modes running in parallel. All observations had data taken in two standard data modes (Standard 1 and Standard 2), but there were five other modes which allowed the user to vary energy and time resolutions depending on the science aims of the observation.

The PCA did not take background readings so models are used for estimations taking into account various properties of the spacecraft (e.g. location in its orbit, position of the current target on the sky). Observations of *RXTE* also have to take into account the South Atlantic Anomoly (SAA), an area of increased background effects which its orbit passed through.

During the course of the mission *RXTE* suffered from various technical issues affecting the operation lifetime of the individual PCA detectors. Impacts from micro-meteorites damaged PCU 0 and 1 in May 2000 and December 2006 respectively, and PCUs 3 and 4 were often out of action due to break-downs. Only PCU 2 was used constantly throughout the mission.

Both these instruments are equipped with proportional counters as their detectors. The proportional counter is a variety of gaseous ionization detectors. The proportional counter is filled with an inert gas (Xenon in the case of *RXTE*). When a photon enter the detector and interact with the gas atoms a number of ion pairs (electrons and partially ionised gas atoms) will be created. Anodes within the detector are held at a positive potential. This causes the electrons to drift towards

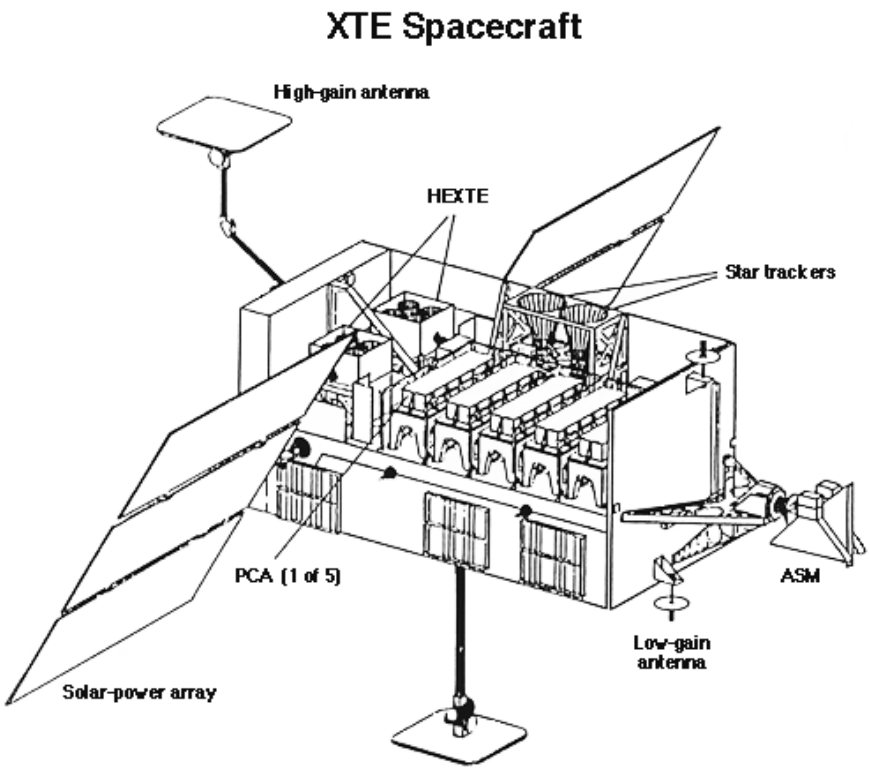

Figure 2.1: Schematic of the RXTE spacecraft.

the anode creating collisions with other gas atoms and more electrons. A runaway process known as an 'avalanche' then begins as more and more electrons drift towards the anode. The quantity of charge produced in the avalanche can then be measured.

Figure 2.1 shows the spacecraft schematic. It shows the location of the three instruments within the satellite as well as the additional features (antenna, solar panels, etc). The third instrument is the High Energy X-ray Timing Experiment (HEXTE). This instrument was not used as part of the work in this thesis so will not be discussed here.

2.2 Swift

The *Swift* Gamma-ray Burst Mission was launched into a low Earth orbit in November, 2004. *Swift* is a multi-wavelength mission primarily concerned with the study of gamma-ray bursts (GRBs), using its rapid slew capabilities to quickly point in the direction of possible GRBs. However, given that two of its three instruments operate in wavebands which include X-rays this mission has also proved useful in the monitoring and study of outbursts from XRBs. The three instruments on *Swift* are: the Burst Alert Telescope (BAT), the X-ray Telescope (XRT) and the Ultraviolet/Optical Telescope (UVOT).

The BAT is *Swift*'s survey instrument. It covers a large area of the sky (up to three steradians) which allows it to monitor known X-ray sources. This instrument consists of a coded-aperture mask of lead tiles above a detector plane of CdZnTe hard X-ray detector tiles, and operates in the 15-150 keV energy range. In the context of observations of XRBs, this means that the BAT will only detect the hard X-ray emission from outbursts and so can be used just track the evolution of the hard X-ray emission, in contrast to the *RXTE*/ASM which extends to much softer X-rays.

The XRT is a sensitive, imaging spectrometer. Due to its imaging capability ($\approx$ 20 arcsec resolution) it has a low background and so is capable of observing outbursts down to much lower fluxes than those accessible by *RXTE* which was background limited. The XRT is equipped with a Wolter Type-1 X-ray telescope with 12 nested mirrors, focused onto a single MOS CCD. The instrument has an energy range of 0.2-10keV.

2.3 XMM-Newton

XMM-Newton (Jansen et al., 2001) was launched in December 1999 by the European Space Agency (ESA). *XMM-Newton* operates in a high elliptical orbit of $\sim$ 2days, and carries three co-

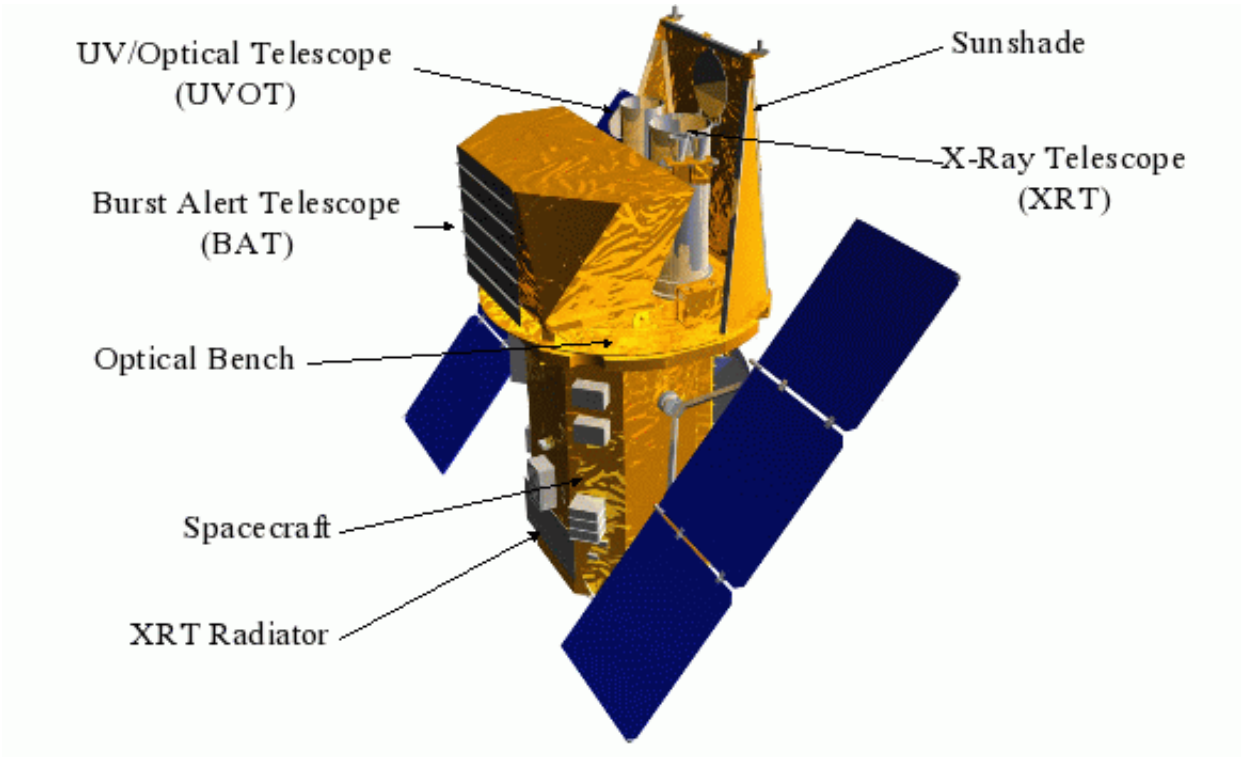

Figure 2.2: Schematic of the Swift spacecraft.

aligned X-ray telescopes, with three EPIC imaging spectrometers (Strüder et al., 2001), two RGS reflection grating arrays (den Herder et al., 2001), and a single Optical Monitor (Mason et al., 2001). The three EPIC cameras are made up of a single EPIC-pn camera and two EPIC-MOS imaging detectors. Only data from the EPIC-pn and RGS instruments are used in this thesis.

The EPIC cameras provide imaging in a 0.2-15 keV energy range. The EPIC-pn camera consists of twelve 3 x 1 cm pn-CCDs arranged into four quadrants onto a single wafer, with each CCD capable of independent operation. Each chip contains 200 x 64 pixels with each pixel measuring 150 microns square. The complete array has an imaging area of 6 x 6 cm^2 covering approximately 97% of the field of view of the camera. The basic time resolution of the pn camera is 73.3 ms, however the instrument can be operated in a variety of different modes to increase this number if required.

These modes can be broadly separated into three categories: full frame, partial window and timing.

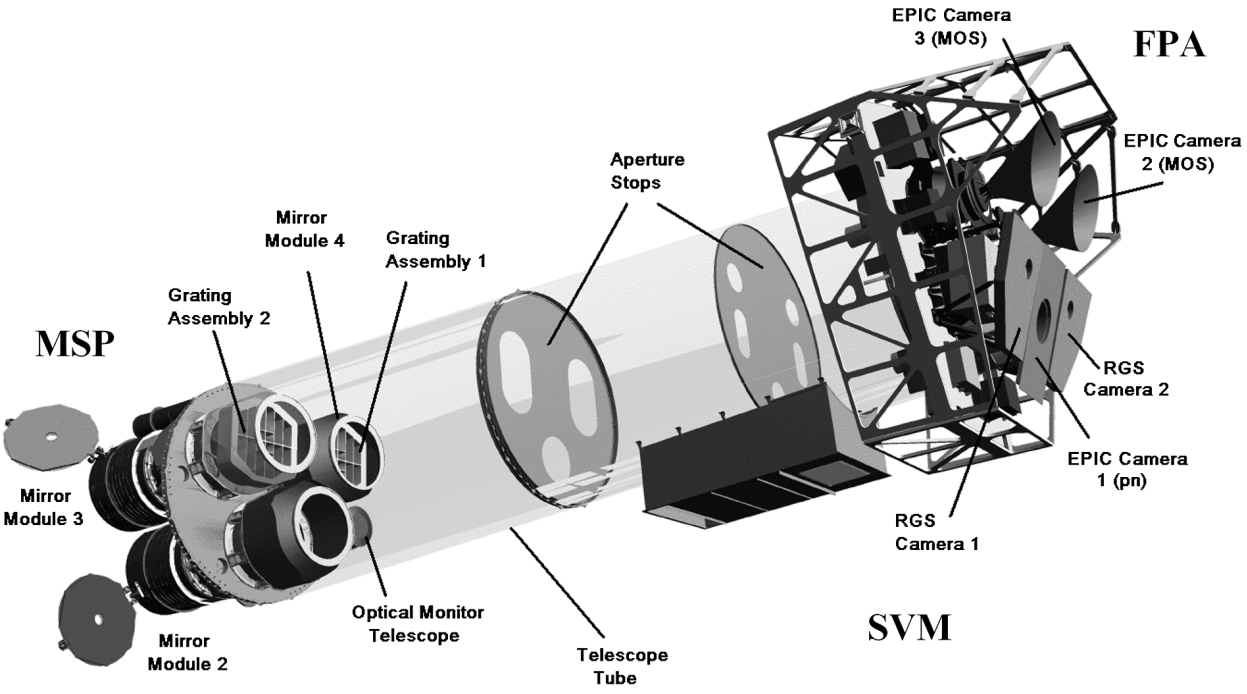

Figure 2.3: Schematic of the XMM-Newton spacecraft.

- In full frame mode all pixels of all CCDs are read out covering the full field of view, with the option of increasing the time resolution to 199.2 ms for observing extended sources.

- In partial window modes only a small section of the full array is used. For large window mode only the inner half of each CCD is used for imaging with a time resolution drop to 47.7 ms. The imaging area and time resolution is further reduced in small window mode, with a 63 x 64 pixel area in a single quadrant used and time resolution of 5.7 ms.

- Timing mode works slightly differently in that imaging is only made in one dimension, along the column axis. 10 x 1 rows for each time slice are shifted up the chip, being read out after 9 transfers. This loses the positional information within each slice, but allows for a time resolution of 30 μs. If an even lower time resolution is required burst mode can be used which achieves 7 μs, but has only a 3% duty cycle.

The areas used on the CCDs for each of the four main modes can be seen in Figure 2.4.

These modes allow the EPIC-pn camera to observe both very bright and very faint sources and

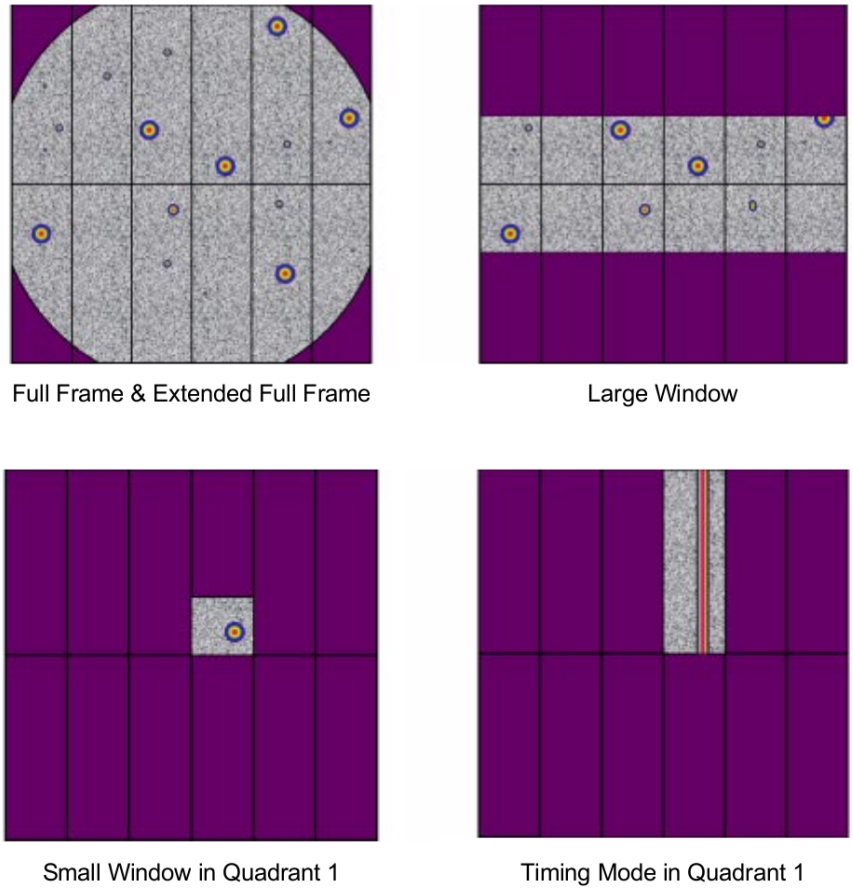

Figure 2.4: Operating modes of the EPIC-pn camera. Taken from Strüder et al. (2001).

still avoid significant pile-up effects. Pile-up occurs when more than one photon is detected as a single event. These photons are now inseparable and the energy of the event becomes the sum of the energy of these incoming photons. This has the affect of making the observed spectrum skewed towards higher energies. Pile-up in CCDs generally occurs when the source flux levels are high enough that there is a decent probability that multiple photons will arrive at the same detector region within one readout time. Changing the operating mode of the CCD allows the data to be read out much faster, reducing the chance of the CCD saturating and pile-up occurring. The downside to these faster modes is that it becomes harder to estimate, and therefore subtract, the background with a smaller imaging window. The background in timing mode will also be higher, due to the loss of imaging information in one direction.

The RGS instrument consists of an array of reflection gratings positioned such that they intercept

around half of the light from the converging beam at the exit of the X-ray telescope. The gratings deflect the intercepted light onto a strip of CCD detectors producing a main (first spectral order) data set, as well as second or third order spectra. These CCDs operate in a single photon counting mode and measure the position and energy of each photon. The instrument operates in the $5-35$Å range which includes the K-shell transitions of oxygen, neon and magnesium, and the L-shell transition of iron, amongst others.

The background count rate in *XMM-Newton* observations generally originate from three main sources. The first is from photons, primarily from the astrophysical background. Thermal emission dominates this component at lower energies, originating from the Local Bubble, Galactic Disc, and Galactic Halo (Carter & Read, 2007). There is also higher energy emission mainly from unresolved cosmological sources. Alongside this there are also contributions from solar wind charge exchange or single reflections from unrelated, out of time events for example.

The second source is from particles. Soft protons create strong flares as they are scattered around the mirror modules. These flares are often required to be removed from the data. Particle background can also originate from cosmic rays which both penetrate the CCDs and cause fluorescence of the satellite material. Finally there are also a contribution from electronic noise (e.g. read-out noise and bright pixels).

2.4 Analysis of Energy Spectra

All the spectral data used in this thesis is analysed using the interactive X-ray spectral-fitting program `XSPEC` (Arnaud, 1996). `XSPEC` obtains an observed spectrum using a combination of four files. The first two of these files are the data (spectrum) file and the background file. When a spectrometer measures the spectrum of a science target it does not record the actual spectrum but instead the the photon count rate within instrumental channels. A spectrum is obtained in

XSPEC by subtracting the background spectrum from the data file. XSPEC is designed in a way that allows it to be completely detector independent. Therefore a third file, the response file, is required to inform XSPEC of the characteristics of the instrument currently being used. In particular, it describes the distribution of incoming photons onto detector channels as a function of incoming photon energy. The response file is also often accompanied by an auxiliary response file which represents the effective area of the detector as a function of incoming photon energy. The combination of these two response files then allows XSPEC to predict the observed spectrum of the chosen instrument given a certain set of model parameters.

The basic XSPEC installation includes a large number of built-in models capable of representing the constituent parts of various X-ray sources. For XRBs, for example, there are a range of power-law (e.g. POWERLAW, SIMPL), black body (e.g. DISKBB, KERRBB) and absorption models (e.g. WABS, TBABS, ISMabs). XSPEC also provides a framework for allowing user-created models to be installed and used.

Once a model has been selected XSPEC then attempts to find the best-fit model parameters using a fitting algorithm. This returns the parameters values and estimated confidence intervals.

2.4.1 Markov Chain Monte Carlo Analysis

Another feature XSPEC provides, and one which will be used in several places throughout this thesis, is the ability to conduct Markov Chain Monte Carlo (MCMC) analysis on any model parameters calculated during the fitting process. MCMC methods allows the user to approximate the posterior distribution of a parameter of interest using random sampling. This provides the user with a representation of all the possible values of the parameter and how likely it is for each value to be found.

There are two main algorithms that are used in MCMC analysis: Metropolis-Hastings (MacKay,

2003; Gregory, 2005) and Goodman-Weare (Goodman & Weare, 2010). As the Goodman-Weare algorithm is the more modern of the two, and outperforms Metropolis-Hastings (Foreman-Mackey et al., 2013), it is the algorithm of choice in this thesis. The goal of the analysis is to construct a 'chain', a series of points in parameter space where each point is related to the point preceding it. The Goodman-Weare algorithm achieves this by using 'walkers', where the position of each walker is related to the current positions of all the other walkers. The chain is created by recording the positions of the walkers which move according to the following process. When updating the position of a single walker another walker is chosen at random. A new position is proposed for the first walker based on the position of this second walker plus a random component. The suitability of this new position is then calculated. If the new position provides a better discription of the data than the old position than this proposed position is accepted with a probability determined by how much better the new position is. If the proposed position is accepted then the position of the walker is updated and recorded, and then the process begins again. This process repeats for a number of iterations, generally set by the user. This algorithm lets the walkers efficiently explore the parameter space and will generally lead to the walkers converging towards a region with the best fit statistics, with the random component added when choosing a new position helping the walkers avoid becoming trapped in local minima.

In `XSPEC` the `chain` command is used to conduct MCMC analysis, allowing the user to set a number of important parameters such as the amount of walkers used, and the number of steps the walkers should take. The 'burn' length can also be specified which deletes a certain number of steps before the chain is recorded. Another popular way to conduct MCMC analysis is using `emcee`, a implementation of the Goodman-Weare algorithm written in the Python language (Foreman-Mackey et al., 2013). Both of these options allow the user to conduct MCMC analysis using optimised algorithms which can be customised to suit the needs of a study in a simple manner.

3

The Radiative Efficiency of Transient X-ray Binaries

3.1 Introduction

Two varieties of accretion flow models, with distinct X-ray emission mechanisms, are often used to explain the differences between the soft and hard states in black hole X-ray binaries. One is the standard, optically thick and geometrically thin accretion disc with its strong thermal emission (Shakura & Sunyaev, 1973). This disc (when extending down to $r_{\rm ISCO}$) produces the thermal emission that dominates the X-ray spectrum and is assumed to have a high radiative efficiency ($\eta \sim 0.1$, Shakura & Sunyaev 1973) that is approximately constant with accretion rate. A linear scaling would therefore be expected between X-ray luminosity and mass accretion rate, $L_X \propto \eta\dot{M} \propto \dot{M}$, at least in the regime where $\dot{M}$ is high enough to maintain a such a disc.

The other type of accretion flow is any of a group of alternatives to the optically thick accretion disc. Examples of these are the Advection Dominated Accretion Flow (ADAF; Narayan & Yi, 1995) and the jet-dominated accretion flow (JDAF; Falcke et al., 2004). These are optically thin and generate X-rays via Comptonization, bremsstrahlung and/or cyclo-synchrotron. In the non-thermal-dominated hard states the inner accretion disc may be replaced by this optically thin flow (e.g. Esin et al., 1997) which has a lower radiative efficiency that depends on the accretion rate, e.g. $\eta \propto \dot{M}$. This leads to a non-linear scaling of X-ray luminosity with accretion rate: $L_X \propto \eta\dot{M} \propto \dot{M}^2$ (Narayan & Yi, 1995).

Knevitt et al. (2014) studied the difference in the period distribution of the known LMXBs with NS and BH primaries. They found a dearth of very short period BH systems relative to NS systems that could be reproduced if the black hole systems are radiatively inefficient below some critical mass accretion rate. Shorter period binaries have a lower maximum luminosity and may be radiatively inefficient through a substantial fraction of their outbursts. Knevitt et al. (2014) compared different models for the switch between efficient and inefficient accretion and found that only a dramatic change, to an efficiency scaling $\eta \propto \dot{M}^{\beta}$ with $\beta \gtrsim 3$, could explain the observed lack of short period BH systems.

When the mass accretion rate is decaying exponentially, and the emission is dominated by a radiatively efficient accretion disc, the X-ray luminosity should decay with the same e-folding time: $L_X \propto \dot{M} \propto \exp(-t/\tau_m)$. If the emission is dominated by a radiatively inefficient flow, the X-ray luminosity will decay faster, e.g. for $\eta \propto \dot{M}$ we will have $L_X \propto \dot{M}^2 \propto \exp(-2t/\tau_m)$. The e-folding time of the luminosity is shorter (e.g. $\tau_m/2$). Therefore, as discussed in Homan et al. (2005), if there is a change from a radiatively efficient to a radiatively inefficient accretion regime during the period of exponential decay in the mass accretion rate, there should be a decrease in the e-folding time of the X-ray luminosity during the decay. In this chapter this hypothesis is tested using some of the best *RXTE* monitoring data of XRB outbursts.

3.2 Observations and Data Reduction

3.2.1 Sample definition

The sample of XRB outbursts is shown in Table 3.1. The selected sources represent all the confirmed and candidate transient BH XRBs listed in Remillard & McClintock (2006). For each one all the long (>few days) outbursts are identified based on daily light curves of each source from the *RXTE* All-Sky Monitor, and where possible the data from the *Swift* Burst Alert Telescope, and *MAXI* (Monitor of All-Sky X-ray Image) Gas Slit Camera as well. These data alone were insufficient to accurately define the decay rates. Therefore a subset of outbursts with a sufficient number (> 20) of pointed *RXTE* observations was selected to estimate decay rates in both soft and hard states.

3.2.2 *RXTE* observations

For each selected outburst pointed *RXTE* data was extracted from the High Energy Astrophysics Science Archive Research Center (HEASARC) archive. Data was taken solely from the Proportional Counter Array (PCA) instrument, in the `STANDARD2` mode which has 129 energy channels. Both source and background spectra were extracted for each observation, along with spectral response files using the standard *RXTE* software HEASOFT v6.15.1). Background-subtracted count rates were then computed in three energy bands: A = channels 4-44 ($\approx$ 3-20 keV), B = channels 4-10 ($\approx$ 3-6 keV) and C = channels 11-20 ($\approx$ 6-10 keV), as in Motta et al. (2012). The background is obtained using models as the *RXTE*/PCA background cannot be measured. The hardness ratio $H = C/B$ (Homan & Belloni, 2005) was also calculated. Using these light curves, hardness ratio curves and hardness intensity diagrams (HIDs; Belloni et al., 2005) were produced for each outburst. Fig. 3.1 shows the full data set for the intensively observed 2005 outburst of

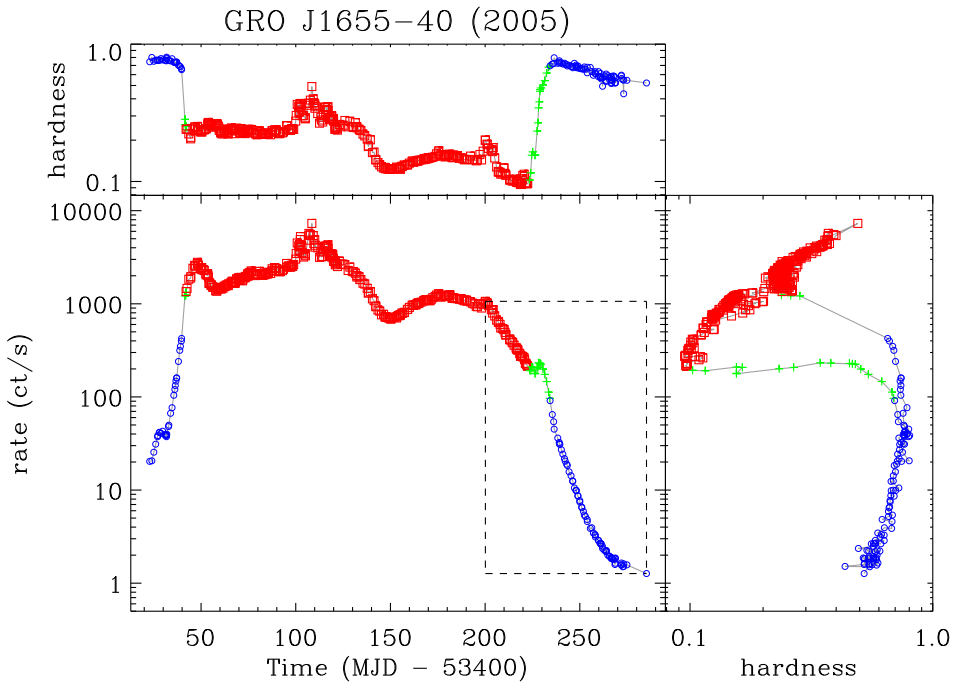

Figure 3.1: *RXTE* light curve in the $\approx 3 - 20$ keV band showing the full 2005 outburst of GRO J1655-40, along with a HID (right-hand panel) and hardness ratio curve (top panel). The plot has been coloured to show the spectral states of the source as the outburst progresses: blue circles for the hard state, green crosses for intermediate and red squares for soft. The dashed lines highlight the decaying region of the light curve. Fig. 3.2 provides a zoomed in view of the later stage of the outburst.

GRO J1655-40, with Fig. 3.2 displaying only the decaying section of the outburst.

At low count rates (< 10 ct s^{-1}), the data could be affected by systematic errors in the background subtraction and by contaminating sources in the PCA field of view, including diffuse Galactic emission. This often makes the decays appear to slow down towards quiescence (e.g. Homan et al., 2005; Jonker et al., 2010). For each count rate, errors were computed based on standard Poisson statistics. However, these usually underestimate the random scatter in the light curves, as the dominant source of variance is systematic, not random, e.g. the intrinsic, rapid variability of the sources (particularly strong in the hard states) and systematic errors resulting from subtraction of the instrumental background (a more significant effect at low fluxes). As a way to assign similar statistical weight to data points that may differ in flux by two to three orders of magnitude 3% errors were assumed for all count rates, in both soft and hard states. Thus, a fit is considered

'good' if the model matches to within ~ 3 per cent for most data points.

3.2.3 *Swift* Observations

Use is also made of *Swift* X-ray Telescope (XRT) observations to track the outburst of GRO J1655-40 to lower count rates than is possible using only the *RXTE* PCA data. As the XRT is an imaging telescope, it is less sensitive to background issues, so *Swift* can be used to verify the *RXTE* background subtraction. Of the sample of systems only GRO J1655-40 has any useful observations. There are six *Swift* observations during the hard-state decay: three just after the end of the state transition back into the hard state at around MJD 53640, and three a few weeks later at around MJD 53665. The *Swift* XRT data were reduced using HEASOFT v6.15.1. Photon event lists and exposure maps were produced using XRTPIPELINE v0.13.1. For each observation, a source spectrum was extracted from photons in a circular extraction region of radius 30 arcsec, and a background spectrum was extracted from a source-free region of the same image. Ancillary Response Files (ARFs) were generated using XRTMKARF v0.6.1.

The energy bandpass and response of the *Swift* XRT differs and *RXTE* PCA, and the *Swift* data was converted to equivalent PCA rates for comparison with the *RXTE* monitoring data. XSPEC v12.8.2 (Arnaud, 1996) was used to fit a model to the *Swift* XRT spectrum for each observation. The model comprised a blackbody plus power law, all modified by neutral absorption (the `TBABS` model; Wilms et al. 2000). The best-fitting model was extrapolated for each observation to cover the PCA energy range and then the PCA response matrix was used to convert this to an equivalent PCA count rate. The resulting PCA-equivalent count rates are shown on Fig. 3.3, after having subtracted a constant factor due to background effects.

3.3 Analysis and Results

3.3.1 The Model

If radiative efficiency is a power-law function of the central mass accretion rate, $\eta \propto \dot{M}^{\beta}$, and the mass accretion rate follows an exponential decay with e-folding time $\tau_{\rm m}$, the X-ray luminosity should follow $L_{\rm X} = A\exp(-t(1+\beta)/\tau_{\rm m})$. Therefore a simple model $L_{\rm X} = A\exp(-t/\tau)+C$ can be fit to decaying intervals of the light curves to estimate the decay time-scales during soft-state and hard-state intervals to give luminosity decay timescales $\tau_{\rm s}$ and $\tau_{\rm h}$, respectively. The constant C accounts for any constant light from contaminating background sources.

Assuming the radiative efficiency is constant at high luminosities ($\beta = 0$ in the soft state), the luminosity decay in the soft state should track the decay in $\dot{M}$, i.e. $\tau_{\rm s} = \tau_{\rm m}$. But if the radiative efficiency scales with accretion rate ($\beta > 0$) in the hard state, the X-ray luminosity will have a different e-folding time, $\tau_{\rm h} = \tau_{\rm m}/(1+\beta)$. β can then be estimated by comparing the decay times in soft and hard states as $\beta = \tau_{\rm s}/\tau_{\rm h} - 1$. If there is no change in radiative efficiency, $\beta = 0$ would be expected, while if there is a change to $\eta \propto \dot{M}$ regime $\beta = 1$ should be found.

3.3.2 Results

The final weeks of all the outbursts listed in Table 3.1 have been studied. Based on an initial, visual inspection of the light curves, for each source two regions of decay separated by the soft–hard state transition were identified. (During this transition – spanning intermediate states – the light curve often stays approximately constant or even rises slightly). The model above was fitted[1] to each of these regions to give estimates of $\tau_{\rm s}$ and $\tau_{\rm h}$. These are given in Table 3.1 and the data and models are plotted in section 3.8. All light curves are in the 3-20 keV band.

[1]The fitting was performed by minimizing the usual χ^2 fit statistic.

System name (1)	Outburst (2)	No. of obs. (3)	τ_s (d) (4)	Decay length (5)	$\chi^2(d.o.f)$ (6)	τ_h (d) (7)	Decay length (8)	$\chi^2(d.o.f)$ (9)	β (10)
GRO J1655-40	2005	495	14.02 ± 0.13	50	18.1(48)	6.85 ± 0.05	73	193.0(70)	1.05 ± 0.01
XTE J1550-564	1998	234	8.97 ± 0.14	21	4.10(19)	2.33 ± 0.05	9	8.86(6)	2.85 ± 0.07
	1999	66	14.80 ± 1.11	8	4.90(6)	6.87 ± 0.03	70	127.2(67)	1.15 ± 0.09
XTE J1650-500	2001	106	16.18 ± 0.25	21	5.51(19)	–	–	–	–
GX 339-4	2002	174	16.28 ± 0.28	13	13.3(11)	18.21 ± 0.13	37	10.7(7)	-0.11 ± 0.01
	2004	251	17.09 ± 1.29	4	5.20(2)	14.15 ± 0.07	56	36.5(53)	0.21 ± 0.02
	2007	244	16.94 ± 0.34	13	25.5(11)	7.43 ± 0.32	28	13.4(25)	1.28 ± 0.06
	2010	294	–	–	–	11.46 ± 0.28	19	14.9(16)	–
4U 1543-475	2002	102	6.10 ± 0.15	12	8.41(10)	4.97 ± 0.04	54	16.5(51)	0.23 ± 0.01
H 1743-322	2003	219	14.06 ± 0.37	11	20.6(9)	4.81 ± 0.07	40	12.5(37)	1.92 ± 0.06
	2004	49	22.06 ± 0.82	7	45.7(5)	5.66 ± 0.14	18	82.7(15)	2.90 ± 0.13
	2005	23	12.92 ± 1.28	4	0.24(2)	5.49 ± 0.12	10	23.1(7)	1.35 ± 0.14
	2009	49	20.07 ± 1.68	9	20.3(7)	8.02 ± 0.17	16	275.2(13)	1.50 ± 0.13
	2010	58	16.92 ± 0.86	10	57.7(8)	6.95 ± 0.11	23	66.0(20)	1.43 ± 0.08
	2011	39	11.75 ± 0.52	8	167.3(6)	7.39 ± 0.15	17	101.3(14)	0.59 ± 0.03

Table 3.1: Details of the outbursts used in the sample. Column 1 gives the source name, column 2 gives the year of each outburst and column 3 gives the total number of *RXTE* observations used. Columns 4 and 6 show the e-folding times, columns 5 and 7 show the number of observations included in the fit, and column 8 shows the β values. Missing values indicate light curves with insufficient data to properly fit exponential curves.

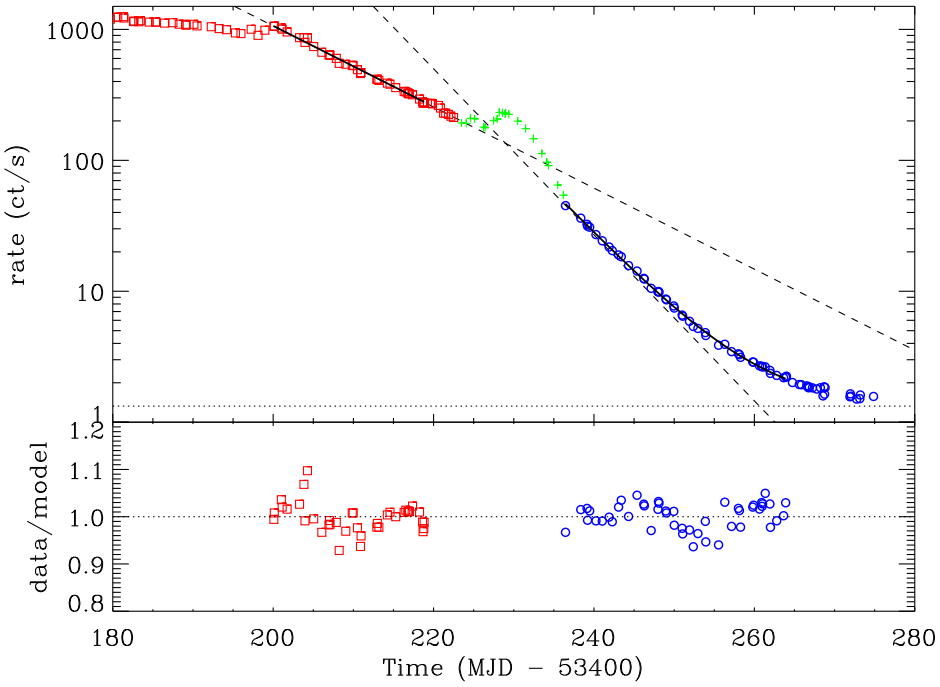

Figure 3.2: The decay of the 2005 outburst of GRO J1655-40, using the same data and energy range as in Figure 3.1, fitted with separate exponential decay models in the soft state (square red points) and hard state (circular blue points). An additional constant is included in the hard-state model to account for the saturation at low fluxes (caused by background contamination). The dashed lines show the exponential decays extrapolated over the full decay region. The bottom panel shows the data/model residuals.

The clearest example of exponential decay comes from the well-observed 2005 outburst of GRO J1655-40 shown in Fig. 3.2. There are two distinct periods of exponential decay, ignoring the intermediate state where there is a small rise in count rate. Fitting these gave $\tau_{\rm s}$ and $\tau_{\rm h}$ values of 14.02 ± 0.13 and 6.85 ± 0.05 d, respectively. The decay rate almost exactly doubled following the transition into the hard state, giving $\beta = 1.05 \pm 0.01$. (Only the *RXTE* data were fitted; the *Swift* data were used only to verify the extrapolation of the source *RXTE* light curve to low fluxes.)

The other sources show more varied results with β value ranging from -0.1 to 2.90. In some cases it was not possible to clearly identify suitable decaying intervals. For some outbursts any period of exponential decay was very short, for some others it was too sparsely sampled (e.g. XTE J1650-500). Even where there are sufficient data, in many cases the residuals for the exponential model fits show systematic structure: deviations from a single, unbroken exponential decay within a

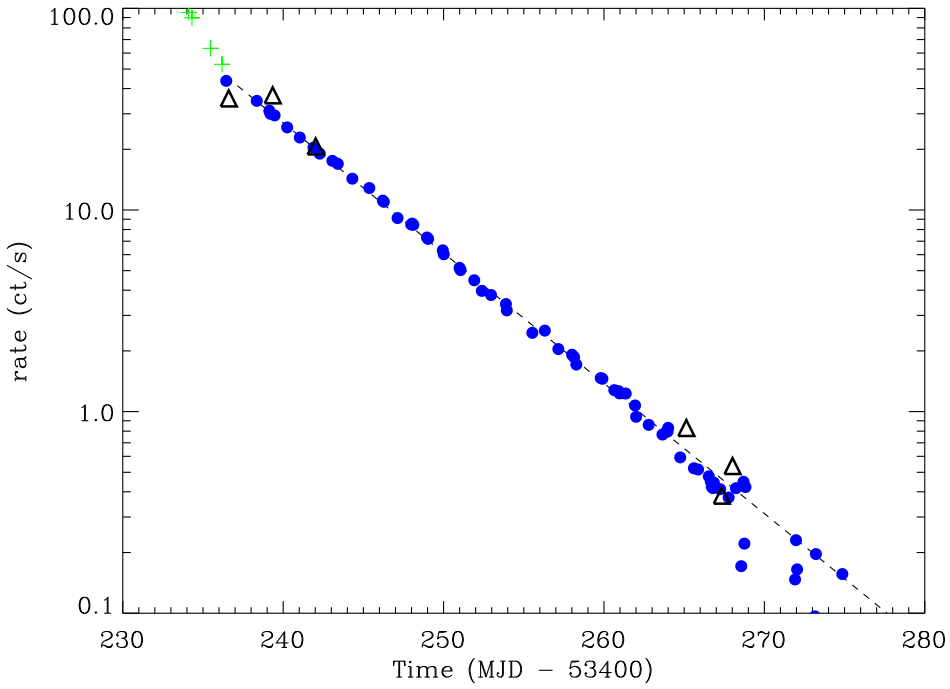

Figure 3.3: Close-up of the hard state decay of the 2005 outburst of GRO J1655-40 after subtracting the constant (as fitted in Fig. 3.2). The black triangular points show the *Swift* data converted to a PCA-equivalent count rate, which agree with the *RXTE* data after the constant has been subtracted.

particular state.

In order to focus on a single period of exponential decay with a constant decay rate, a different fitting strategy was used. Specifically, 'local' τ values were calculated for each point by fitting only that point and the next four. The modal τ value was found and the longest interval in the light curve consistent with this decay rate (dominated by τ values within 1 d of the mode) identified. New values of $\tau_{\rm s}$, $\tau_{\rm h}$ and β were then estimated by fitting over these smaller intervals of consistent decay rate. Furthermore, intervals containing fewer than eight consecutive points were ignored. Table 3.2 shows the results. Section 3.8. shows the results of the fitting and provides notes on individual outbursts. This more conservative analysis yielded five β estimates; with the exception of GX $339-4$ these lie in the range 1.0 ± 0.3.

System name (1)	Outburst (2)	τ_s (d) (3)	Decay length (4)	$\chi^2(d.o.f)$ (5)	τ_h (d) (6)	Decay length (7)	$\chi^2(d.o.f)$ (8)	β (9)
GRO J1655-40	2005	13.85 ± 0.15	40	37.3(38)	6.72 ± 0.08	48	36.9(45)	1.06 ± 0.02
XTE J1550-564	1998	9.76 ± 0.26	15	20.8(13)	–	7	–	–
	1999	14.80 ± 1.11	8	1.92(6)	6.95 ± 0.08	22	34.5(31)	1.13 ± 0.09
XTE J1650-500	2001	16.12 ± 0.27	20	5.20(18)	–	–	–	–
GX 339-4	2002	12.04 ± 0.45	8	20.8(6)	8.46 ± 1.24	9	4.15(6)	0.42 ± 0.06
	2004	–	4	–	8.78 ± 0.70	21	27.9(18)	–
	2007	–	7	–	8.87 ± 1.32	16	8.15(22)	–
	2010	–	–	–	5.88 ± 0.68	8	4.66(5)	–
4U 1543-475	2002	6.10 ± 0.15	12	8.41(10)	2.70 ± 0.08	12	23.7(9)	1.26 ± 0.05
H 1743-322	2003	12.96 ± 0.51	8	6.48(6)	7.41 ± 0.91	14	10.2(11)	0.75 ± 0.10
	2004	–	6	–	5.19 ± 0.27	13	30.0(10)	–
	2005	–	6	–	–	6	–	–
	2009	–	7	–	–	6	–	–
	2010	–	6	–	10.69 ± 2.40	10	4.26(7)	–
	2011	–	–	–	–	7	–	–

Table 3.2: The same parameters as in Table 3.1 after fitting only restricted sections of the light curves (see the text for details).

3.4 Discussion

The decaying stages in the X-ray light curves of 15 outbursts of six BH X-ray binaries have been examined. In all cases it was found that the last few weeks of each outburst can be described in terms of nearly exponential decays. For the seven outbursts with well-observed exponential decays in the soft state, the mean e-folding time is 12 ± 1 d, while for the ten outbursts with well observed exponential decays in the hard state, the mean e-folding time is 7 ± 1 d (see Table 2). Several outbursts (e.g. of GX 339-4) show more complicated behaviour, sometimes with little or no obvious decay during the soft state. As such, it is difficult to say whether the models discussed above will apply to all BH LMXB systems/outbursts or just a subset. Homan et al. (2005) previously noted the factor 2 change in decay time-scale in their early analysis of the 2005 outburst of GRO J1655-40. Here, results for that one outburst have been confirmed and has shown that similar behaviour can be seen in the other four outbursts with well-constrained exponential decays in both states.

The change in the decays during soft and hard states was characterised using a parameter $\beta = \tau_{\rm s}/\tau_{\rm h} - 1$. Assuming constant η in the soft state, such that $\tau_{\rm s} = \tau_{\rm m}$ (the decay of $\dot{M}$), this parameter can be interpreted as the index of the efficiency scaling: $\eta \propto \dot{M}^{\beta}$. Of the five systems with the most reliable β estimates, four show $\beta \approx 1$, while GX 339-4 shows $\beta \approx 0.4$.

The decay rates were estimated using broad-band light curves (3-20 keV) from the *RXTE* PCA. Such a dramatic change in the decay rate is not an artifact of spectral evolution: within each of the soft and hard states, the spectral evolution is relatively modest (see Fig.3.1). The conclusion is that there is a genuine change in the speed at which the X-ray luminosity drops. If $L_{\rm X} = \eta \dot{M} c^2$, then either the decay rate of $\dot{M}$ changes around the state transition or η decreases with time (and luminosity) after the state transition.

The change in the decay could signal the switch from a disc-dominated, radiatively efficient soft

state to a radiatively inefficient mode of accretion (such as an ADAF or JDAF type flow) in the hard state. As discussed above, such a model – in which the soft state has η constant with $\dot{M}$, but the hard state is governed by an accretion flow that becomes radiatively inefficient at low $\dot{M}$ according to $\eta \propto \dot{M}$ – matches the results. This interpretation is consistent with other studies comparing radio and X-ray luminosities over a sample of binaries (Fender et al., 2003; Merloni et al., 2003). By contrast, Knevitt et al. (2014) required a steeper efficiency scaling (with $\beta > 3$) to explain the lack of known short period BH LMXBs relative to NS LMXBs. Reconciling these results – the factor ≈ 2 change in the decay slopes implying $\eta \propto \dot{M}$ scaling, and the lack of short period BH LMXBs – would require either that there is another explanation for the absence of short-period BH systems, or that the efficiency scaling becomes much steeper at lower luminosities, below those accessible with the *RXTE* data. For example, perhaps there are winds in these systems that reduce the observed luminosity even further at low mass accretion rates, steepening the decay to a level in which it would become consistent with a larger beta value.

It is the average radiative efficiency (averaged over any contributing spectral components) that is required to change. There could be two emission components with radiative efficiencies that are very different, but each is constant with time. The observed faster decay in the hard state could be produced if the source emission evolves from being dominated by the more radiatively efficient component to being dominated by the least radiatively efficient component, so that the weighted average of the radiative efficiency drop with $L_{\rm X}$. But such a model requires fine-tuning to explain the observed results. Consider two emission processes with spectra $S_1(E)$ and $S_2(E)$, and radiative efficiencies η_1 and η_2 (with $\eta_2 < \eta_1$). The mass accretion rate $\dot{M}$ powering the source is divided such that a fraction a drives the first component and $(1-a)$ drives the second. The total luminosity is $L \propto \dot{M}(\eta_1 a S_1 + \eta_2(1-a)S_2)$. The term in brackets is the emission-averaged radiative efficiency. In order to reproduce the doubling in decay rate, a would have to be a function of $\dot{M}$ in the hard state in such a way to make the emission-averaged radiative efficiency scale linearly with $\dot{M}$, which seems contrived. Further, the relatively modest evolution of the spectrum during the hard-state decay does not support such a model unless the two components

have very similar spectra over the observed X-ray band.

The above interpretation assumes that the mass accretion rate decays as $\dot{M} \propto \exp(-t/\tau_{\rm m})$ through most of the outburst decay, and in particular, $\tau_{\rm m}$ does not change around the state transition. An alternative explanation is that η is constant and there is a change in $\tau_{\rm m}$ coincident with the state transition. The coincidence in time would require that the state transition and the change in the decay rate of $\dot{M}$ are causally linked (either one causes the other or they are both triggered by some other event) by some mechanism not included in the current models of disc outbursts (van Paradijs, 1996; King & Ritter, 1998; Dubus et al., 2001; Lasota, 2001)

To conclude, it seems that the most plausible explanation is in terms of a change in the radiative efficiency, and that the soft- to hard-state transition is the result of the inner accretion flow transforming from a standard, efficient accretion disc to a radiatively inefficient flow as suggested by models such as Narayan & Yi (1995) and Esin et al. (1997).

3.5 The case of XTE J1752-223

Since the publication of the paper that makes up the majority of this chapter a small number of outbursts that were not part of the main study were investigated. Many were shorter outbursts with few *RXTE* observations and so not worth discussing further, but there is a single source that has a unique, stand-out feature that is an interesting addition to the results already discussed earlier in the chapter.

The system XTE J1752-223 is a $10{\rm M}_{\odot}$ LMXB that had an outburst in 2009 that lasted around 300 days. The rising phase of the outburst was not sampled particularly well by the *RXTE*/PCA instrument, but the decaying phase has approximately 150 data points spread evenly along the soft state decay, state transition and the majority of the hard state decay. This allowed for a good

estimate of the e-folding times for both states. The light curve, HID and hardness curve are shown in Figure 3.4.

An estimate of β was then computed for this outburst. The value came out to be almost exactly zero, i.e. the decay rate in the soft state and the decay rate in the hard state were almost identical. This is the first time this behaviour has been seen in any of the sources that have been studied. There isn't anything particularly unusual about the overall shape of the outburst: it proceeds as would be expected with a period of exponential decay in the soft state following a peak in X-ray luminosity, then a short transitional period, where there is a sudden increase in the luminosity, then directly into the hard state decay.

The light curve then becomes more unusual around MJD55320. At this point, after 3 weeks of decay in the hard state, these is a sharp decrease in the e-folding time. Measuring the exact value of this e-folding time produces a value of 12.91 ± 0.64 days, nearly half that of the original hard state value of 24.12 ± 1.54 days. This secondary hard state decay period then continues until it is interrupted by a flaring event.

This increase in decay rate happens in a very short amount of time, much less than the length of the average intermediate state. Secondly, there is virtually no change in the spectral behaviour of the source, the falling hard track on the HID stays mostly vertical during the majority of the decay.

This could suggest then that the observed change in decay rate and therefore the switch to the radiatively inefficient regime does not necessarily have to be coincident with the state transition. The soft state will always be in the $\eta \sim 0.1$ regime, and if there is some 'switch' luminosity at which the source becomes radiatively inefficient, then if a source goes through state transition before this luminosity then the disc could remain in an efficient state during some fraction of the hard state before hitting the switch and entering the inefficient regime. Sources such as GRO J1655-40 would pass through this luminosity in the soft state and so immediately switch to the inefficient regime, whereas XTE J1752-223 will have only hit this point during the hard state.

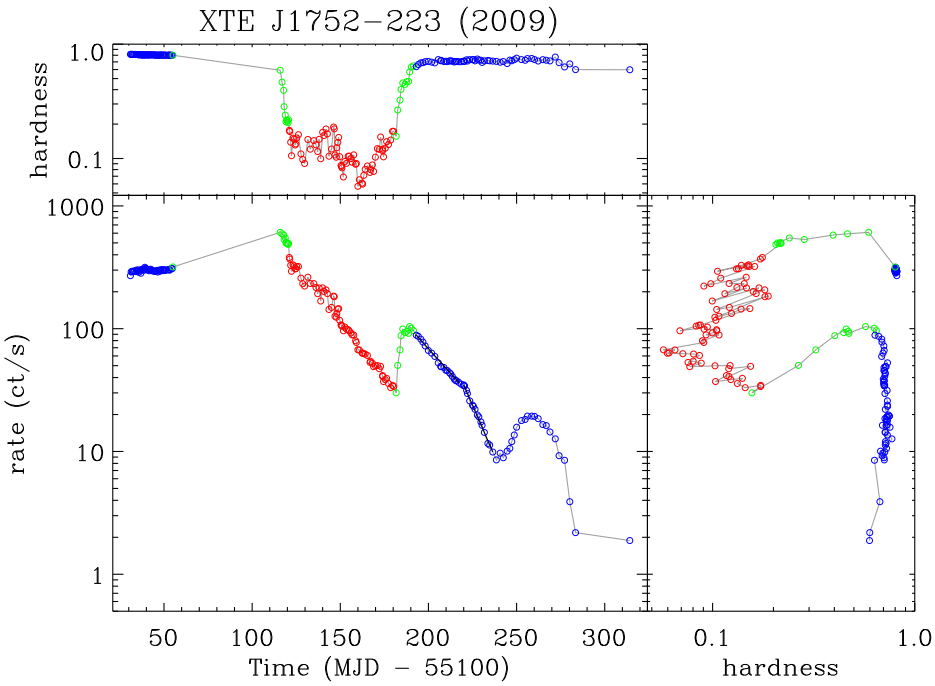

Figure 3.4: The full *RXTE*/PCA lightcurve, hardness intensity diagram and hardness curve for the 2009 outburst of XTE J1752-223. In this case the two decaying regions, both marked with a black line, are both in the hard state, and suggest a situation in which a change in radiative efficiency is not necessarily coincident with a state change.

Other sources have shown some evidence to suggest that something like this could be the case. The source GS 1354-64 had an outburst in 2015 in which it never entered the soft state despite being having a peak luminosity of $> 0.15L_{Edd}$ (Kolijonen et al., 2016). The outburst shows a roughly exponential decay with two changes in the e-folding time, the first of which drops by a factor of 2, without ever changing state.

3.6 The Rising State

So far only the change in the decaying stage of outbursts have been considered, but if this change is due to the change in the accretion region then it should be possible to see the same effects as the inefficient accretion flow changes to the efficient accretion disc as mass accretion rate increases.

There are some key differences in these two stages of the outbursts though that make the task of investigating the rise significantly more difficult though. The first is phenomenological, the rises of outbursts are generally much faster than the decay, and can be measured more in days than weeks. The second is more practical, but leads on from the first, in that there simply aren't as many PCA observations during the rising state due to the fast response time and rate of observation required. The full light-curve plot of GRO J1655-40 in Fig. 3.1 demonstrates these problems, the observations only begin when the source is already at 20 ct/s and the total rise time is only about 20 days compared to the 90 days the decay is observed for.

Therefore almost all of the outbursts in the main sample are unsuitable for studying the rising state, with there being little-to-no *RXTE*/PCA data and the ASM data having a signal-to-noise too low to provide a useful alternate. The only outburst with an adequately well observed rising section is the 2004 outburst of GX 339-4. For this outburst a β value can be measured in the same way as the decaying regions, only now it is a exponential rise. The full lightcurve with the selected regions highlighted can be found in Fig. 3.5. Two clear sections are found that are well described by an exponential function with a break inbetween at MJD53051. The first, comprising the first 15 days of available *RXTE*/PCA data, is fit with $\tau_1 = 6.22 \pm 0.11$, while the second came out at $\tau_2 = 15.8 \pm 0.32$ with 25 days worth of well sampled data. The β value was found to be 1.55 ± 0.04. Unfortunately this is one of the lightcurves with the more unusual decaying sections and no β value was found, so no direct comparison can be made for this outburst, but can still be compared with the results of the whole study.

These numbers are not too far off the 1 week/2 week e-folding time pairs that have been seen in the decay of the XRB sample, suggesting that the mechanism behind this switch in the rate of exponential rise is the direct reverse of that during the decaying period. Also, given that this switch takes place during the hard state, many weeks before the beginning of the soft state, adds another piece of evidence to the idea that the change in radiative efficiency does not have to be coincident with the state change.

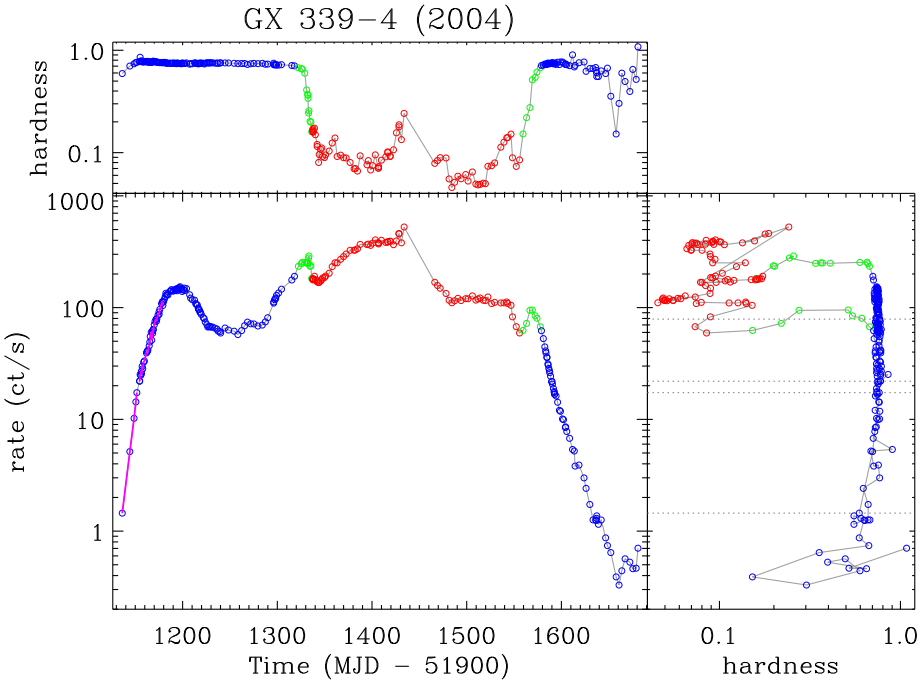

Figure 3.5: The full *RXTE*/PCA lightcurve, hardness intensity diagram and hardness curve for the 2004 outburst of GX 339-4. This plot is meant to illustrate the behaviour of the rising hard state with relation to the decaying stages of the outburst. The two sections which are used for the measurement of the exponential rise are highlighted.

While this line of investigation can no longer be persued within this data sample, there have been other examples of similar results found in the literature. For example, Kolijonen et al. (2016) fitted two periods of exponential rise with e-folding times of 13^{+1}_{-2} days and 26^{+2}_{-3} days. Hopefully future observational campaigns will allow for more results of this nature with greater focus on the rising and decaying phases of outbursts down to lower luminosities.

3.7 Outbursts of Neutron Star X-ray Binaries

The bulk of the chapter has been concerned with only black hole XRB systems. However, neutron star XRBs are similar in many ways, such as having outbursts, and more importantly show outbursts with a similar rising then decaying profile. So can a similar study into the decay rates

of their outbursts be performed? And would it be expected to see the same change in the decay rates?

One of the key differences between BHs and NSs when thinking about accretion is the NS's solid surface. This means that while a BH might be able to advect some portion of the energy liberated from accretion through its event horizon, a NS would not be able to do the same, the energy would be released when the matter hits the surface. BHs are known to be fainter during the quiescent phase than NSs, so this could be naturally explained by the presence of a ADAF. There are other possibilities though, such as jet-dominated states. ADAF theory states that the X-ray luminosity relates to the mass accretion rate depending on the compact object: so while for BHs $L_X \propto \dot{M}^2$, for NSs the relation is $L_X \propto \dot{M}$. So following the same logic as in Section 3.3.1, if the luminosity is used to track the mass accretion rate the parameter β can be estimated, which in the case of NSs, a value of zero might be expected.

The *RXTE* data for the NS outbursts have been processed and analysed in exactly the same way as the BH data detailed earlier in this chapter. A small number of lightcurves are shown below to provide examples of the differences between the NS and BH outbursts, and to hopefully show the difficulties present in trying the calculate any change in the rate of the decays.

There are two data sets from the source 4U 1608−522, from the 2005 and 2011 outbursts (Figures 3.6 and 3.7 respectively). This is a source unlike many of the BH systems in that it underwent a large number of very short outbursts during the *RXTE* era. Two of the longer outbursts are presented, but even with these immediate issues with locating and measuring exponentially decaying regions are apparent. In the 2005 outburst the source rapidly transitions from the soft to a bright hard state where it remains for ~ 100 days before increasing in luminosity again back into the soft state. The source then soon returns to a bright hard state before suddenly dropping down to a fainter level. This then gives three regions of decay, none of which suitable for further investigation. The first two exist during the rapid transitional periods between the soft and hard states,

rather than during the soft state itself, and the third is too poorly sampled to allow anything other than the crudest estimation of the e-folding time to be performed. The 2011 outburst is similar in that it lacks a smooth soft state decay, and then has a sudden drop in count rate as the source transitions. Once in the hard state there is still no smooth exponential decay, only a series of valleys and peaks slowly decreasing in average count rate. The example of SLX 1746−311 shows similar behaviour to that seen in 4U 1608−522 as well, with a second peak where the HID loops round back into the soft state after a rapid drop in count rate for a small period of time following a slow decay from the peak of the outburst.

Aquila X−1 provides the most promising opportunities of all the NS systems being the best sampled of all those considered in this study. The light curve for the 2005 outburst is shown in Figure 3.8. The outburst profile is much more standard than those of the 4U 1608−522 examples, with a simple rise, plateau and decay structure. With the hard state decay being quick and containing few data points, and the soft state decay far from a smooth exponential decay, the procedure used for the BH systems is not quite feasible, but a simpler approximation of the e-folding times can be attempted. Both are found to be faster than those of the BH sample, with the soft state decay at ~ 5 days and ~ 2 days in the hard state. The soft state in particular here has a large uncertainty on that value but does at least show that there is some evidence for a change in decay rate in this source.

The end results of looking at a sample of available NS outbursts is that there does seem to be a difference from the BH systems. Primarily this is the speed and length of the decay, these outbursts can go from peak to below the background level in a small number of days. This makes analysing the lightcurves in a similar fashion to the BH systems a challenge. Due to the speed of the decay the light curves simply aren't sampled well enough to get a good fit for the e-folding time, or even to tell exactly where a state transition occurs, and even have additional features such as flaring to further complicate the issue. So while it is difficult to say exactly what is happening in these NS outbursts in relation to changes in the radiative efficiency, it does seem to be the case that these

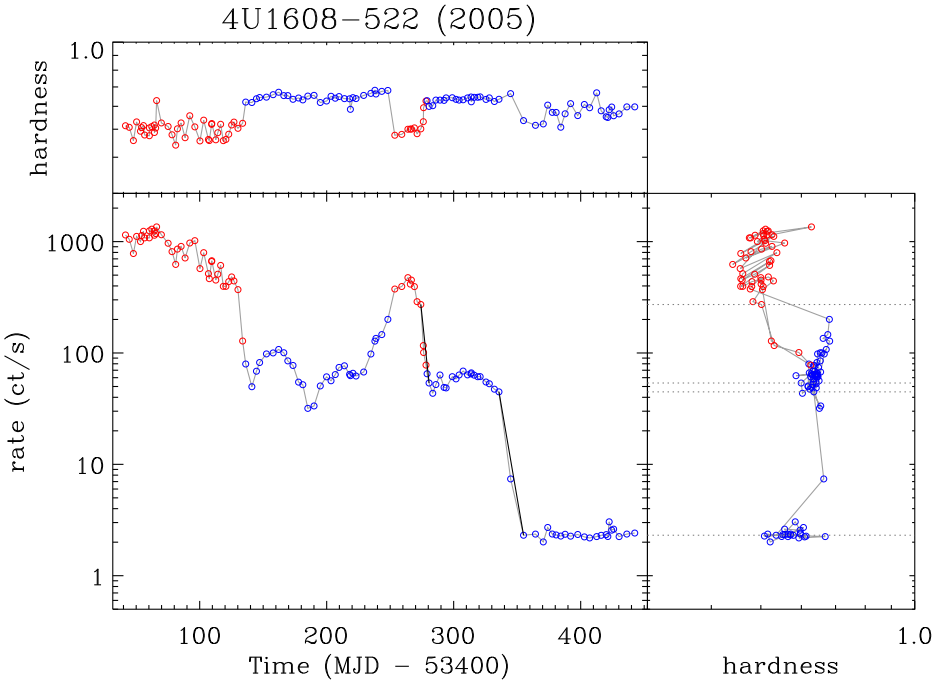

Figure 3.6: Light curve, HID and hardness curve for the 2005 outburst of 4U 1608−522.

objects are showing a different behaviour to BHs.

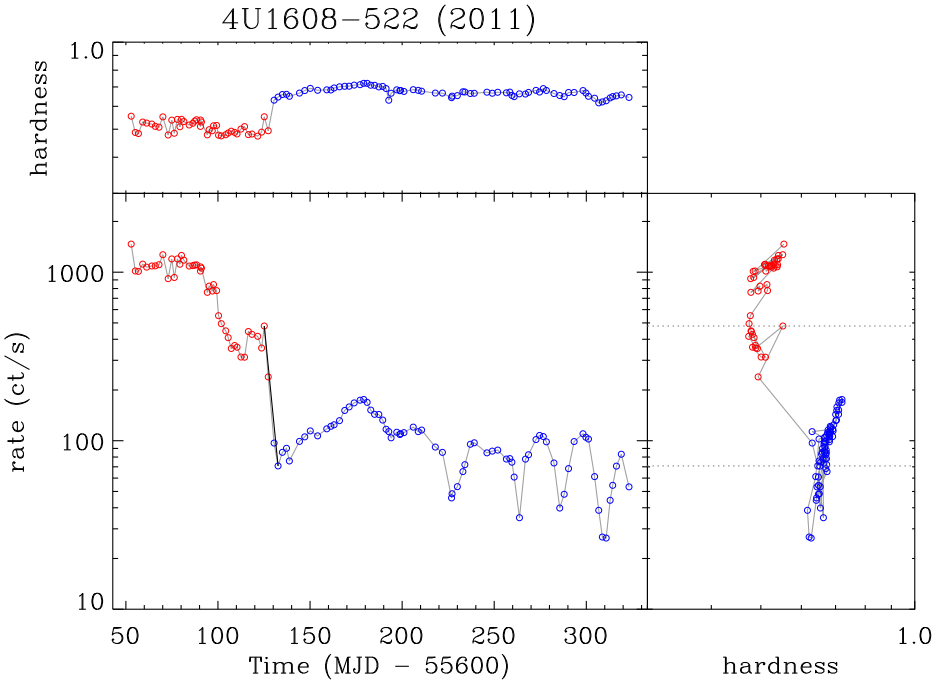

Figure 3.7: Light curve, HID and hardness curve for the 2011 outburst of 4U 1608−522.

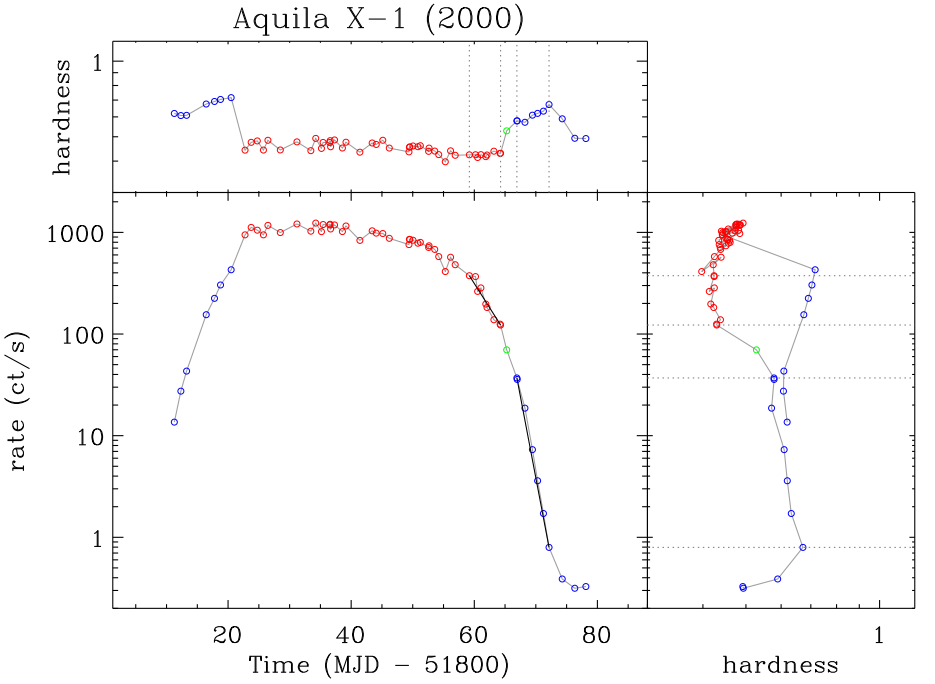

Figure 3.8: Light curve, HID and hardness curve for the 2000 outburst of Aquila X−1.

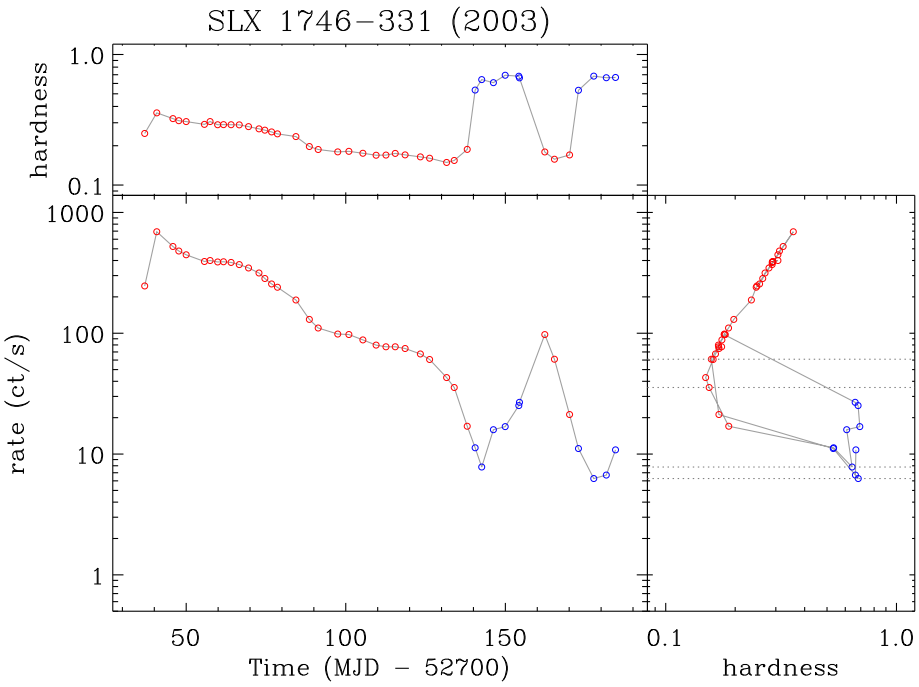

Figure 3.9: Light curve, HID and hardness curve for the 2003 outburst of SLX 1746−311.

3.8 Additional Plots

This section contains all the light curves for the systems included in Tables 3.1 and 3.2, to display graphically the results presented in those tables. In each case the top panel shows the 3-20 keV light curve during the closing phase of the outburst with exponential decay models (black) fitted to both soft-state (red squares) and hard-state (blue circles) data. The bottom panel shows the residuals from the fit described in Table 3.1, the middle panel shows the results from the fit described in Table 3.2, using only intervals of nearly uniform decay. (A constant component was added to the model as described in the text.)

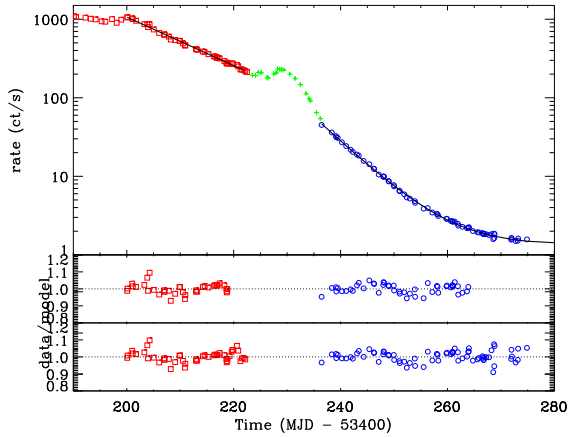

Figure 3.10: The decaying stages of the 2005 outburst of GRO J1655-40.

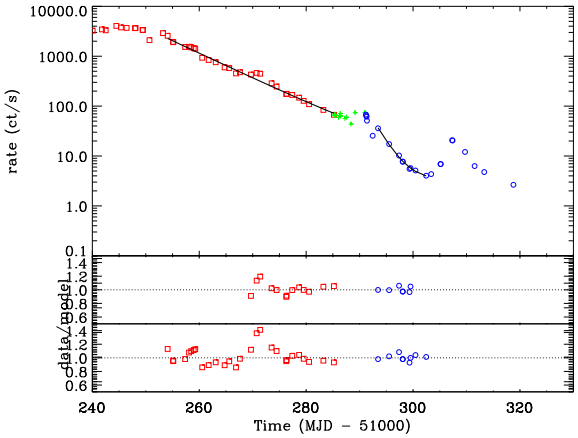

Figure 3.11: The decaying stages of the 1998 outburst of XTE J1550-564. The soft-state has a more complicated decay that is not a single exponential decay due to the flare around MJD 51270. The hard state itself is also affected by a flare, this time dominating the whole decay, leaving only a small section that could be fit.

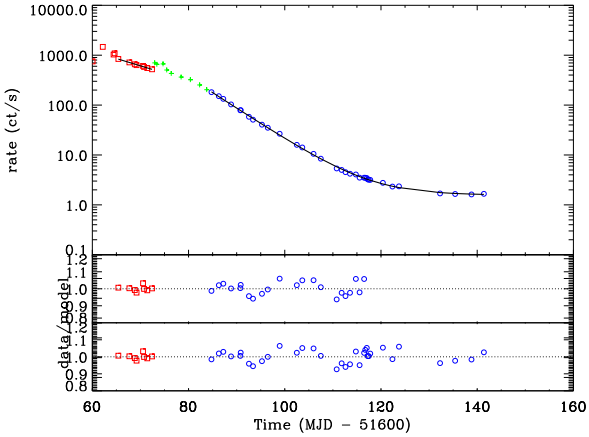

Figure 3.12: The decaying stages of the 1999 outburst of XTE J1550-564.

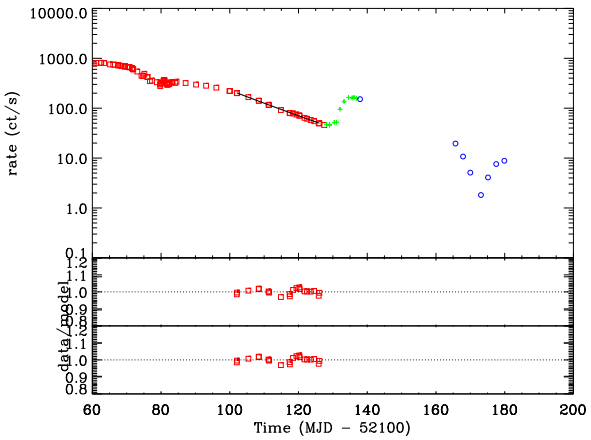

Figure 3.13: The decaying stages of the 1999 outburst of XTE J1650-500.

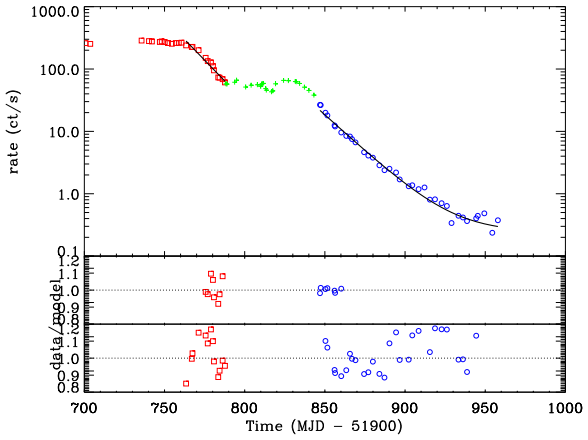

Figure 3.14: The decaying stages of the 2002 outburst of GX 339-4. We have β for this outburst, however there are certain features of the GX 339-4 outbursts that should be noted. Compared to the overall length of the soft state, the soft decaying interval is very short, with the source staying at near constant luminosity for many weeks.

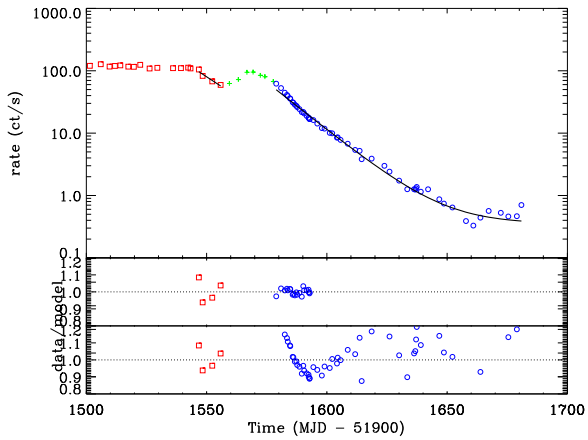

Figure 3.15: The decaying stages of the 2004 outburst of GX 339-4. The soft-state decay only lasts for around a week, making it too short to reliably measure its properties.

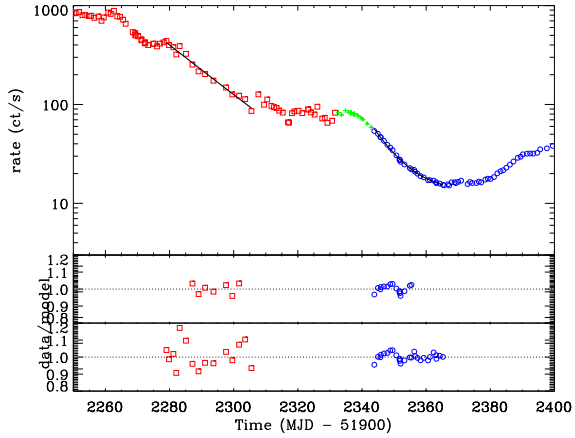

Figure 3.16: The decaying stages of the 2007 outburst of GX 339-4.

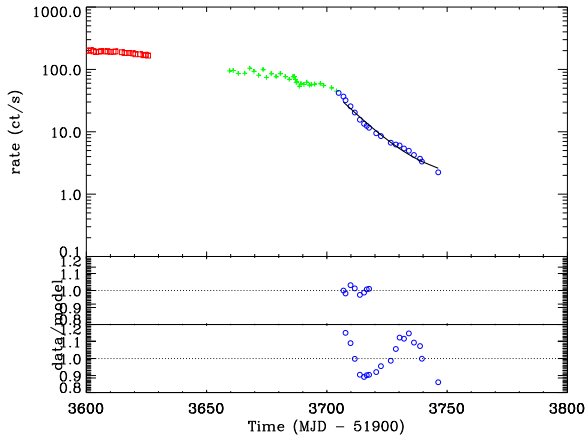

Figure 3.17: The decaying stages of the 2010 outburst of GX 339-4.

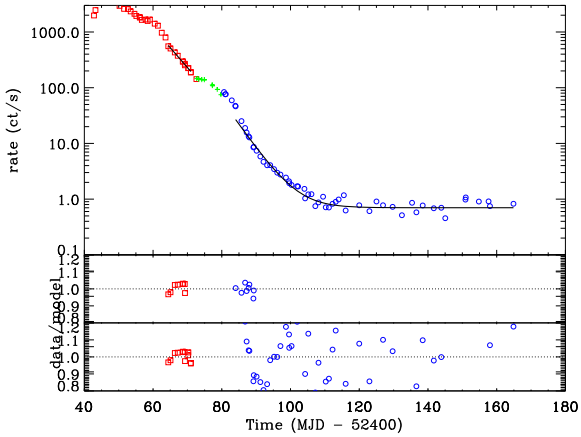

Figure 3.18: The decaying stages of the 2002 outburst of 4U 1543-475.

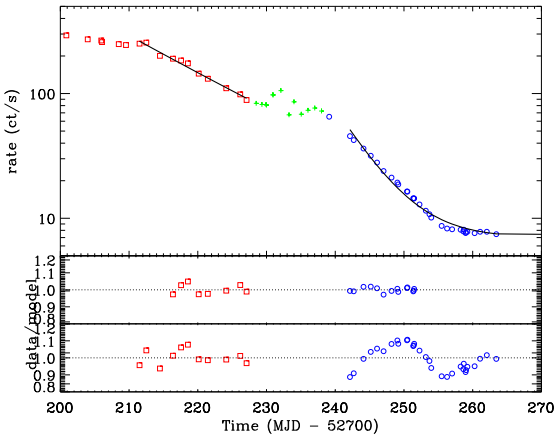

Figure 3.19: The decaying stages of the 2003 outburst of H 1743-322.

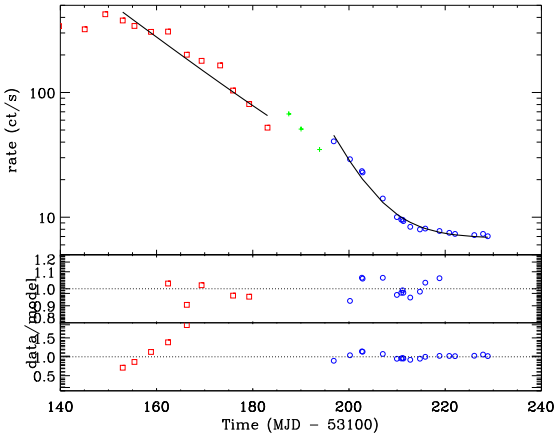

Figure 3.20: The decaying stages of the 2004 outburst of H 1743-322.

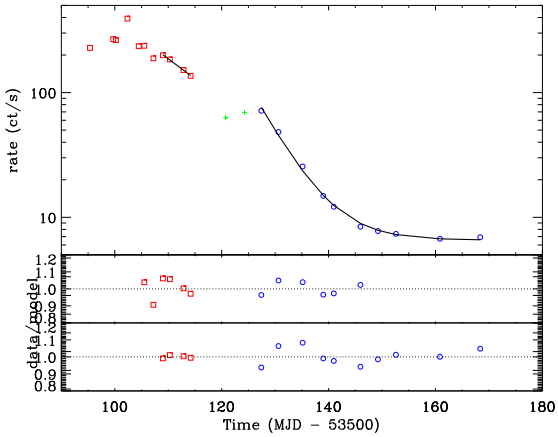

Figure 3.21: The decaying stages of the 2005 outburst of H 1743-322.

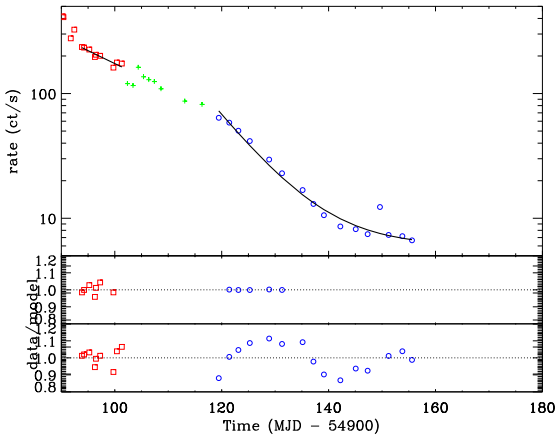

Figure 3.22: The decaying stages of the 2009 outburst of H 1743-322.

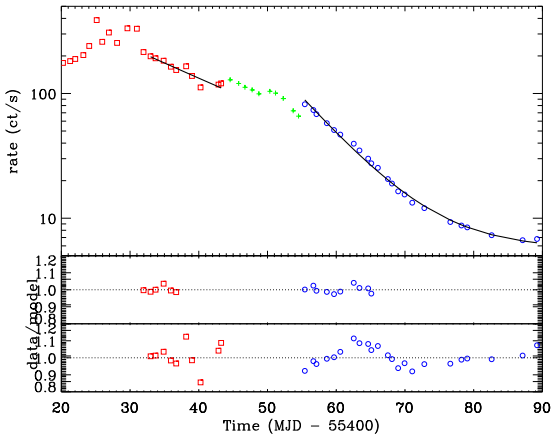

Figure 3.23: The decaying stages of the 2010 outburst of H 1743-322.

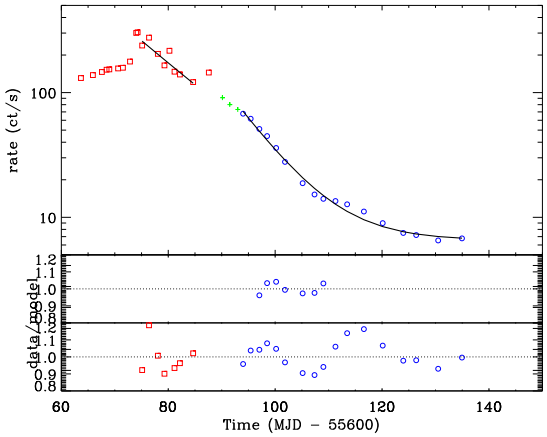

Figure 3.24: The decaying stages of the 2011 outburst of H 1743-322.

4

Spectral Fitting of the Intersteller Medium Around X-ray Binaries

4.1 Introduction

Modelling the observed X-ray spectra of XRBs requires combining several spectral components. The two dominant emission components are a thermal (blackbody-like) emission spectrum from the accretion disc and non-thermal (power law-like) emission spectrum from the corona. The relative strengths of these two distinguish between the soft and hard states. The third component is 'reflection' (Fabian et al., 1989; Reynolds & Novak, 2003; Dauser et al., 2010). Finally there is absorption, as photons pass through gas and dust in the interstellar medium (ISM), imprinting features in the observed X-ray spectrum.

Absorption from the ISM affects all X-ray observations. In order to better study the X-ray emission spectra of BH XRBs it would be useful to have both absorption models which account for both neutral and ionised species, accurate atomic data, and accurate column densities for each target source. A list such as this would allow one to quickly and accurately incorporate absorption into spectral analysis by simply selecting the best publicly available model and inserting the necessary abundances. Gatuzz et al. (2016) already provides this function for a number of BH and NS systems, here we expand on the number of BH sources. The 21cm maps (Dickey & Lockman, 1990; Kalberla et al., 2005; Willingale et al., 2013) are often used in a similar fashion, with many published spectral analyses using the hydrogen column densities found in these surveys. However, there is evidence to suggest that much of the absorption from LMXBs originate from hot gases intrinsic to the sources (Gatuzz et al., 2014; Luo & Fang, 2014). Furthermore, the 21cm maps are integrated through the entire Galaxy, while the locations of LMXBs are generally close to the centre, which could lead to a factor of two difference in the column densities. There has also been a suggestion that the column density is related to spectral states (Cabanac et al., 2009). In this chapter analysis is presented of *XMM-Newton* data for a number of BH XRBs, which attempts to assess the impact of a poor choice of absorption model and parameters on spectral analysis of such systems, and test the feasibility of a using a single set of column densities for any given system regardless of the time of observation.

4.2 Observations and Data Reduction

XMM-Newton (Jansen et al., 2001) operates in a high elliptical orbit of $\sim$ 2days, and carries three co-aligned X-ray telescopes, with three EPIC imaging spectrometers (Strüder et al., 2001), two RGS reflection grating arrays (den Herder et al., 2001), and a single Optical Monitor (Mason et al., 2001). Here only data from the RGS instrument will be analysed, chapter 5 will discuss the corresponding EPIC broad-band X-ray spectra.

In total data from 96 observations of 35 different systems have been processed. These represent all publicly available observations of BH XRBs up until 30th September 2015. The observation log in Appendix A contains all the information on the observations included in this study, along with the system parameters (mass of primary, distance and inclination) used in the RGS fitting (values taken from Tetarenko et al. (2016) and references therein). If not known, a mass of $10\mathrm{M}_{\odot}$, a distance of 5 kpc and a disc inclination of 50° is assumed.

The processing of the raw Observational Data Files (ODFs) was achieved using the standard processing chains with the *XMM-Newton* Science Analysis Software (SAS V14.0.0) and the current calibration files. RGS spectra are extracted for all observations over our sample of systems. Source and background spectral files and responses were generated using RGSPROC V$1.34.7$. The spectra from RGS1 and RGS2, along with separate exposures within each observation, were combined together using RGSCOMBINE V$1.3.4$. The tool SPECGROUP V1.6 was then used to group the spectra such that each bin is no narrower than $1/3$ of the instrumental (FWHM) energy resolution.

Here only the first-order spectra with a count rate above 1.0 counts^{-1} were examined, all those below this are labelled as faint in the observation log and were rejected from the sample. Some of the observations were bright enough that pile-up became an issue. Because of this, a number of the observations (e.g. Swift J1753.5-0127 rev2979) have been excluded from the RGS analysis.

4.3 Results

4.3.1 RGS Spectral Fitting

Spectra from each source were fit using `XSPEC` 12.9.0. `ISMabs` (Gatuzz et al., 2015) was used to model the absorption. This model includes photoabsorption from both neutral and ionised species of a number of cosmically abundant elements. Although the model includes elements

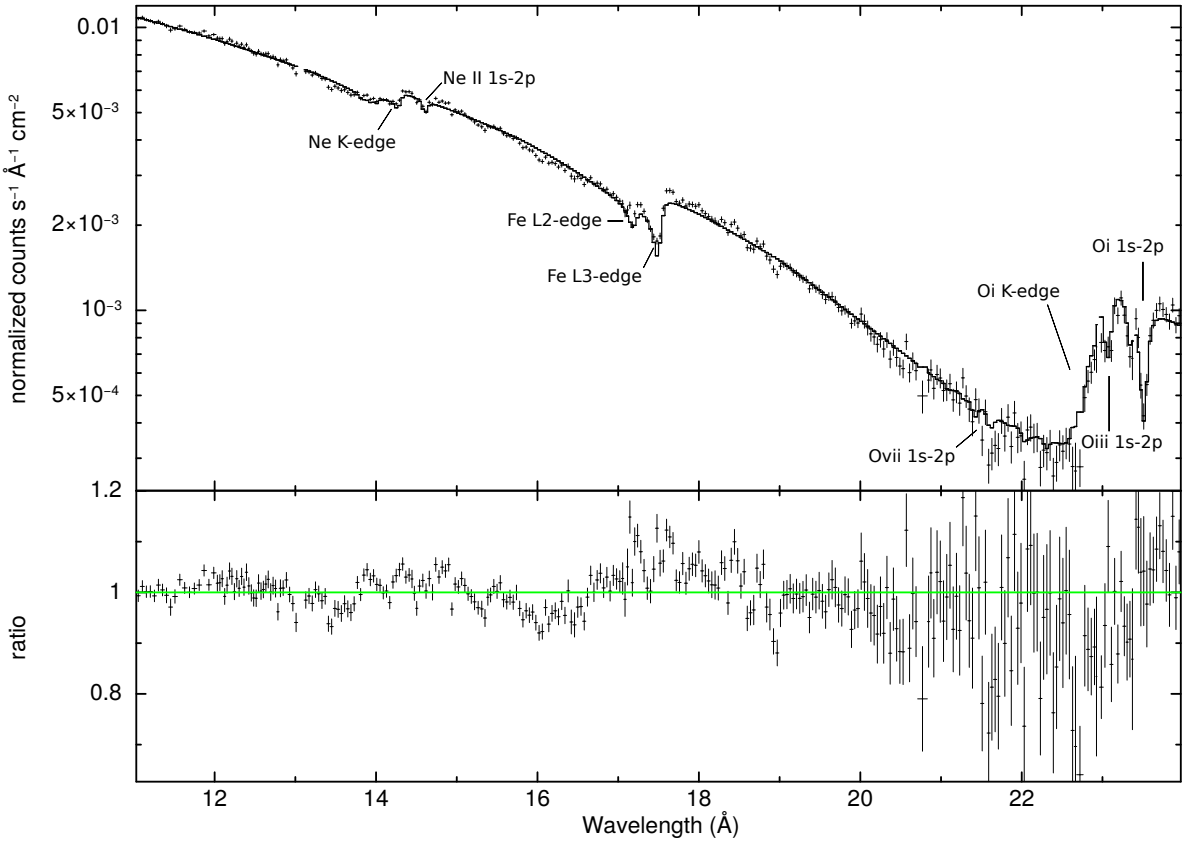

Figure 4.1: XMM-Newton RGS spectrum of the source GX 339-4 (rev0782) and the residuals. The key atomic features being modelled are labelled.

such as N, Mg, Si, and S, the aim of this analysis was to get a fit of the ISM absorption properties independent from the EPIC analysis, not to get a complete model for all features. Therefore only column densities of H, O, Ne and Fe were fitted, as these have the strongest effect on the shape of the soft X-ray absorption (the He abundance was fixed as this parameter is degenerate with the H column density). The `ISMabs` model also includes singly and doubly ionised species, so the effects of OII, OIII, NeII and NeIII were also taken into consideration. All the other elemental abundances (e.g. C, N, Si, S, Ar, Ca) were tied to N_H so that their relative abundances are equal to the ISM data in Wilms et al. (2000). Contributions from the highly ionised hot gas component of the ISM have been found to be very small and so were not included here (Gatuzz et al., 2013a,b; Luo & Fang, 2014).

To provide the soft X-ray continuum expected for a black hole X-ray binary the model `ISMabs*`

(SIMPL*KERRBB) was used. SIMPL (Steiner et al., 2009) computes a non-thermal spectrum with an approximately power law form, as might be expected from the inverse-Compton scattering of soft photons from the disc, by removing a fraction (f_{scat}) of photons from the observed disc spectrum and 'scatters' them into a power law extended to high energies. KERRBB (Li et al., 2014) models the disc spectrum, providing a multi-temperature blackbody model for a thin disc around a Kerr BH. The photon index and scattering fraction from SIMPL, and the mass accretion rate from KERRBB were allowed to vary for each individual spectrum, with SIMPL allowing both up- and down-scattering. Mass, distance and inclination were fixed at the values stated in the observation log. In KERRBB, η, the ratio of disc power produced by a torque at the inner disc boundary to the disc power arising from accretion, was set to 0, and the spectral hardening fraction, f_{col} was fixed at 1.7. The effects of self-irradiation and limb-darkening were included. It was decided to neglect the reflection component as it is a weak feature in the chosen wavelength range. At this stage, the purpose of the model is not to produce the physically plausible broad-band spectrum for a BH XRB, but to capture the basic shape of the soft X-ray continuum.

The data were fitted over a wavelength range of 11-24Å. Many of the observations have poor signal-to-noise outside of this range. Extending the fitted range up to 30Å was attempted for a small number of the sample and it was found that the N_H values were consistent with those from the smaller wavelength range. N_H was allowed to vary independently for each observation, while the abundances for O, Ne and Fe were fitted such that their abundances relative to hydrogen are kept constant across all observations.

An example of a fitted spectrum is shown in Figure 4.1 with the remainder presented in Section 4.6. The majority of the observations detailed in the observation log have a signal-to-noise ratio too low for any useful analysis and so any spectra with a net count rate lower than 1 ct/s were dropped from this part of the study, leaving 19 spectra. For the remaining sources with good data quality the values found for the column densities of the fitted elements can be seen in Table 4.1. In almost all cases the model is able to capture the main features of the data, leaving residuals of

$< 10\%$ and usually much smaller. Due to the high quality of the data though, the fit statistics were often unacceptable (using a χ^2 test) even when the residuals were small in an absolute sense. In a few cases (e.g. GRO J1655-40, GX 339-4) there are clear, systematic residuals around the Fe-L region ($17 - 18$ Å) indicating that the model does not fully capture the complexity of the iron absorption.

4.3.2 GX 339-4

The system GX 339-4 has the largest number of observations in the sample, allowing a test of the time dependence of the column densities. There are a total of 8 RGS spectra from GX 339-4 taken over 13 years with a mix of soft and hard states. The observation at rev0782 (which is merged with rev0783 to create a total exposure time of > 250ks) was fit first in the same way as the other systems. The remaining 7 observations were then fit with the N_H free, but now with the O, Ne and Fe column densities fixed so that their relative abundances are equal to those of the rev0782 spectrum. The column densities for all 8 fits are found in Table 4.1.

4.3.3 Comparison of hydrogen column density

The N_H values found in the RGS fitting can then be compared with those determined through other methods to judge how realistic they might be. The first of these methods is the use of 21cm radio maps, as in Dickey & Lockman (1990) and Kalberla et al. (2005). However these are sensitive to just atomic, neutral hydrogen. Willingale et al. (2013) used X-ray observations of gamma-ray bursts to estimate N_H, with the key difference being that they derive an empirical relationship between molecular (H_2) and atomic hydrogen. Molecular hydrogen does contribute significantly to X-ray absorption, so this allows for a more accurate estimation of the total column density. Table 4.2 shows the N_H values for the three 21cm surveys, along with the `ISMabs`

System Name	N(H)	N(OI)	N(OII)	N(OIII)	N(NeI)	N(NeII)	N(NeIII)	N(Fe)	C-stat(d.o.f)
GRO J1655-40	0.73 ± 0.01	467.4 ± 5.5	5.67 ± 2.92	9.53 ± 3.99	106.2 ± 2.3	17.3 ± 2.1	1.81 ± 0.35	21.8 ± 0.4	3016(950)
GS 1354-64	0.694 ± 0.014	443.9 ± 13.5	–	–	74.5 ± 7.8	28.6 ± 6.6	–	15.7 ± 1.3	416(316)
GX 339-4 rev0782	0.551 ± 0.057	334.9 ± 7.6	11.4 ± 4.1	12.5 ± 2.8	40.9 ± 1.9	16.6 ± 1.4	2.41 ± 0.58	17.2 ± 0.4	1093(311)
rev0514	0.557 ± 0.007	–	– –	–	–	–	–	–	1375(317)
rev1318	0.548 ± 0.013	–	–	–	–	–	–	–	689(317)
rev1325	0.539 ± 0.013	–	–	–	–	–	–	–	582(314)
rev1338	0.536 ± 0.014	–	–	–	–	–	–	–	499(316)
rev1702	0.589 ± 0.025	–	–	–	–	–	–	–	396(314)
rev1886	0.554 ± 0.008	–	–	–	–	–	–	–	953(315)
rev2879	0.544 ± 0.018	–	–	–	–	–	–	–	578(315)
Swift J174510.8-262411	1.19 ± 0.02	503.0 ± 36.9	–	405.3 ± 28.5	232.1 ± 6.4	34.3 ± 6.4	5.77 ± 1.87	39.3 ± 1.5	492(277)
Swift J1753.5-0127	0.275 ± 0.005	165.6 ± 5.07	1.87 ± 0.93	3.53 ± 0.74	21.2 ± 2.7	4.64 ± 1.36	0.98 ± 0.45	5.58 ± 0.56	1983(1240)
XTE J1720-318	1.27 ± 0.14	770.7 ± 59.9	–	–	168.1 ± 9.8	33.9 ± 8.2	–	34.2 ± 3.8	496(314)
XTE J1752-223	0.71 ± 0.01	361.5 ± 6.0	–	5.49 ± 2.95	104.2 ± 3.7	30.2 ± 3.1	3.60 ± 1.22	13.9 ± 0.7	960(313)

Table 4.1: Column densities values from `ISMabs`. N(H) is in units of 10^{22} cm^{-2}, while the metals are in units of 10^{16} cm^{-2}. Errors represent 90% confidence regions.

System Name	N_H	21cm survey[a]	21cm survey[b]	21cm+H_2 correction[c]	N_H[d]
GRO J1655-40	0.730 ± 0.010	0.684	0.578	0.722	0.784 ± 0.029
GS 1354-64	0.827 ± 0.017	0.914	0.727	0.871	–
GX 339-4	0.551 ± 0.057	0.526	0.374	0.518	0.41 ± 0.5
Swift J174510.8-262411	1.19 ± 0.02	0.659	0.652	0.796	–
Swift J1753.5-0127	0.275 ± 0.005	0.164	0.166	0.298	0.001 ± 0.026
XTE J1720-318	1.27 ± 0.14	0.477	0.525	0.635	–
XTE J1752-223	0.710 ± 0.011	0.454	0.456	0.600	–

Table 4.2: Comparison of N(H) values in units of 10^{22} cm^{-2}. [a]Dickey & Lockman (1990); [b]Kalberla et al. (2005); [c]Willingale et al. (2013) and [d]Gatuzz et al. (2016).

hydrogen column densities found in this paper and in Gatuzz et al. (2016), another recent study of X-ray absorption in XRBs using the same absorption model and a similar method. H column density estimates at any point on the sky based on the 21cm maps are weighted averages of nearby measurements, typically within 1° of the target position.

4.4 The Effect of Incorrect Absorption Estimates on Disc Parameters

The majority of spectral analysis of LMXBs in the literature will have been performed with absorption models and column densities different from those presented in this work. If comparisons are to be made between disc parameters found from the results presented here and those using an older model or N_H estimates from the 21cm maps for instance, then an awareness of any systematic biases originating from an incorrect treatment of absorption is necessary. For example, the inner radius of the accretion disc is often estimated from spectral fitting so a bias in the disc temperature caused by the use of an unsuitable model or column densities would lead to an inaccurate measure of the disc surface area.

To test this a model was fit to simulated energy spectra. The `XSPEC` tool `fakeit` was used, which

- given a spectral model, and relevant response matrix data - returns a simulated energy spectrum. Here the response files from a *XMM-Newton* EPIC-pn observation of Swift J1753.5-0127 were used. The exposure time of the simulated observation was set at 40 ks. The parameters for the continuum were set to numbers typical for each state. For the hard state: $\Gamma = 1.7$, $f_{scat} = 0.5$, $\dot{m} = 0.1 \times 10^{18}$ g s^{-1} and $f_{col} = 1.5$, and in the soft state: $\Gamma = 2.5$, $f_{scat} = 0.1$, $\dot{m} = 1.0 \times 10^{18}$ g s^{-1} and $f_{col} = 2.0$. For the `ISMabs` parameters three different N_H values were selected: 0.3, 0.9, and 1.5$\times$ 10^{22} cm^{-2}. These three N_H values extend the study to test both heavily and lightly absorbed sources. This gives six spectra in total, a soft and a hard state for each N_H value. The column densities for O, Ne and Fe were set such that the relative abundances match those in Wilms et al. (2000).

The model of `WABS*(SIMPL*KERRBB)` was then fit to each of these simulated spectra over an energy range of $0.8 - 10.0$ keV, and the disc parameters were calculated as a function of the hydrogen column density inputted and frozen into `wabs`. Five different N_H values were chosen to be fit to each simulated spectra. Given the range of N_H values to be fit it was impossible to choose a set of five values that would be suitable in all cases, so instead they were decided separately, in such a way that the spread represents the range of values in which a well constrained fit is still possible. The plots showing the free parameter values are shown in Figure 4.2. One fit was also performed for each simulated N_H value where the fitted N_H value was allowed to go free. The results of these fits can be seen on the plots as the larger data points.

In these fits with N_H allowed to vary, the degeneracies between the hydrogen column density and the other free parameters can be tested by performing Markov Chain Monte Carlo (MCMC) analysis. The 'emcee' Python code (Foreman-Mackey et al., 2013) was used to complete this analysis. The Goodman-Weare algorithm was used with 100 walkers each performing 1000 iterations (in each case an additional 100 were performed first and ignored - this is the 'burn in' period). The initial distribution of the walkers was determined by the best-fit value found by XSPEC. A contour plot with the results for the $N_H = 0.3 \times 10^{22}$ cm^{-2} hard state spectrum can be seen in Figure 4.3

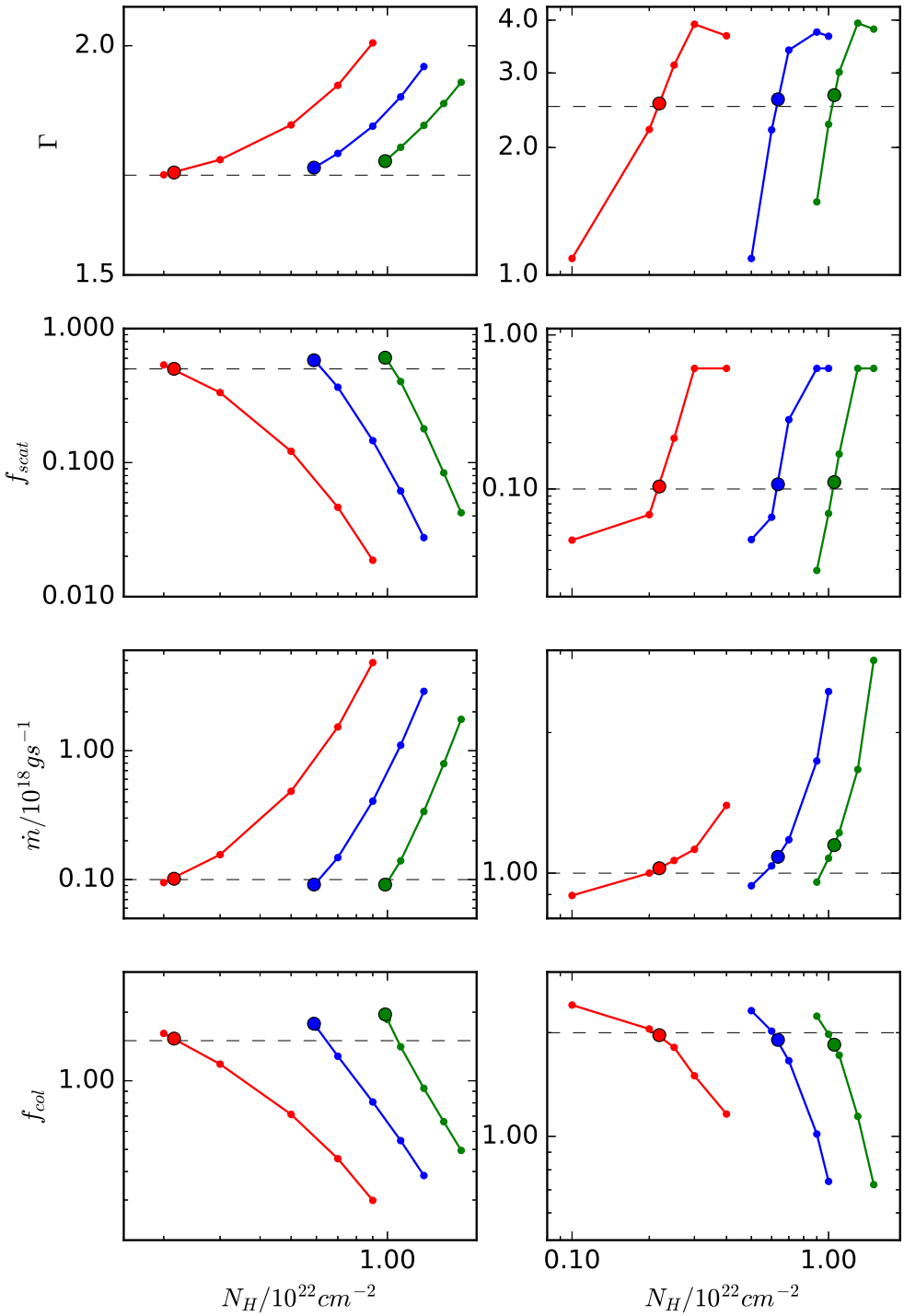

Figure 4.2: The best-fitting emission model parameters as a function of the assumed N_H, for different true values of N_H, based on fitting simulated EPIC data. The results from the hard state are found in the left column, with the soft state on the right. The N_H=0.3, 0.9 and 1.5$\times$ 10^{22} cm^{-2} results are shown in the red, blue and green data points respectively. The larger points represent the results when N_H is included as a free parameter. The dashed line on each plot represents the true parameter value.

(This plot was created using the 'corner' Python code (Foreman-Mackey, 2016)).

4.4.1 The Effect of Dust

`ISMabs` is a model which only includes the affects of the atomic and gaseous ISM, it does not include contributions from dust and molecules. Some studies (e.g. Pinto et al. 2010, 2013) have suggested that a significant amount of OI and FeI is found in dust, so it would be useful to understand the effect of not including solids has on the determination of the disc parameters. To do this the model `TBvarabs` was used, which includes absorption from grains and molecules in the ISM, and crucially, includes 'grain depletion fractions' as free parameters which allows the user to control the ratio between gas and solids (Wilms et al., 2000).

Here a hard state EPIC-pn observation was simulated using the same response files, exposure time and continuum parameters as in the previous section, but with a model of `ISMabs*TBvarabs*(SIMPL*KERRBB)`. The `TBvarabs` component was set such that its contribution to the total absorption is completely in the form of solids, i.e. the grain depletion fraction parameters were all set to 0. The fraction of the total column density which is in grains was based on the results in Pinto et al. (2013), specifically the measured column densities for GX 339-4 in their Table 3. Two models were then fit to the simulated data set. The first was a model with both `ISMabs` and `TBvarabs`, and the second was one with only `ISMabs`. The results of the spectral fits can be found in Table 4.3. It was found that not including the dust model has a very small effect on the disc parameters, with only a $\sim 1\%$ deviation from the true parameters values.

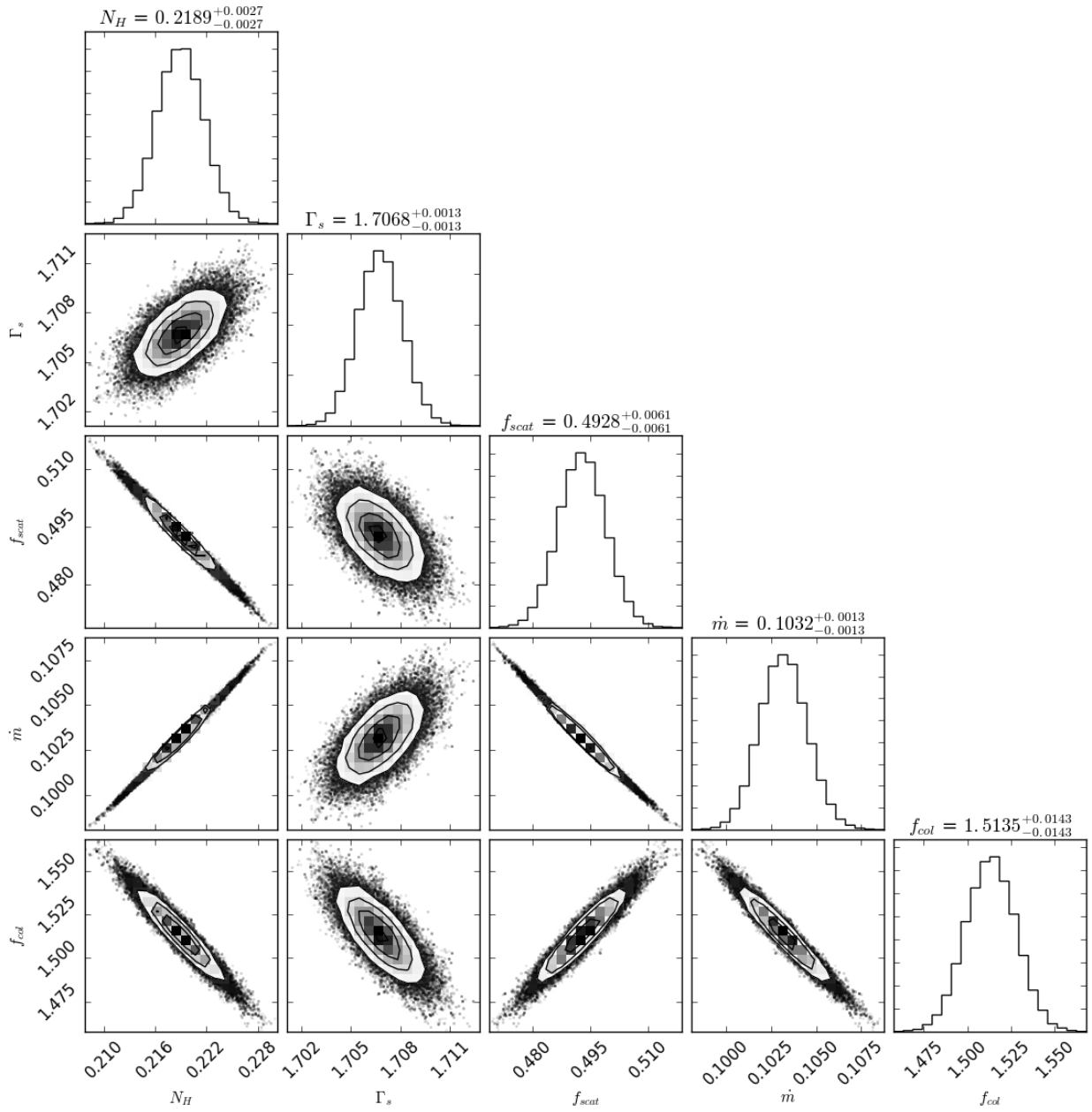

Figure 4.3: Contour plots from the MCMC analysis of a simulated hard state EPIC broad-band spectrum fitted with a model with free parameters: N_H, Γ, f_{scat}, $\dot{m}$ and f_{col}. Contours represent 1, 2 and 3σ confidence levels. The true parameter values are: $N_H = 0.3 \times 10^{22}$ cm^{-2}, $\Gamma = 1.7$, $f_{scat} = 0.5$, $\dot{m} = 0.1 \times 10^{18}$ g s^{-1} and $f_{col} = 1.5$.

Parameter	`ISMabs*TBvarabs`	`ISMabs`
Γ	1.699 ± 0.001	1.700 ± 0.001
f_{scat}	0.501 ± 0.001	0.497 ± 0.001
$\dot{m}$	0.998 ± 0.002	1.012 ± 0.004
f_{col}	1.504 ± 0.001	1.490 ± 0.007
$\chi^2_{red}(dof)$	$1.04(146)$	$1.11(146)$

Table 4.3: Results of tests on the effect of including dust in the ISM model. An EPIC spectrum is simulated with a gas+dust model, and fitted with a gas+dust model (left) and a gas-only model (right). Here $\dot{m}$ is in units of 10^{17} g s^{-1}.

4.5 Discussion

An analysis of soft X-ray grating spectra from BH XRBs has been performed to estimate the amount of absorption affecting such sources. Overall it has been found the `ISMabs` model is capable of adequately fitting the majority of the features of the RGS spectra, with the most significant residuals appearing around the Fe and O edges at ~ 17Å and ~ 23Å respectively. One possible explanation for these residuals is dust: the model that was used only accounts for absorption due to the gaseous ISM. Pinto et al. (2010, 2013) found evidence for large percentages of O and Fe existing in the form of solids, so the residuals could be due to features associated with this dust. This may also explain the fact that the OIII column densities are always higher than OII if it is overestimating OIII to make up for the lack of solids at 23Å. At the oxygen K-edge though, Gatuzz et al. (2016) find that using more recent atomic cross-sections than those used in Pinto et al. (2010) can provide a good fit in the $21 - 24$Å region. The effects of adding dust to the model have also been tested and it was found that it makes only a very minor difference in the determination of disc parameters as shown from the results in Table 4.3. So while a more complete model of all three phases of the ISM may be able to fit the finer features of the RGS data more effectively, not including dust leads to only a very small bias in the results of broad-band spectral fitting.

From the best fits of the data a wide range of hydrogen column densities are found, some of which

differ greatly from those presented in previous surveys. The best agreement seems to come from the results of Willingale et al. (2013) with GRO J1655-40, GX 339-4 and Swift J1753.5-0127 in particular having approximately the same column density. The GS 1354-64 estimate sits between the Kalberla et al. (2005) and Willingale et al. (2013) results. The XTE J1720-318 results is more than two times larger than all three 21cm maps, but is in agreement with a value found in Cadolla Bel et al. (2004). In general there seems to be a tendency for finding higher N_H values from soft X-ray fitting compared to those from the 21cm maps, in agreement with previous work. X-ray absorption spectroscopy cannot distinguish between absorption due to H, He I and He II. Unlike the metals, H and He do not produce the narrow edges found at specific wavelength, and instead produce broader features that cannot be disentangled. Differences in the abundance of He (relative to H) compared to that assumed in the `ISMabs` model (N_{He}/N_H=0.1) may explain slight differences in the N_H values inferred from X-ray spectroscopy and from 21cm maps.

The results for three of the systems can be compared with those from Gatuzz et al. (2016), who also used the `ISMabs` model for their calculations. A slightly smaller N_H for GRO J1655-40 is found here, but a larger value for GX 339-4 and Swift J1753.5-0127, with Swift J1753.5-0127 having a significant discrepancy (more than two orders of magnitude). Gatuzz et al. (2016) claim the choice of continuum model can produce different column densities despite similar fit statistics. This could explain the disagreements as they used a broken power law to model the continuum. This was tested by performing similar fits with `ISMabs*bknpower` and column densities were found that were mostly in agreement with the values in Gatuzz et al. (2016), except in the case of Swift J1753.5-0127, with the broken power law giving slightly better fit statistics. The value for Swift J1753.5-0127 presented in Gatuzz et al. (2016) is inconsistent with all other estimates of this source (their value is more than 100 times lower than those from the 21cm maps). This in turn means the relative abundances of the metals are two orders of magnitude higher that typical, (e.g. Wilms et al. 2000), and would require a H column density towards Swift J1753.5-0127 lower than that through the Lockman Hole (Lockman et al., 1986). Therefore, the results presented in this chapter would likely represent the more plausible situation.

Given the level of disagreement between the results from the model used here and those from the literature, it is clear that the value of N_H does need to be treated with care, and that estimates of N_H derived from spectral analysis of RGS data can be very sensitive to the choice of continuum. However, the best way to deal with these model dependencies is still unclear.

The 21cm maps can only act as a proxy for X-ray absorption. Soft X-ray absorption on BH XRBs spectra has strong contributions from molecular H, atomic and ionised He, and from metals in the ISM. There is also the possibility of small-scale variations in the ISM that are not resolved by most 21cm maps, or absorption local to the source, perhaps even influenced by the source, such as an accretion disc wind. None of these will show up in 21cm data and have to be assumed unless explicitly estimated from the soft X-ray data. Therefore, if the differences that are seen are due to a combination of these additional factors then this at least justifies the use of the soft X-ray grating data to provide more specific column density estimates for a given source.

From the analysis of the GX 339-4 observations it has been possible to track changes in absorption features over ~ 13 years. The fitted N_H values can be found in Table 4.1. In all cases an acceptable fit is found and a good agreement over all observations with a spread of N_H=$(0.536-0.589)\times 10^{22}$ cm^{-2}. These are generally consistent with the value of $5.1 \pm 0.4 \times 10^{22}$ cm^{-2} found in Pinto et al. (2013), but higher than the $4.1 \pm 0.5 \times 10^{22}$ cm^{-2} in Gatuzz et al. (2016). There does appear to be some variation in N_H values found, with the largest and smallest values not being consistent within their errors, though this variation does not seem to be strongly correlated with luminosity. While there is a slight tendency for finding smaller N_H in the brighter observations there are several exceptions even within this small data set (e.g. rev514 is a bright soft state with the second highest N_H), and a Spearman's Rank test finds a fairly weak negative correlation of -0.31. In addition, no strong correlation is found between N_H and spectral state as presented in Cabanac et al. (2009). For the eight GX 339-4 RGS spectra in this study we have an equal distribution of soft and hard states, with a mix of values within each state.

An attempt has also been made to estimate the affect of using older models and incorrect column densities on the spectral fitting of EPIC data. It is found that using a model such as `wabs` instead of the more detailed `ISMabs` can have a systematic effect on disc parameters. For all values of true N_H it can be seen that using `wabs` produces a stronger absorption component, which will simply be due to the differences in the cross-section data. Beyond that, it can also be seen that there are some clear relations between the level of absorption and the true values of the disc parameters. In the hard state, getting the N_H value wrong affects all four free parameters. The spectral index of the power law increases with the tested N_H, with values approaching 2 for the worst fits. The scattering fraction decreases, ultimately producing results much more characteristic of the soft state than the hard. The largest impact though is on the black body component, with both $\dot{m}$ and f_{col} rapidly entering unrealistic values. The picture is similar in the soft state only with f_{scat} trending in the opposite direction with higher N_H leading to a higher number of photons scattered into the power law. The use of MCMC analysis illustrates the level of covariance N_H has with the four spectral parameters. Figure 4.3 shows contour plots for each of the free parameters when fitting the simulated data. N_H is very strongly correlated with f_{scat} and $\dot{m}$, with an overestimation of N_H leading to an underestimation of f_{scat} and a simultaneous overestimation of $\dot{m}$. Allowing the fitted N_H values to go free has a much less significant effect on the disc parameters, with in most cases the fitted values being very close to those simulated. They do require though a much smaller fitted hydrogen column density, with an approximately 30% drop in each case.

In general then it would appear that for any spectral fitting in which there is no independent assessment of the amount of absorption present then it is in all cases better to allow the hydrogen column density as a free parameter. Not doing so systematically changes the inferred temperature of the disc for even small inaccuracies in the N_H value. This will ultimately lead to a bias on estimates of basic system parameters such as the BH mass or disc inner radius.

4.6 Additional Plots

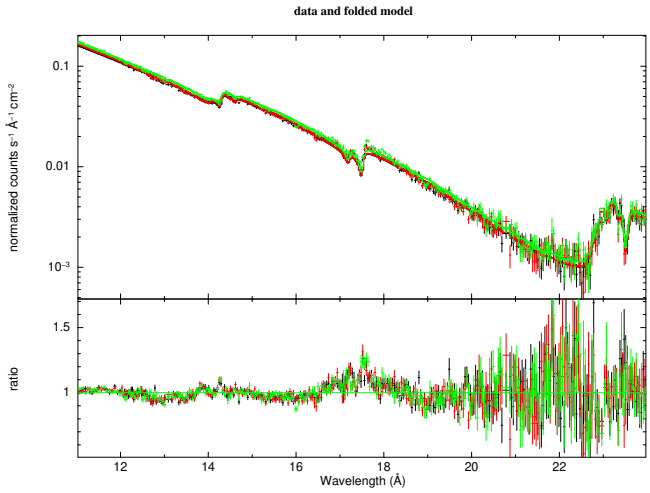

Figure 4.4: XMM-Newton rgs spectrum of the source GRO J1655-40 when fit with the model `ISMABS(SIMPL*KERRBB)`

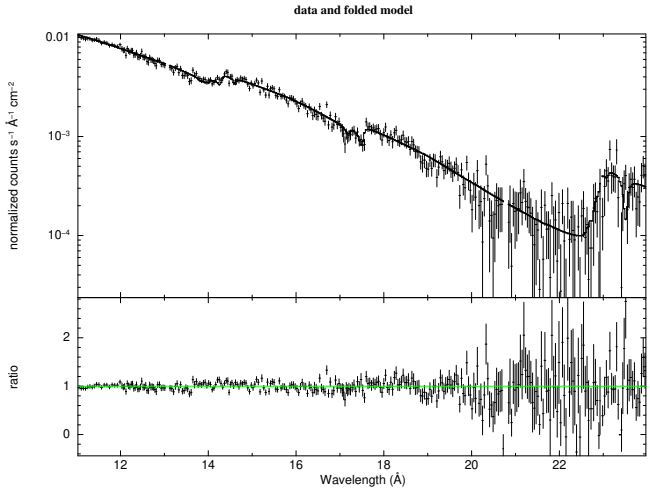

Figure 4.5: XMM-Newton RGS spectrum of the source GS 1354-64 and the residuals.

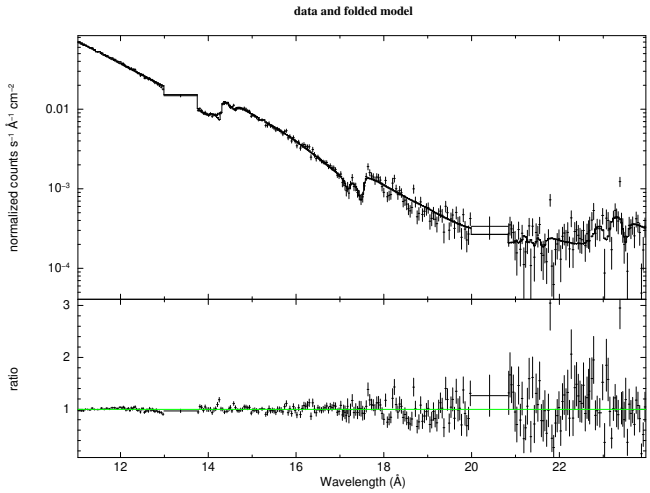

Figure 4.6: XMM-Newton RGS spectrum of the source Swift J174510.8-262411 and the residuals.

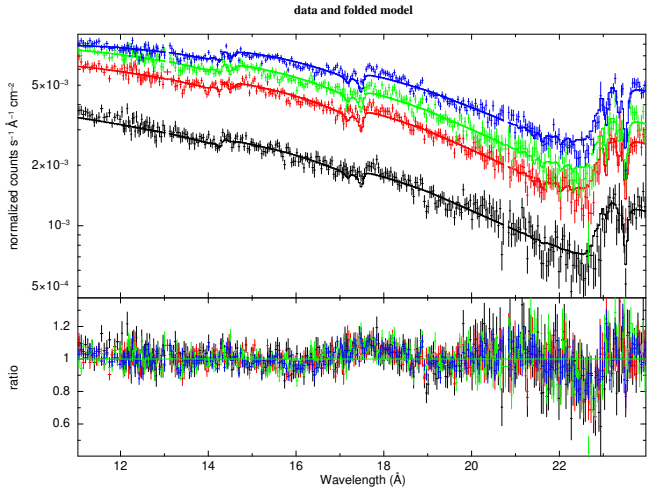

Figure 4.7: XMM-Newton RGS spectrum of the source Swift J1753.5-0127 and the residuals.

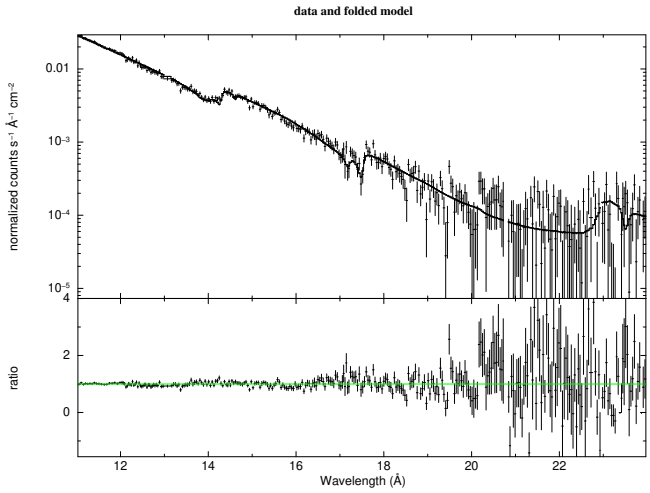

Figure 4.8: XMM-Newton RGS spectrum of the source XTE J1720-318 and the residuals.

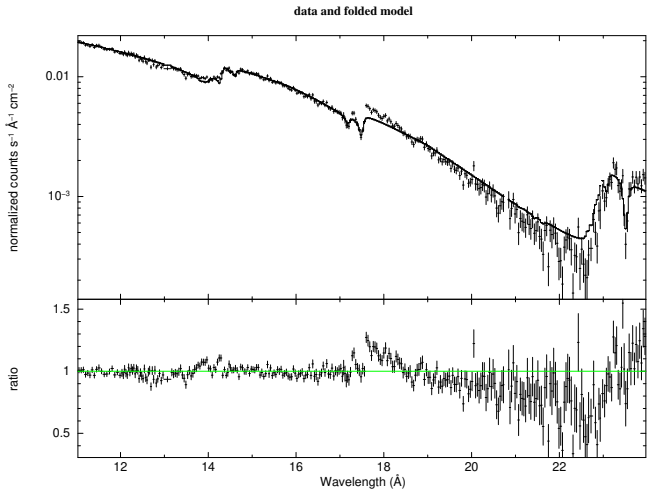

Figure 4.9: XMM-Newton RGS spectrum of the source XTE J1752-223 and the residuals.

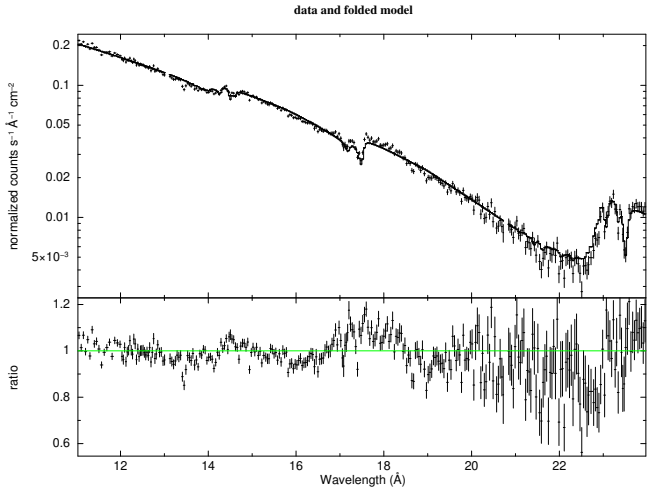

Figure 4.10: XMM-Newton RGS spectrum of the source GX 339-4 (rev0514) and the residuals.

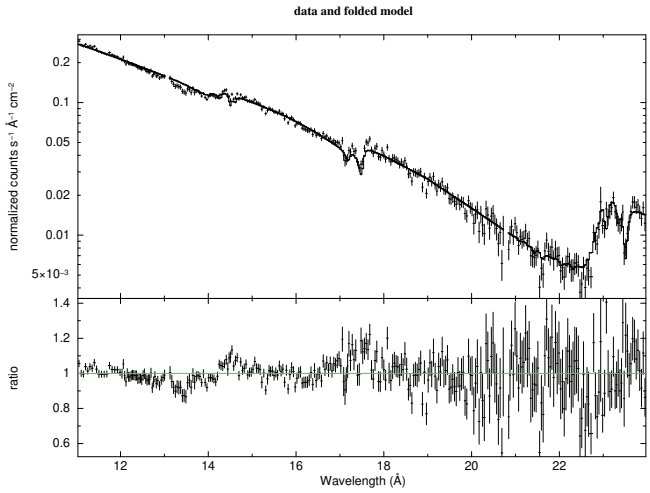

Figure 4.11: XMM-Newton RGS spectrum of the source GX 339-4 (rev1318) and the residuals.

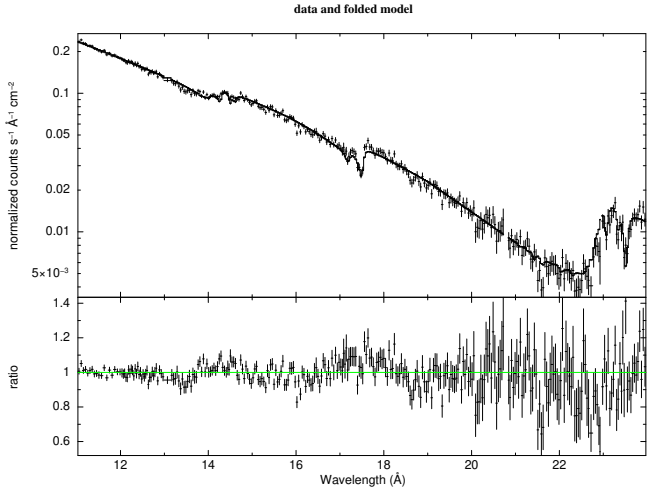

Figure 4.12: XMM-Newton RGS spectrum of the source GX 339-4 (rev1325) and the residuals.

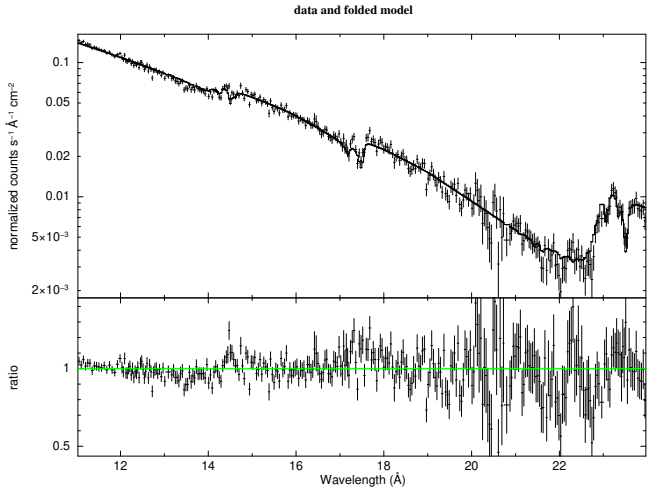

Figure 4.13: XMM-Newton RGS spectrum of the source GX 339-4 (rev1338) and the residuals.

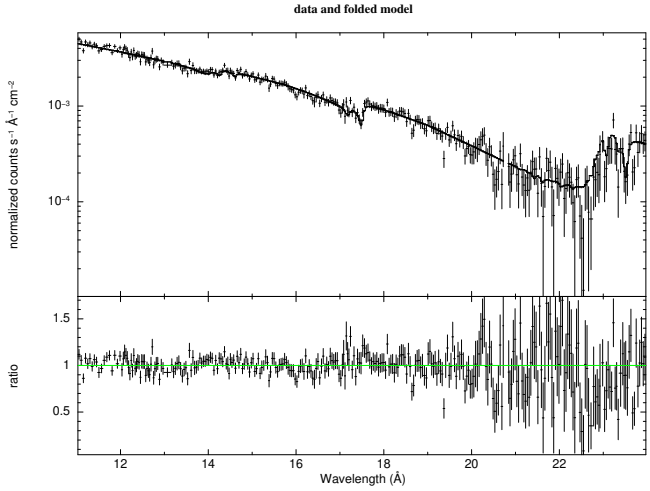

Figure 4.14: XMM-Newton RGS spectrum of the source GX 339-4 (rev1702) and the residuals.

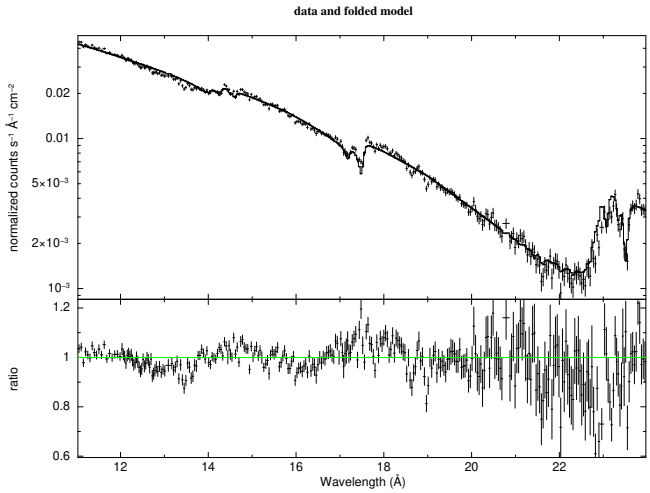

Figure 4.15: XMM-Newton RGS spectrum of the source GX 339-4 (rev1886) and the residuals.

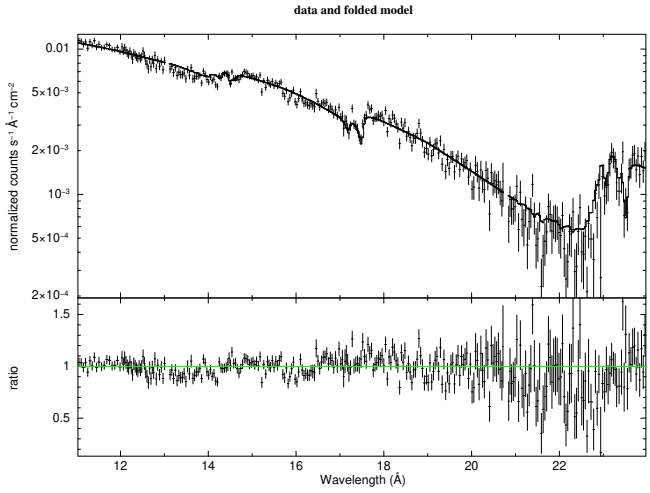

Figure 4.16: XMM-Newton RGS spectrum of the source GX 339-4 (rev2879) and the residuals.

5

A Test of Truncation in the Accretion Discs of Transient Low Mass X-ray Binaries

5.1 Introduction

The aim of this chapter will be to use the best available spectral models, some of the best available data from *XMM-Newton*, and the independent fit of the ISM from Chapter 4, to construct a single 'standard' model of an accretion disc around a BH. The test will then be to attempt to fit spectra from both the soft and hard state with physically consistent parameters under the assumption that the accretion disc extends all the way into the innermost stable orbit around a non-spinning black hole.

As has been discussed in detail in the Introduction section of this thesis there has been plenty

of discussion on this topic in the past, with no definitive conclusions yet on the extent to which truncation would occur during bright hard state. Most studies in the literature tend to focus on a relatively small sample of observations. Different papers by different groups may use slightly different data reduction methods, and often use different spectral models, making comparisons between results less simple. The chapter presents a uniform analysis of *XMM-Newton* spectra from several black hole X-ray binaries. A spectral model is constructed for a 'standard' accretion disc around a non-spinning ($a = 0$) black hole, which extends down to $r_{in} = r_{ISCO} = 6r_g$, including thermal and non-thermal continuum sources, reflection and relativistic effects. The primary goal is to fit the model to the data and search for systematic deficiencies in the model fits that would be indicative of truncation of the classical accretion disc.

5.2 Observations and Data Reduction

Data from 96 different observations of 35 LMXB systems have been processed. These represent all publicly available observations of BH XRBs up until 30th September 2015. Long term lightcurves for each system are shown in Appendix B. These were produced using data from *RXTE*/ASM, *Swift*/BAT and MAXI. The times of the *XMM-Newton* observations are labelled in red. These are included to provide context for each observation (to help distinguish between rising and decaying hard or intermediate states, for example). The table in Appendix A contains all the information on the observations included in this study, along with the system parameters (mass of primary, distance and inclination) used during the spectral analysis (values taken from Tetarenko et al. (2016) and references therein). If not known, a mass of $10\mathrm{M}_{\odot}$, a distance of 5kpc and an inclination of 50° is assumed.

The raw Observational Data Files (ODFs) were processed using the standard processing chains with the *XMM-Newton* Science Analysis Software (SAS V15.0.0) and the current (as of October 2016) calibration files. The data was checked for periods of high background count rates, with

these regions being removed where necessary. The EPIC-pn event files were also filtered to allow only events with `PATTERN <= 4` and `FLAG==0`. For observations taken in timing or burst mode, events were extracted using EVSELECT V3.62 in a rectangular region with a width in `RAWX` of 15 centered around the brightest column. Observations taken in an imaging mode used a circular region centered on the source. Background regions were extracted by using the same sized regions away from the source. Response matrices and ancillary files were produced using the tools RMFGEN V2.5.1 and ARFGEN V1.93.1 respectively. Finally, the data is binned using SPECGROUP V1.6 such that each bin contains at least 25 source counts, and is no narrower than 1/3 the instrumental (FWHM) energy resolution.

Some of the data, particularly those taken in timing mode during brighter periods, may be affected by pile-up. The tool EPATPLOT V1.20 was used to check for the presence of pile-up. Where necessary this pile-up was decreased to an acceptable level by the removal of a small section of the extracted region centered around its brightest point.

5.3 Analysis

5.3.1 Model

Energy spectra from each source were fitted using `XSPEC` 12.9.0. To provide the soft X-ray continuum expected for a BH XRB the model `ISMabs*(SIMPL*KERRBB) + RELXILL` was used. Here we briefly describe the model components.

`KERRBB` (Li et al., 2014) models the disc spectrum, providing a multi-temperature blackbody model for a thin disc around a Kerr BH. A disc model was required that could include the range of temperatures expected from an accretion disc around a BH, but also takes into account relativistic effects and any modifications of the spectrum by a disc atmosphere. Preferably, the model would

also have parameters in physical units for the system (e.g. mass accretion rate), and that the values of the spin of the BH can be specified and modified if necessary. Many disc models commonly used in studies of XRBs are unsuitable here. DISKBB does not include the effects of General Relativity, and does not work directly in physical units, with only a temperature and normalisation as parameters. DISKPN works as an extension of DISKBB, by including corrections which approximate the potential in General Relativity. These corrections only modify the temperature distribution near to the BH though, still neglecting the effects on the emerging radiation, such as redshift, and self-irradiation. KERRBB includes parameters to model those latter processes, and fulfils all the other criteria. To account for the effects of the disc atmosphere on the emergent spectrum KERRBB uses a simple colour correction factor (also called spectral hardening factor) which shifts the spectrum up in energy by a constant factor f_{col} (Shimura & Takahara, 1995). BHSPEC (Davis et al., 2005) can provide an alternative to this, self-consistently modelling the vertical structure and radiative transfer of disc annuli, using calculations from stellar-like atmospheres. These additional physical considerations though lead to slower and poorer fits, suggesting the model is not yet capable of modelling realistic disc spectra. This means KERRBB remains the strongest option, offering the simplest, fastest model which contains all the features relevant to this study.

SIMPL (Steiner et al., 2009) computes a non-thermal spectrum with an approximately power law form, as might be expected from the inverse-Compton scattering of soft photons originating in the disc. It removes a fraction (f_{scat}) of photons from the observed disc spectrum and 'scatters' them into a power law extended to high energies. SIMPL operates in a self-consistent, photon conserving manner, by linking the seed disc spectrum with the power law. This means that it has a low-energy cut-off, unlike POWERLAW which continues to increase in flux at low energies. The naive power law model would therefore overpredict the soft X-ray emissions (relative to a more realistic treatment of Compton scattering). In order to fit a spectrum, the soft, thermal disc emission would need to be weaker to compensate. Salvesen et al. (2013) call this 'flux stealing'. There are more advanced models available which provide a more detailed physical model of Comptonization, e.g. COMPTT (Titarchuk, 1994) and EQPAIR (Coppi, 2000). However these models

can bring other disadvantages, such as potentially running at a slower rate, or being more difficult to couple with the disc spectrum. For example, COMPTT requires an input temperature. KERRBB does not produce emission at a single temperature, and does not have T_{peak} as a parameter. By coupling the SIMPL model to KERRBB a reasonable approximation can be produced to inverse-Compton scattering of thermal disc emission, and the model conserves photon number, and does not suffer from 'photon stealing'. This self-consistency is hard to achieve using alternative model components.

The photon index and scattering fraction from SIMPL, and the mass accretion rate from KERRBB were also allowed to vary for each individual spectrum, with SIMPL allowing both up- and down-scattering. Mass, distance and inclination were fixed at the values stated in Appendix A. In KERRBB, η, the ratio of disc power produced by a torque at the disc boundary to the disc power arising from accretion, was set to 0, and the spectral hardening fraction, f_{col} was also included as a free parameter. The effects of self-irradiation and limb-darkening were included.

To model the spectrum of 'reflection' from the relativistic disc the model RELXILL (García et al., 2014) was used. This combines the ionised reflection model XILLVER (García & Kallman, 2010; García et al., 2011, 2013) with the relativistic smearing kernel of RELLINE (Dauser et al., 2010, 2013), which then accounts for the angular distribution of the reflected X-rays. There are few alternative models for relativistic disc reflection, so RELXILL was the natural choice, being easily coupled with the other components. The input spectrum can be set to the index from SIMPL if required, and r_{in} can be set in units of R_{ISCO} and the spin set equal to that from KERRBB. Within RELXILL the disc ionisation parameter, $log(\xi)$, and reflection normalisation, N_r were included as free parameters. Many models of disc reflection use a 'reflection fraction' parameter R, meant to represent $R = \Omega/2\pi$ where Ω is the solid angle subtended by the disc as seen from a point-like illuminating X-ray source above the disc. A value $R \approx 1$ represents a flat disc extending to very large and very small radii. Although our model has a very simple and fixed disc geometry, we do not enforce $R = 1$ and instead let the reflection normalisation be a free parameter. The photon

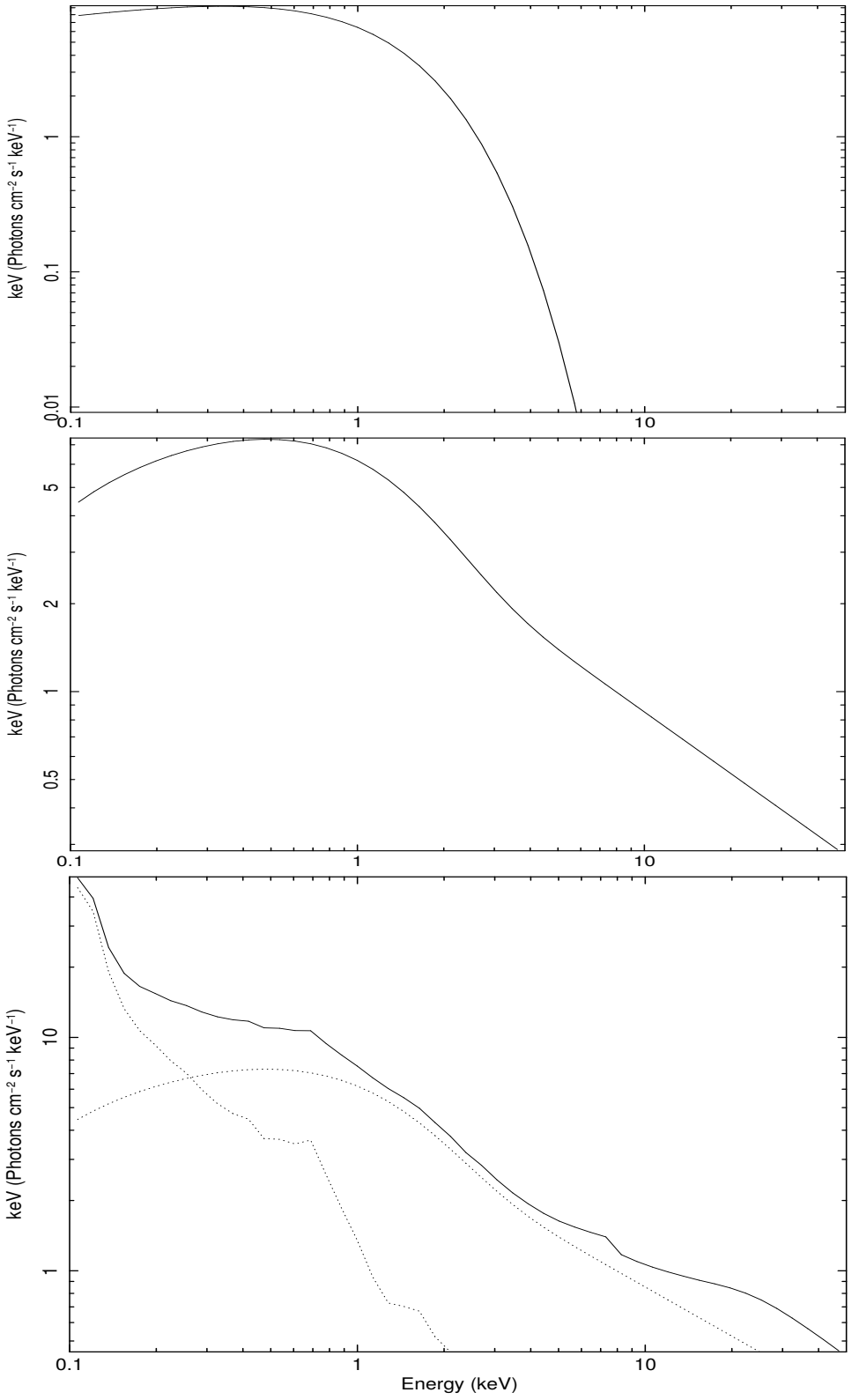

Figure 5.1: Plot demonstrating the spectra produced by each of the chosen model components. Top.`KERRBB`, Middle. `SIMPL*KERRBB`, Bottom. `SIMPL*KERRBB + RELXILL`

index as seen by the reflection component was also allowed to vary independently from that from SIMPL, as used in Fürst et al. (2015). One possible limitation of RELXILL is that the rest-frame reflection spectra, generated by the XILLVER model, are computed assuming the illuminating hard X-ray spectrum dominates over any intrinsic soft X-ray (disc) spectrum. This situation is appropriate for AGN but will not be valid in XRBs in states where the thermal disc component contributes a significant fraction of the X-ray luminosity. As such, the limitations of the model are expected to be more apparent in thermal-dominated soft states. Another issue with RELXILL is that the rest-frame reflection spectra are computed assuming that the incident spectrum is a simple power law extending down to very low energies, which is not likely to be the case if the non-thermal emission is inverse-Compton scattering of disc photons. As our spectra only extend down to 0.8 keV, this is likely to be a relatively minor issue.

A visual demonstration of each of these three model components has been provided in Figure 5.1. The top panel shows the thermal disc spectrum produced by KERRBB assuming $\dot{M} = 10^{18}$ g s^{-1}, $f_{col} = 1.7$, $a = 0$, $\eta = 0$, and that the system has a BH mass of $10\mathrm{M}_{\odot}$, is at a distance of 5kpc and an inclination of 50°. The middle panel includes the inverse-Compton spectrum produced by SIMPL⋆KERRBB, with $\Gamma_s = 1.7$ and $f_{scat} = 0.5$. The bottom panel includes the additional reflection component, using SIMPL⋆KERRBB + RELXILL. Here it has been assumed that $r_{in} = r_{ISCO}$ (for $a = 0$), and also that the spectrum illuminating the reflector (RELXILL) has the same photon index as the observed non-thermal continuum (from SIMPL), i.e. $\Gamma_r = \Gamma_s$. Furthermore, the inner radius is set at $6r_g$, the disc ionisation parameter is fixed at 2.5, and the reflection fraction is -1. In each plot the normalisations of each component are left at their default value, and so the relative normalisations between the plots are not consistent.

Finally, the model ISMabs (Gatuzz et al., 2015) was used to model absorption from the ISM. The details and motivation for using this model has already been discussed in Chapters 1.5.2 and 4.3.1. Wherever possible we fixed the absorption parameters to those found from analysis of *XMM-Newton*/RGS data in Chapter 4. Not all of the sources included in that study had good

Model	Parameter	Meaning	Value
SIMPL	Γ_s	Power law index	Free
	f_{scat}	Scattering fraction	Free
KERRBB	η	Torque at inner boundary	0
	a	Spin of the BH	0[1]
	i	Inclination	Various[2]
	M	Mass of the BH	Various
	$\dot{M}$	Mass accretion rate (10^{18} g s^{-1})	Free
	D	Distance to source (kpc)	Various
	f_{col}	Colour correction factor	Free
	N_K	Normalisation	1
RELXILL	q_1	Emissivity index (R_{in} to R_{br})	3
	q_2	Emissivity index (R_{br} to R_{out})	3
	R_{br}	Emissivity break radius	10 r_g
	a	Spin of the BH	0[1]
	i	Inclination	Various[2]
	R_{in}	Disc inner radius	6 r_g
	R_{out}	Disc outer radius	100 r_g
	z	Redshift	0
	Γ_r	Power law index of incident spectrum	Free
	$log(\xi)$	Ionisation of the accretion disc	Free
	A_{Fe}	Disc iron abundance	1
	E_{cut}	High energy cut-off	300 keV
	R	Reflection fraction	-1
	N_r	Normalisation	Free

Table 5.1: Table summarising the model parameters. The parameters for each component are listed, described and they value they are assumed to take if they are not free is given. [1,2] The spin and inclination values are always set equal to one another.

quality RGS data though. In those cases the hydrogen column density N_H was allowed to vary freely within each observation, with all the other elemental column densities included in `ISMabs` (C, N, O, Ne, Mg, S, Si, Ar, Ca, Fe) tied to N_H such that their relative abundances are equal to those in Wilms et al. (2000).

As the aim of this work was to assess the physicality of assuming the inner radius of the accretion disc remains at r_{ISCO} at all times a number of parameters were fixed at specific values. The spin parameter from `KERRBB` and `RELXILL` were fixed to 0, and the inner and outer radii of the disc were set to r_{ISCO} and 100 r_g respectively for all spectra. An emissivity profile of r^{-3} was assumed, the high energy cut-off was set at 300 keV, and the iron abundance, A_{Fe}, is set equal to the solar value for all observations. The `RELXILL` model can also add its own power law continuum. `SIMPL` was used to produce the non-thermal continuum emission in the model, and so we included only the reflected spectrum from `RELXILL` (by setting the reflection fraction parameter to -1), and (initially) coupled the photon indices of `SIMPL` and `RELXILL`.

5.3.2 Fitting Procedure

The spectra were analysed in the 0.8-10.0 keV range. Going significantly below 0.8 keV is problematic because of the O edge in the instrumental response. Also, the data between 1.75-2.35 keV was also ignored from the fit to avoid any systematic residuals due to the instrumental Si-K and Au-M edges from the detector and mirror respectively, which can affect bright observations. As the data has exceptionally high signal to noise (see Figure 5.2), any deficiencies in the instrumental calibration (even at the $< 1\%$ level) can have profound effects on the statistical quality of the fit. Therefore only the best-calibrated part of the EPIC bandpass was chosen.

Figure 5.2 shows the normalised spectra (cts s^{-1} keV^{-1}) with data/model ratio against energy as an example of a hard state data set from GX 339-4. Plots for the other spectra can be found in Appendix B. The fit parameters and reduced χ^2 for each observation can be found in full in Table

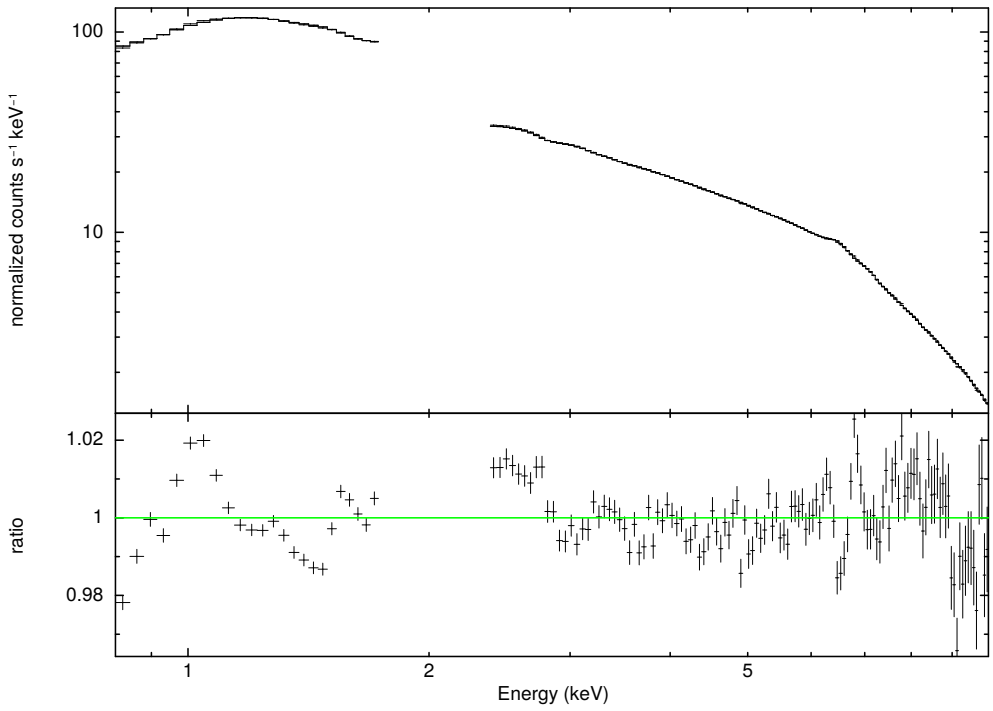

Figure 5.2: XMM-Newton pn spectrum of the source GX 339-4 (rev0782). This is a hard state observation fit with the model `SIMPL*KERRBB + RELXILL + XILLVER`.

5.2. In most cases the fits are statistically unacceptable, despite residuals being at the $\lesssim 1\%$ level. Therefore, formal goodness-of-fit tests are not employed to assess the quality of the model fitting, instead we judge this based on whether the residuals are at the $< 2\%$ level. Any model that passes this test can reproduce the observed spectrum to a level comparable with calibration uncertainties.

After an initial fit of each spectra it was clear that for some of the observations there were significant residuals between 6 and 9 keV. These features will likely be due to an ionised absorber in the form of an out-flowing wind, as found in GRO J1655-40 (Díaz Trigo et al., 2007) and 4U 1630-47 (Díaz Trigo et al., 2014) for example. Due to this feature additional components were included in the model when necessary in the form of a Gaussian centered at the affected energies. This was done using the `GAUSS` model which adds three more free parameters: E_{gs}, the line energy, σ_{gs}, the line width and N_{gs}, the normalisation. The line widths of these components were generally found to be in the $0.01 - 0.1$ keV range. Doing this not only improves the overall fit, but allowed us to conduct an additional test on the frequency in which these winds occur in our sample of

LMXBs.

Another issue was also noted around the lower energies, an apparent excess at $\sim$ 1 keV. This has been noticed before in studies of numerous sources (e.g. Boirin et al. 2005; Sala et al. 2008; Hiemstra et al. 2011), all observed by the EPIC-pn camera in timing mode. Given that this is likely a detector issue and not a real feature it was decided to ignore the data in the affected energy range. This issue does not affect all systems (4U 1630-47 and H 1743-322 are the most heavily affected), so the size of the energy range ignored was decided on a source-by-source basis.

Markov Chain Monte Carlo (MCMC) analysis was also performed for all the fitted spectra to explore the parameter space and investigate any degeneracies. The 'emcee' Python code (Foreman-Mackey et al., 2013) was used to complete this analysis. The Goodman-Weare algorithm was used with 100 walkers each performing 1000 iterations (in each case an additional 100 were performed first and ignored - this is the 'burn in' period). The initial distribution of the walkers was determined by the best-fit value found by `XSPEC`. Contour plots showing the distributions of all the free parameters can be found below their respective spectra, along with their errors (contour plots are created using the 'corner' Python code (Foreman-Mackey, 2016)). The contour plot for GX 339-4 rev0782 is shown in Figure 5.3. (This is equivalent to a Bayesian analysis, with the contours representing 'credible' regions, assuming uniform priors on each parameter.)

5.4 Results

This section will discuss the results in a general manner. A description of each source, and a comparison with other studies using the same data sets, can be found in Section 5.6.

Around half of our sample of observations are during the soft state where a disc-dominated state would be expected, and therefore no significant truncation. The results agree with this prediction,

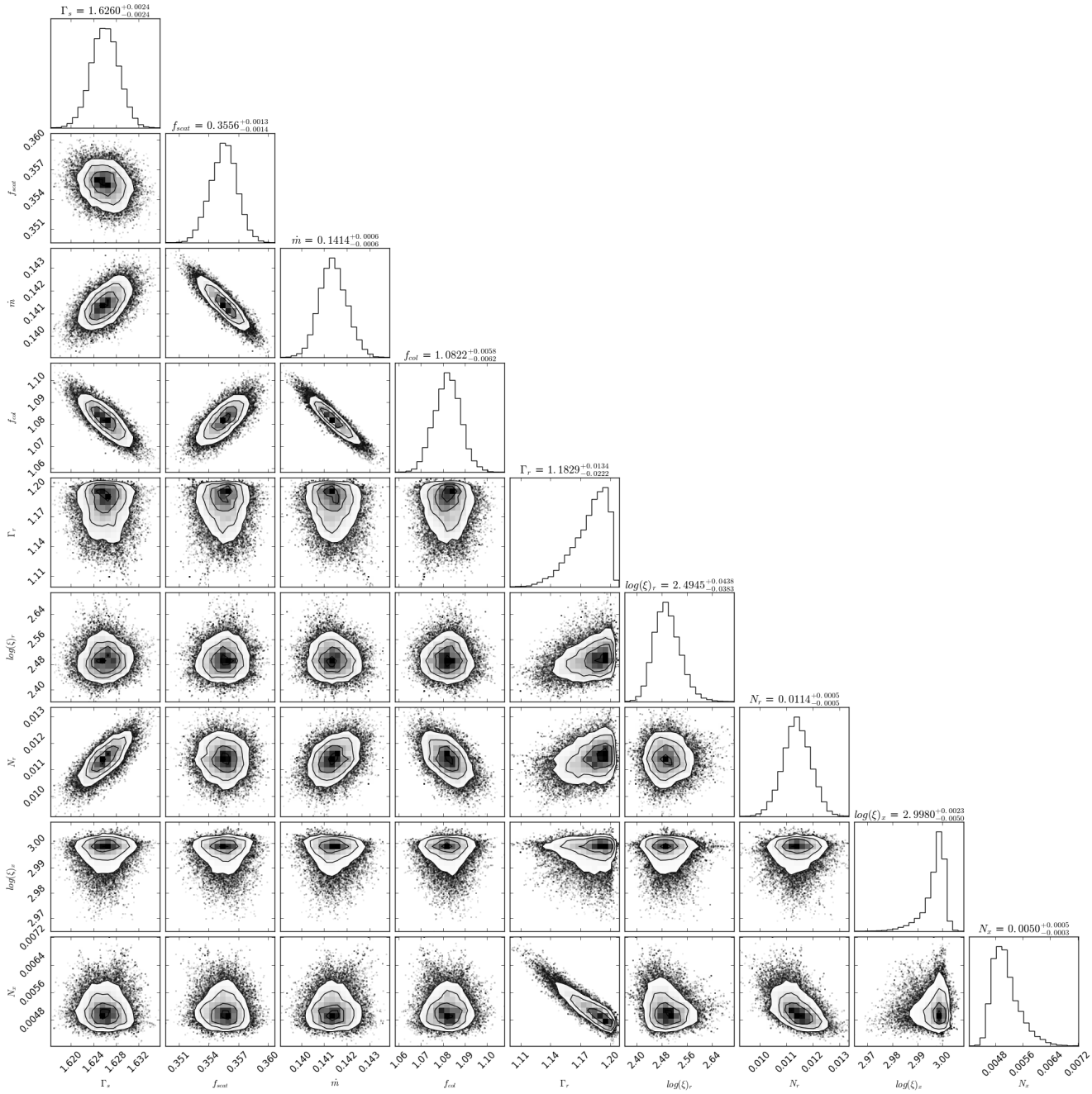

Figure 5.3: Contour plots from the MCMC analysis of the GX 339-4 rev0782 EPIC-pn spectrum fitted with a model with free parameters: Γ_s, f_{scat}, $\dot{m}$, f_{col}, Γ_r, $log(\xi)$, N_r, $log(\xi)_x$ and N_x. Contours represent 1, 2 and 3σ confidence levels.

System Name	Rev	Γ_s	f_{scat}	$\dot{M}$ (gs^{-1})	f_{col}	Γ_r	$log(\xi)$	N_{Ref}	χ^2_{red} ($d.o.f$)	Gaussian component(s)?
GX 339-4	513	$4.24^{+0.08}_{-0.08}$	$0.63^{+0.04}_{-0.04}$	$3.10^{+0.01}_{-0.01}\times\ 10^{18}$	$1.90^{+0.01}_{-0.01}$	$3.84^{+0.01}_{-0.01}$	$1.74^{+0.10}_{-0.14}$	$2.96^{+0.56}_{-0.48}\times\ 10^{-1}$	1.21(141)	
	782	$1.63^{+0.01}_{-0.01}$	$0.36^{+0.01}_{-0.01}$	$1.41^{+0.01}_{-0.01}\times\ 10^{17}$	$1.08^{+0.01}_{-0.01}$	$1.18^{+0.01}_{-0.02}$	$2.49^{+0.04}_{-0.04}$	$1.14^{+0.01}_{-0.01}\times\ 10^{-2}$	9.88(141)	
	783	$1.58^{+0.01}_{-0.01}$	$0.48^{+0.01}_{-0.01}$	$1.07^{+0.01}_{-0.01}\times\ 10^{17}$	$1.34^{+0.01}_{-0.01}$	$1.40^{+0.01}_{-0.01}$	$2.69^{+0.01}_{-0.01}$	$3.30^{+0.20}_{-0.20}\times\ 10^{-3}$	13.9(141)	
	1318	$2.67^{+0.30}_{-0.30}$	$5.57^{+2.11}_{-1.57}\times\ 10^{-2}$	$4.39^{+0.01}_{-0.01}\times\ 10^{18}$	$2.14^{+0.01}_{-0.01}$	$3.92^{+0.04}_{-0.03}$	$1.78^{+0.10}_{-0.13}$	$2.99^{+0.66}_{-0.58}\times\ 10^{-1}$	1.10(140)	
	1325	$3.20^{+0.08}_{-0.09}$	$0.52^{+0.05}_{-0.06}$	$3.06^{+0.02}_{-0.03}\times\ 10^{18}$	$1.82^{+0.03}_{-0.02}$	$2.12^{+2.96}_{-0.73}$	$2.53^{+1.49}_{-1.68}$	$1.80^{3.10}_{1.40}\times\ 10^{-3}$	1.04(140)	
	1338	$3.06^{+0.26}_{-0.24}$	$7.59^{+2.12}_{-1.69}\times\ 10^{-2}$	$1.97^{+0.01}_{-0.01}\times\ 10^{18}$	$2.00^{+0.01}_{-0.01}$	–	–	–	1.08(132)	
	1702	$1.58^{+0.02}_{-0.02}$	$0.40^{+0.04}_{-0.03}$	$6.55^{+0.49}_{-0.82}\times\ 10^{16}$	$1.21^{+0.11}_{-0.08}$	$1.27^{+0.13}_{-0.13}$	$2.97^{+0.06}_{-0.15}$	$9.50^{+1.60}_{-1.60}\times\ 10^{-3}$	1.16(142)	
	1886	$1.71^{+0.07}_{-0.08}$	$0.56^{+0.06}_{-0.05}$	$1.48^{+0.10}_{-0.15}\times\ 10^{17}$	$1.50^{+0.17}_{-0.18}$	$1.33^{+0.29}_{-0.19}$	$2.58^{+0.45}_{-0.84}$	$3.93^{+4.60}_{-2.93}\times\ 10^{-2}$	0.90(125)	
	2879	$2.01^{+0.01}_{-0.01}$	$0.32^{+0.01}_{-0.01}$	$1.62^{+0.01}_{-0.01}\times\ 10^{17}$	$1.17^{+0.01}_{-0.01}$	$1.35^{+0.18}_{-0.21}$	$2.98^{+0.02}_{-0.03}$	$1.17^{+0.06}_{-0.06}\times\ 10^{-2}$	2.22(143)	
	2881	$1.81^{+0.02}_{-0.02}$	$0.31^{+0.01}_{-0.01}$	$1.01^{+0.02}_{-0.02}\times\ 10^{17}$	$1.28^{+0.02}_{-0.02}$	$1.52^{+0.09}_{-0.10}$	$2.93^{+0.06}_{-0.10}$	$9.50^{+0.10}_{-0.10}\times\ 10^{-3}$	1.35(143)	
	2884	$1.72^{+0.01}_{-0.01}$	$0.47^{+0.01}_{-0.01}$	$4.88^{+0.07}_{-0.10}\times\ 10^{16}$	$1.62^{+0.04}_{-0.03}$	$1.50^{+0.09}_{-0.08}$	$2.93^{+0.05}_{-0.08}$	$8.90^{+0.70}_{-0.60}\times\ 10^{-3}$	1.45(141)	
	2886	$1.59^{+0.02}_{-0.02}$	$0.61^{+0.01}_{-0.01}$	$2.49^{+0.08}_{-0.10}\times\ 10^{16}$	$2.15^{+0.06}_{-0.06}$	$1.35^{+0.04}_{-0.06}$	$2.73^{+0.02}_{-0.02}$	$2.20^{+0.04}_{-0.03}\times\ 10^{-3}$	1.14(141)	
	2889	$1.65^{+0.02}_{-0.02}$	$0.39^{+0.05}_{-0.05}$	$2.38^{+0.29}_{-0.23}\times\ 10^{16}$	$1.46^{+0.11}_{-0.11}$	$1.31^{+0.08}_{-0.07}$	$1.04^{+0.12}_{-0.10}$	$1.00^{+0.30}_{-0.20}\times\ 10^{-3}$	1.33(135)	yes
	2895	$1.54^{+0.01}_{-0.01}$	$0.47^{+0.05}_{-0.04}$	$1.11^{+0.09}_{-0.11}\times\ 10^{16}$	$1.41^{+0.12}_{-0.09}$	$1.36^{+0.06}_{-0.09}$	$2.64^{+0.08}_{-0.12}$	$6.00^{+2.00}_{-2.00}\times\ 10^{-4}$	1.23(143)	yes
Swift J1357.2-0933	2044	$1.58^{+0.02}_{-0.02}$	$0.59^{+0.05}_{-0.05}$	$2.80^{+0.21}_{-0.21}\times\ 10^{16}$	$1.62^{+0.12}_{-0.10}$	$1.23^{+0.07}_{-0.10}$	$2.43^{+0.12}_{-0.18}$	$3.90^{+1.30}_{-0.90}\times\ 10^{-3}$	0.93(140)	
GS 1354-64	2826	$1.25^{+0.05}_{-0.04}$	$0.67^{+0.03}_{-0.03}$	$2.11^{+0.18}_{-0.21}\times\ 10^{18}$	$3.24^{+0.18}_{-0.14}$	$1.63^{+0.02}_{-0.02}$	$3.03^{+0.01}_{-0.01}$	$1.25^{+0.11}_{-0.10}\times\ 10^{-2}$	1.72(141)	yes
4U 1543-475	493	$1.79^{+0.07}_{-0.19}$	$0.50^{+0.17}_{-0.14}$	$2.00^{+1.00}_{-1.00}\times\ 10^{14}$	$3.56^{+1.64}_{-1.21}$	$2.20^{+0.51}_{-0.35}$	$4.28^{+0.32}_{-1.39}$	$< 10^{-5}$	0.99(85)	
4U 1630-47	2241	–	–	$2.83^{+0.18}_{-0.19}\times\ 10^{18}$	$3.10^{+0.11}_{-0.12}$	$3.56^{+0.01}_{-0.01}$	$1.69^{+0.03}_{-0.04}$	$27.3^{+2.67}_{-2.42}$	1.20(116)	yes
	2249	–	–	$5.42^{+0.23}_{-0.17}\times\ 10^{18}$	$3.07^{+0.05}_{-0.06}$	$2.64^{+0.13}_{-0.12}$	$4.31^{+0.19}_{-0.23}$	$4.77^{+2.01}_{-1.17}\times\ 10^{-2}$	1.47(120)	yes
	2251	–	–	$6.83^{+0.03}_{-0.03}\times\ 10^{18}$	$2.72^{+0.02}_{-0.02}$	$3.41^{+0.03}_{-0.03}$	$3.00^{+0.07}_{-0.06}$	$1.84^{+0.25}_{-0.24}$	1.78(106)	yes
	2336	–	–	$8.03^{+0.04}_{-0.04}\times\ 10^{18}$	$2.79^{+0.02}_{-0.02}$	$3.37^{+0.03}_{-0.03}$	$2.96^{+0.05}_{-0.08}$	$2.27^{+0.35}_{-0.30}$	1.83(103)	yes
	2337	–	–	$8.22^{+0.09}_{-0.12}\times\ 10^{18}$	$3.34^{+0.05}_{-0.04}$	$3.45^{+0.07}_{-0.13}$	$2.64^{+0.33}_{-0.59}$	$1.40^{+0.91}_{-0.58}$	1.44(103)	
	2345	$5.17^{+0.62}_{-1.15}$	$0.50^{+0.27}_{-0.24}$	$9.70^{+0.23}_{-0.24}\times\ 10^{18}$	$3.07^{+0.11}_{-0.10}$	$3.52^{+0.07}_{-0.08}$	$0.73^{+0.90}_{-0.56}$	$2.11^{+2.25}_{-1.36}$	1.22(111)	
XTE J1652-453	1777	$3.96^{+0.69}_{-0.77}$	$2.27^{+3.73}_{-1.62}\times\ 10^{-2}$	$5.72^{+0.21}_{-0.16}\times\ 10^{16}$	$2.76^{+0.06}_{-0.07}$	$2.13^{+0.02}_{-0.03}$	$3.45^{+0.06}_{-0.06}$	$2.10^{+0.10}_{-0.10}\times\ 10^{-3}$	1.43(122)	
GRO J1655-40	956	$1.49^{+0.12}_{-0.12}$	$0.59^{+0.16}_{-0.11}$	$7.10^{+1.90}_{-2.20}\times\ 10^{15}$	$1.98^{+0.69}_{-0.66}$	$1.46^{+0.25}_{-0.25}$	$2.80^{+0.37}_{-0.72}$	$3.40^{+3.10}_{-1.60}\times\ 10^{-3}$	1.15(124)	
	964a	$1.14^{+0.17}_{-0.08}$	$1.59^{+1.35}_{-0.42}\times\ 10^{-2}$	$1.81^{+0.03}_{-0.01}\times\ 10^{18}$	$2.55^{+0.01}_{-0.01}$	$3.86^{+0.01}_{-0.01}$	$2.74^{+0.03}_{-0.02}$	$0.28^{+0.05}_{-0.04}$	1.93(143)	yes
	964b	–	–	$1.90^{+0.01}_{-0.01}\times\ 10^{18}$	$2.60^{+0.01}_{-0.01}$	$3.81^{+0.01}_{-0.01}$	$2.49^{+0.16}_{-0.14}$	$0.50^{+0.14}_{-0.07}$	1.19(143)	yes
	965	–	–	$2.19^{+0.01}_{-0.01}\times\ 10^{18}$	$2.63^{+0.01}_{-0.01}$	$3.86^{+0.01}_{-0.01}$	$2.73^{+0.02}_{-0.05}$	$0.48^{+0.07}_{-0.05}$	1.72(145)	yes
	966	–	–	$2.31^{+0.01}_{-0.01}\times\ 10^{18}$	$2.70^{+0.01}_{-0.01}$	$3.84^{+0.01}_{-0.01}$	$2.29^{+0.02}_{-0.03}$	$0.51^{+0.04}_{-0.05}$	2.27(145)	yes
	970	–	–	$3.75^{+0.01}_{-0.02}\times\ 10^{18}$	$2.59^{+0.03}_{-0.02}$	$3.74^{+0.06}_{-0.07}$	$0.07^{+0.01}_{-0.01}$	$439.1^{+3.5}_{-2.2}$	3.00(145)	
MAXI J1659-152	1978	$1.43^{+0.11}_{-0.09}$	$6.94^{+1.74}_{-1.16}\times\ 10^{-2}$	$3.42^{+0.13}_{-0.11}\times\ 10^{17}$	$1.23^{+0.03}_{-0.03}$	$2.20^{+0.02}_{-0.02}$	$3.70^{+0.01}_{-0.02}$	$3.33^{+0.10}_{-0.11}\times\ 10^{-2}$	1.34(141)	
	2066	$1.75^{+0.04}_{-0.06}$	$0.53^{+0.15}_{-0.13}$	$1.00^{+0.30}_{-0.20}\times\ 10^{15}$	$1.72^{+0.62}_{-0.51}$	$2.84^{+0.43}_{-0.56}$	$2.26^{+0.88}_{-1.59}$	$< 10^{-5}$	0.97(105)	
IGR J17091-3624	2069	$3.17^{+0.59}_{-0.79}$	$0.49^{+0.33}_{-0.26}$	$2.07^{+0.07}_{-0.09}\times\ 10^{18}$	$2.33^{+0.18}_{-0.16}$	$2.97^{+1.05}_{-0.72}$	$3.80^{+0.66}_{-2.06}$	$1.70^{+2.80}_{-1.00}\times\ 10^{-3}$	1.13(133)	
	2346	$1.41^{+0.03}_{-0.03}$	$0.60^{+0.04}_{-0.03}$	$9.66^{+0.35}_{-0.43}\times\ 10^{16}$	$1.56^{+0.12}_{-0.11}$	$1.13^{+0.10}_{-0.09}$	$3.07^{+0.08}_{-0.09}$	$1.10^{+0.60}_{-0.40}\times\ 10^{-4}$	1.57(143)	
SAX J1711.6-3808	225	$1.38^{+0.03}_{-0.02}$	$0.13^{+0.03}_{-0.03}$	$4.42^{+0.95}_{-0.85}\times\ 10^{16}$	$1.12^{+0.11}_{-0.08}$	$1.21^{+0.14}_{-0.13}$	$2.93^{+0.18}_{-0.36}$	$1.80^{+1.80}_{-1.10}\times\ 10^{-3}$	1.15(123)	
XTE J1719-291	1521	$4.17^{+0.59}_{-0.48}$	$0.60^{+0.26}_{-0.21}$	$6.00^{+1.00}_{-1.00}\times\ 10^{14}$	$3.35^{+0.44}_{-0.55}$	$2.23^{+0.10}_{-0.14}$	$3.13^{+0.11}_{-0.17}$	$< 10^{-5}$	1.15(99)	
XTE J1720-318	586	–	–	$5.89^{+0.04}_{-0.04}\times\ 10^{16}$	$2.59^{+0.01}_{-0.01}$	$3.53^{+0.01}_{-0.01}$	$2.22^{+0.08}_{-0.12}$	$2.47^{+0.43}_{-0.41}\times\ 10^{-1}$	1.10(119)	
IGR J17285-2922	1969	$1.59^{+0.02}_{-0.05}$	$0.29^{+0.05}_{-0.05}$	$3.10^{+0.50}_{-0.40}\times\ 10^{15}$	$1.63^{+0.23}_{-0.28}$	$2.67^{+0.44}_{-0.44}$	$4.10^{+0.40}_{-0.96}$	$< 10^{-5}$	1.11(137)	yes
H 1743-322	1613	$1.38^{+0.02}_{-0.01}$	$0.63^{+0.08}_{-0.07}$	$1.79^{+0.20}_{-0.17}\times\ 10^{17}$	$1.15^{+0.30}_{-0.12}$	$1.80^{+0.38}_{-0.33}$	$2.22^{+0.36}_{-0.72}$	$1.30^{+0.90}_{-0.70}\times\ 10^{-3}$	0.92(123)	
	1984	$1.49^{+0.02}_{-0.02}$	$0.39^{+0.08}_{-0.07}$	$5.60^{+1.10}_{-1.10}\times\ 10^{15}$	$2.11^{+0.41}_{-0.43}$	–	–	–	1.31(129)	
	2708	$1.49^{+0.04}_{-0.03}$	$0.47^{+0.05}_{-0.04}$	$3.25^{+0.43}_{-0.42}\times\ 10^{17}$	$1.17^{+0.09}_{-0.09}$	$1.04^{+0.03}_{-0.03}$	$3.05^{+0.05}_{-0.05}$	$3.41^{+0.73}_{-0.83}\times\ 10^{-2}$	1.53(130)	
	2709a	$1.53^{+0.01}_{-0.01}$	$0.38^{+0.03}_{-0.02}$	$3.68^{+0.27}_{-0.25}\times\ 10^{17}$	$1.04^{+0.04}_{-0.03}$	$1.05^{+0.05}_{-0.03}$	$1.80^{+0.24}_{-0.35}$	$4.15^{+0.56}_{-0.56}\times\ 10^{-2}$	1.63(127)	
	2709b	$1.10^{+0.01}_{-0.01}$	$0.26^{+0.01}_{-0.02}$	$3.23^{+0.17}_{-0.16}\times\ 10^{17}$	$1.13^{+0.04}_{-0.04}$	$1.60^{+0.01}_{-0.02}$	$3.53^{+0.03}_{-0.03}$	$5.60^{+0.30}_{-0.30}\times\ 10^{-3}$	2.61(120)	
Swift J174510.8-262411	2345	$2.02^{+0.03}_{-0.03}$	$0.46^{+0.02}_{-0.02}$	$1.06^{+0.05}_{-0.05}\times\ 10^{18}$	$1.86^{+0.08}_{-0.08}$	$2.86^{+0.18}_{-0.15}$	$3.63^{+0.25}_{-0.19}$	$4.13^{+0.89}_{-0.75}\times\ 10^{-2}$	1.02(142)	yes
IGR J17497-2821	1243	$1.39^{+0.13}_{-0.12}$	$8.09^{+1.16}_{-1.12}\times\ 10^{-2}$	$1.10^{+0.17}_{-0.11}\times\ 10^{17}$	$1.24^{+0.07}_{-0.08}$	$1.25^{+0.15}_{-0.15}$	$3.30^{+0.08}_{-0.11}$	$1.20^{+1.30}_{-0.80}\times\ 10^{-3}$	1.12(121)	
	1245	$1.43^{+0.01}_{-0.02}$	$0.17^{+0.02}_{-0.02}$	$6.01^{+0.54}_{-0.52}\times\ 10^{16}$	$1.66^{+0.10}_{-0.10}$	$3.66^{+0.06}_{-0.04}$	$4.61^{+0.06}_{-0.16}$	$4.70^{+1.90}_{-1.50}\times\ 10^{-3}$	1.51(120)	
XTE J1752-223	1891	$1.35^{+0.08}_{-0.07}$	$0.14^{+0.01}_{-0.01}$	$2.70^{+0.11}_{-0.13}\times\ 10^{16}$	$2.80^{+0.04}_{-0.05}$	$2.40^{+0.05}_{-0.04}$	$4.00^{+0.03}_{-0.03}$	$4.00^{+0.20}_{-0.20}\times\ 10^{-3}$	3.41(130)	
Swift J1753.5-0127	1152	$1.67^{+0.01}_{-0.01}$	$0.54^{+0.06}_{-0.06}$	$7.40^{+0.70}_{-0.60}\times\ 10^{15}$	$1.75^{+0.17}_{-0.17}$	$1.28^{+0.05}_{-0.05}$	$3.45^{+0.03}_{-0.03}$	$2.00^{+0.20}_{-0.10}\times\ 10^{-3}$	1.04(143)	yes
	1716	$2.98^{+0.10}_{-0.09}$	$0.30^{+0.02}_{-0.02}$	$7.56^{+0.05}_{-0.05}\times 10^{16}$	$1.21^{+0.01}_{-0.01}$	$1.42^{+0.02}_{-0.02}$	$3.21^{+0.03}_{-0.02}$	$3.40^{+0.20}_{-0.10}\times\ 10^{-3}$	1.24(143)	
	2336	$1.60^{+0.09}_{-0.12}$	$0.18^{+0.04}_{-0.04}$	$4.50^{+0.30}_{-0.30}\times\ 10^{15}$	$1.58^{+0.08}_{-0.08}$	$1.16^{+0.03}_{-0.05}$	$3.65^{+0.03}_{-0.05}$	$4.70^{+0.30}_{-0.30}\times\ 10^{-3}$	1.23(143)	
	2350	$1.73^{+0.01}_{-0.01}$	$0.48^{+0.01}_{-0.01}$	$8.90^{+0.10}_{-0.10}\times\ 10^{15}$	$1.62^{+0.03}_{-0.03}$	$1.25^{+0.03}_{-0.03}$	$2.65^{+0.04}_{-0.07}$	$4.50^{+0.50}_{-0.50}\times\ 10^{-3}$	1.32(143)	
	2704	$1.82^{+0.01}_{0.01}$	$0.35^{+0.01}_{-0.01}$	$1.17^{+0.02}_{-0.02}\times\ 10^{16}$	$1.40^{+0.03}_{-0.02}$	$1.33^{+0.05}_{-0.04}$	$2.61^{+0.09}_{-0.08}$	$4.00^{+0.50}_{-0.40}\times\ 10^{-3}$	1.42(143)	
	2724	$5.34^{+0.08}_{-0.09}$	$0.78^{+0.10}_{-0.08}$	$2.35^{+0.01}_{-0.01}\times\ 10^{17}$	$1.15^{+0.02}_{-0.03}$	$3.01^{+0.04}_{-0.04}$	$2.35^{+0.04}_{-0.03}$	$1.04^{+0.16}_{-0.14}\times\ 10^{-2}$	1.33(138)	yes
GRS 1758-258	143	$2.35^{+0.05}_{-0.05}$	$0.42^{+0.03}_{-0.03}$	$6.66^{+0.41}_{-0.34}\times\ 10^{16}$	$3.18^{+0.17}_{-0.16}$	$2.42^{+0.15}_{-0.19}$	$3.02^{+0.25}_{-0.26}$	$1.70^{+0.80}_{-0.50}\times\ 10^{-3}$	1.39(134)	
	235	$3.40^{+0.31}_{-0.23}$	$6.19^{+1.50}_{-1.24}\times\ 10^{-2}$	$6.71^{+0.13}_{-0.13}\times\ 10^{16}$	$3.12^{+0.04}_{-0.04}$	$3.35^{+0.16}_{-0.28}$	$0.83^{+1.32}_{-0.60}$	$3.60^{+5.80}_{-2.90}\times\ 10^{-3}$	1.22(111)	yes
	513	$1.49^{+0.06}_{-0.07}$	$0.10^{+0.03}_{-0.03}$	$4.94^{+1.10}_{-0.97}\times\ 10^{16}$	$1.25^{+0.16}_{-0.13}$	$1.38^{+0.10}_{-0.10}$	$3.28^{+0.06}_{-0.10}$	$4.50^{+2.00}_{-2.00}\times\ 10^{-3}$	0.98(133)	
XTE J1817-330	1146	$3.33^{+0.14}_{-0.15}$	$0.20^{+0.03}_{-0.03}$	$1.62^{+0.01}_{-0.01}\times\ 10^{17}$	$3.03^{+0.02}_{-0.02}$	$4.77^{+0.71}_{-0.39}$	$1.64^{+0.12}_{-0.13}$	$2.93^{+1.73}_{-1.28}\times\ 10^{-2}$	1.45(135)	
XTE J1856+053	1330	–	–	$2.56^{+0.02}_{-0.02}\times\ 10^{17}$	$3.70^{+0.02}_{-0.02}$	–	–	–	1.52(123)	
Swift J1910.2-0546	2355	$3.28^{+0.16}_{-0.11}$	$0.20^{+0.02}_{-0.01}$	$2.42^{+0.03}_{-0.03}\times\ 10^{17}$	$1.99^{+0.02}_{-0.02}$	$1.83^{+0.03}_{-0.02}$	$3.29^{+0.03}_{-0.04}$	$3.20^{+0.10}_{-0.10}\times\ 10^{-3}$	2.08(142)	
	2715	$1.84^{+0.37}_{-0.13}$	$0.54^{+0.23}_{-0.20}$	$< 10^{14}$	$1.61^{+0.39}_{-0.31}$	$1.56^{+0.14}_{-0.22}$	$3.25^{+0.21}_{-0.25}$	$< 10^{-5}$	1.38(96)	

Table 5.2: Parameter values from the fitting of the EPIC-pn spectral data.

with all soft state observations being well fitted by a model with a strong disc component. It is generally found that these spectra can be fitted with a dominant blackbody component and a weak, steep power law, with an additional contribution from reflection. A tendency for larger values of f_{col} is seen, with values > 2.5 common. Some soft state observations (e.g. XTE J1856+053 and GRO J1655-40) are almost completely dominated by the disc, with extremely small f_{scat} or N_r values, showing they require little-to-no contribution from the non-thermal or reflection components respectively. There are also a small number of unusual soft state observations where we find fairly large f_{scat} values, comparable to those more likely to be seen in the hard state (e.g. $f_{scat} = 0.50^{+0.27}_{-0.24}$ in 4U 1543-475 rev2345).

The soft state observations also contain the majority of cases where the additional Gaussian components are required. GRO J1655-40 and 4U 1630-47 are most heavily affected, each with observations showing multiple of these absorption features caused by ionised winds. Ponti et al. (2012) suggested that these winds have an equatorial geometry so are only observed in systems with a high inclination. GRO J1655-40 has a inclination of 69°, and 4U 1630-47 has an estimate of $\lesssim$70° (Seifina et al., 2014). Of the six other sources with some evidence of wind features and estimates of inclination all are generally quoted as having $i \sim$50° (Casares et al., 2009; Shidatsu et al., 2011; Froning et al., 2014). Our results therefore broadly agree with Ponti et al. (2012) in that winds are fairly common in the soft states of high inclination systems.

It is in the hard state where issues with the model would be expected if truncation is real. Many of the hard state observations in our sample show no requirement for truncation, being well fitted with a model where both the disc and reflection have $r_{in} = r_{ISCO}$. In general these spectra can be fitted with lower spectral indices, high scattering fractions and low colour-correction fractions. In many cases the spectral index from the reflection component Γ_r is lower than that from `SIMPL`, in agreement with Fürst et al. (2015), which can be explained by the reflected emission being Compton-scattered (Steiner et al., 2017). There are small number of observations with parameters showing exceptions to the general trends found: in GRS 1758-258 a lower f_{scat} is found than in

most hard states at 0.10 ± 0.03, and in GS 1354-64 we find $f_{col} = 3.24^{+1.80}_{-0.14}$, where f_{col} is usually $\lesssim 1.7$.

The large amount of observations studied in this project should allow a test to be performed investigating any correlations between the fitted parameters. Figure 5.4 displays the correlations between the fitted parameters for all sources. There were almost no strong correlations when looking over all sources, with a Spearmans Rank test only suggesting a correlation between $\dot{m}$ and N_r with a coefficient (and p-value) $\rho = 0.73$ ($p = 5.13 \times 10^{-5}$). Given that the sample of systems have such a wide range of masses, distances, inclinations etc., it was possible that any correlations that exist were being hidden and so it became necessary to look at the results

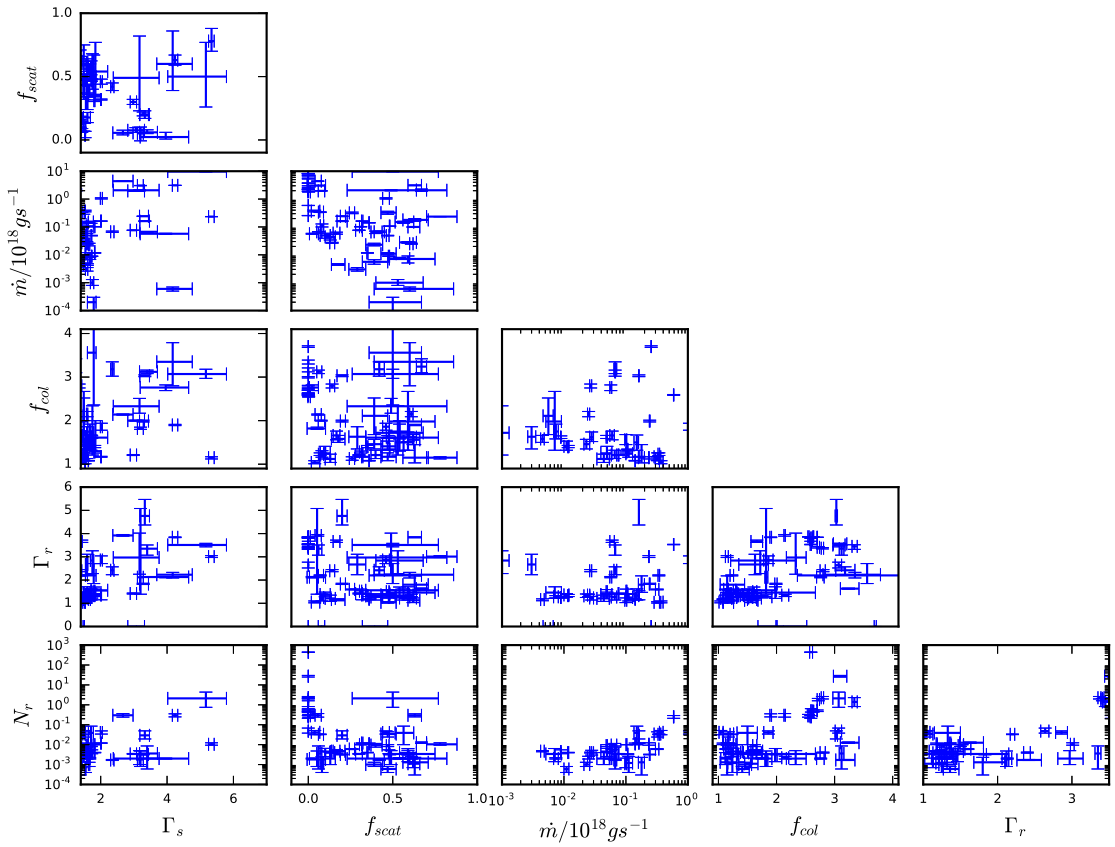

Figure 5.4: Plot to demonstrate the correlations between the results of the spectral analysis. This plot shows the spectral parameters for all observations.

on a system-by-system basis. Sources with fewer than five observations were excluded from this part of the analysis, leaving only five suitable systems. The plot for GX 339-4 is shown in Figure 5.5, the remainder can be found at the end of the chapter in Section 5.7. Spearmans Rank correlation analysis can be performed for each individual subplot and in a small number of cases correlations appear between some of the fitted parameters. For GX 339-4, the only strong correlation is found between the spectral index from `SIMPL` and the mass accretion rate with a correlation coefficient of $\rho = 0.79$ ($p = 6.91 \times 10^{-4}$). This will primarily be due to the fact that the higher mass accretion rate observations are all in the soft state which naturally has the higher Γ values, although it does also seem to suggest that even within states a higher mass accretion rates leads to a softer spectrum. If only the hard state observations are considered though a small

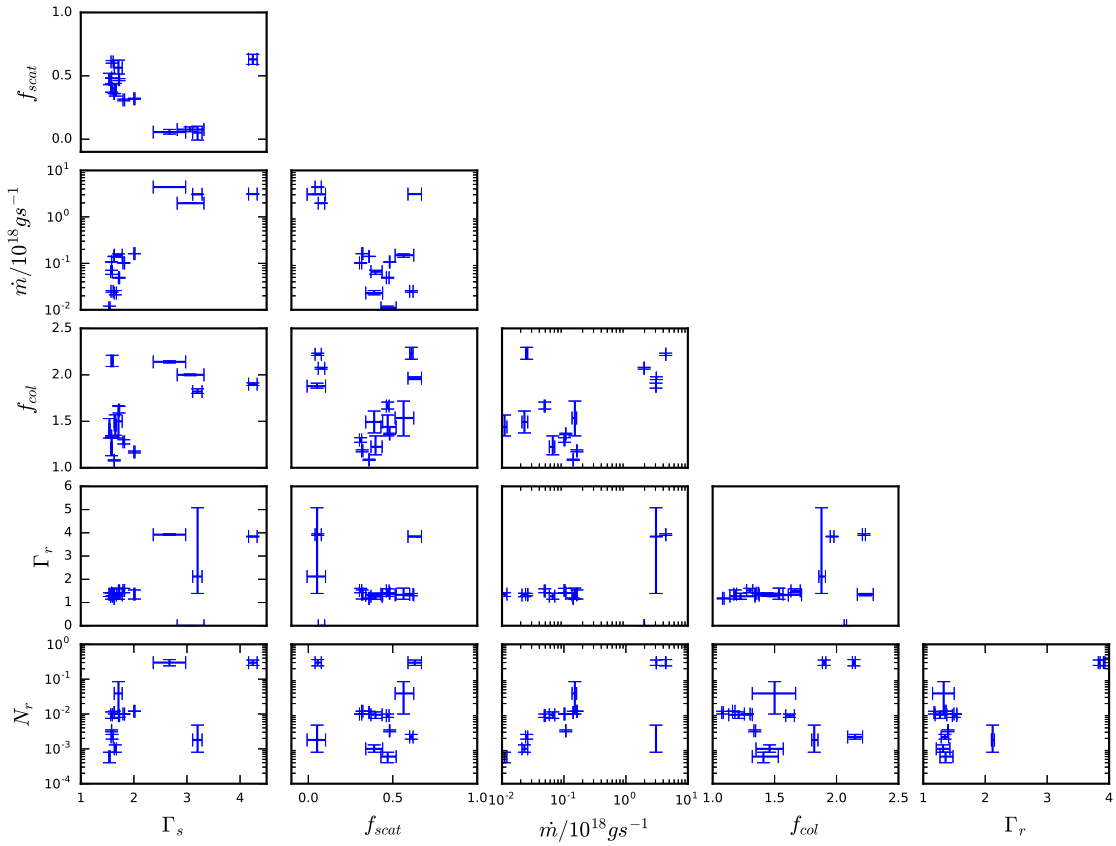

Figure 5.5: Plot to demonstrate the correlations between the results of the spectral analysis. This plot shows the spectral parameters from GX 339-4.

number of other relationships appear. The mass accretion rate and RELXILL normilisation plot returns the largest correlation at $\rho = 0.94$ ($p = 2.21 \times 10^{-5}$), but f_{col} against f_{scat} and N_r against Γ_s also show positive correlations with $\rho = 0.80$ ($p = 3.30 \times 10^{-3}$) and $\rho = 0.71$ ($p = 0.014$) respectively. The results from Swift J1753.5-0127 show similar behaviour to GX 339-4 with strong positive correlations between Γ_s and $\dot{m}$ with $\rho = 0.94$ ($p = 4.8 \times 10^{-3}$) and Γ_s and Γ_r with $\rho = 0.87$ ($p = 7.1 \times 10^{-3}$). This latter relation helps show that even though the two spectral indeces have been allowed to vary independetly they still produce values that are consistent with one another, with the RELXILL spectral index being slightly harder than the one from SIMPL in almost all cases. Also in Swift J1753.5-0127, there is a smooth decrease in f_{col} as $\dot{M}$ increases, producing a negative correlation of $\rho = -0.83$ ($p = 0.042$). This relationship is not replicated in any of the other systems though. A general problem with this analysis is still the lack of data points. The plots for GRO J1655-40 and 4U 1630-47 are particularly poor, having mostly soft state observations which do not tend to vary much between observations (this is especially true for GRO J1655-40 as its observations are spread over a small time period). The cause of the small number of correlations is still likely due to the observations used spanning different phases of different outbursts, which may all differ in important ways, even within the same system.

While a large proportion of the hard state observations can be fit with the standard disc, there is a group of hard state observations in which the model fails in the same way, all of which come from GX 339-4. With its frequent, bright outbursts GX 339-4 has been a common target of observation for X-ray missions and so has already received a great deal of discussion on the topic of truncation by a number of authors. Many of these come to the conclusion that truncation is evident in the hard state, with estimates of the inner radius from a reflection model a common method. After an initial fit of the data using the standard model large residuals were found at ≈ 7 keV, likely from a poor fit of the Fe K line. To deal with these residuals the assumptions of our model were then relaxed, by first allowing the spin of the black hole to change. The KERRBB model has r_{in} fixed to r_{ISCO} and so cannot model a truncated disc. However, we can approximate some modest truncation by allowing for a negative spin parameter (disc and BH spin anti-aligned), as

this produces a larger r_{ISCO} and hence larger r_{in} (up to 9 r_g). The spin parameter from KERRBB and RELXILL were tied together which allowed a test of the models sensitivity to moderate truncation while still maintaining a self-consistent model. Taking the observation at rev0782 as an example, it was found that there was an improved χ^2 with decreasing values of the spin parameter, with a minimum of $\Delta\chi^2 = -115.34$ at $a = -1$. While improving the fit statistics such modest truncation did little to alleviate the issues present in the residuals. At this point it then became necessary to question the other assumptions, which were done in two separate ways. The first was to allow the emissivity profile of RELXILL to vary freely. This determines how the reflection spectrum is distributed as a function of disc radius. The indeces of the power law model (q_1 and q_2) of the emissivity were allowed to be free parameters. This provides the ability to modify the reflector but in a way which still maintains a self-consistent model. The second method was to accept truncation and to allow the inner radius parameter to go free. This has the disadvantage of untying the reflector from the blackbody, as KERRBB will be unaware of the change in r_{in} thereby forcing an unphysical model.

Both of these two methods greatly improved the fit statistics. Allowing for truncation in the reflection model reduced the $\chi^2(d.o.f)$ from $2732.2(142)$ to $1688.4(142)$, with the best fit requiring a truncation radius of $r_{in} = 58.8 \pm 3.4$. Freeing the emissivity profile provided the largest improvement with a change to $\chi^2(d.o.f) = 1358.6(141)$. However, the values at which the two emissivity indices were fit at are extreme, with $q_1 = 19.7 \pm 2.7$ and $q_2 = 0.74 \pm 0.30$. Here we assume the break still occurs at 10 r_g. A fit was attempted here in which the break radius was also allowed to vary, but lead to a unconstrained value. This presents a situation where the reflection model is effectively trying to create two areas of reflection, the first just outside the event horizon, and the second a distant reflector towards the outer edge of the accretion disc. The viability of this geometry could be tested in a more physical fashion by directly including this distant reflector in the model. To do this a XILLVER component was added to the model, which provides the reflection emission from an accretion disc, but without the relativistic smearing which affects the RELXILL model. This added three more parameters to the model: Γ_x, $log(\xi)_x$ and N_x. The spectral index

Γ_x is tied to Γ_s, but the other two parameters are allowed to vary freely. The addition of this secondary reflector leads to a fit with $\chi^2(d.o.f) = 1393.2(140)$, slightly higher than that with the free emissivity profile.

This picture was the same for all of the GX 339-4 hard state observations. A geometry in which there is a distant reflector produced a better fit than one in which the accretion disc is truncated. This idea has been presented before in Steiner et al. (2017) who also find a solution involving a distant reflector provides a good fit of the data without requiring significant truncation. Therefore, the conclusion is that while there is not necessarily a disagreement found with previous authors who present evidence of truncation in these GX 339-4 observations (e.g. Done & Diaz Trigo 2010; Plant et al. 2015; Basak & Zdziarski 2016), there are other solutions available, and in the case of an additional reflection component can lead to statistically preferable result.

There are also two observations in intermediate states in which the standard model was insufficient. The first was from MAXI J1659-152 rev1978 during the rising phase of its 2010 outburst. The standard model produced large residuals above 5 keV and a large $\chi^2(d.o.f)$ of $436.0(142)$. In this case including truncation was found to produces the greatest improvement with a truncated radius $r_{in} = 63.8 \pm 16.9$ for $\chi^2(d.o.f) = 189.0(141)$, and a much lesser effect with the addition of a distant reflector with $\chi^2(d.o.f) = 368.6(139)$. The second observation, Swift J1910.2-0546 rev2335, required less of a deviation from the assumptions with a spin of $a = -0.85 \pm 0.25$ adequately dealing with residuals in the data.

5.5 Discussion

Analysis of *XMM-Newton* EPIC-pn spectra for a sample of transient LMXBs has been presented, using the most up-to-date models and results from some of the best spectroscopic data from *XMM-Newton*/RGS to model absorption. It is found that in most cases there is no evidence that truncation

of the accretion disc is required to provide an acceptable fit of the data.

All of the soft state observations are fit adequately with a disc extending to $r_{in} = r_{ISCO}$. Virtually all models of accretion geometries predict an extended disc during the soft state, so this is likely an uncontroversial conclusion. Furthermore, no observations in the soft state require a modification of the spin parameter. Few of the systems here have spin estimates, but there is some disagreement with those that do. For example, GRO J1655-40 is thought to have a maximally spinning BH from a comparison between its observed X-ray properties and theoretical flux distributions from a thin disc around a Kerr BH (Zhang et al., 1997).

The small number of intermediate state observations studied show a mix of results. Two systems show evidence of truncation, both require a deviation from the model with truncation the most statistically acceptable solution. On the other hand, XTE J1652-453 has a observation in a hard-intermediate state and is the sole example of an observation that needs a non-zero spin. A positive spin is required implying a need for a lower value of r_{in} and a larger disc component. Given that it is during the intermediate state that the change in accretion geometry will likely take place, it is perhaps unsurprising that these spectra are non-trivial to fit.

All of the hard state observations also show no strong need for truncation. This is in agreement with some studies of the same data sets, e.g. Miller et al. (2006b); Sánchez-Fernández et al. (2006); Reis et al. (2011); Cassatella et al. (2012); Del Santo et al. (2016); Steiner et al. (2017). However, spectra from the system GX 339-4 are often considered to show evidence of truncation (Done & Diaz Trigo, 2010; Plant et al., 2015; Basak & Zdziarski, 2016). Observations from GX 339-4 are more difficult to fit, but it was possible to find reasonable fits with a non-truncated disc if ones allows for a second, distant source of reflection. This provides narrower reflection features. If these features really are from a distant source of reflection, then modelling with a single (disc) reflection will produce high values for r_{in} due to the narrower composite line profiles. It is not obvious what the physical origin of this distant reflector actually is, but could be related

to a flared outer disc for example. This is in agreement with results from Steiner et al. (2017). The model used in Steiner et al. (2017) is a little different than the one presented in this chapter. They use a modified version of `SIMPL` which includes the reflection fraction as a free parameter. This means their model can conserve photons not only between the thermal and non-thermal components, but also between the non-thermal emission and the reflector. However, their thermal disc component does not include relativistic effects. They claim this self-consistency to be an important factor in spectral studies, and one that is often ignored. In particular, they compare their results to those from Basak & Zdziarski (2016), another study of GX 339-4 data using a similar model, but one in which they find large scale disc truncation. The model used in Basak & Zdziarski (2016) though does not conserve photons between the disc and power law components. Steiner et al. (2017) calculate that an accretion disc truncated to the levels measured in Basak & Zdziarski (2016) would require an extremely high mass accretion rate, higher than the brightest soft states. It seems clear that any future studies of XRBs should strive to employ the most self-consistent model possible to provide the most physically feasible representation of the accretion disc, something which as been rarely achieved in the past.

The trend of generally fitting lower Γ_r than Γ_s values is also in agreement with Steiner et al. (2017). They also follow the method presented in Fürst et al. (2015) of allowing the two spectral indeces to be fit independently. A difference between the two indeces of $\Delta\Gamma \approx\ 0.2 - 0.3$ woud be easily explained by the reflected emission being Compton scattered.

Many of the hard state observations are at relatively bright parts of their outbursts where we might expect lower levels of truncation, but there are also a smaller number of much fainter examples. This range of observations at various mass accretion rates can then be used to attempt to pinpoint a luminosity at which a system transitions from requiring a blackbody component with $r_{in} = 6r_g$ to appearing truncated. Observations from GX 339-4, Swift J1357.2-0933 and Swift J1753.5-0127 provide examples of higher quality hard state spectra, while 4U 1543-475, MAXI J1659-152 (rev2066) and Swift J1910.2-0546 (rev2715) are closer to quiescence. The lat-

ter group seem insensitive to the inclusion of the thermal disc and reflection components, with a simple, absorbed power law providing an acceptable fit. As such, they could be consistent with a heavily truncated disc. The model can be used to estimate the flux (between 0.8 and 10.0 keV) of the source and therefore calculate the luminosity as a function of the Eddington luminosity. For the Swift J1357.2-0933, Swift J1753.5-0127 (rev 1152) and GRO J1655-40 (rev596) observations the luminosity is found to be $L \approx 2 \times 10^{-3} L_{Edd}$ for all three. For Swift J1357.2-0933 a fit without a blackbody component gives a poorer fit ($\chi^2_{red} = 1.75(148)$), implying the necessity of a extended disc at this luminosity. The effect is less severe for GRO J1655-40 and Swift J1753.5-0127, but a disc contribution is still favoured. The three fainter observations have a range of luminosities: $L = 1.88 \times 10^{-4} L_{Edd}$ for MAXI J1659-152, $L = 6.60 \times 10^{-5} L_{Edd}$ for 4U 1543-475, and $L = 7.34 \times 10^{-6} L_{Edd}$ for Swift J1910.2-0546. The lowest luminosity observation, Swift J1910.2-0546, is close to the level at which point some models would predict a truncation radius of $> 100 R_g$ (e.g. Narayan et al. (1996)), which could explain the insensitivity to a blackbody component. The other two are brighter but have the same indifference towards the blackbody and reflection component, with the luminosity change only a single order of magnitude from the brighter hard states, so this could suggest these systems switching from an extended disc to one that would appear heavily truncated at $L \approx 10^{-3} L_{Edd}$ mark. For GX 339-4 this luminosity is slightly higher, with the hard state observations which can all be fit with a truncated disc having luminosities in a range of $L = (7.64 - 1.00) \times 10^{-3} L_{Edd}$. These results are summarised in Figure 5.6, which plots the mass accretion rate against the luminosity as a fraction of the Eddington luminosity. The figure shows the split at around $L \approx 10^{-3} L_{Edd}$ between the sources that do and do not require a blackbody component, as well as the luminosities found for GX 339-4. Figure 5.7 displays the measured truncation radius for the observations in which the blackbody was not required and truncation was directly tested for. For some of the most faint observations (e.g Swift J1910.2-0546, 4U 1543-475) the model was not capable of constraining the value of r_{in} and were not included in this plot. There appears to be no real correlation between the mass accretion rate and the calculated inner radius location, with two observations having larger trucation radii

and the remainder fairly constant at $\sim 10 r_g$.

From the results it would appear that truncation is not required for bright hard states down to a luminosity of approximately $0.1\% L_{Edd}$, and is never required for the soft state. GX 339-4 is the primary complication to this conclusion, clearly showing more unique behaviour, and transitioning into a less standard accretion state at a slightly higher luminosity. However a solution is still available that does not require truncation. Hopefully future observational campaigns will be able to track the decay of outbursts to a deeper level for a larger number of systems, and to check whether or not GX 339-4 is a truly anomalous source.

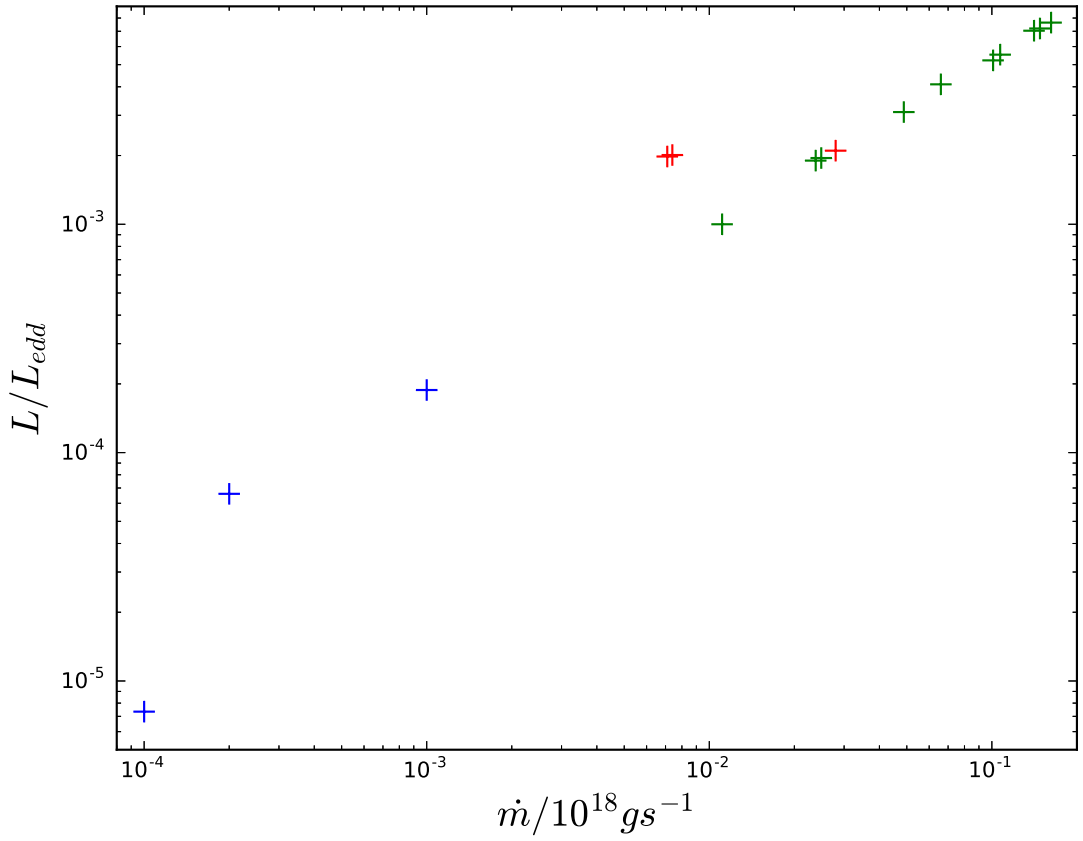

Figure 5.6: Plot showing the luminosities of the hard state observations which were tested for the requirement of a blackbody component. The blue data points represent the observations in which the fit is insensitive to the blackbody component, the red points are those in which the blackbody component was necessary, and the green points represent the GX 339-4 results which can be fit with a truncated disc.

These results are consistent with a number of other studies which also see no need for truncation in bright hard states. Results presented in Reis et al. (2010) arrive at a similar conclusion finding no requirement for truncation down to luminosities as low as $L \approx 5 \times 10^{-4} L_{Edd}$ from a sample of eight systems. Rykoff et al. (2007) also find a similar value for the system XTE J1817-330. There are also theoretical models that can match this observed behaviour and offer alternate explanations for the differences between the hard and soft states. For example, Markoff et al. (2005) present a model where the hard X-ray emission originates from the base of the jet so requires no truncation of the disc. Salvesen et al. (2013) suggest that a change in the vertical structure of the disc could explain the state change, and test this theory on GX 339-4 data. They find that an increase in f_{col} during the hard state can provide an alternative to truncation. This could help explain the higher

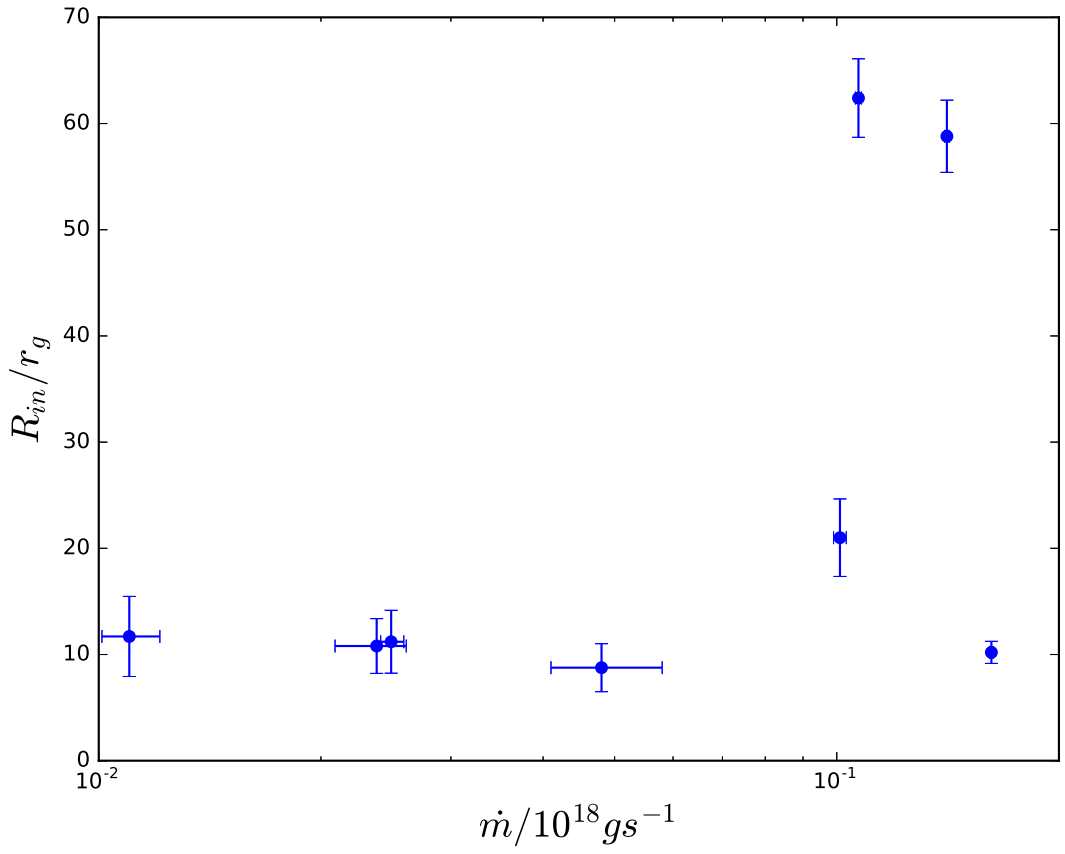

Figure 5.7: Plot to show the truncation radius against the mass accretion rate for each observation in which the inner radius was allowed to vary, and in which a value for the inner radius was found.

f_{col} values found in some of the observations here. There are also models that can involve the emergence of an ADAF in the hard state. Liu et al. (2007a) offer a geometry where a cool inner disc can exist within a corona. The model was tested on data from GX 339-4 and Swift J1753.5-0127, and they found that it can describe the observations down to a luminosity of $L \approx 10^{-3} L_{Edd}$. A model such as this could potentially help explain the results found here. Instead of a geometry in which the disc has to be truncated during the hard state, perhaps the disc could simply get cooler and less luminous due to the lower mass accretion rate and is then enveloped by the corona. But it is not until closer to quiescence that the disc fully evaporates. A geometry similar to this might not even necessarily need to be all that different from the truncated disc model as r_{in} would just represent the boundary between the ADAF/thin disc structure and the thicker outer disc. This similarity with the truncated disc model might also allow the QPO results to be tied in easily as well if the type C QPOs are due to this boundary between the two disc structures.

This picture of the accretion geometry with a ADAF/thin disc structure could also help reconcile the results of Chapter 3. Evidence for the emergence of radiatively inefficient emission was found during the hard state. While this would fit well with the truncated disc picture, the results of this chapter seem to show that truncation is not required during bright hard states. A solution would therefore be required in which both a disc and a radiatively inefficient accretion flow is present. There are only three observations where there is a direct overlap between the results of Chapters 3 and 5. The 2010 outburst of H 1743-322 was one of the more inconclusive examples from Chapter 3. There was no estimate possible of the soft state decay, and only an ambiguous hard state decay estimate of τ_h = 10.69 ± 2.40. The *XMM-Newton* observation shows no need for truncation, but is at a relatively low luminosity, so could support the idea of a faint disc component. The second example is from XTE J1752-223. This is the outburst which remained in the radiatively efficient state during the brighter stages of the hard state. The time of the *XMM-Newton* observation is just after the source enters the hard state, during the radiatively efficient decay. This observation also shows the need for an extended disc component, with the light curve suggesting one which is still the dominant source of emission during the bright hard state. The GX 339-4 observations

at rev0782/0783 take place during the rising state of its 2004 outburst, the only *RXTE* lightcurve where a measurement of an exponential rise was possible. The observations take place at the brightest part of the hard state, brighter than some of the soft state, after the source appears to have entered a radiatively efficient regime, and do support a solution requiring no truncation. This again, could support the idea of an extended disc component during the brighter regions of the hard state.

The overall conclusion to this chapter is that there are no hard state observations in which truncation is absolutely required. This is in direct disagreement with the truncated disc model, which requires significant truncation even during bright hard states. The use of an alternate geometry would therefore be required to explain the results presented here. There are also no soft state observations which show evidence of a non-zero spin, meaning that in the majority of cases the 'standard' model used here can be fit to both soft and hard state observations in a satisfactory manner.

5.6 Notes on Individual Sources

Swift J1357.2-0933 has a single hard state observation. A good fit was found for this spectrum with the photon index from `SIMPL` at $\Gamma_s = 1.58 \pm 0.02$, in general agreement with the value presented in Armas Padilla et al. (2014), and the $\Gamma \sim 1.55$ from the two *Swift* observations performed a day either side of the *XMM-Newton* observation (Armas Padilla et al., 2013). The fit overall requires no truncation with a disc component with $f_{col} = 1.62^{+0.12}_{-0.10}$, a reflection component with $\Gamma_r = 1.23^{+0.07}_{-0.09}$ present and no significant residuals.

The GS 1354-64 observation was during its 2015 failed outburst, in which it never transitioned to the soft state. The observation was performed near the peak of the outburst so it is in a relatively bright hard state. The free parameters from `SIMPL` and `RELXILL` are typical of a hard state

source, however, a high f_{col} value is also present. This could be due to an incorrect distance estimate. The lower limit of 25kpc from Casares et al. (2009) is used here, but could also be related to the poor fit at low energies.

4U 1543-475 has just a faint hard state observation with a low signal-to-noise ratio. The results of the MCMC analysis show a poorly constrained set of parameters. However, the photon index of $\Gamma_s = 1.79^{+0.07}_{-0.19}$, while being slightly lower than those presented in La Palombara & Mereghetti (2005), is in the range acceptable for a hard state spectrum. While there is no direct evidence of truncation from our fit, given that the mass accretion rate is very low, and the contribution from the blackbody and reflection components being so small, this is one of the observations where the recession of the disc would be most likely, but distinguishing between such a situation from one with a cool disc for example it difficult to achieve.

4U 1630-47 has six bright soft state observations. This is the source most heavily affected by absorption and the excess at $\sim 1keV$, so has smaller fitted energy range than the remainder of the sample. Fits were still able to be performed on the data though, and it was found that each observation is in a disc dominated state with very high mass accretion rates with a negligible contribution from `SIMPL`, except in the final spectrum where the scattering fraction suddenly increases to $0.51^{+0.32}_{-0.25}$. There are also strong reflection components in most of the observations, which were fit with a high spectral index and, as has already been noted in Díaz Trigo et al. (2014), significant absorption effects from a wind in the first four observations. There is no evidence for truncation for these observations, even for the unusual sixth spectrum with its high rate of Compton scattering.

XTE J1652-453 has a single observation during the hard-intermediate state of its 2009 outburst. After an initial fit large residuals were found at around 7 keV, likely due to the strong Fe emission line being poorly modelled (see Hiemstra et al. (2011) and Chiang et al. (2012) for a more detailed discussion of this feature in this source). To fix this issue the assumption of having a BH

with a spin of 0 was relaxed. A significant improvement was then found in the fit statistics with an increase in the spin of the BH, although the spin value itself was very poorly constrained. This general behaviour is in agreement with the results of Hiemstra et al. (2011) who find $a = 0.45 \pm 0.02$, and Chiang et al. (2012) who, while finding it harder to find a well constrained spin parameter, present an upper limit of $a \sim 0.5$ under certain assumptions.

The results from the brighter GRO J1655-40 observations are all fairly consistent with that expected from the soft state, with a negligible contribution from `SIMPL` in a number of cases. The fit is also greatly improved ($\Delta\chi^2 \approx 200$) with the addition of the Gaussian component at approximately 7 keV. The results are also fairly consistent with one another, with the f_{col}, Γ_r and $log(\xi)$ having a good agreement across all observations. The two observations at rev966 and rev970 show much more prominent absorption features above 7 keV, but similar parameters otherwise. The observation at rev956 is the sole example of GRO J1655-40 in the hard state, taken during the same outburst. This observation has much worse signal-to-noise than the soft state observations but a fit was still possible. The parameters arrive at values fairly typical of a hard state spectrum, with $f_{col} = 1.79^{+0.83}_{-0.56}$ and $\Gamma_s = 1.46^{+0.11}_{-0.10}$. The results can be compared with previous studies of these observations, such as Sala et al. (2007b). For the rev956 observation they fit a power law with a spectral index of 1.48 ± 0.01 which gives a good agreement with our Γ_S value. Similar numbers ($1.4-1.6$) were also reported during the *RXTE* monitoring at around that time (Markwardt et al., 2005). However, for rev964a/b and rev956 Sala et al. (2007b) find much smaller spectral indeces at $\Gamma \approx 2.20$.

MAXI J1659-152 has two observations, one in a faint hard state and one in an intermediate state. An initial fit of the intermediate state observation gave a poor fit, particularly between $5-7$keV. Relaxing the assumption of a spin 0 BH we find that there is a large improvement in the fit statistics for a spin of -1, which would represent moderate truncation. For the faint hard state observation the fit is poorly constrained, particularly for the `RELXILL` and `KERRBB` parameters indicating a weak disc component which, given the results of the brighter observation, could potentially

suggest this as a source showing true truncation.

IGR J17091-3624 has both a soft and hard state observation. The soft state spectrum has a good fit with standard soft state parameters of a large mass accretion rate and a steep power law. The hard state observation returned a fit with a strong power-law component and a very low f_{col} value.

SAX J1711.6-3808 has a hard state observation from its 2001 outburst. The data was well fit with a power law with $\Gamma_s = 1.55^{+0.05}_{-0.04}$ and a blackbody component with a low f_{col}, along with the reflection component with a very low spectral index. Compared to a previous study of this observation in Sánchez-Fernández et al. (2006) the spectral indeces found are similar, and agree on a disc with $r_{in} = r_{ISCO}$.

XTE J1719-291 is classed as a very faint X-ray transient so the one spectrum available has relatively low signal-to-noise and the constraints on the parameters are fairly poor. For a hard state observation we fit very high values for the spectral indices in complete disagreement with the findings of Armas Padilla et al. (2011). From the large differences in hydrogen column density this could be an issue with the absorption parameters.

XTE J1720-318 is another example of a soft state observation with a very weak contribution from `SIMPL`, and is well fit by a blackbody component with $f_{col} = 2.61^{+0.01}_{-0.01}$. Cadolla Bel et al. (2004) find similar results requiring a combination of a blackbody component and a steep power law ($\Gamma = 2.81^{+0.60}_{-0.66}$) for a good fit.

IGR J17285-2922 has just one hard state observation. A good fit is found with a spectral index $\Gamma_s = 1.61^{+0.02}_{-0.02}$. The free parameters from `KERRBB` however were poorly constrained, indicating a very weak soft component, but one without a requirement of truncation. Sidoli et al. (2011) test a variety of models on this data set and reach a similar conclusion in that the data can be well fit with an absorbed power law but a faint disc cannot be ruled out.

There are five observations for H 1743-322 all in the hard state. All five are fit with a low Γ_s and

f_{col}. The first observation provides a reasonable fit without the need for truncation, but the later observations, particularly the final one arrive at much worse fits. An attempt was made to find a fit with inner radius and spin included but found no notable improvement in the fit statistics.

In 2012 Swift J174510.8-262411 underwent a failed outburst remaining in a hard-intermediate state during which the observation took place before returning the quiescence. The results of the spectra fitting for this observation match the properties expected from during such a state, with $\Gamma = 2.05^{+0.04}_{-0.04}$, and a relatively large mass accretion rate of $1.04^{+0.03}_{-0.04} \times 10^{16} gs^{-1}$. These results agree with previous analysis of *Swift* observations at a similar time (Del Santo et al., 2016), who also find $\Gamma \sim 2.0$ and a significant improvement in the fit statistics with the addition of a black body component.

IGR J17497-2821 has two hard state observations. The first gives reasonable fit statistics with a low f_{scat} and f_{col}. The second can be fit with parameters expected from the hard state with the exception of a very high spectral index from Γ_r. Neither are improved though by modifying the spin or location of the inner radius.

The single XTE J1752-223 hard state observation has a poor fit at low energies, with a large f_{col} and Γ_r. There is also no significant improvement by allowing the spin to vary freely. The spectral index from `SIMPL` $\Gamma_s = 1.35^{+0.08}_{-0.07}$ is smaller than those presented in a previous examination of this observation, $\Gamma = 1.83 \pm 0.01$ (Reis et al., 2011), and a simultaneous RXTE and Swift observations, $\Gamma = 1.81^{+0.01}_{-0.02}$ (Chun et al., 2013). Reis et al. (2011) also find the need for a higher spin value, suggesting a inner radius of $3.7^{+0.6}_{-0.7} r_g$ at this luminosity.

The source Swift J1753.5-0127 went into outburst in 2006 and remained in the hard state for the majority of its 11 year outburst, and has provided some of the better quality hard state spectra, 5 in total. The rev1152 observation is the faintest of the 5, so is the observation in which in might be expected to see issues with if truncation is occurring. The model gives a good overall fit, with the spectral indeces and scattering fraction close to that expected from the hard state, and is in

good agreement with the results of Miller et al. (2006a) and Cassatella et al. (2012) who also conclude that there is no evidence of truncation at this luminosity. The next observation, rev1716, was taken during one of the brighter sections of the outburst and had to be corrected for noticeable pile-up. The model produces a fit with reasonable fit statistics, although the two spectral indexes significantly disagree with an unusually high value from `SIMPL` for the hard state, which is in disagreement with the $\Gamma = 1.961$ in Cassatella et al. (2012). The remaining three Swift J1753.5-0127 hard state observations have similar properties to rev1152. The final Swift J1753.5-0127 observation was taken during an unusual low-luminosity soft state and can be fit with a very high spectral index and scattering fraction, with no need for truncation. Shaw et al. (2016) present a extensive study of this observation and also find a steep power law, but also claim the need for truncation, up to an inner radius of $28.0^{+0.7}_{-0.4} r_g$

GRS 1758-258 has three observations, one each in a soft, intermediate and hard state. The soft state observation (rev235) shows a weak power-law component with $\Gamma_s = 3.40^{+0.31}_{-0.23}$ and $f_{scat} = 6.19^{+1.50}_{-1.24} \times\ 10^{-2}$, and a blackbody with $f_{col} = 3.12^{+0.04}_{-0.04}$. The intermediate state observation (rev143), the brightest of the three, has a less steep power-law with $\Gamma_s = 2.35^{+0.05}_{-0.05}$, with the hard state observation's power law decreasing further still to $\Gamma_s = 1.49^{+0.06}_{-0.07}$ and a blackbody with $f_{col} = 1.25^{+0.16}_{-0.13}$. These changes are typical of each state, and no evidence of truncation was found in any of the three.

XTE J1817-330 has one soft state observation. The spectrum has a high spectral index of $\Gamma_s = 3.33^{+0.14}_{-0.15}$, a relatively low f_{scat} and a high f_{col} as is typical for the soft state. No requirement of truncation in this observation, in agreement with previous studies of this data set (Sala et al., 2007a).

XTE J1856+053 has a soft state observation completely dominated by the blackbody component. With the `RELXILL` normalisation being set at 0 and an extremely low f_{scat} present both components were removed from the model for the fit and MCMC analysis. There is also evidence

of an absorption feature at ≈ 6.4 keV, as already pointed out in Sala et al. (2008). They also arrive at a best-fit requiring only a blackbody component and a similar hydrogen column density of $N_H = 4.5 \pm 0.1 \times 10^{22} cm^{-1}$.

Swift J1910.2-0546 is very similar to MAXI J1659-152 with two observations: one faint hard state, and a intermediate state with a large excess at ≈ 7 keV. The fainter observation is another poorly constrained fit with very weak contributions from the blackbody and reflection components. The intermediate state observation is another candidate for truncation, with an moderate improvement in the fit statistics with a negative spin.

5.7 Additional Plots

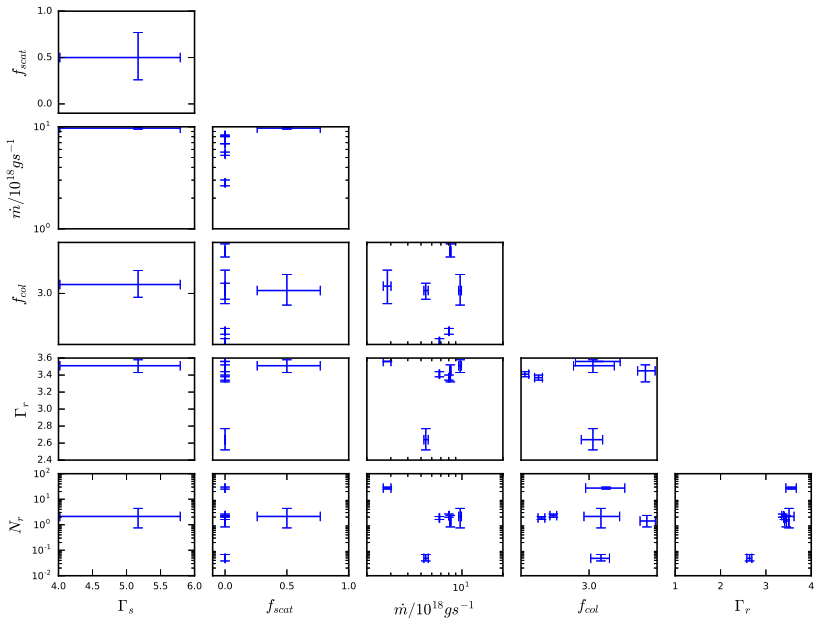

Figure 5.8: Plot to demonstrate the correlations between the results of the spectral analysis. This plot shows the spectral parameters from 4U 1630-47.

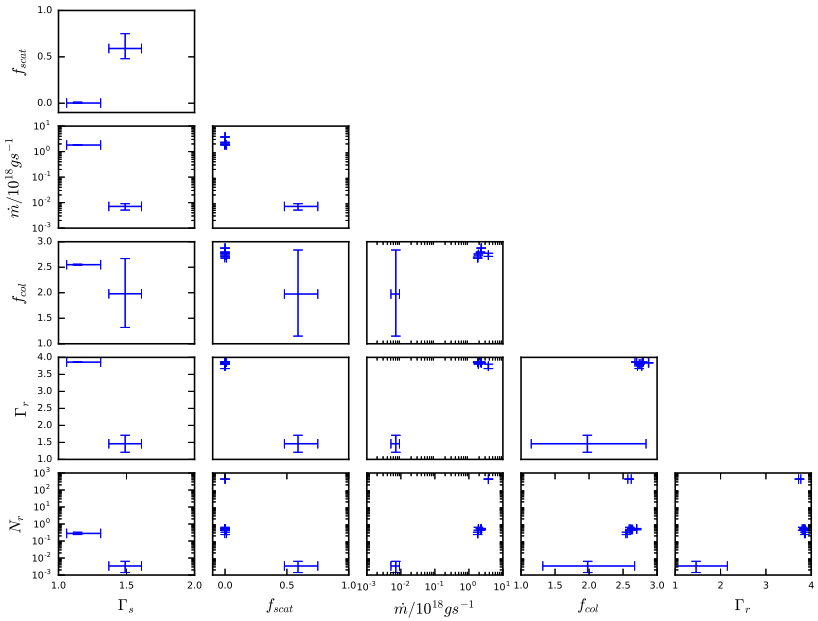

Figure 5.9: Plot to demonstrate the correlations between the results of the spectral analysis. This plot shows the spectral parameters from GRO J1655-40.

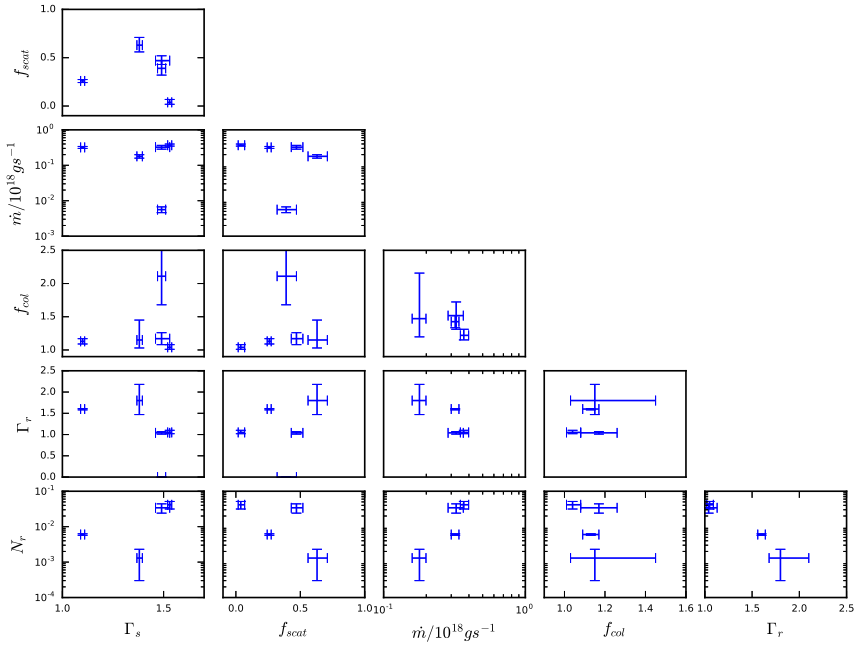

Figure 5.10: Plot to demonstrate the correlations between the results of the spectral analysis. This plot shows the spectral parameters from H 1743-322.

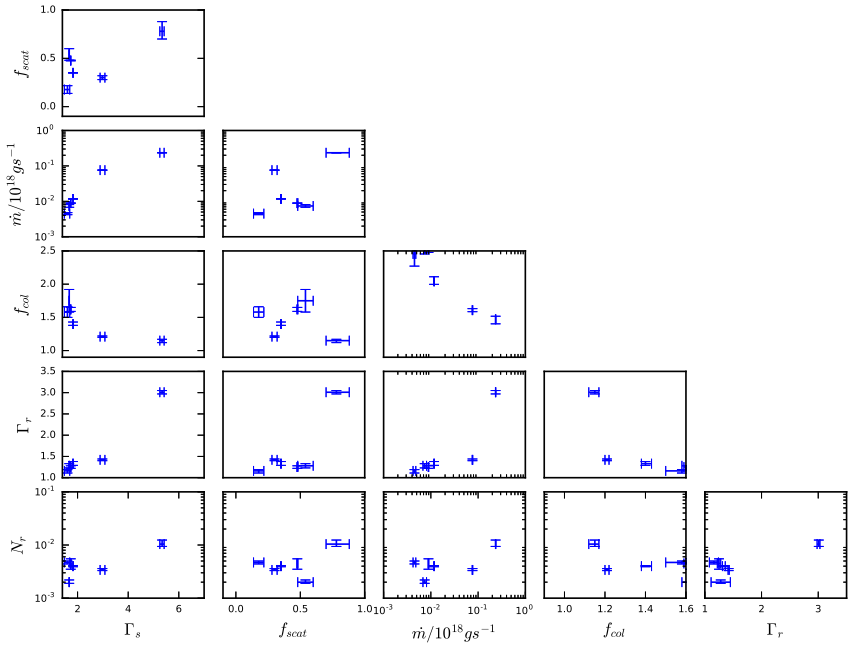

Figure 5.11: Plot to demonstrate the correlations between the results of the spectral analysis. This plot shows the spectral parameters from Swift J1753.5-0127.

6

Conclusions and Future Prospects

The overall aim of this thesis was to present analyses of observational data from XRBs, and specifically on the nature of the accretion disc as these systems evolve throughout an outburst. The most commonly accepted picture of the accretion flow of XRBs is that during the soft state a geometrically thin, optically thick accretion disc extends down to r_{ISCO}. In the hard state the disc truncates to a radius r_{in}, being replaced by a geometrically thick, optically thin accretion flow. Instruments such as *RXTE*, *Swift*, and *XMM-Newton* have provided large amounts of archival data which can be used to test the predictions of current theoretical models, and to slowly piece together a picture of how these XRB systems function. Here two separate studies have been performed using archival light curves and spectra which analyse the structure of the accretion disc, and one study which can assist in the study of XRBs.

In Chapter 3, results are presented that are consistent with the emergence of a radiatively inefficient flow during the hard state. The nature of the accretion disc is probed by using *RXTE* light

curves to measure the exponential decays of outbursts. It is found that there are usually two periods of exponential decay as the outburst fades. The first, in the soft state, were found to have e-folding times of around two weeks. The second, in the hard state, have e-folding times of approximately one week. Assuming that the mass accretion rate (through the inner disc) falls as a simple exponential across both states, these numbers imply that there is a radiatively efficient disc in the soft state, which transitions into a radiatively inefficient flow as the source enters the hard state. The change in the observed X-ray decay rates coincides with the X-ray spectrum changing through 'intermediate' states in all but one of the systems included in the sample. This suggests that while the switch in the radiative efficiency is more likely to be found during state transition, that does not have to be the case. With the exception of the one more unusual system the results here could be used to support the idea of truncation. The results match those expected from the truncated disc model as the disc will be replaced by a radiatively inefficient flow (e.g. an ADAF). These results alone though are insufficient to explicitly state whether or not truncation is occurring, only that a radiatively inefficient X-ray emissions seems to be become dominant at some point during the decay though the hard state.

Chapter 4 contains a supplementary study designed to aid the work done in Chapter 5 and any future analysis using a similar method. The photo-electric absorption model `ISMabs` is used to calculate the H, O, Ne and Fe column densities towards a sample of XRBs using data from *XMM-Newton*/RGS. Many spectral analyses of XRBs have been performed in the past using less sophisticated models and potentially unsuitable estimates of elemental column densities from older surveys. The high-resolution soft X-ray spectra provided by the RGS are necessary to properly disentangle absorption from H and He from that due to other species, particularly O, Ne an Fe. By fitting the RGS data - using a very general continuum model - the absorption is accurately modelled in a way that is largely independent of the details of the broad-band EPIC fitting, removing the degeneracy between parameters that determined the continuum emission and absorption components in the broad-band model. With the model being publicly available the results presented in Chapter 4 can now be used as a standard look-up table for any analysis of the systems included in

the sample. This will be useful for any studies not directly interested in the properties of the ISM, but simply need a quick and accurate way to model its effects. Some of the hydrogen column density values found showed large disagreements with the values from the 21 cm maps meaning care does need to be taken when choosing absorption parameters. Having an incorrect value of N_H was found to influence the values of all continuum parameters, thereby potentially affecting estimations of the inner radius.

Chapter 5 attempts a more direct test of truncation by fitting *XMM-Newton* energy spectrum from both hard and soft states with a single, standard model. The assumption is made that there is no truncation in any state and the disc always extends to $r_{in} = r_{ISCO}$ for an $a = 0$ BH. If this model fails to fit spectra, and how it fails, would support the truncation model. If the model does adequately fit the spectra, then truncation is not necessary to explain the differences in X-ray spectra between states. This model was found to be capable of fitting the observed spectrum in a large number of cases. In agreement with the majority of models none of the soft states required a deviation from a non-truncated disc. The hard state though presents a more complicated case with the brighter observations also not requiring a truncated disc, with the exception of all the GX 339-4 observations. The GX 339-4 hard state observations can all be fitted with a truncated disc, although a model which includes the effects of a distant reflector present a more statistically preferable solution. There are also a small number of fainter hard states which are insensitive to the black body component. The conclusion is that large scale truncation does not need to occur above a luminosity of $\sim 10^{-3} L_{Edd}$.

Hopefully future observational campaigns will have the ability to track the decay of outbursts to lower luminosities, and also have the opportunity to catch a wider range of systems in a hard state. With going through frequent, long outbursts in both the *RXTE* and *XMM-Newton* eras, GX 339-4 has many more observations than the remainder of the sample presented in this thesis, and as a result tends to appear more frequently when truncation is discussed in the literature. The results of Chapter 5 seem to show that GX 339-4 is noticeably different than the other XRB

systems, and is consistent with a non-truncated disc model only once one allows for the presence of the additional reflection component, one that can mimic the effects of truncation. This could suggest that drawing any general conclusions based solely on GX 339-4 data could be completely unrepresentative of the population of XRBs as a whole. An observation campaign on a source such as Swift J1357.2-0933 or GRO J1655-40 during the hard state would be ideal to check the results of Chapter 5. For example, a series of observations spread evenly between the end of the soft state and the faint hard state would be able to capture the evolution of the disc. With *XMM-Newton* more than capable of providing high quality spectra scheduled in such a way, and is likely to be operational for the foreseeable future, an observation campaign to study the decaying phase of an outburst is certainly feasible and only needs a suitable target.

Widening the observational energy range could also allow new insights into the structure of the accretion disc. Many of the more detailed observations which have been available in the recent past are from XMM-Newton, and perhaps including observations from missions with different energy bands could improve our ability to model the disc spectrum in the faint hard state observations in which truncation could be occurring. For example, with future missions such as the X-ray Astronomy Recovery Mission (XARM) or the Advanced Telescope for High Energy Astrophysics (ATHENA) it will be possible to extend the available energy range lower than the 0.8 keV used in Chapter 5. Improvements in our ability to capture the behaviour of the soft disc emission would allow for greater accuracy in finding signatures of a truncated disc. Expanding the investigation to include observations from different parts of the electromagnetic spectrum could also provide complementary results to the ones presented in this thesis. XRBs are not just bright in X-rays, and using optical light curves for example could represent an alternative way of studying the rise and decay of outbursts.

Of course, the ability to observe a wider range of systems is dependent on these objects actually having outbursts, but work could be done to optimise the scientific value of any observations that can take place. A useful study to perform using the same data set as in Chapter 3 could be to study

the light curves for any systematic behaviours or patterns that could help predict the soft to hard state transition. With observations having to be planned in advance it can be easy to miss valuable data by triggering observations too early or too late in the outburst. Any work that could help predict outburst variables such as length of outburst or the length of the soft state by analysing previous outbursts would prove helpful. The outbursts could be divided into 'regions' based on spectral properties of the outburst (e.g. rising hard state, decaying hard state, intermediate states) and based on features of the outburst (many of the outbursts show distinct peaks in the soft states with a plateau in the count rate occurring directly afterwards). An attempt at this method was performed on the available *RXTE* data but was not finished. It was found that the longer outbursts ($>$300 days) could be fairly consistently divided into these well defined regions, while the shorter outbursts were found to show simpler behaviour, often just missing some of the regions. This work could be finished by looking for correlations between the length of these regions. If a relation can be found between these lengths, and a loose estimate of how long the soft state is likely to last, then this could make optimising observation time much simpler for future missions interested in targeting very specific parts of outburst evolution.

Chapter 5 has only considered the spectral properties of the *XMM-Newton* observations. The most natural extension to that project would be to also consider the timing and spectral-timing (Cassatella et al., 2012) properties. Several systems have been found here that show hard state observations with no requirement for truncation. However, with the analysis of QPOs often presenting convincing evidence for truncation, it will be necessary to have these two techniques agree if any definitive conclusions are to be made.

In any case, there is a large amount of data sitting in the *RXTE* and *XMM-Newton* archives, and hopefully this thesis has helped prove there are still interesting science results within those waiting to be found with the right approach.

A

Observation Log

The observation log for all the data used in Chapters 4 and 5. All mass, distance and inclination values are from those collected in Tetarenko et al. (2016), with the exception of Swift J1753.5-0127 which are based on calculations in Froning et al. (2014). Bracketed letters next to pn mode refer to the reason for the RGS observation being rejected from the sample in Chapter 4 (n=no data, f=faint, p=piled-up).

System Name	Mass ($M_\odot$)	Distance (kpc)	Inclination (deg)	Obs ID	Rev	Duration (ks)	Date	pn mode (RGS Data Quality)
1E 1740.7-2942	-	-	-	0112971701	240	12.0	31/3/2001	Small Window(n)
				0144630101	688	9.0	11/9/2003	Small Window(f)
				0303210201	1065	23.9	2/10/2005	Small Window(f)
				0673550201	2256	134.0	3/4/2012	Small Window(f)
4U 1543-475	9.4	7.5	30.0	0155762201	493	28.5	18/08/2002	Small Window(f)
4U 1630-47	-	-	-	0670671301	2249	23.8	20/3/2012	Timing(f)
				0670671501	2241	79.2	4/3/2012	Timing(f)
				0670672901	2251	65.4	25/3/2012	Timing(f)
				0670673001	2336	69.5	9/9/2012	Timing(f)
				0670673101	2337	32.9	11/9/2012	Burst(f)
				0670673201	2345	53.9	28/9/2012	Burst(f)

System Name	Mass ($M_\odot$)	Distance (kpc)	Inclination (deg)	Obs ID	Rev	Duration (ks)	Date	pn mode (RGS Data Quality)
GRO J1655-40	5.4	3.2	69.0	0112921301	956	42.5	27/2/2005	Burst
				0112921401	964	15.6	14/3/2005	Burst
				0112921501	964	15.6	15/3/2005	Burst
				0112921601	965	15.6	16/3/2005	Burst
				0155762501	966	23.9	18/3/2005	Burst
				0155762601	970	22.3	27/3 2005	Burst
GRS 1009-45	5.95	3.82	62.0	0073340201	453	26.3	30/5/2002	Full Frame(f)
GRS 1716-249	-	-	-	0112410101	316	12.8	31/8/2001	Full Frame(f)
GRS 1758-258	-	-	-	0112971301	143	13.9	9/9/2000	Small Window(n)
				0136140201	235	22.2	22/3/2001	Large Window(f)
				0144630201	513	8.9	28/9/2002	Small Window(f)
GS 1124-684	5.99	5.89	60.0	0085960101	222	34.0	24/2/2001	Full Frame(f)
GS 1354-64	7.47	35.0	50	0727961501	2868	25.0	6/8/2015	Burst
GX 339-4	-	8.0	-	0156760101	514	76.3	29/9/2002	Burst(f)
				0204730201	782	137.9	16/3/2004	Timing
				0204730301	783	138.5	18/3/2004	Timing
				0410581201	1318	15.8	19/2/2007	Burst
				0410581301	1325	16.7	5/3/2007	Burst
				0410581701	1338	18.3	30/3/2007	Burst
				0605610201	1702	33.5	26/3/2009	Timing
				0654130401	1886	35.0	28/3/2010	Timing
				0760646201	2879	20.0	28/8/2015	Timing
				0760646201	2881	19.2	2/9/2015	Timing
				0760646201	2884	23.7	7/9/2015	Timing
				0760646201	2886	22.1	12/9/2015	Timing
				0760646201	2889	53.8	17/9/2015	Small Window
				0760646201	2895	49.2	30/9/2015	Small Window
H 1743-322	-	8.5	-	0553950201	1984	86.4	9/10/2010	Small Window(f)
				0554110201	1613	22.1	29/9/2009	Timing(f)
				0724400501	2708	140.1	21/9/2014	Timing(f)
				0724401901	2709a	82.0	23/9/2014	Timing(f)
				0740980201	2709b	52.5	24/9/2014	Timing(f)
H 1755-338	-	-	-	0032940101	228	19.0	8/3/2001	Extended Full Frame(f)
				0203750101	875	45.9	18/9/2004	Extended Full Frame(f)
				0500540101	1514	80.6	15/3/2008	Extended Full Frame(f)
IGR J17091-3624	-	-	-	0406140101	1229	8.18	25/8/2006	Full Frame(f)
				0406140401	1318	16.1	19/2/2007	Full Frame(f)
				0677980201	2069	39.0	27/3/2011	Burst(f)
				0700381301	2346	48.9	29/9/2012	Timing(f)
				0721200101	2520	45.8	13/9/2013	Full Frame(f)
IGR J17285-2922	-	-	-	0405182701	1969	22.2	9/9/2010	Large Window (f)
IGR J17497-2821	-	-	-	0410580401	1243	33.0	22/9/2006	Timing(f)
				0410580501	1245	32.4	26/9/2006	Timing(f)
MAXI J1659-152	6.0	-	70.0	0656780601	1978	51.9	27/9/2010	Timing(f)
				0677980101	2066	29.8	22/3/2011	Large Window(f)
MWC 656	5.0	2.6	-	0691630201	2287	14.9	4/6/2012	Full Frame(f)
				0723610201	2470	13.9	4/6/2013	Full Frame(f)
SAX J1711.6-3808	-	-	-	0135520401	225	13.0	2/3/2001	Full Frame(f)
Swift J1357.2-0933	-	-	-	0674580101	2044	36.9	5/2/2011	Timing(f)
				0724320101	2488	52.5	10/7/2013	Full Frame(f)
Swift J174510.8-262411	-	-	-	0693020301	2345	38.8	28/9/2012	Burst
Swift J1753.5-0127	5.0	3.0	55.0	0311590901	1152	42.0	24/4/2006	Timing
				0605610301	1796	38.4	29/9/2009	Timing
				0691740201	2336	40.1	10/9/2012	Timing
				0694930501	2350	30.9	8/10/2012	Timing
				0744320201	2704	50.0	13/9/2014	Timing
				0770580201	2797	48.3	19/3/2015	Timing(p)
Swift J1910.2-0546	-	-	-	0691271401	2355	51.2	17/10/2012	Timing(p)
				0741590101	2715	63.0	5/10/2014	Full Frame(f)
V404 Cyg	7.15	2.39	80.1	0304000201	1084	40.7	8/11/2005	Full Frame(f)
				0723310201	2553	54.3	13/10/2013	Full Frame(f)
V4641 Sgr	6.4	6.2	72.3	0144490101	612	48.9	12/4/2003	Small Window(f)

System Name	Mass ($M_\odot$)	Distance (kpc)	Inclination (deg)	Obs ID	Rev	Duration (ks)	Date	pn mode (RGS Data Quality)
XTE J1550-564	10.4	4.4	65.0	0400890101	1321	58.9	25/2/2007	Full Frame(f)
XTE J1650-500	4.72	2.6	75.2	0206640101	960	45.8	6/3/2005	Extended Full Frame(f)
XTE J1652-453	-	-	-	0610000701	1777	42.5	22/8/2009	Timing(f)
XTE J1719-291	-	-	-	0552002601	1521	44.7	30/3/2008	Full Frame(f)
XTE J1720-318	-	-	-	0154750501	586	17.4	20/2/2003	Small Window
XTE J1748-288	-	-	-	0030540101	504	28.8	9/9/2002	Small Window(f)
XTE J1752-223	9.6	3.5	-	0653110101	1891	41.9	6/4/2010	Timing
XTE J1817-330	-	-	-	0311590501	1146	20.6	13/3/2006	Burst(p)
XTE J1856+053	-	-	-	0510010101	1330	8.7	14/3/2007	Timing(f)

B

Additional Plots

This appendix contains all the additional fitted energy spectra and MCMC corner plots from Chapter 5. The long term lightcurves for each individual system can also be found towards the end of this section.

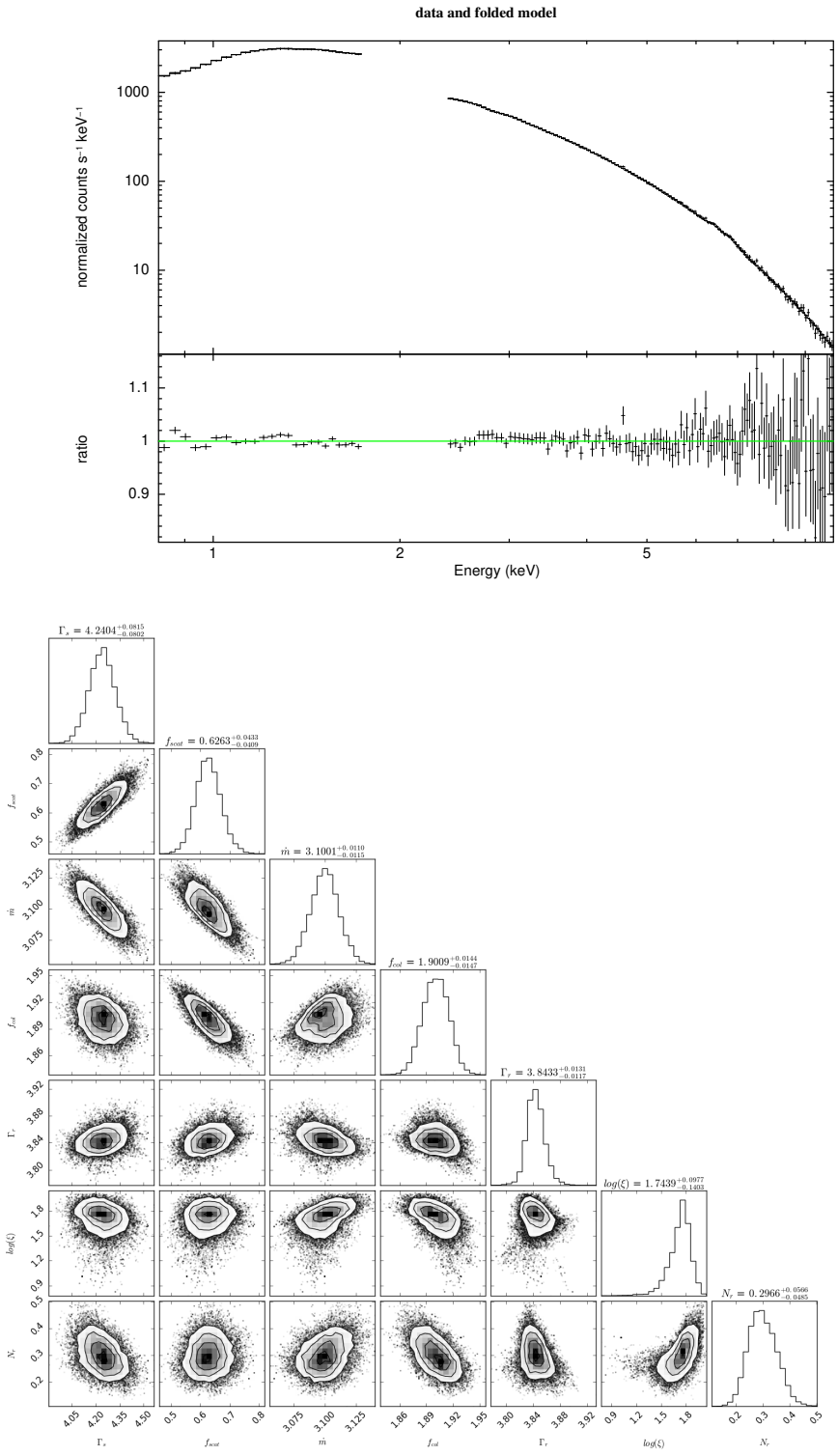

Figure B.1: XMM-Newton pn spectrum of the source GX 339-4 (rev0514). (Soft state)

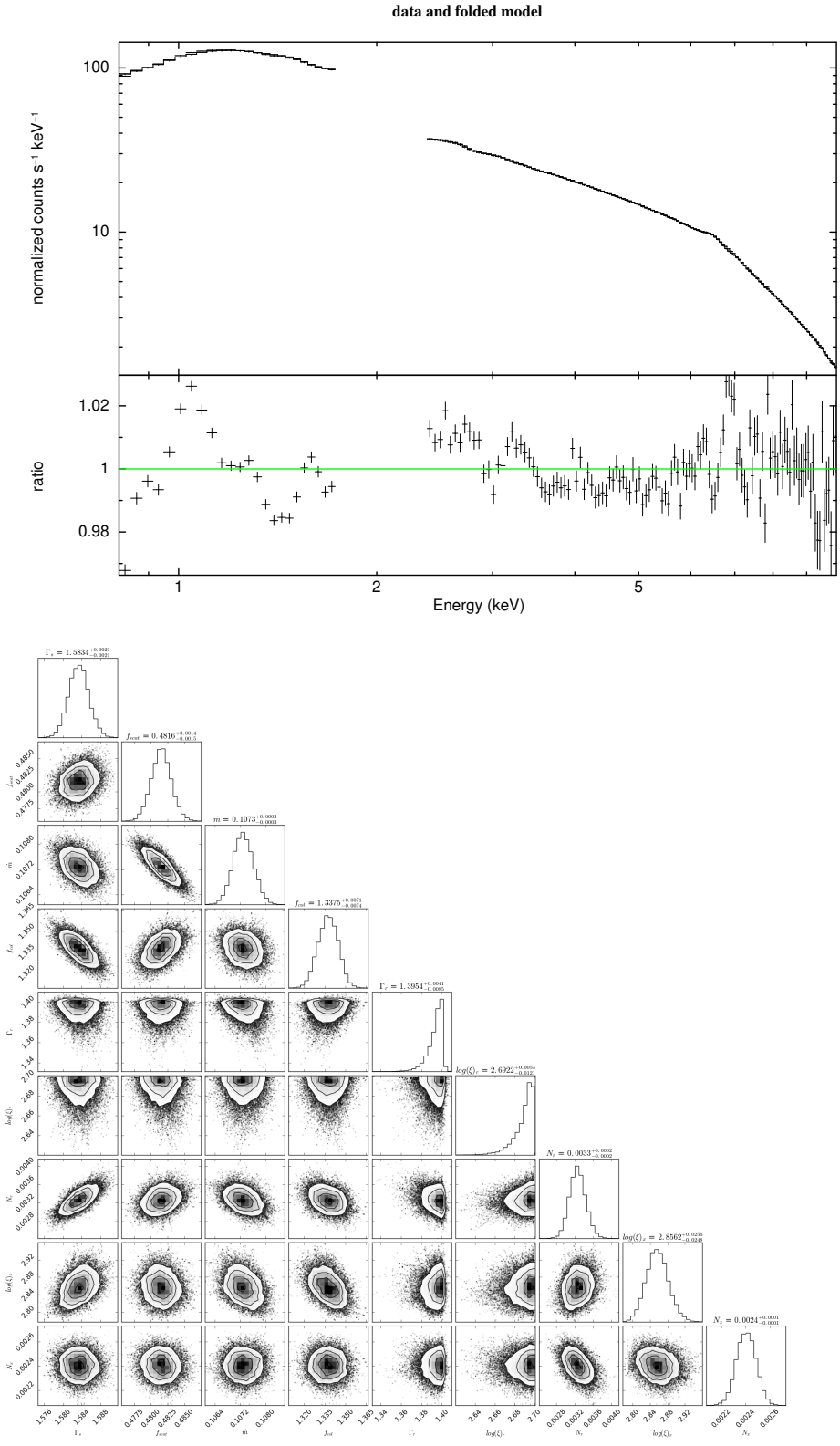

Figure B.2: XMM-Newton pn spectrum of the source GX 339-4 (rev0783). (Hard state)

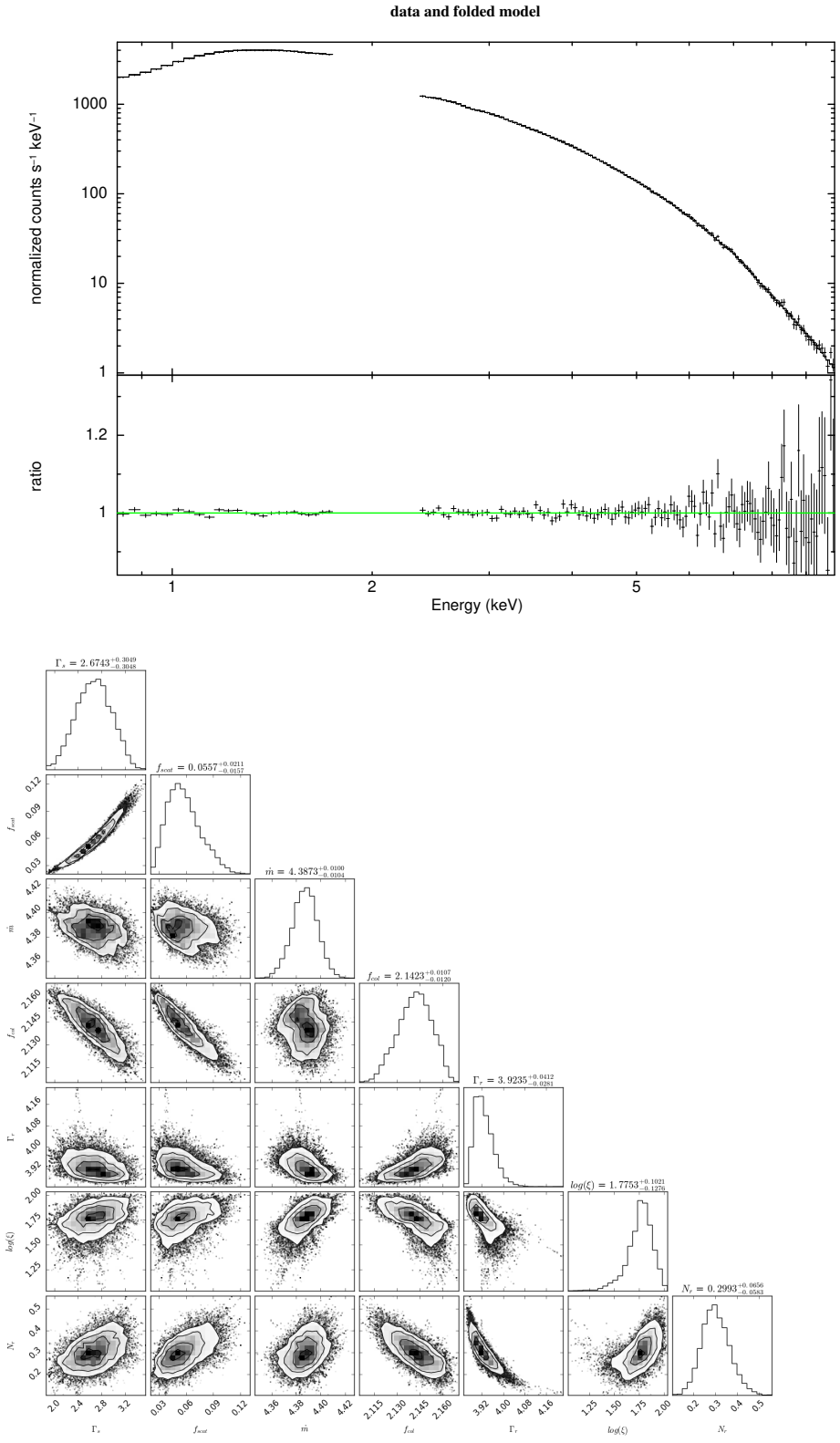

Figure B.3: XMM-Newton pn spectrum of the source GX 339-4 (rev1318). (Soft state)

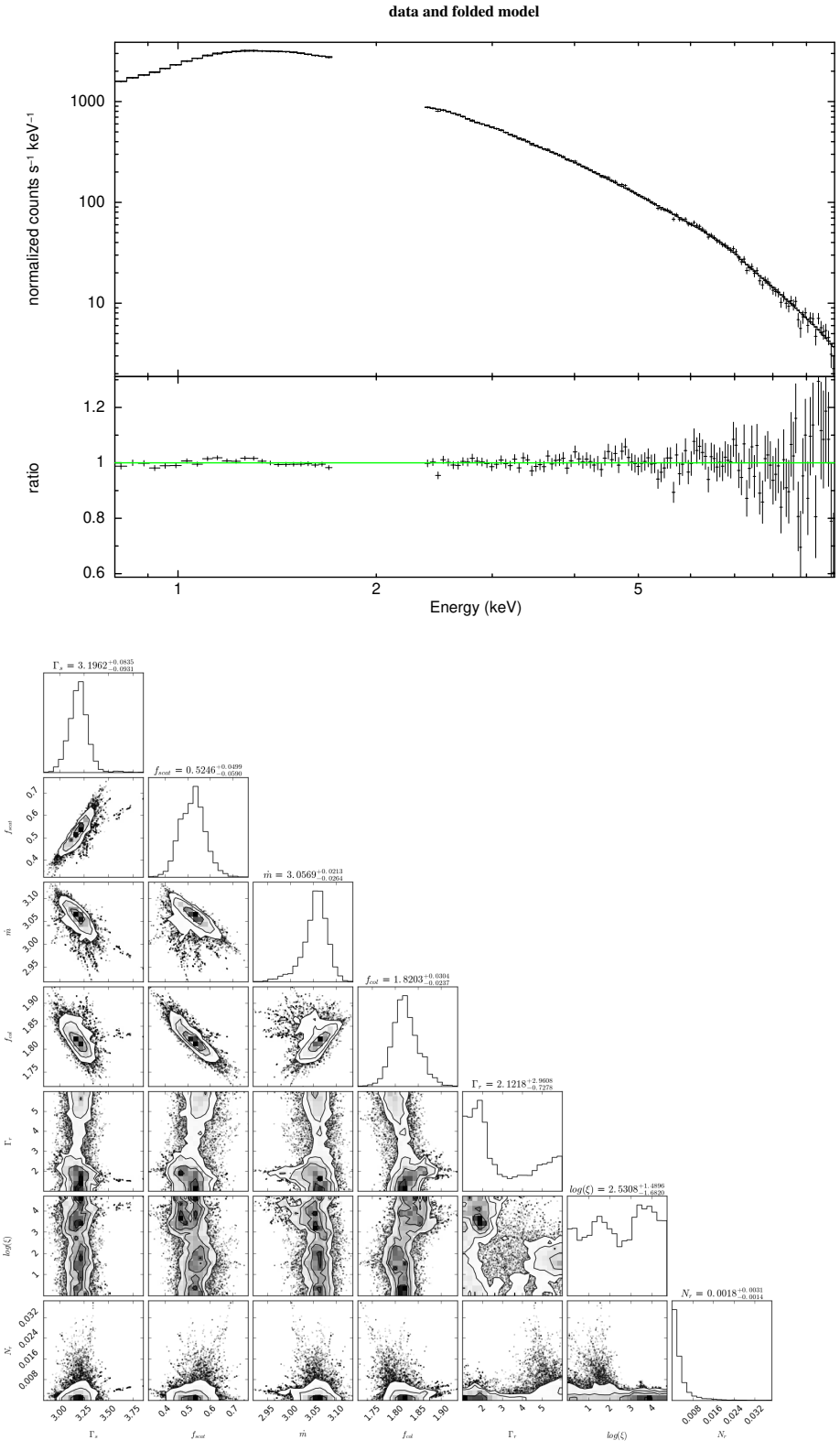

Figure B.4: XMM-Newton pn spectrum of the source GX 339-4 (rev1325). (Soft state)

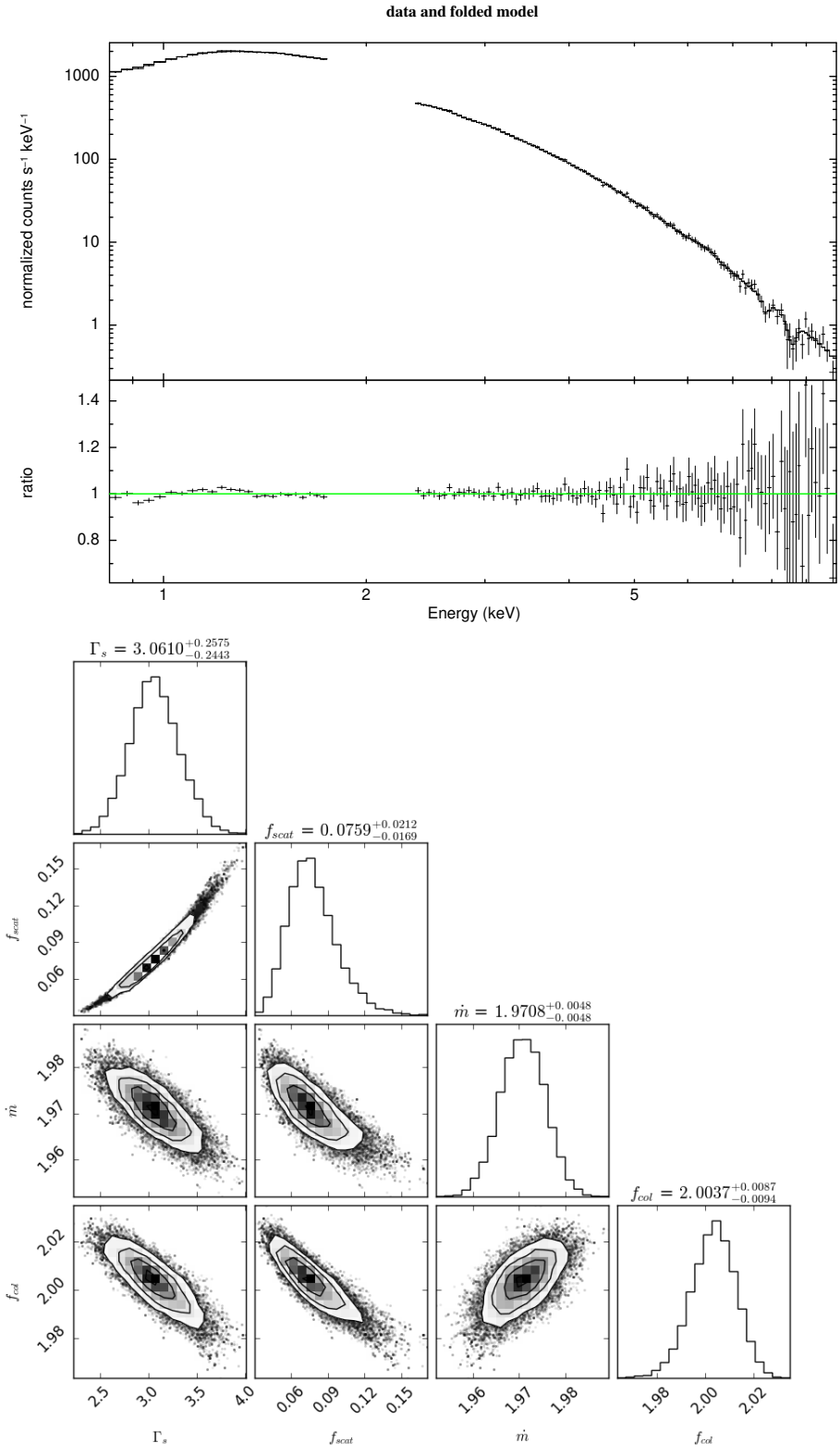

Figure B.5: XMM-Newton pn spectrum of the source GX 339-4 (rev1338). (Soft state)

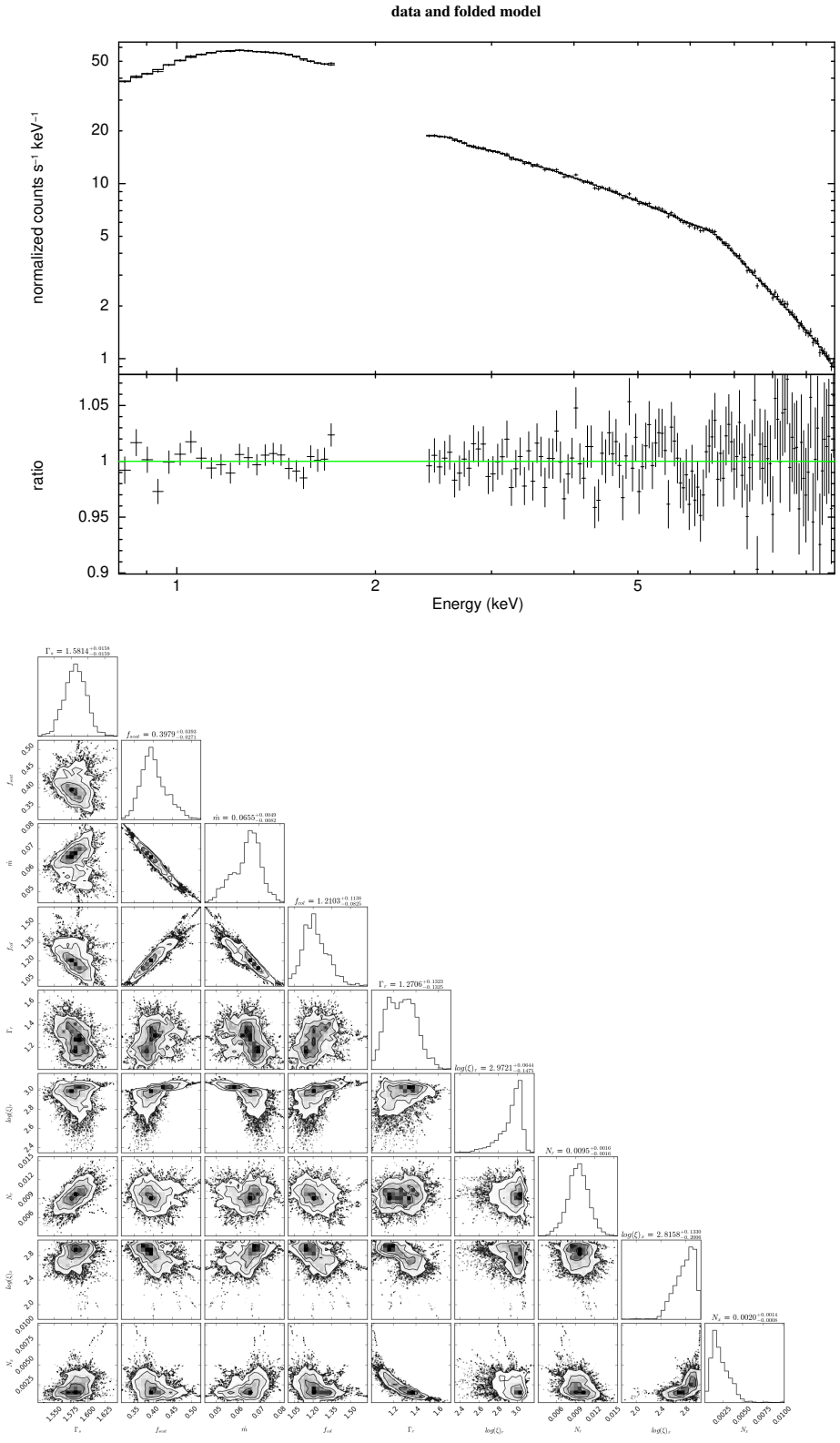

Figure B.6: XMM-Newton pn spectrum of the source GX 339-4 (rev1702). (Hard state)

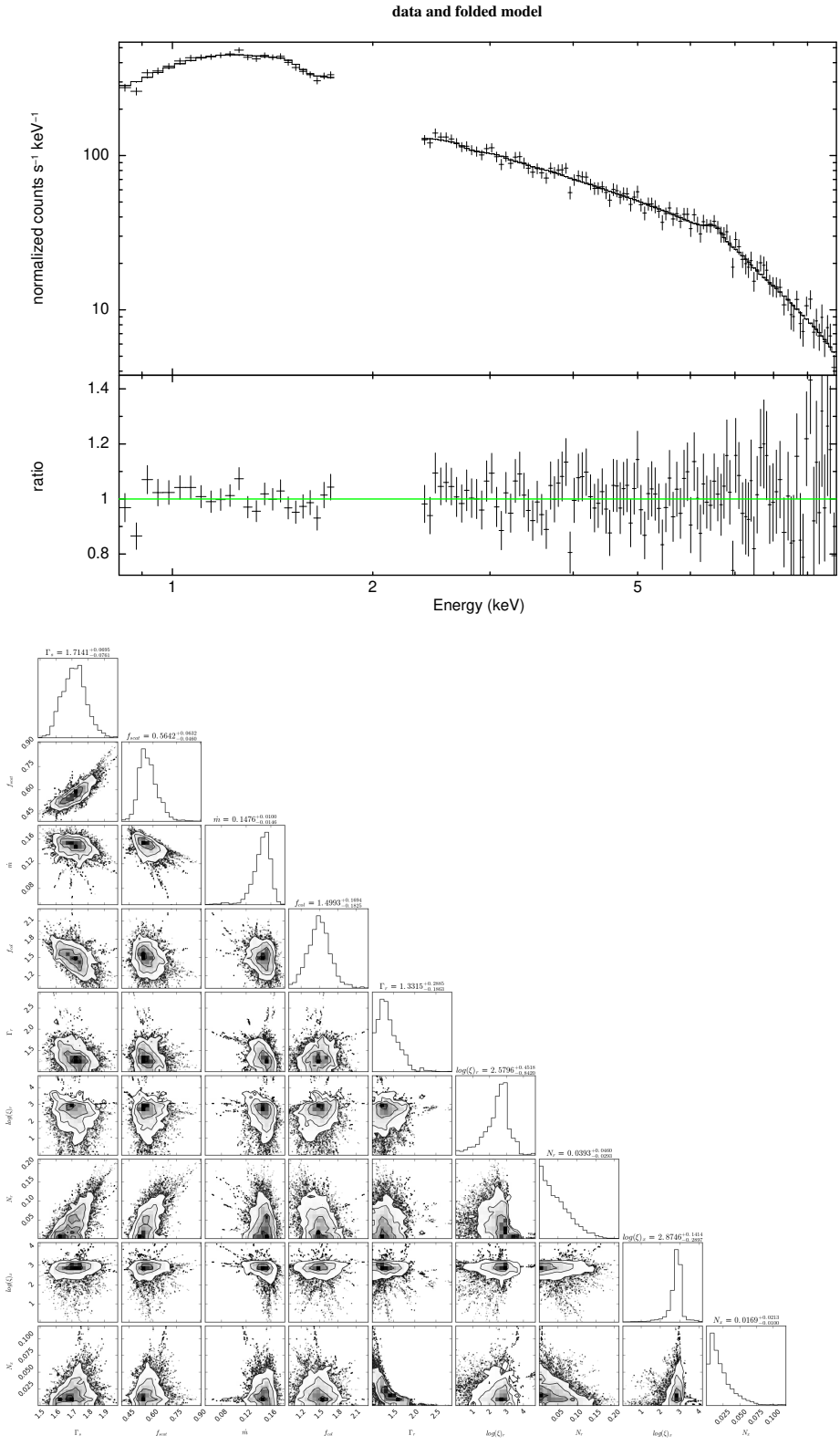

Figure B.7: XMM-Newton pn spectrum of the source GX 339-4 (rev1886). (Hard state)

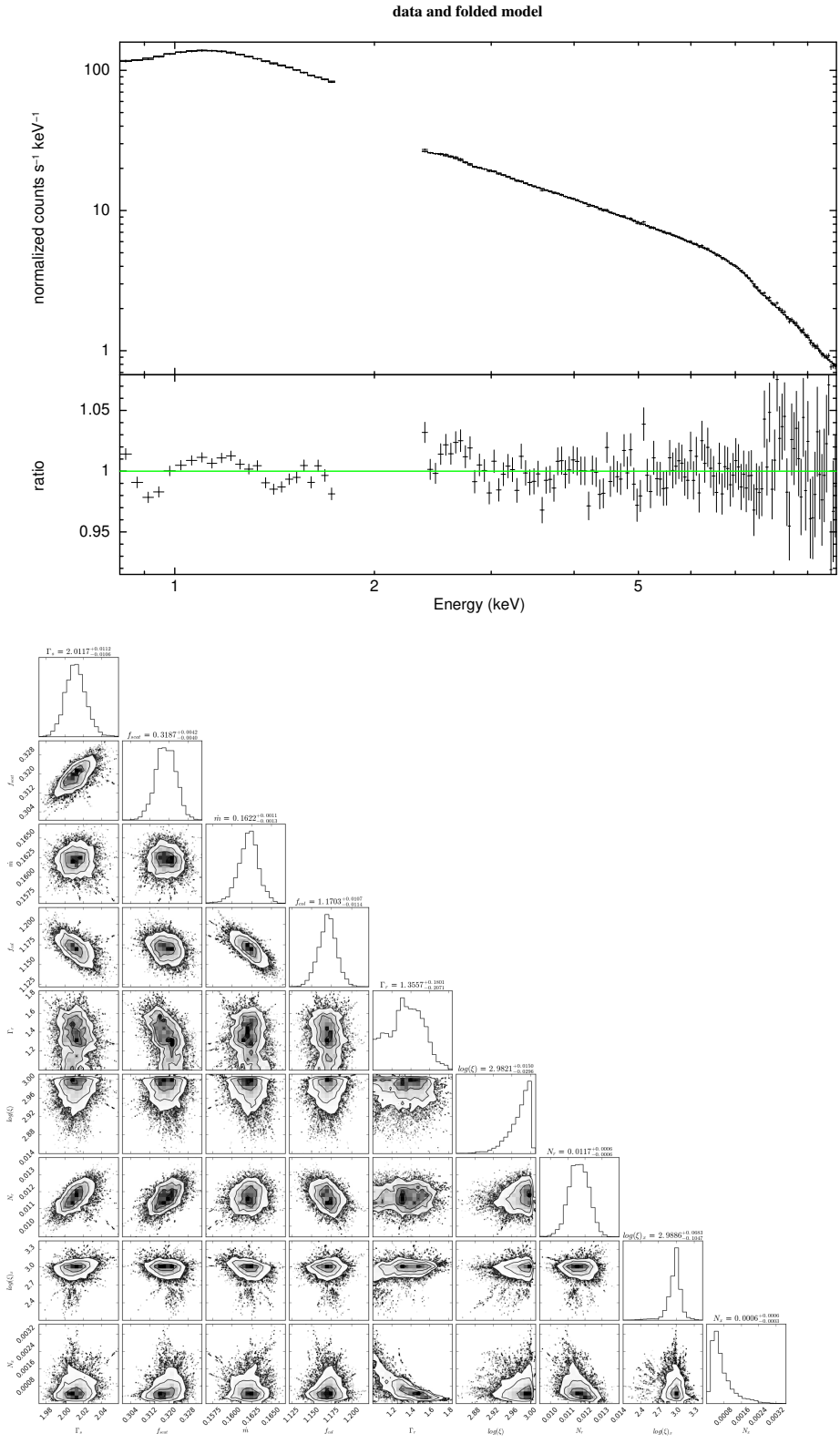

Figure B.8: XMM-Newton pn spectrum of the source GX 339-4 (rev2879) and residuals. (Hard state)

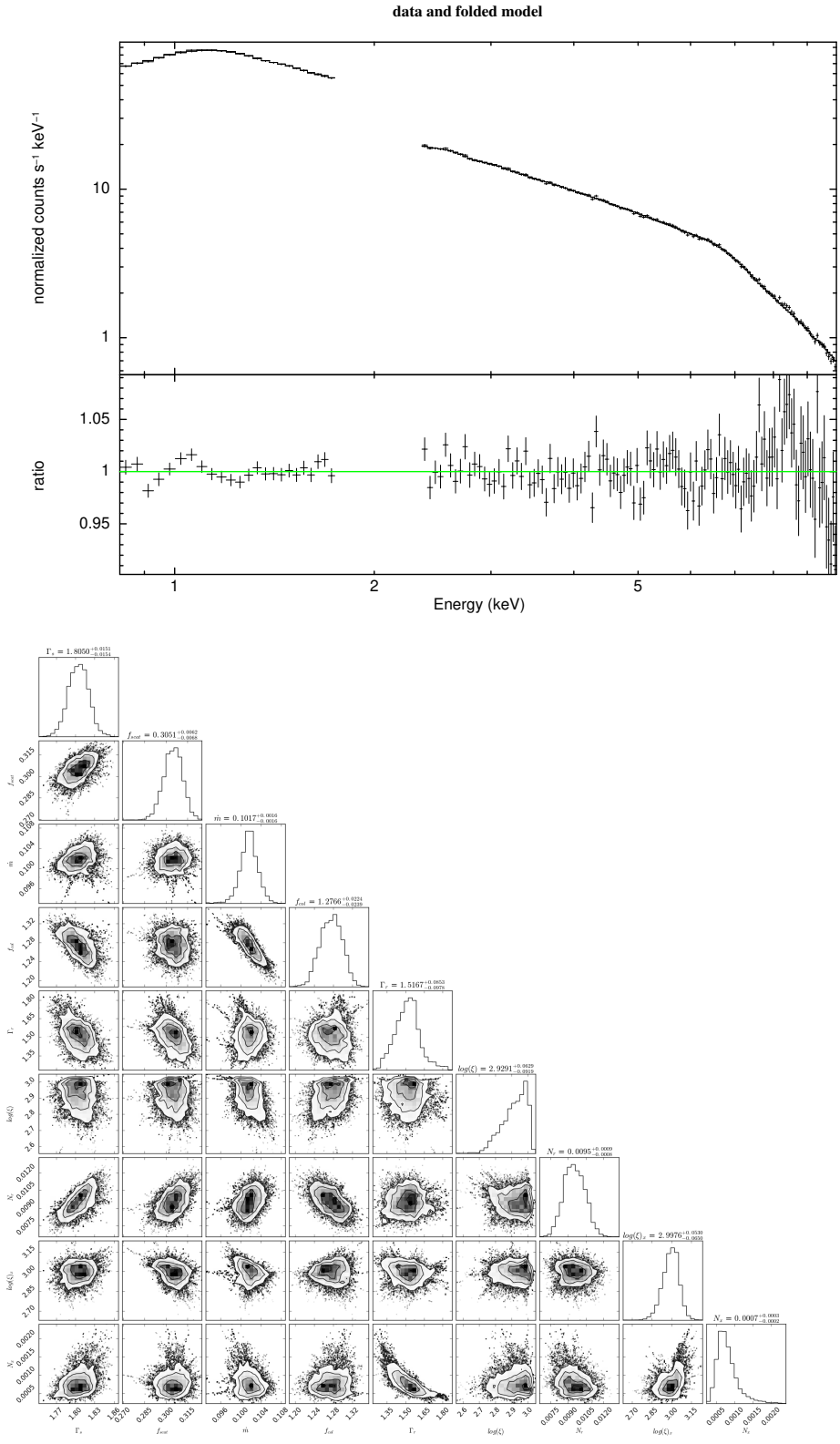

Figure B.9: XMM-Newton pn spectrum of the source GX 339-4 (rev2881) and residuals. (Hard state)

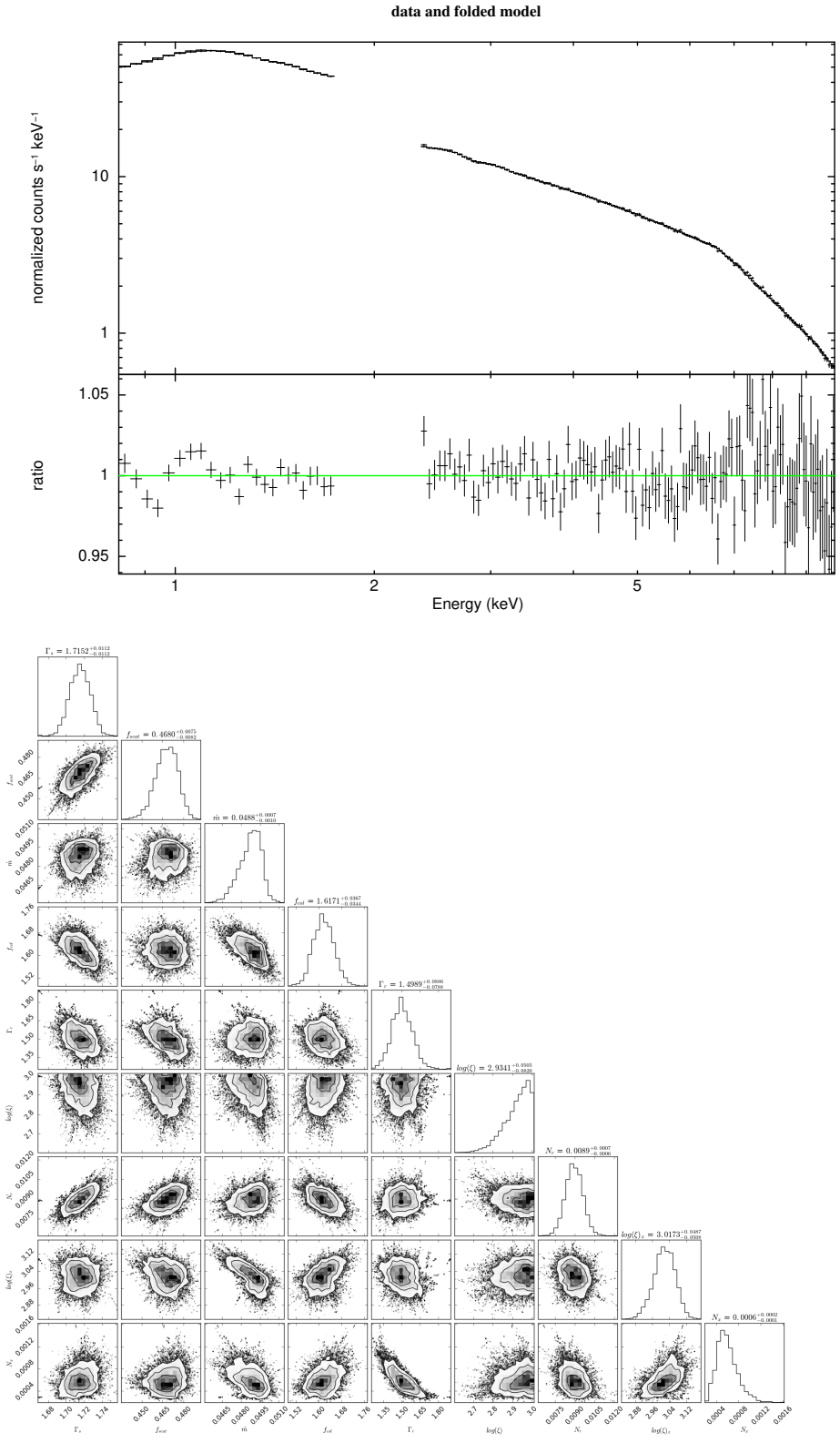

Figure B.10: XMM-Newton pn spectrum of the source GX 339-4 (rev2884) and residuals. (Hard state)

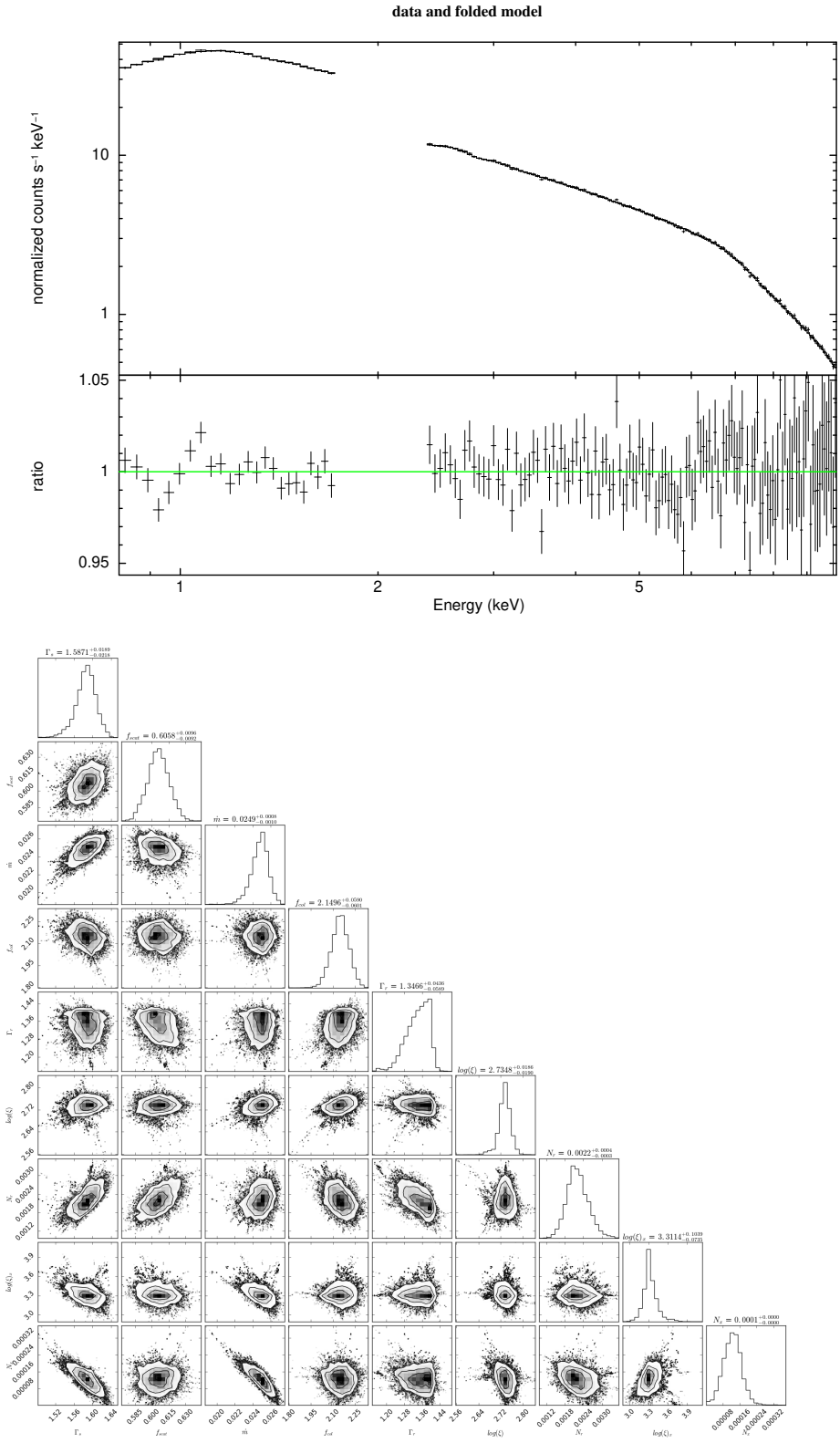

Figure B.11: XMM-Newton pn spectrum of the source GX 339-4 (rev2886) and residuals. (Hard state)

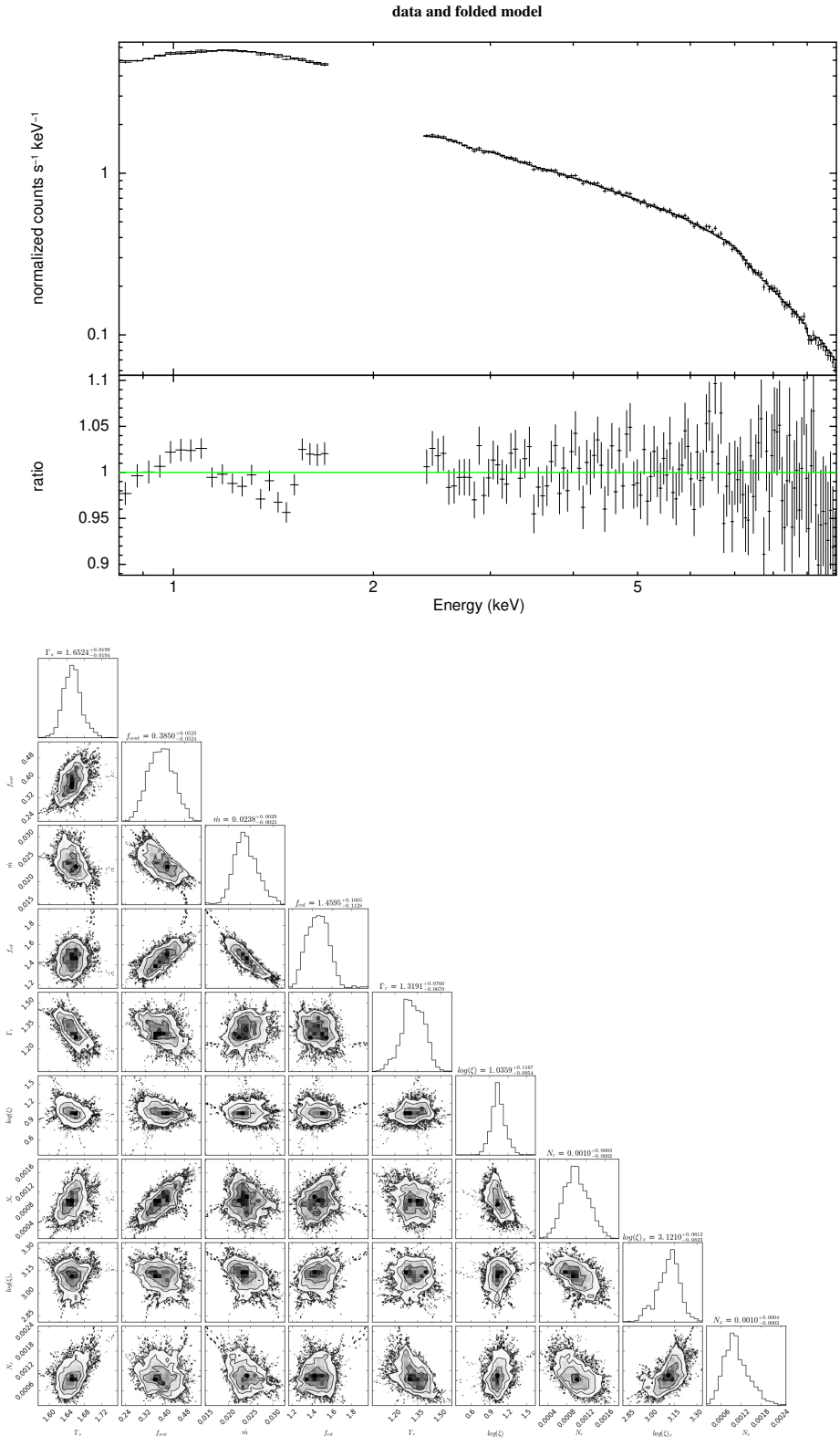

Figure B.12: XMM-Newton pn spectrum of the source GX 339-4 (rev2889) and residuals. (Hard state)

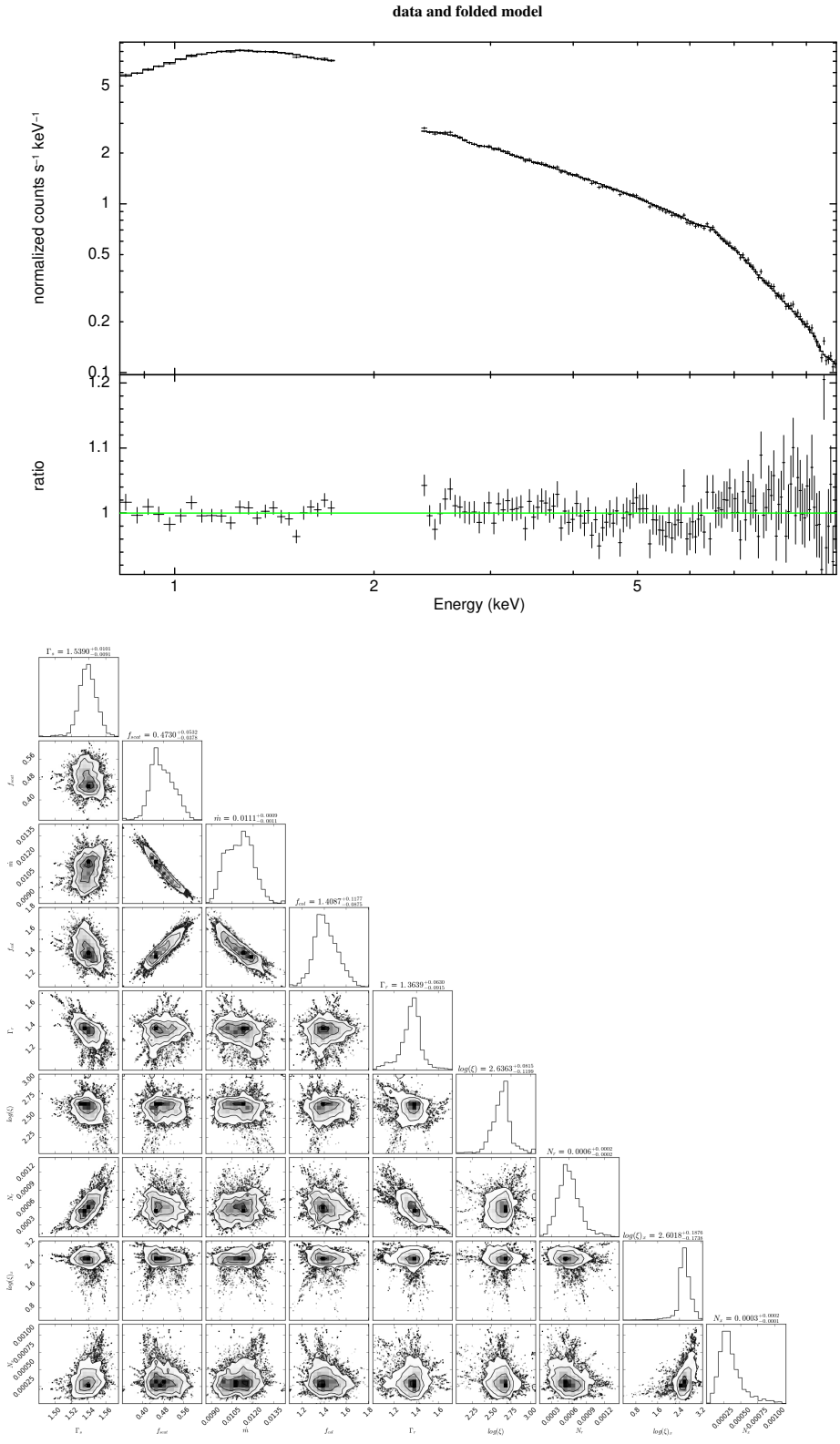

Figure B.13: XMM-Newton pn spectrum of the source GX 339-4 (rev2895) and residuals. (Hard state)

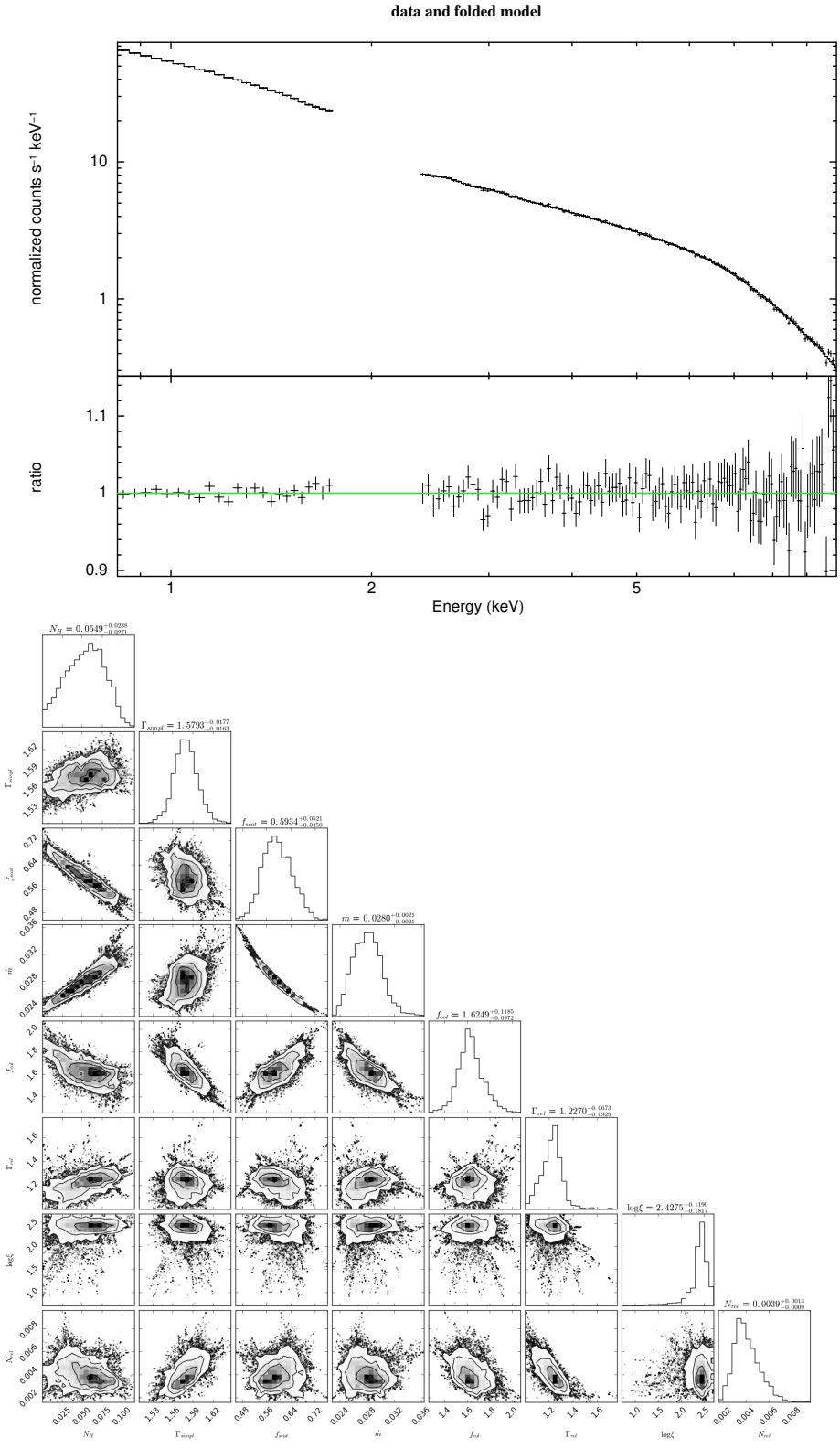

Figure B.14: XMM-Newton pn spectrum of the source Swift J1357.2-0933 (rev2044) and the residuals. (Hard state)

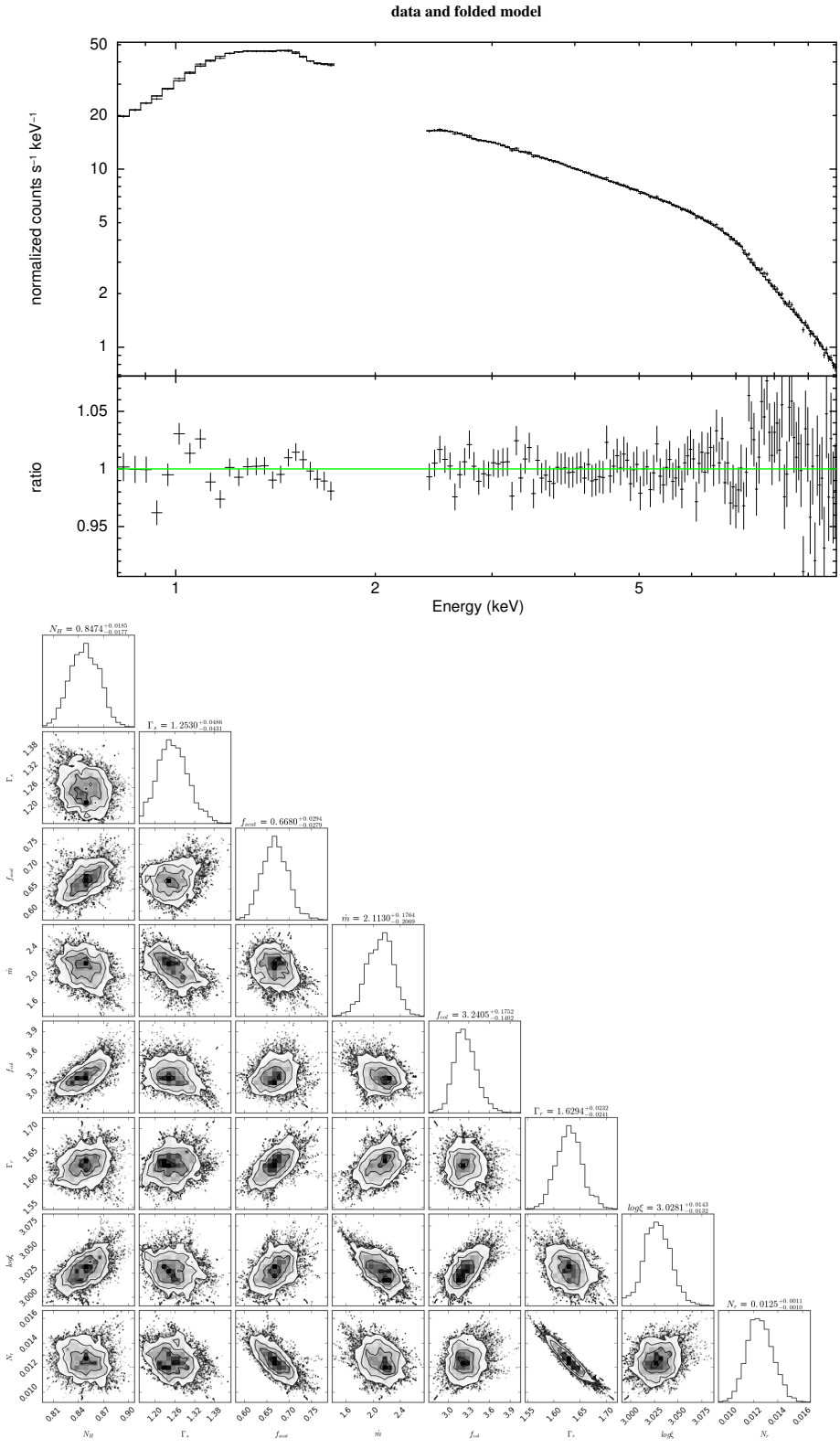

Figure B.15: XMM-Newton pn spectrum of the source GS 1354-64 and the residuals. (Hard state)

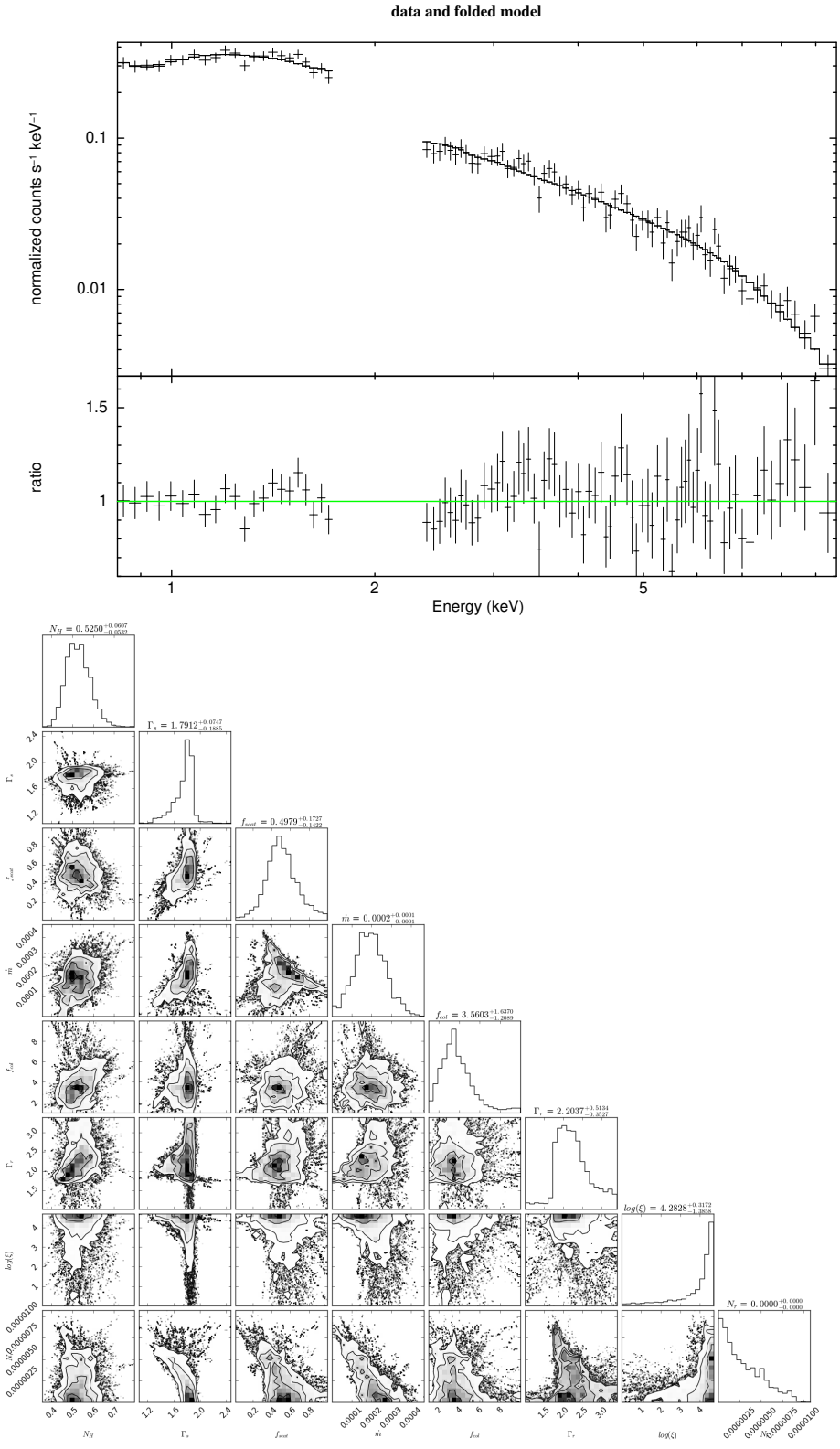

Figure B.16: XMM-Newton pn spectrum of the source 4U 1543-475 and the residuals. (Hard state)

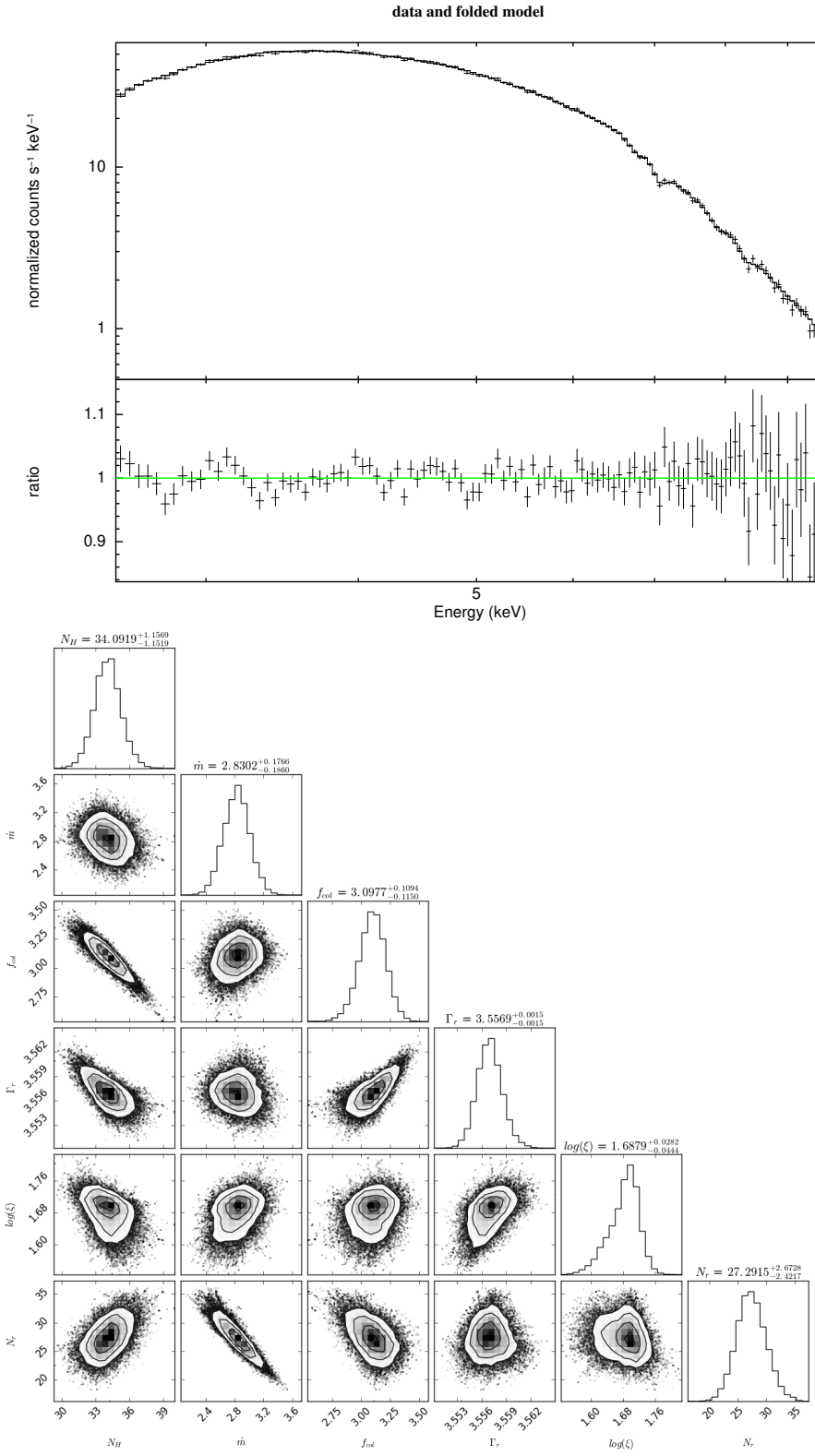

Figure B.17: XMM-Newton pn spectrum of the source 4U 1630-47 (rev2241) and the residuals. (Soft state)

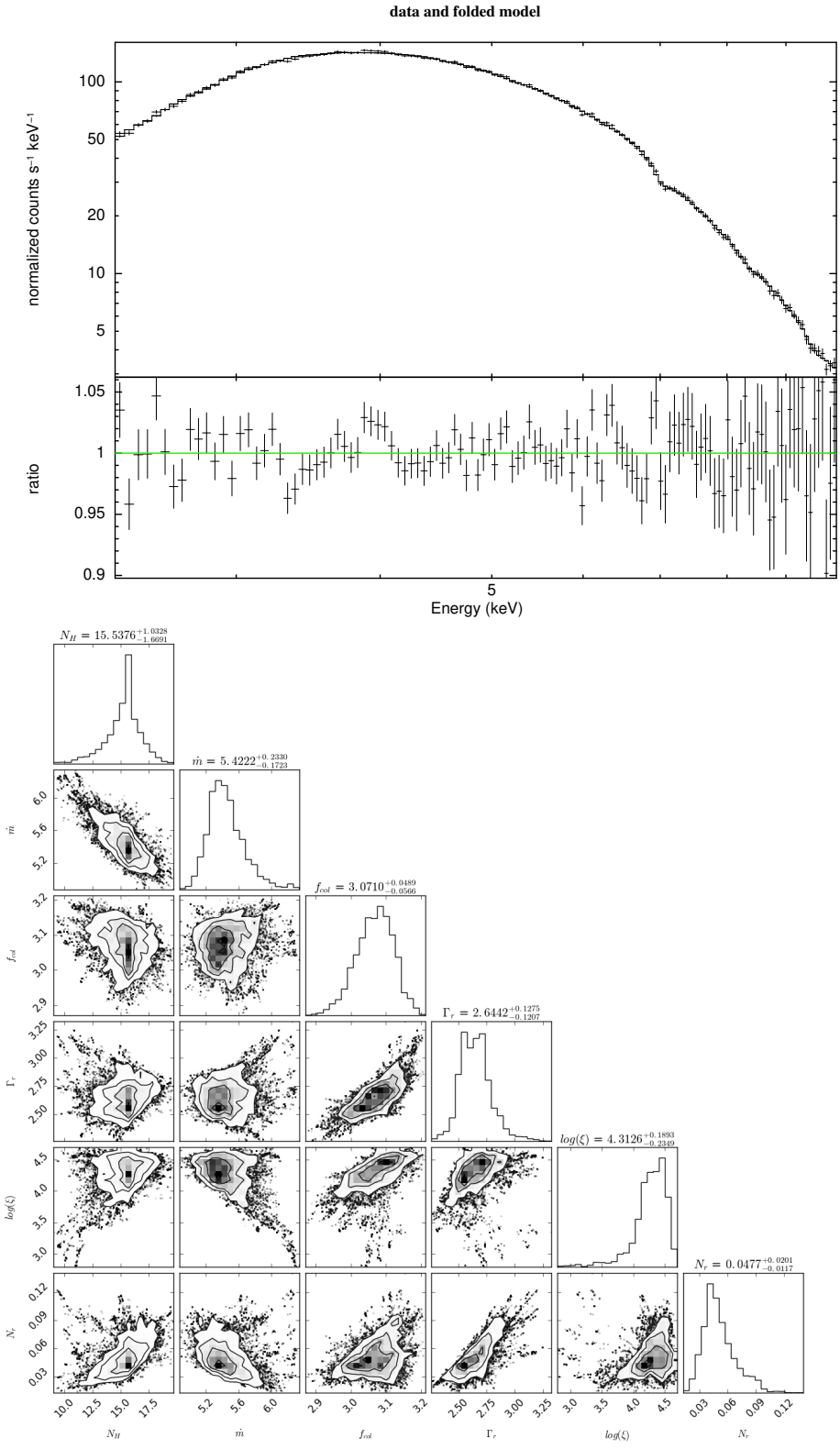

Figure B.18: XMM-Newton pn spectrum of the source 4U 1630-47 (rev2249) and the residuals. (Soft state)

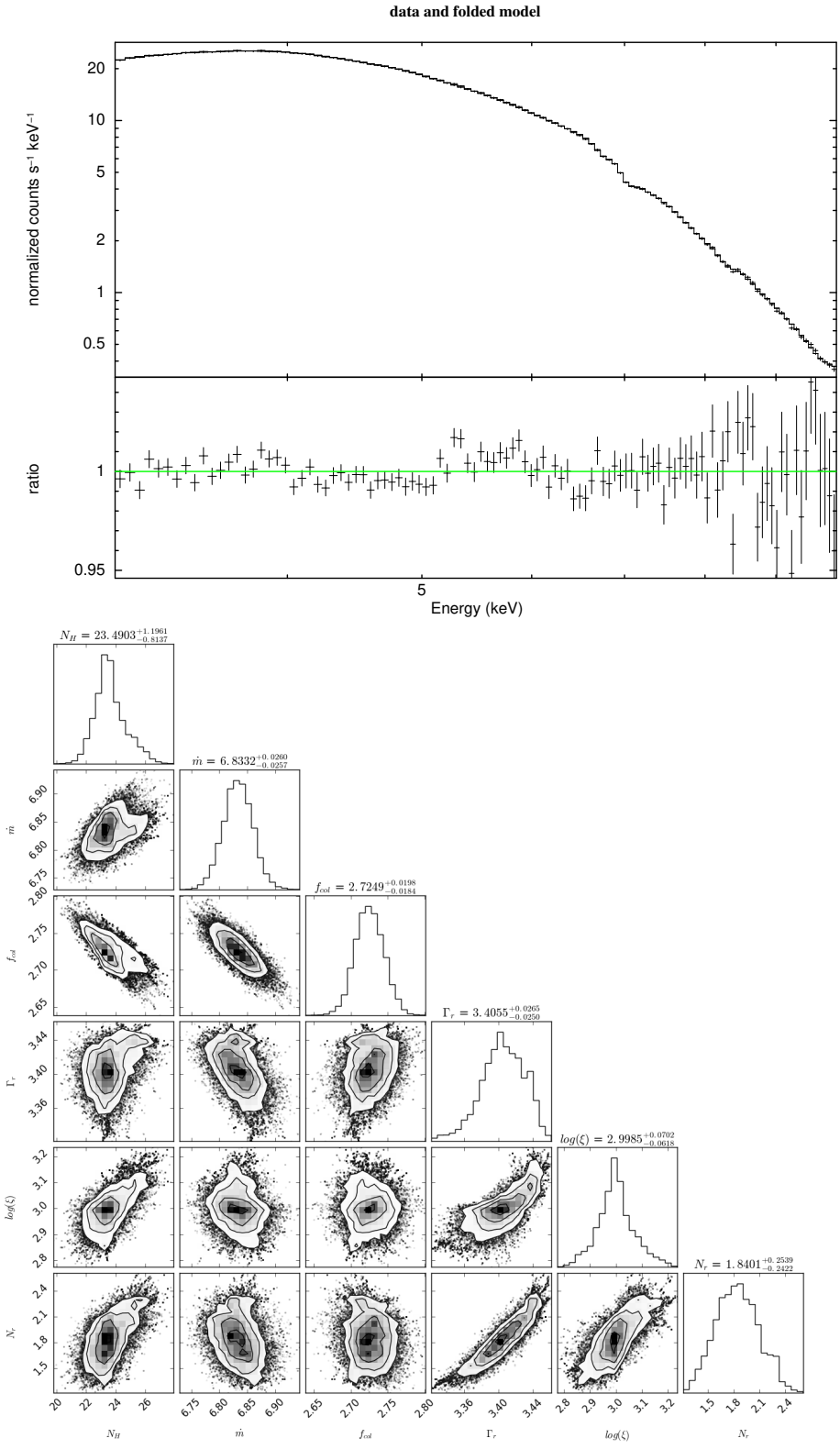

Figure B.19: XMM-Newton pn spectrum of the source 4U 1630-47 (rev2251) and the residuals. (Soft state)

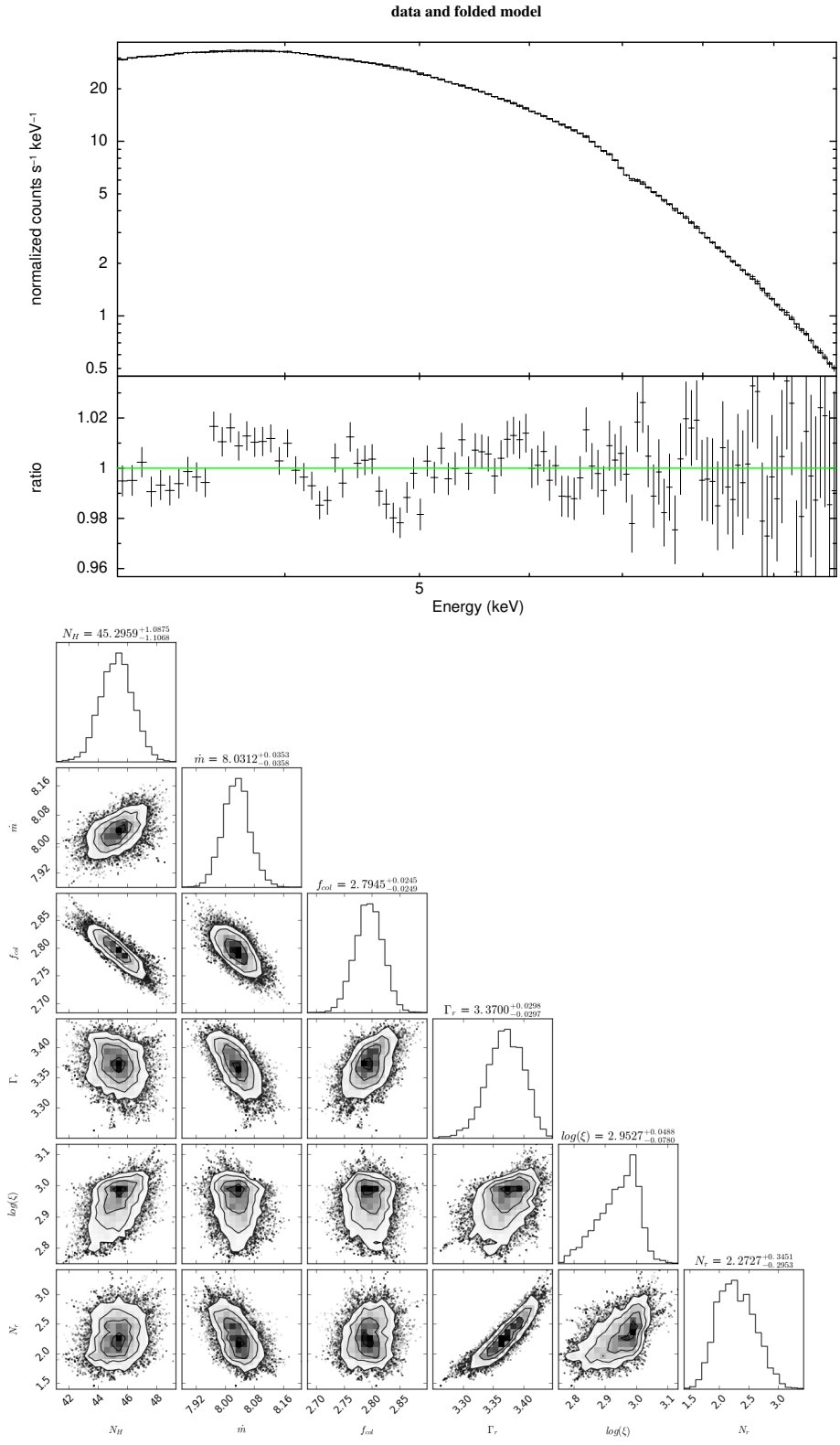

Figure B.20: XMM-Newton pn spectrum of the source 4U 1630-47 (rev2336) and the residuals. (Soft state)

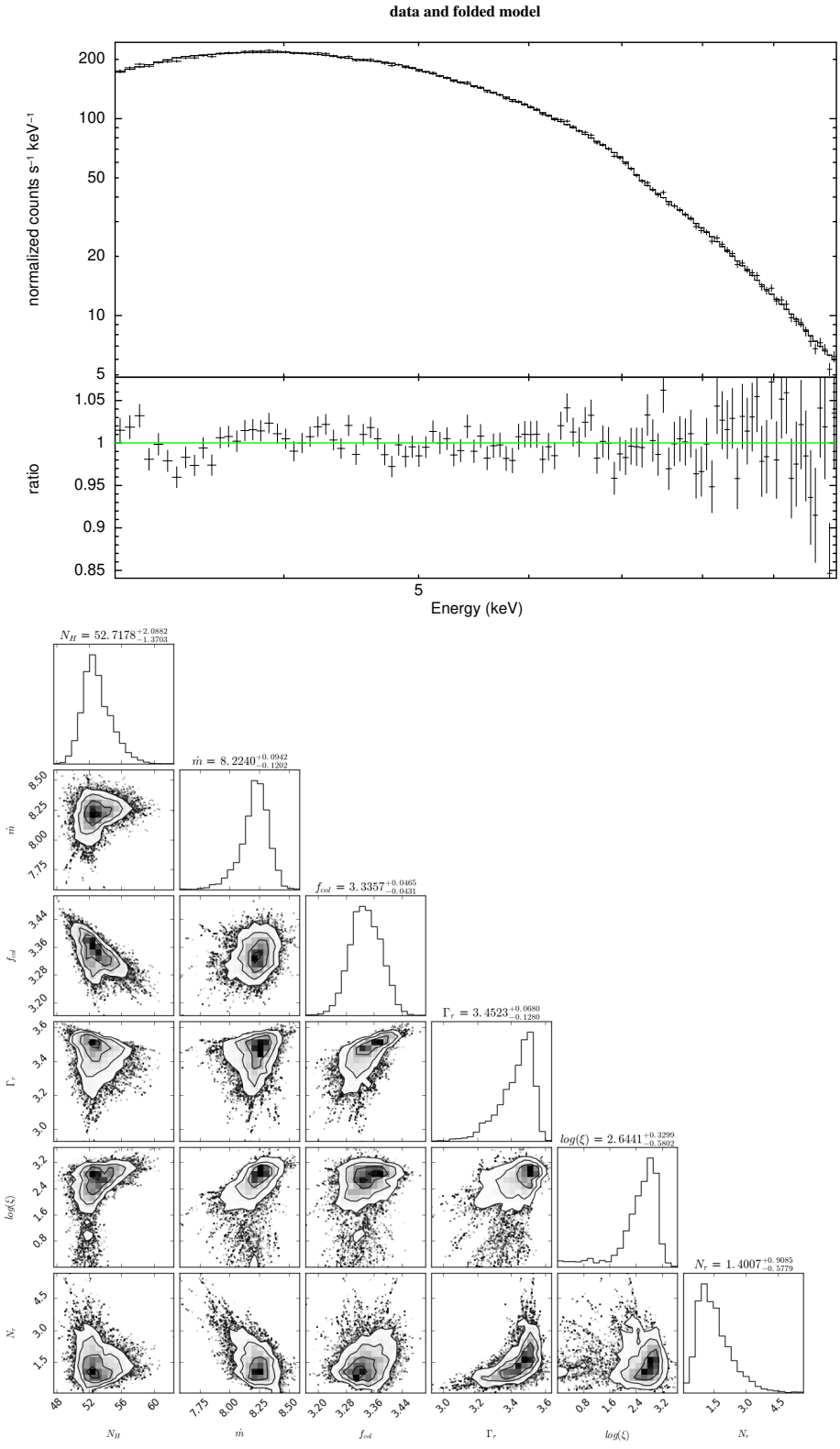

Figure B.21: XMM-Newton pn spectrum of the source 4U 1630-47 (rev2337) and the residuals. (Soft state)

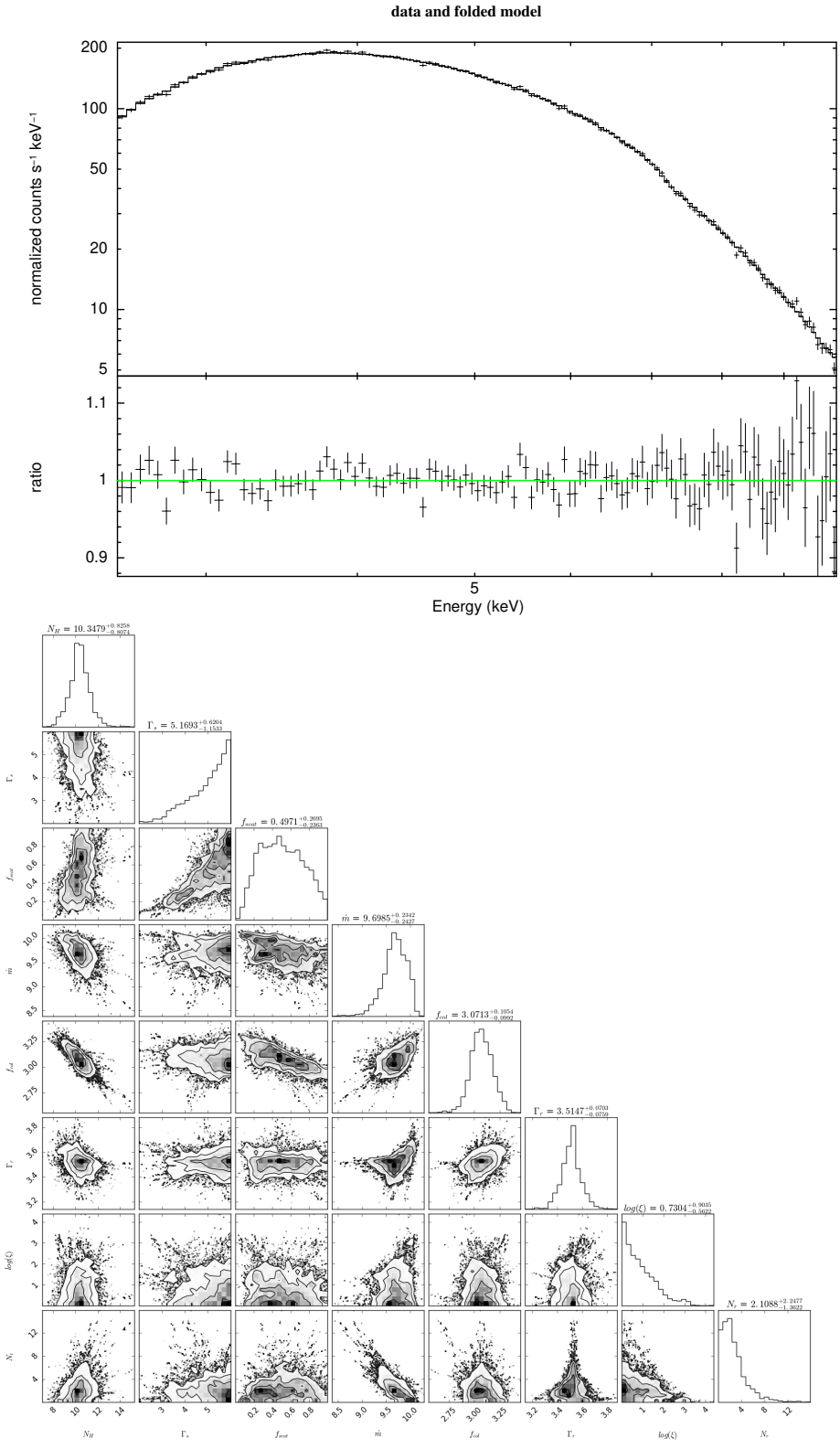

Figure B.22: XMM-Newton pn spectrum of the source 4U 1630-47 (rev2345) and the residuals. (Soft state)

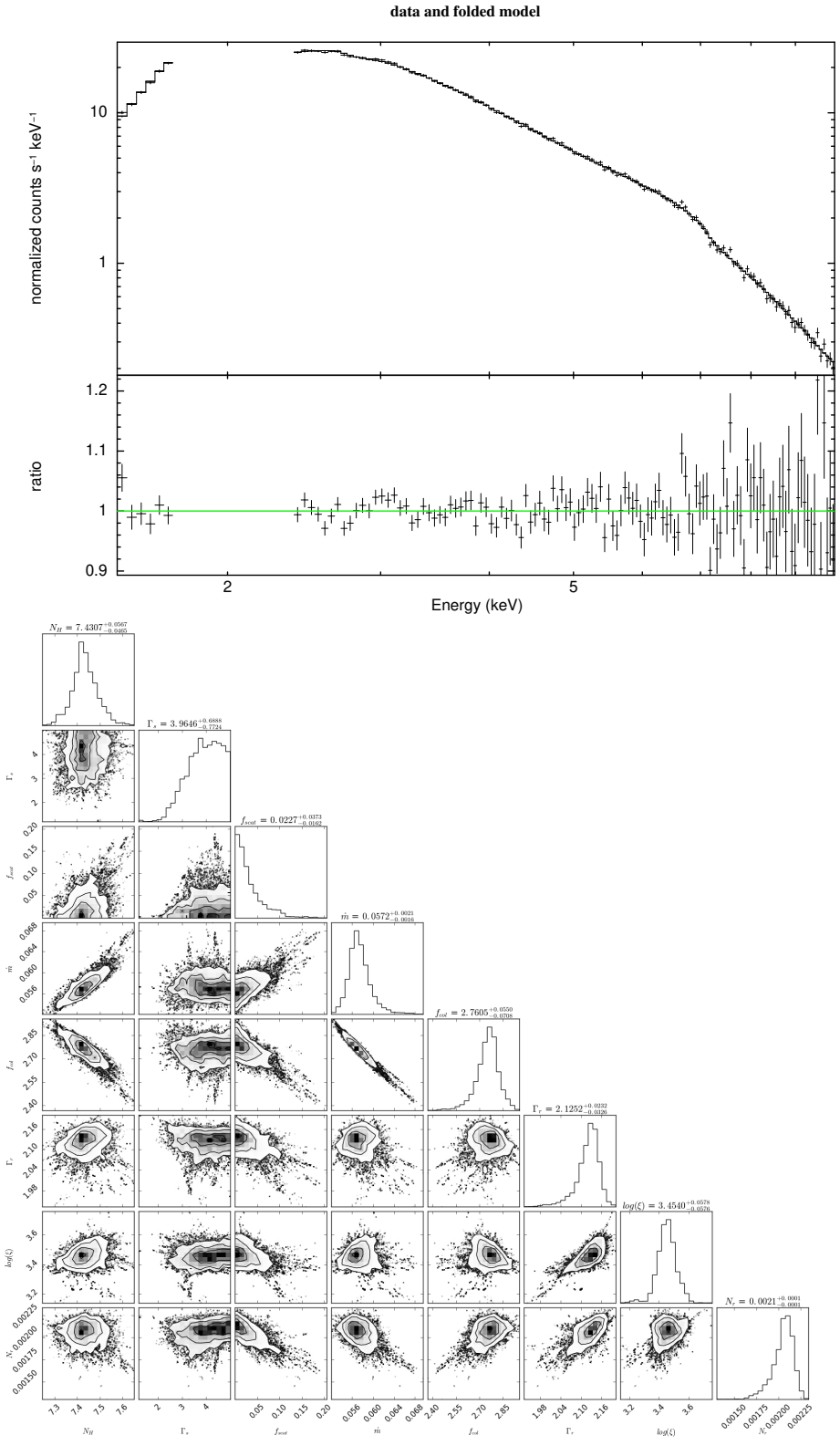

Figure B.23: XMM-Newton pn spectrum of the source XTE J1652-453 and the residuals. (Intermediate state)

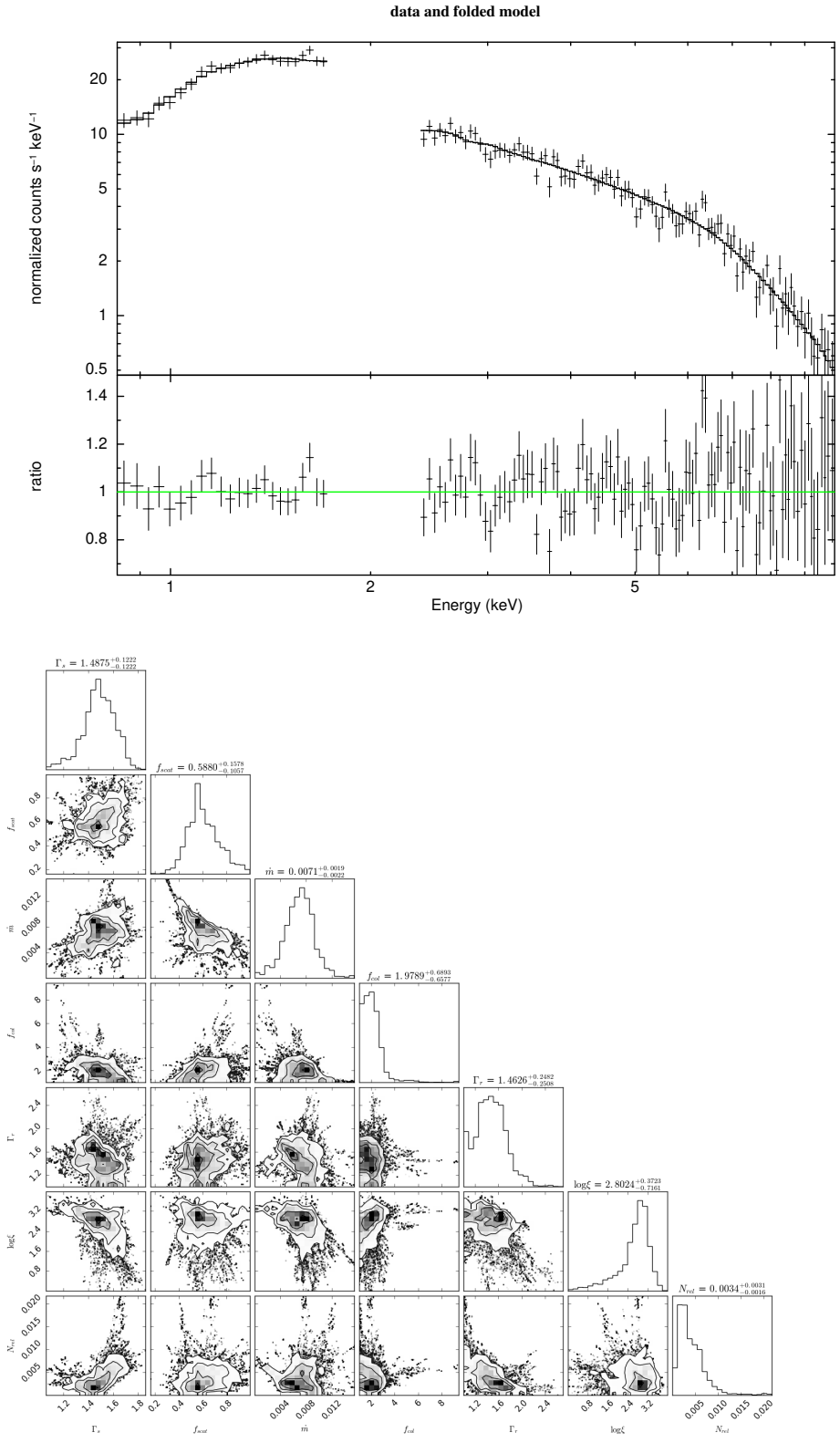

Figure B.24: XMM-Newton pn spectrum of the source GRO J1655-40 (rev956) and the residuals. (Hard state)

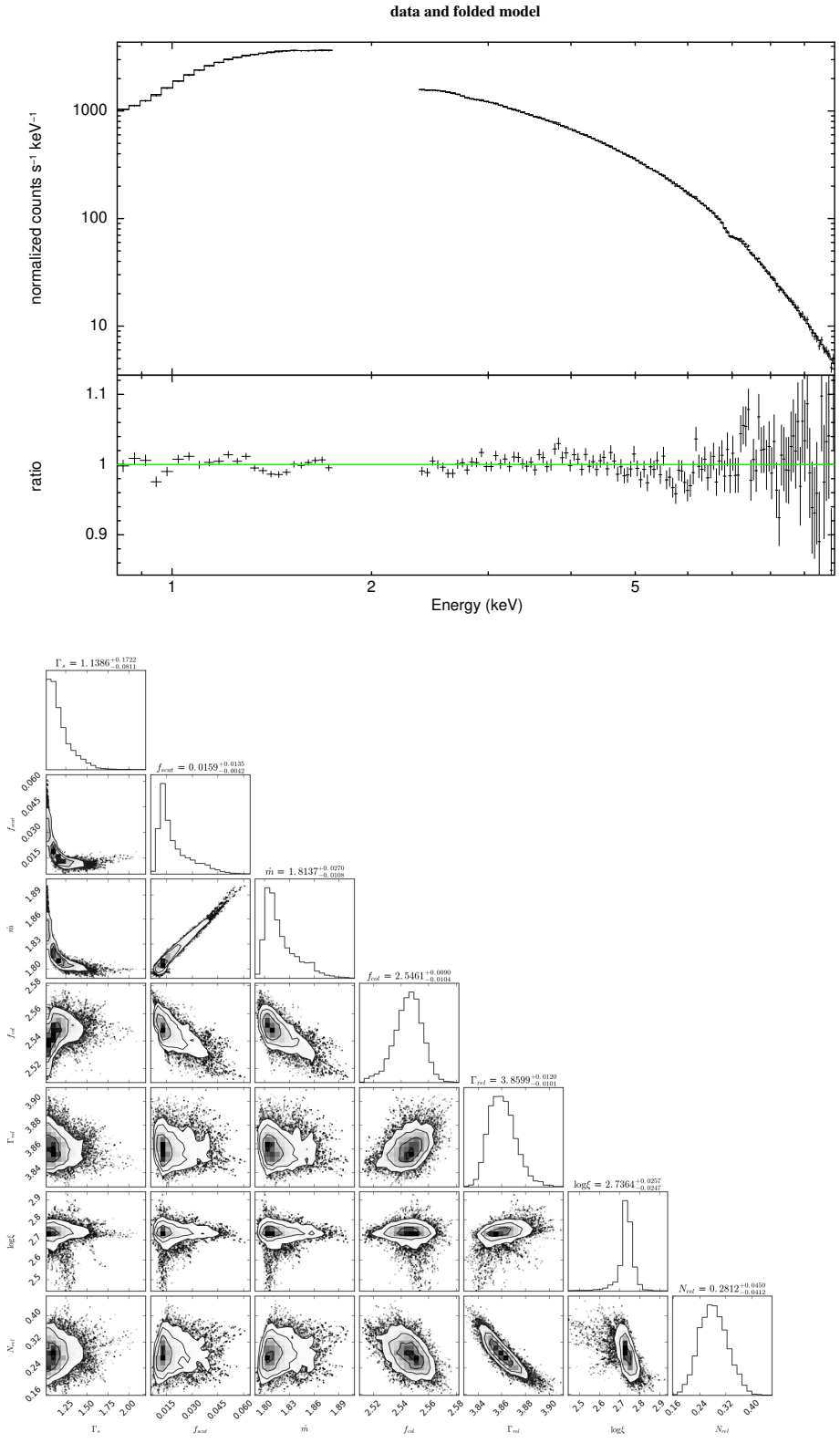

Figure B.25: XMM-Newton pn spectrum of the source GRO J1655-40 (rev964a) and the residuals along with the MCMC analysis output

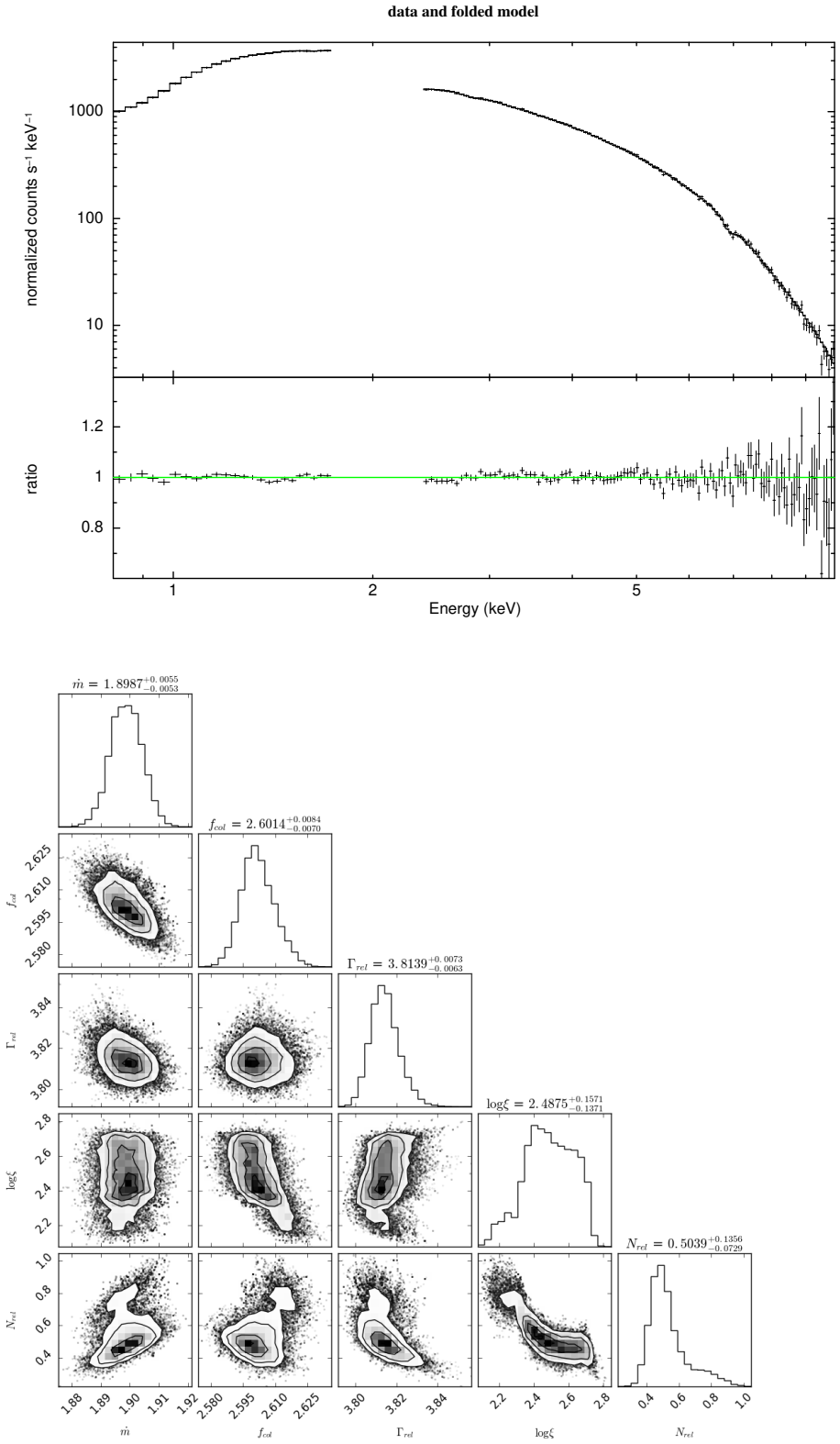

Figure B.26: XMM-Newton pn spectrum of the source GRO J1655-40 (rev964b) and the residuals. (Soft state)

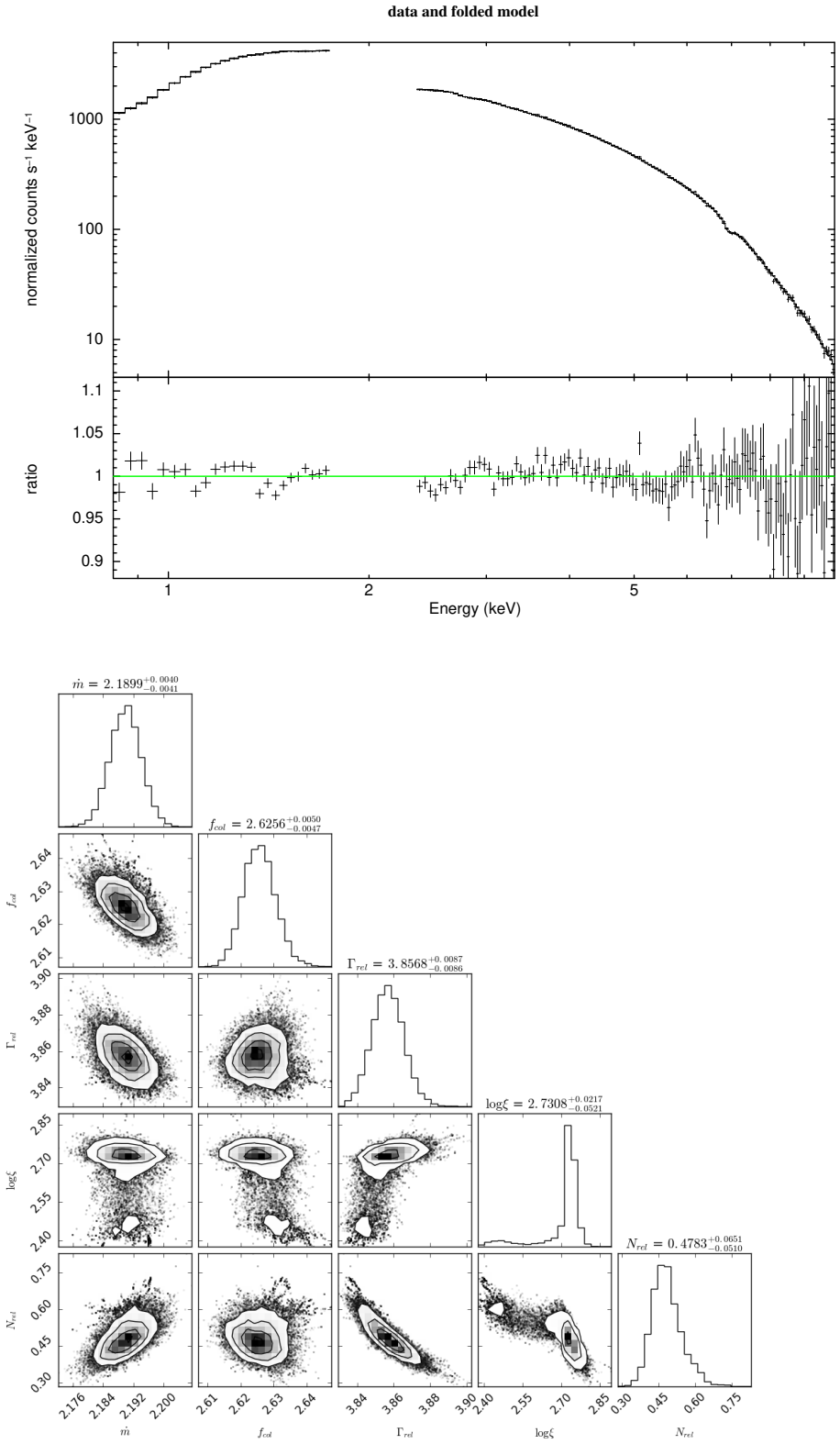

Figure B.27: XMM-Newton pn spectrum of the source GRO J1655-40 (rev965) and the residuals. (Soft state)

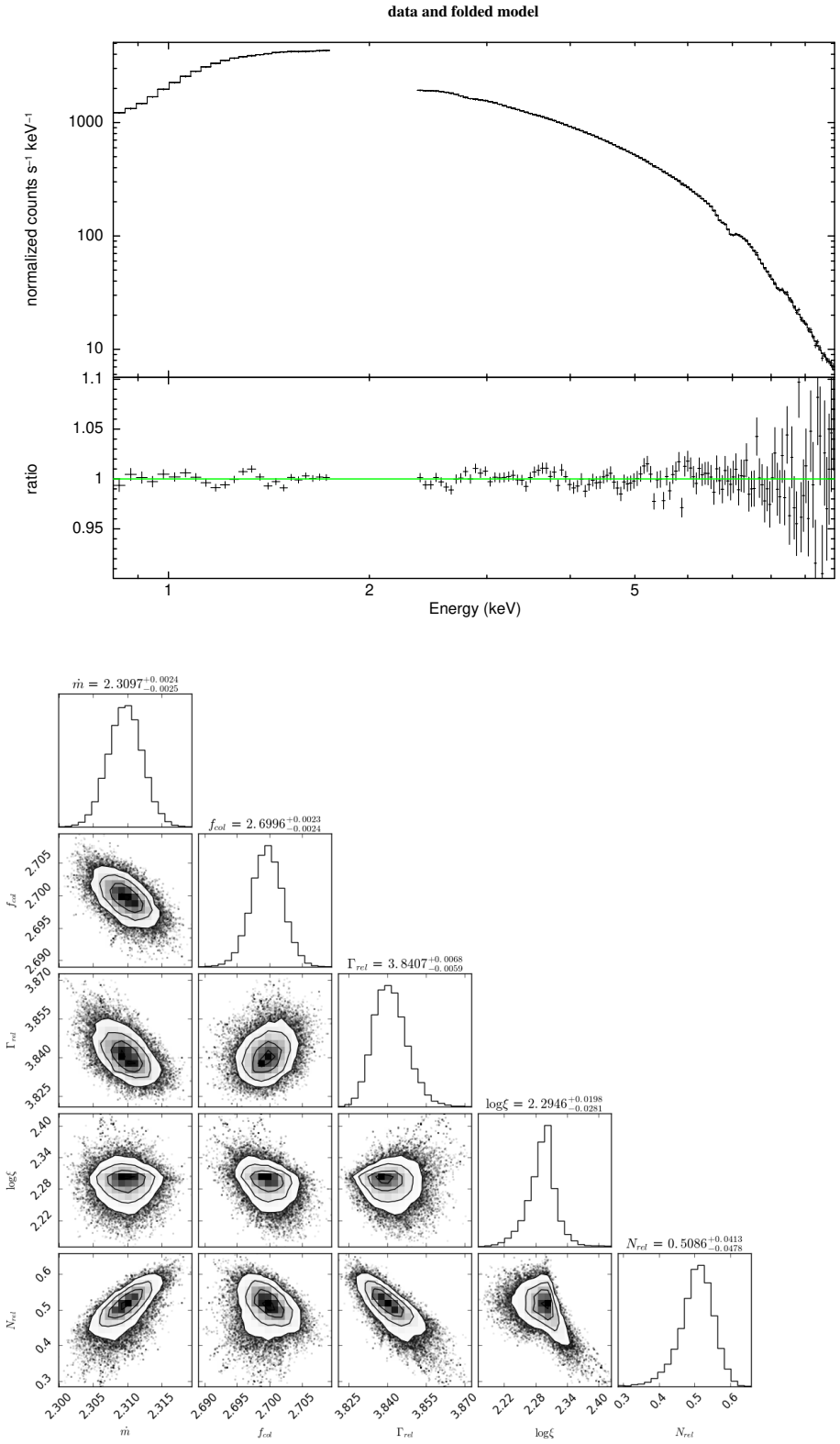

Figure B.28: XMM-Newton pn spectrum of the source GRO J1655-40 (rev966) and the residuals. (Soft state)

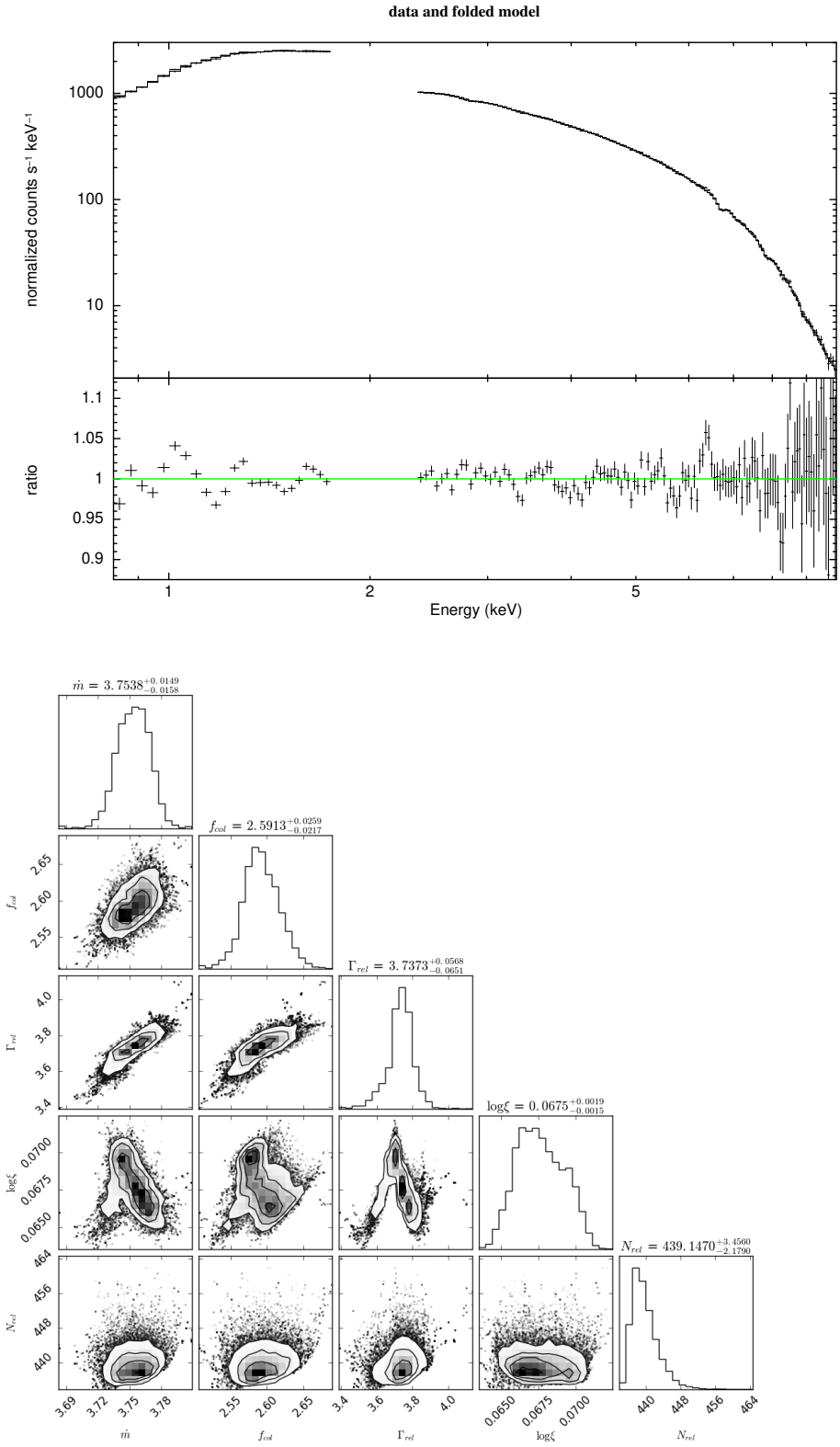

Figure B.29: XMM-Newton pn spectrum of the source GRO J1655-40 (rev970) and the residuals. (Soft state)

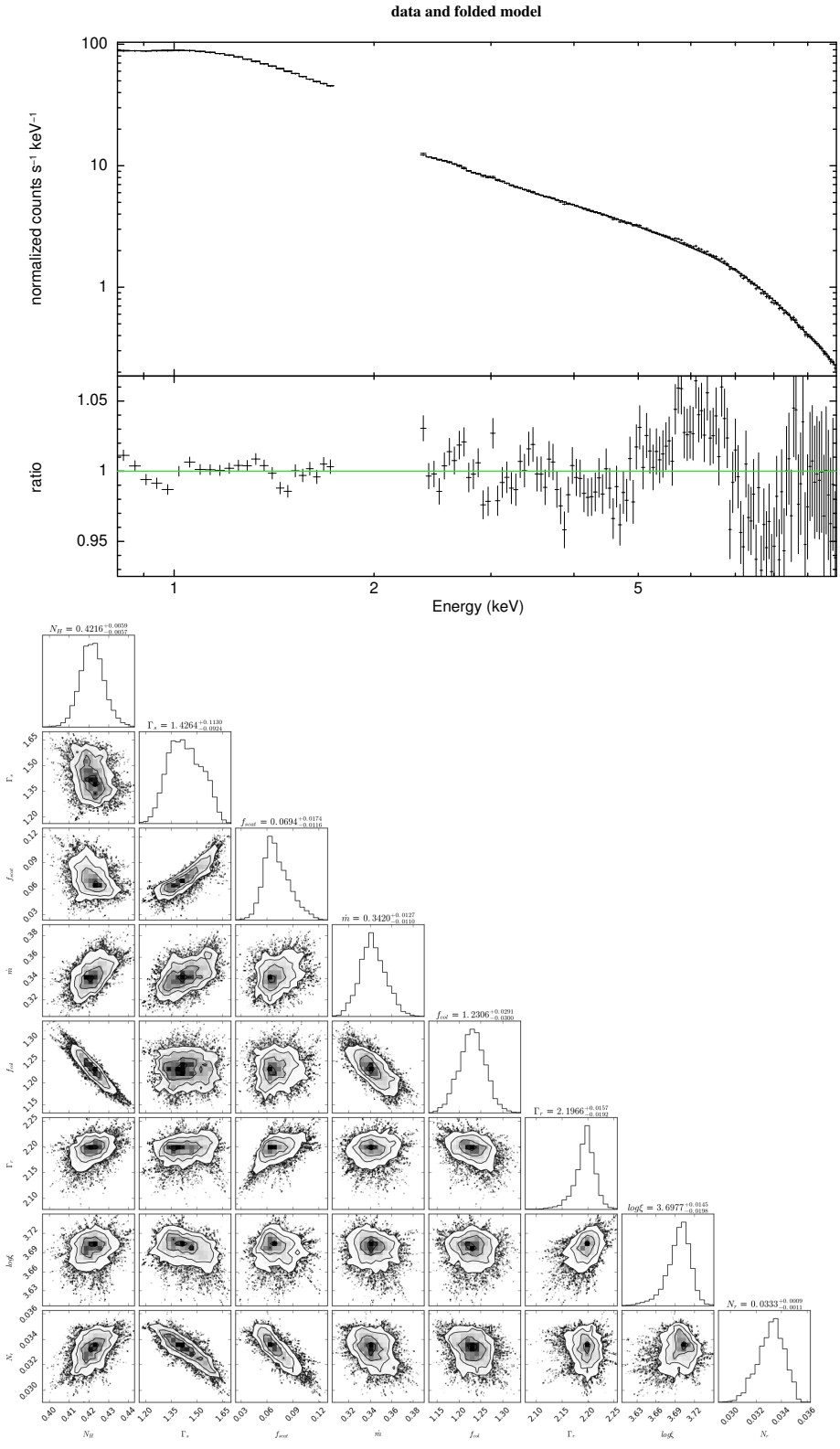

Figure B.30: XMM-Newton pn spectrum of the source MAXI J1659-152 (rev 1978) and the residuals. (Intermediate state)

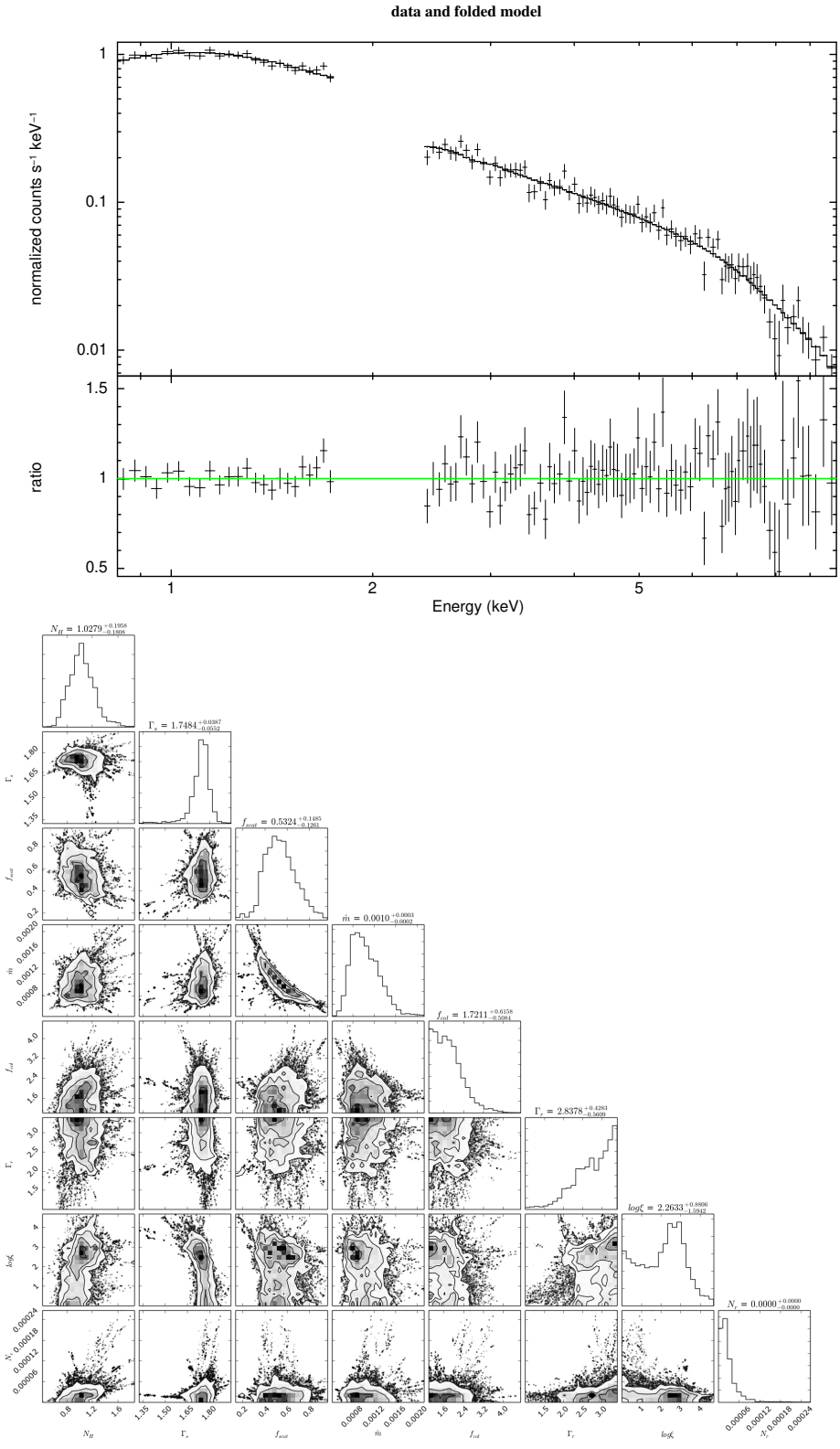

Figure B.31: XMM-Newton pn spectrum of the source MAXI J1659-152 (rev 2066) and the residuals. (Hard state)

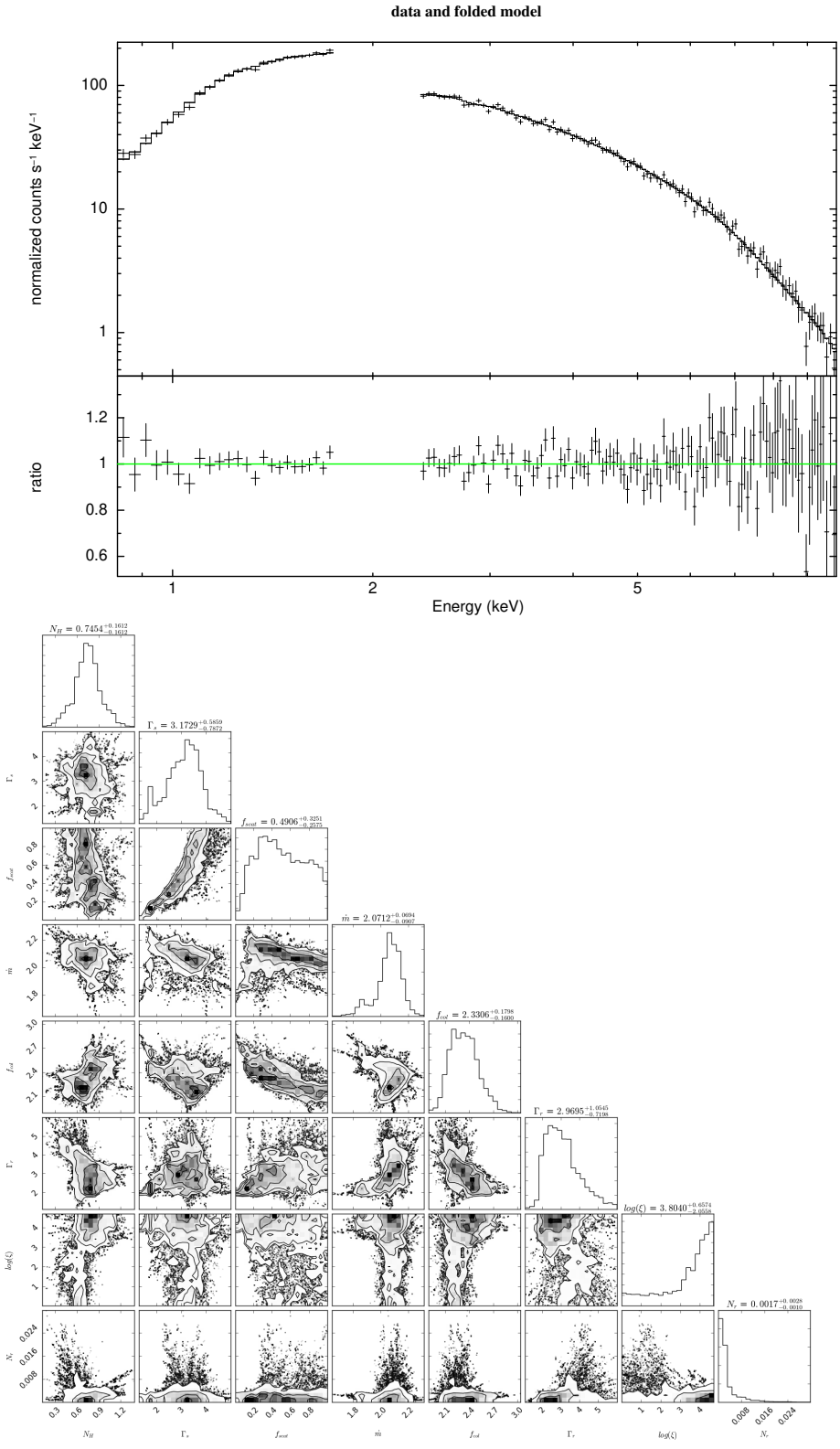

Figure B.32: XMM-Newton pn spectrum of the source IGR J17091-3624 and the residuals. (Soft state)

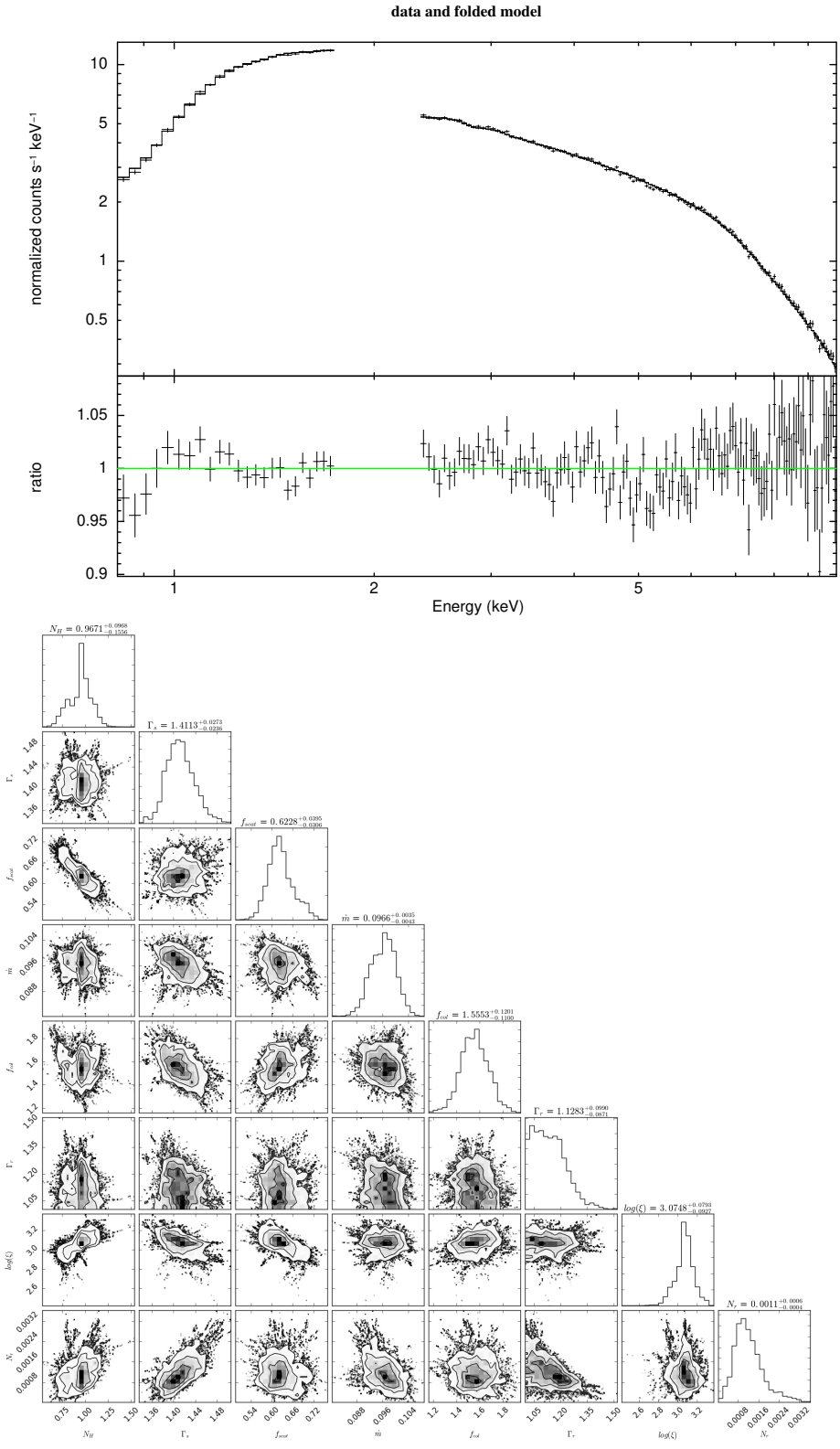

Figure B.33: XMM-Newton pn spectrum of the source IGR J17091-3624 and the residuals. (Hard state)

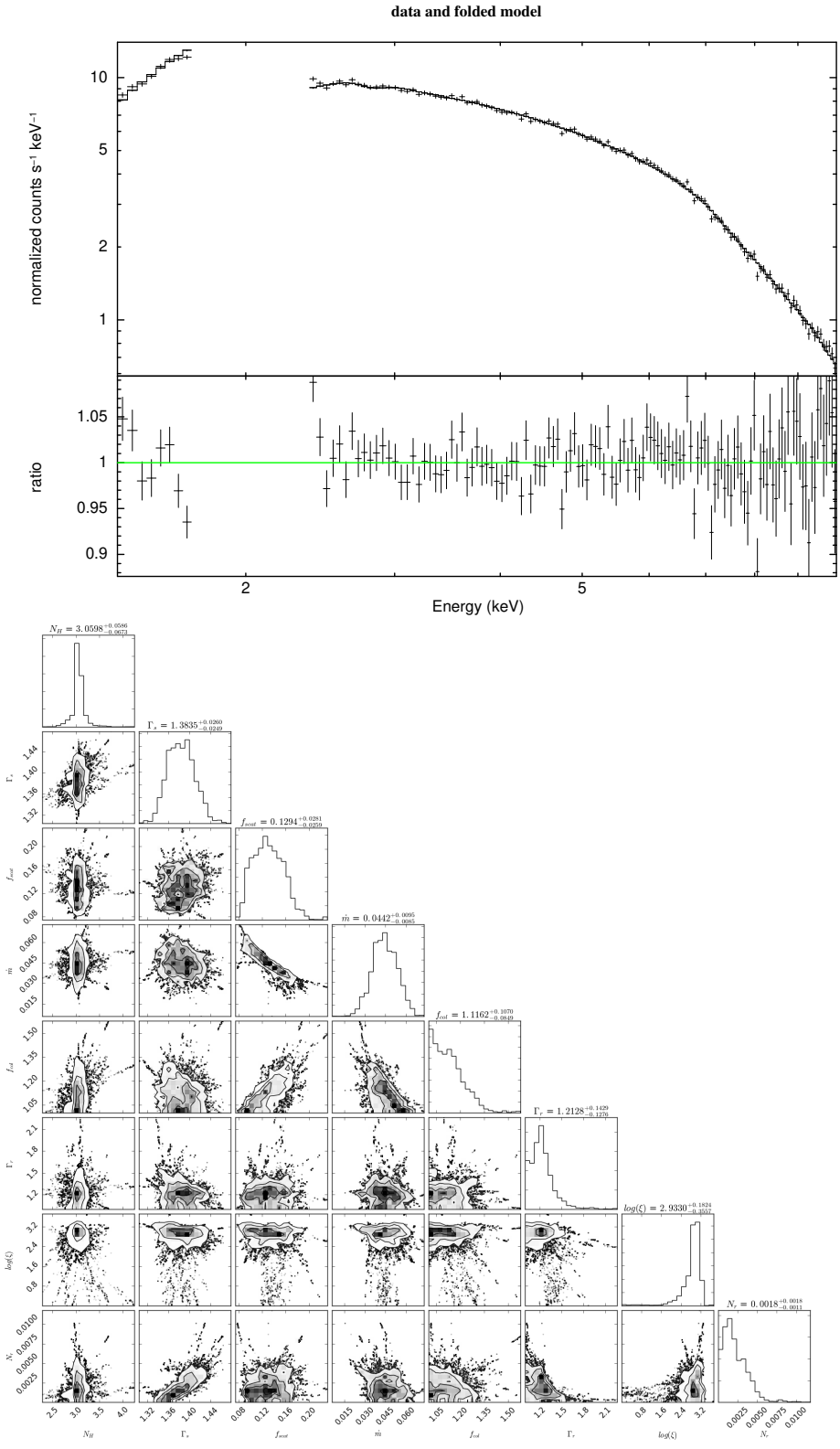

Figure B.34: XMM-Newton pn spectrum of the source SAX J1711.6-3808 and the residuals. (Hard state)

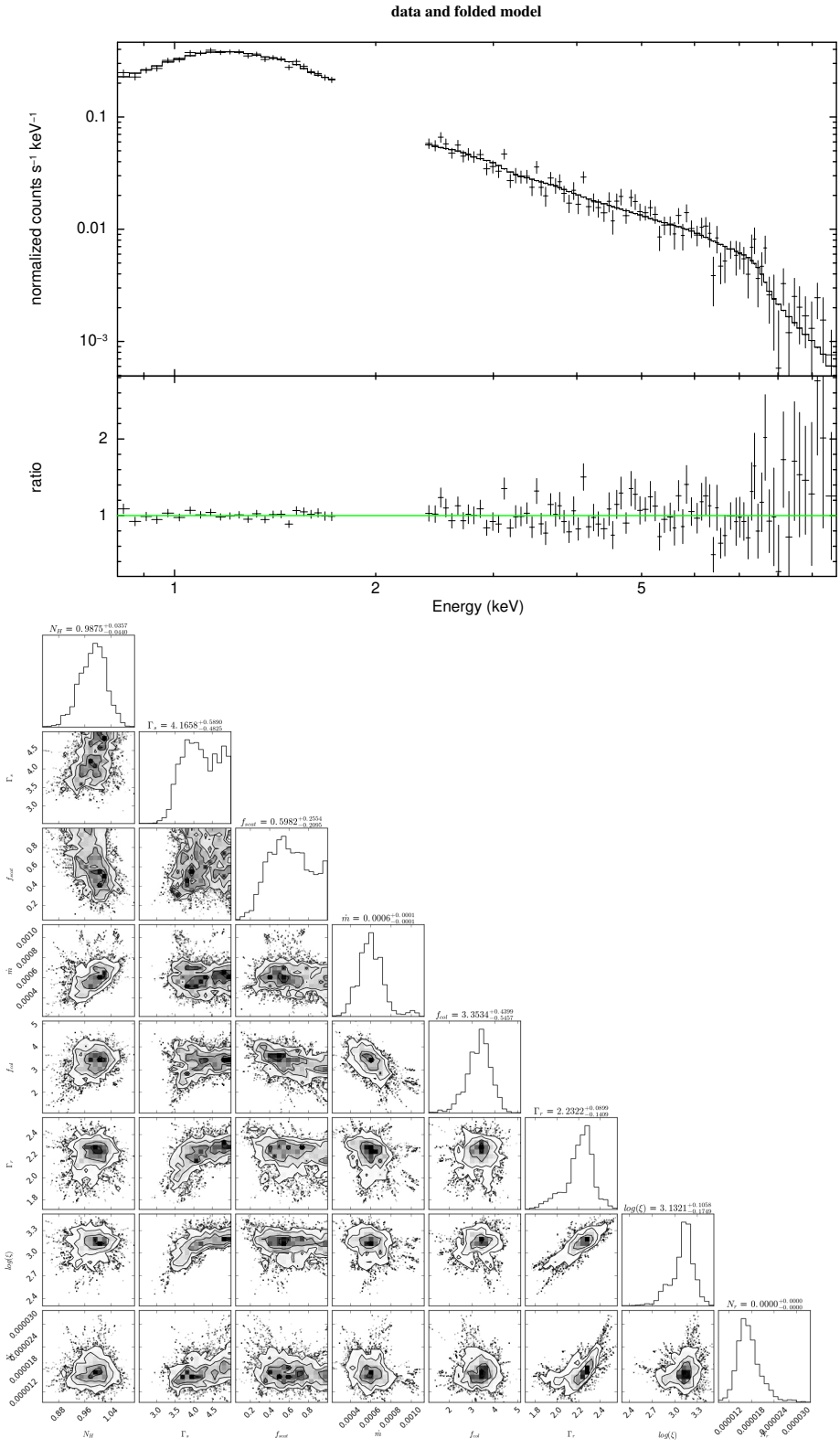

Figure B.35: XMM-Newton pn spectrum of the source XTE J1719-291 and the residuals. (Hard state)

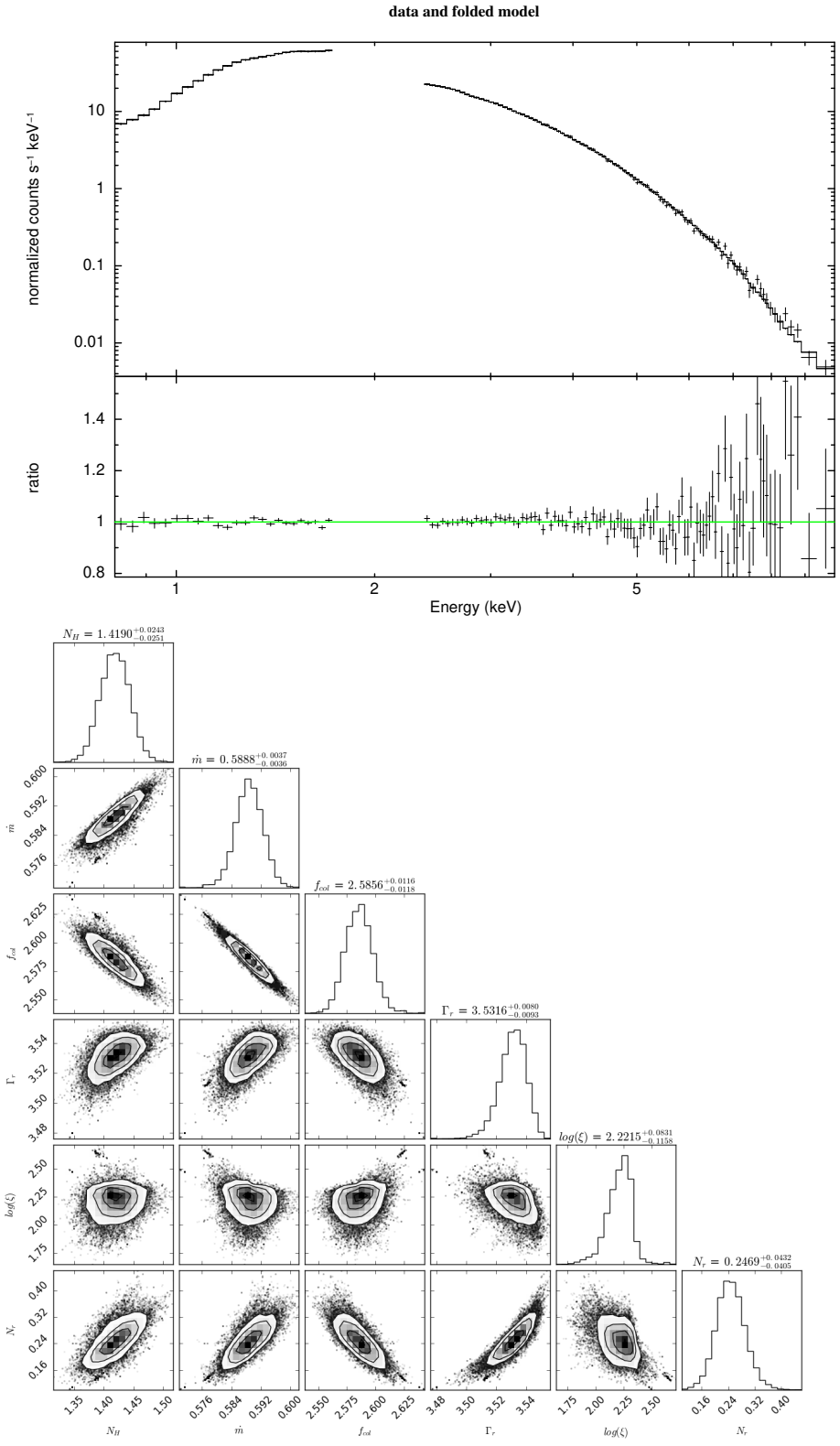

Figure B.36: XMM-Newton pn spectrum of the source XTE J1720-318 and the residuals. (Soft state)

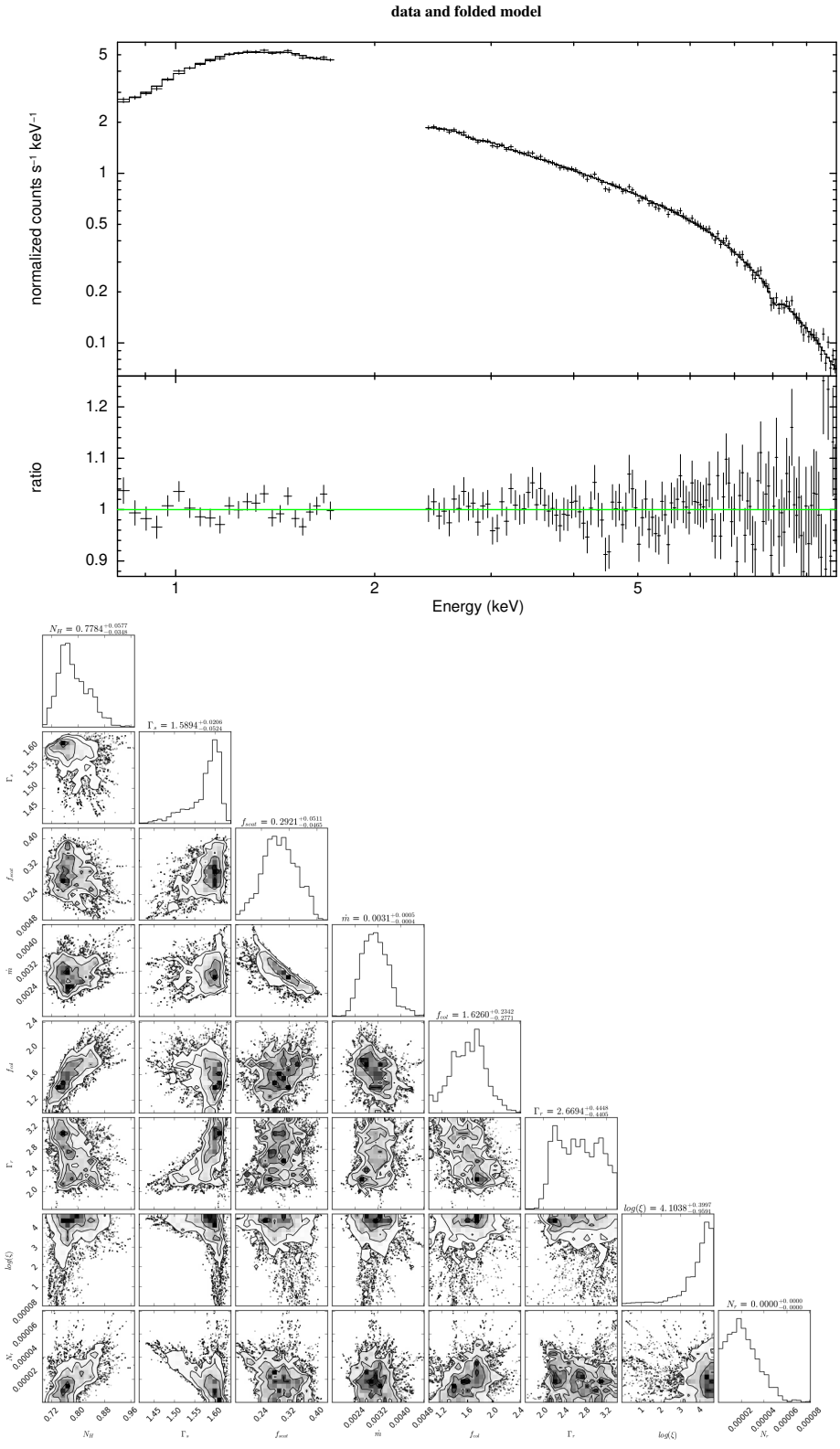

Figure B.37: XMM-Newton pn spectrum of the source IGR J17285-2922 and the residuals. (Hard state)

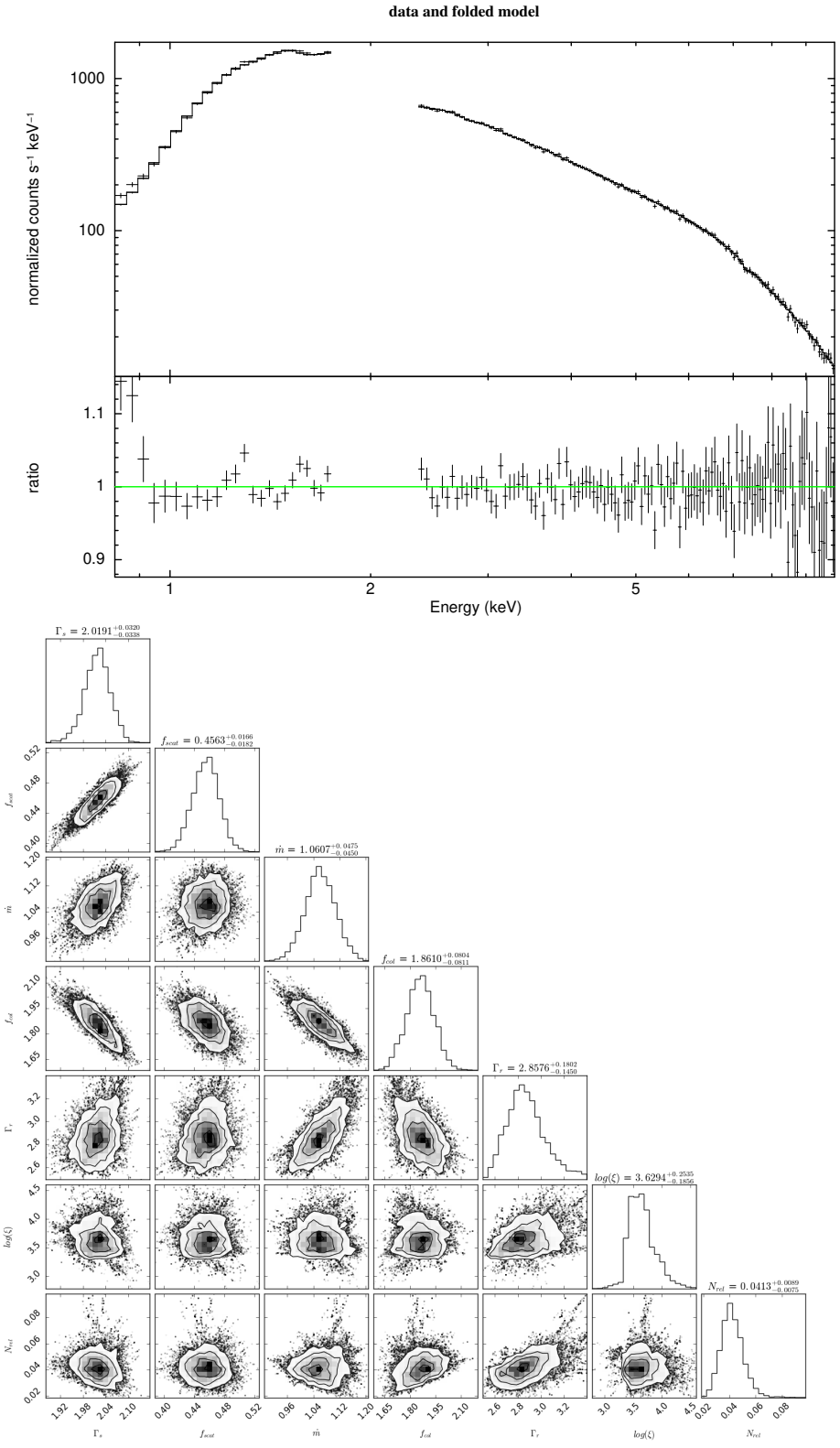

Figure B.38: XMM-Newton pn spectrum of the source Swift J174510.8-262411 and the residuals. (Intermediate state)

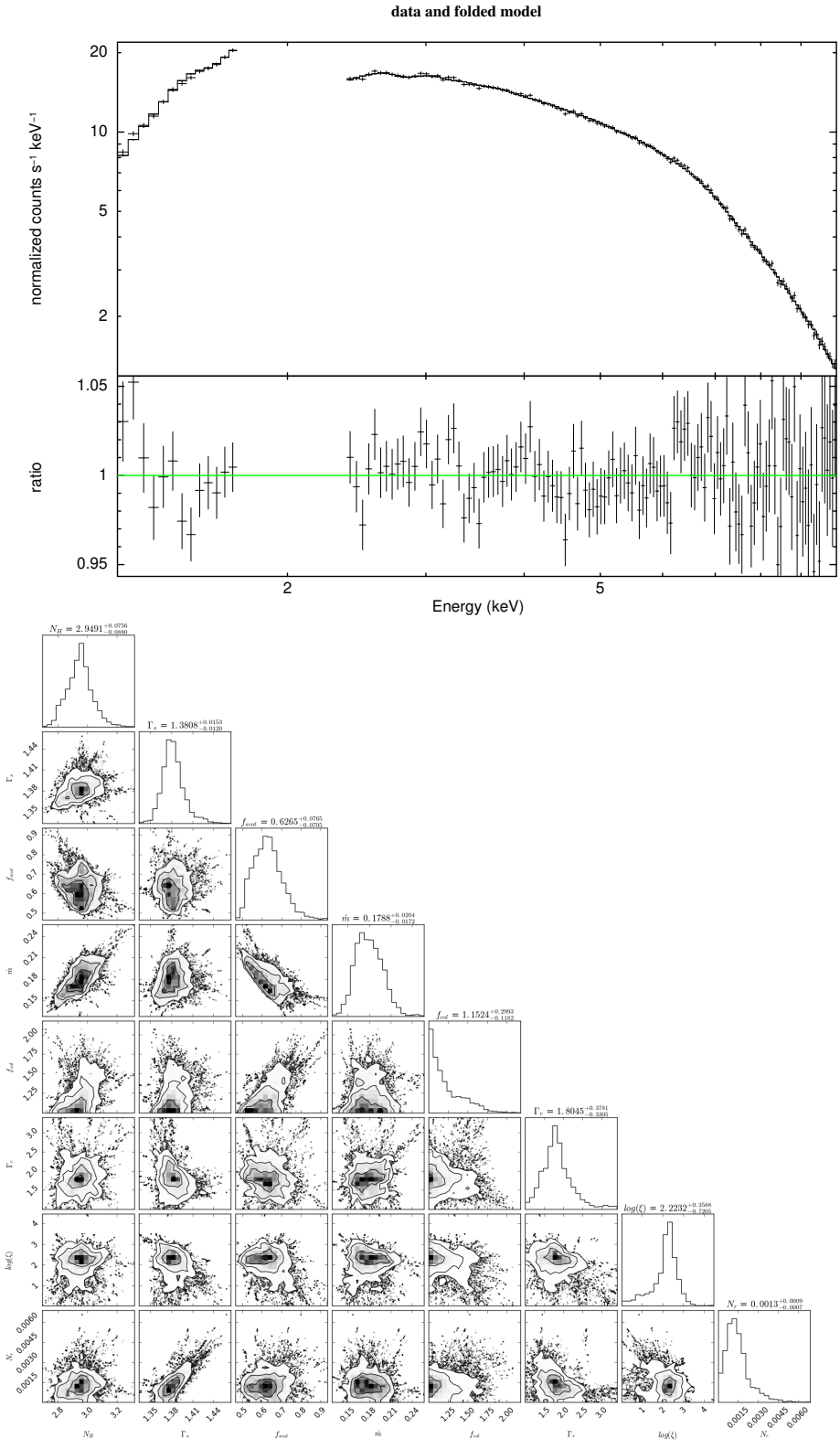

Figure B.39: XMM-Newton pn spectrum of the source H 1743-322 (rev1613) and the residuals. (Hard state)

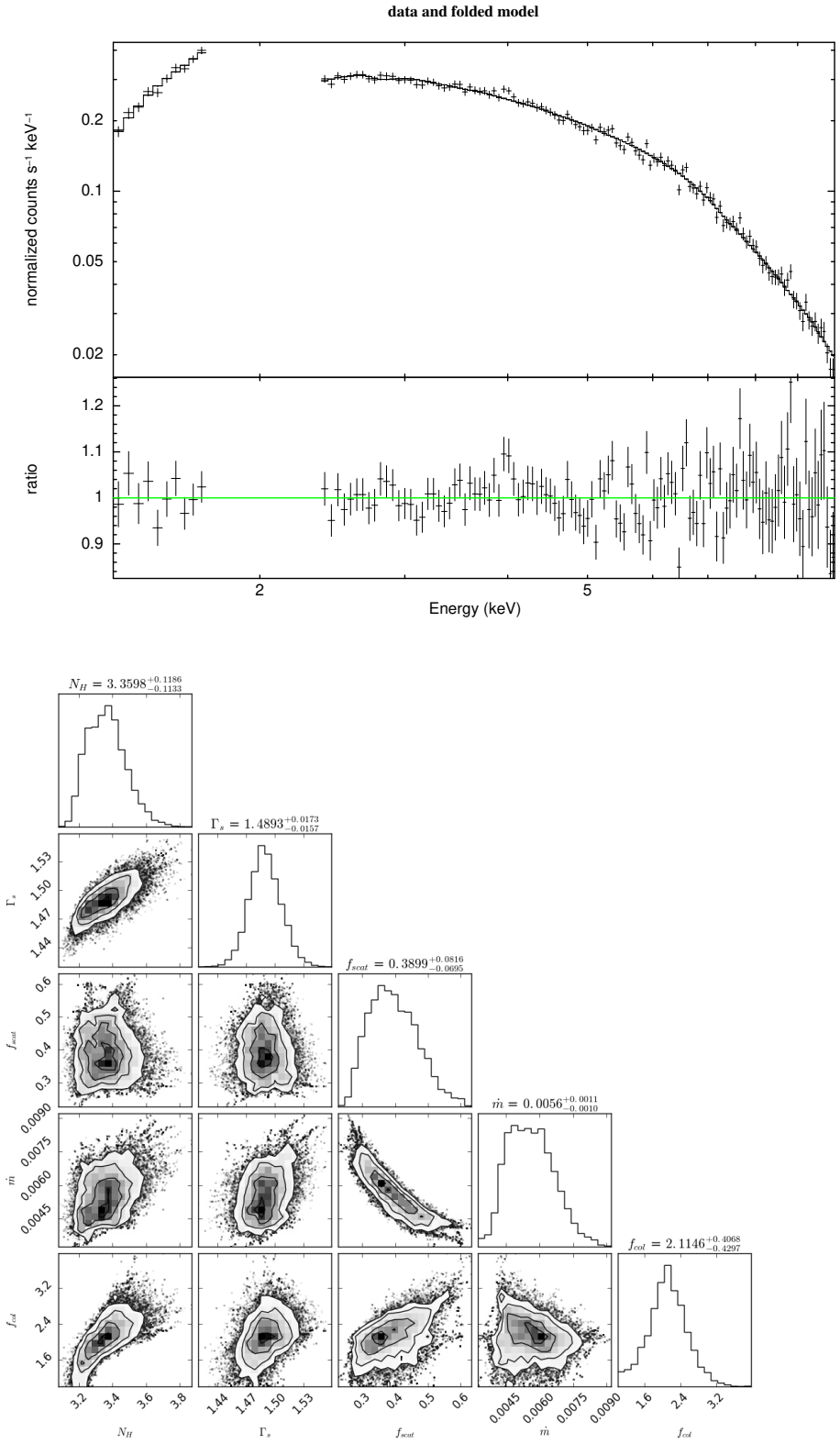

Figure B.40: XMM-Newton pn spectrum of the source H 1743-322 (rev1984) and the residuals. (Hard state)

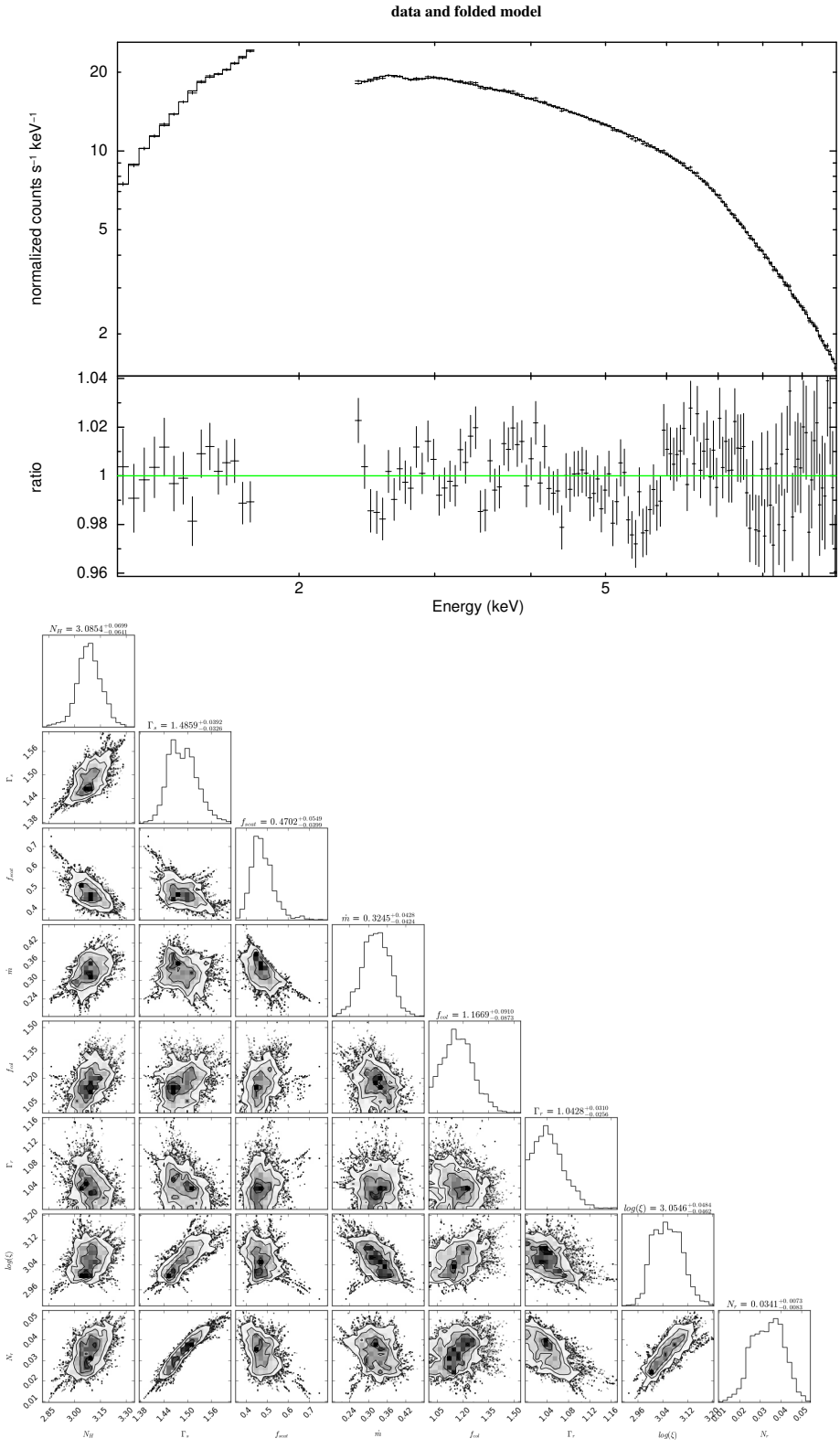

Figure B.41: XMM-Newton pn spectrum of the source H 1743-322 (rev2708) and the residuals. (Hard state)

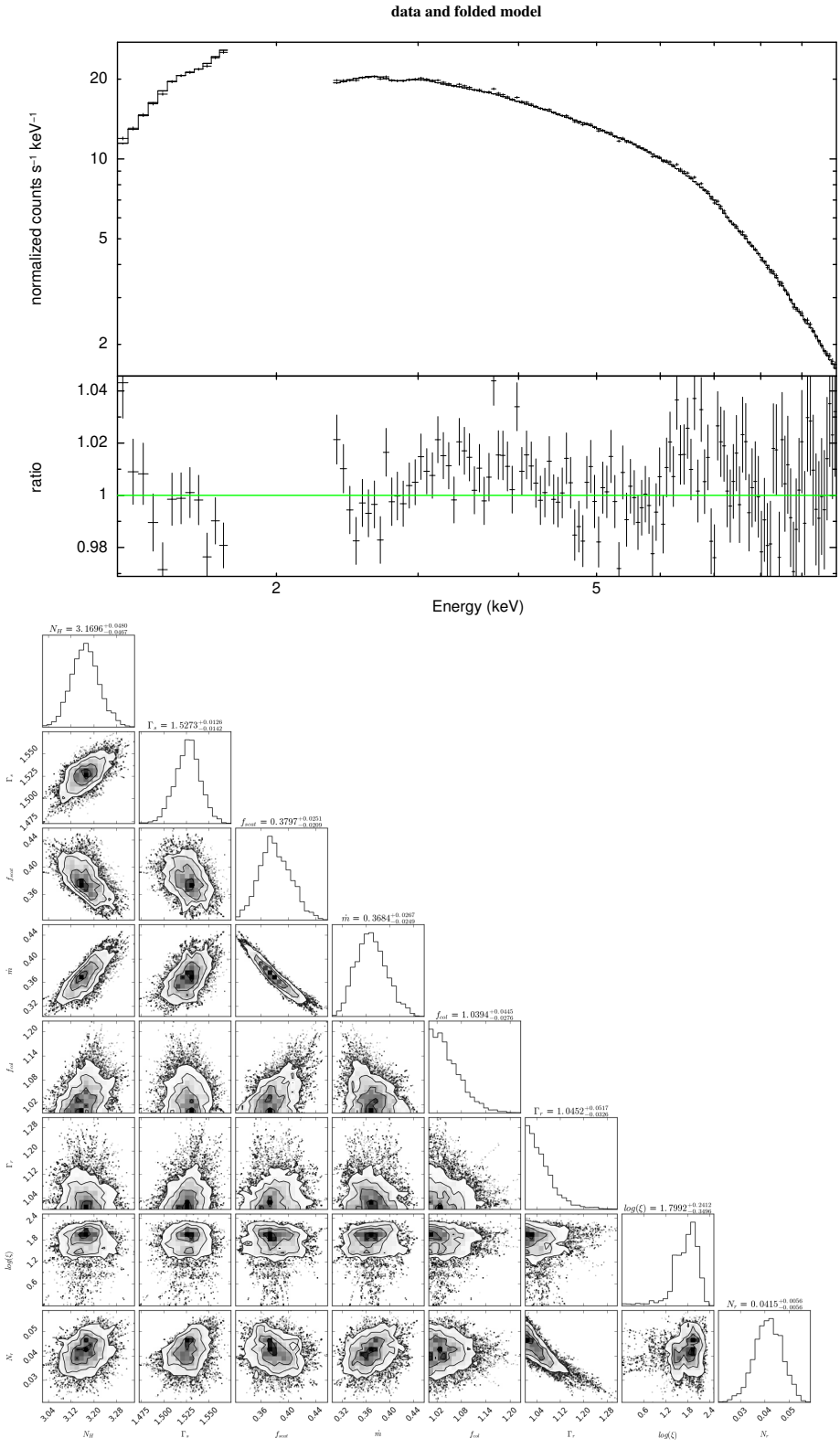

Figure B.42: XMM-Newton pn spectrum of the source H 1743-322 (rev2709a) and the residuals. (Hard state)

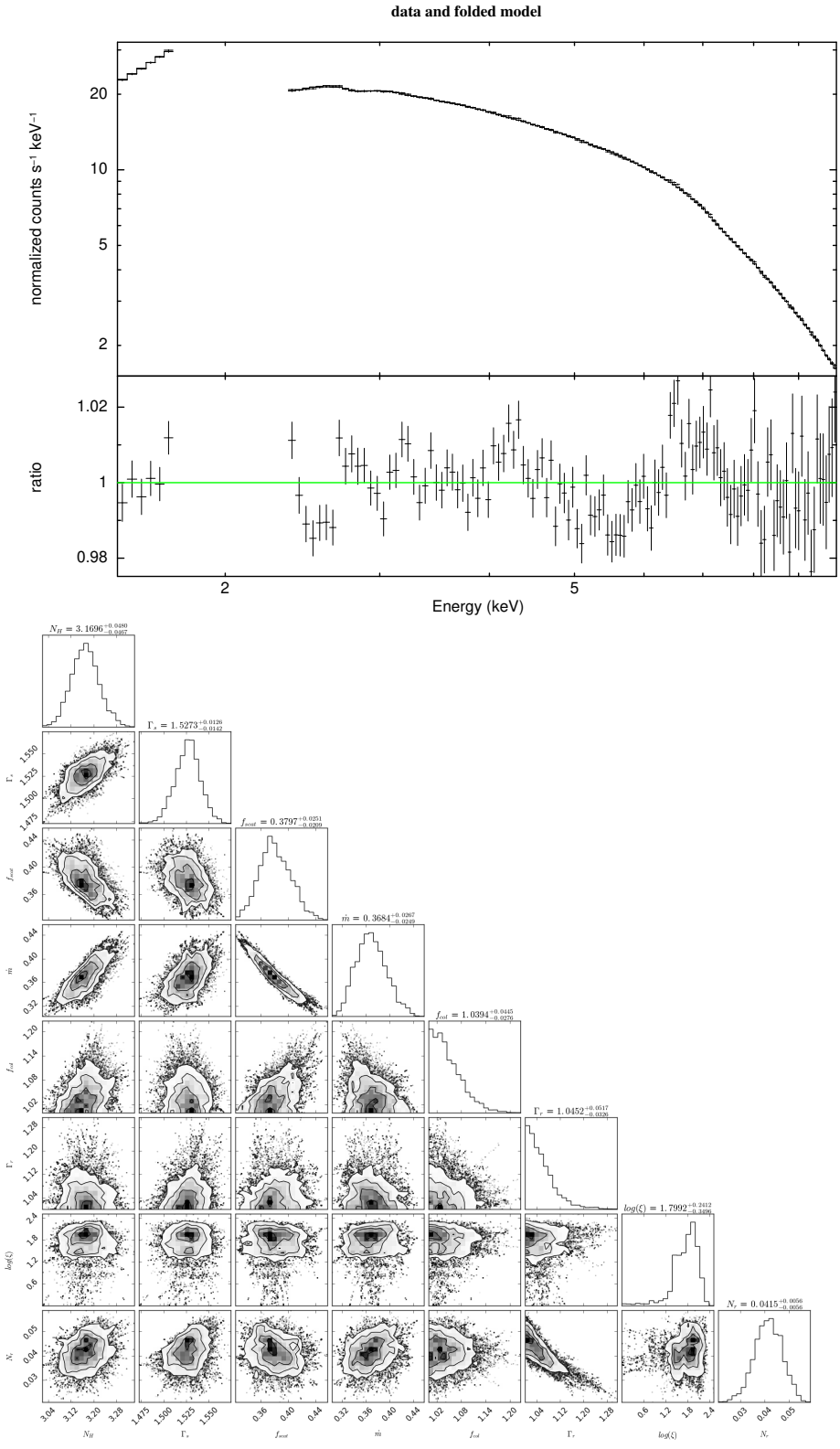

Figure B.43: XMM-Newton pn spectrum of the source H 1743-322 (rev2709b) and the residuals. (Hard state)

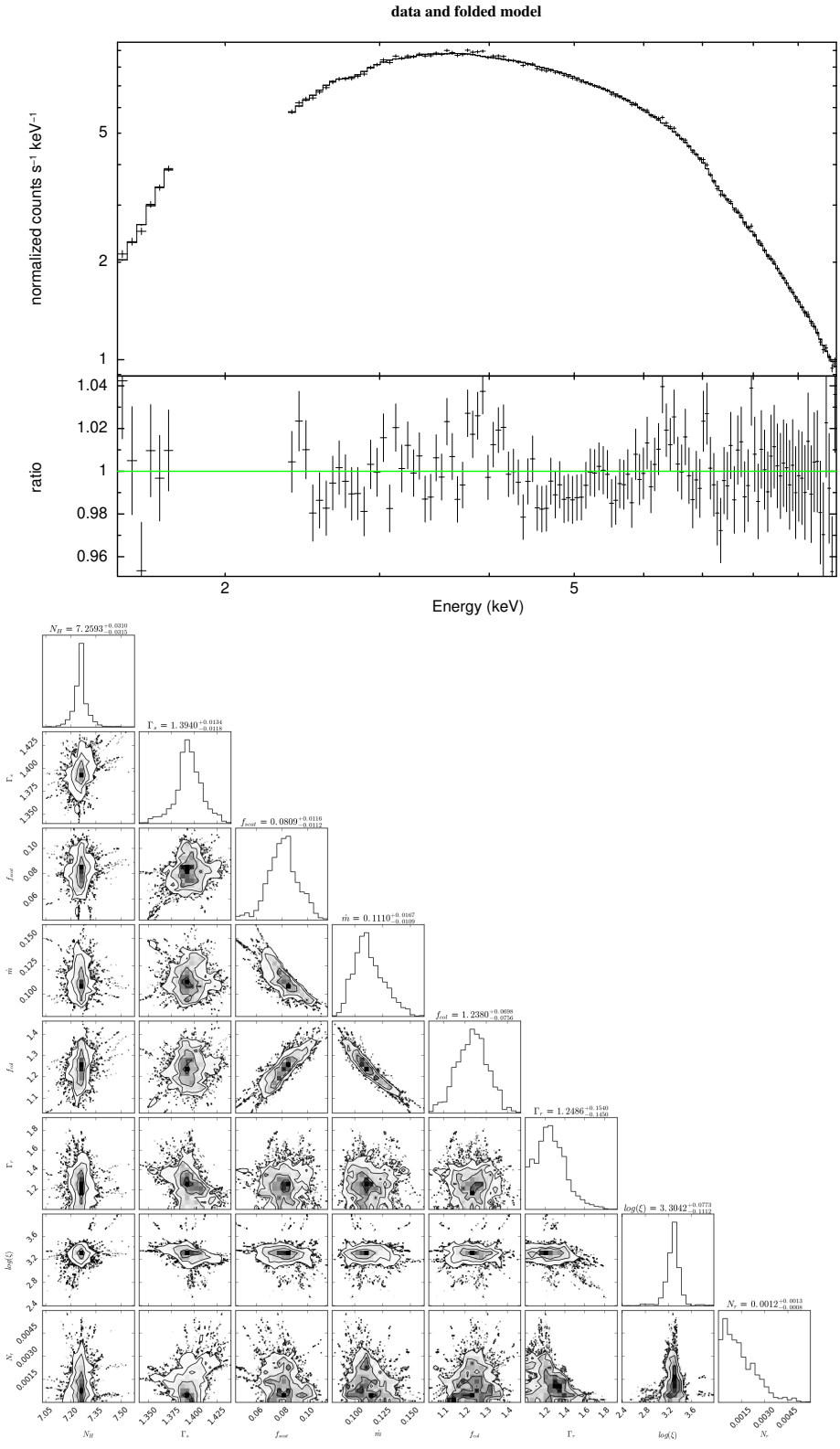

Figure B.44: XMM-Newton pn spectrum of the source IGR J17497-2821 (rev1243) and the residuals. (Hard state)

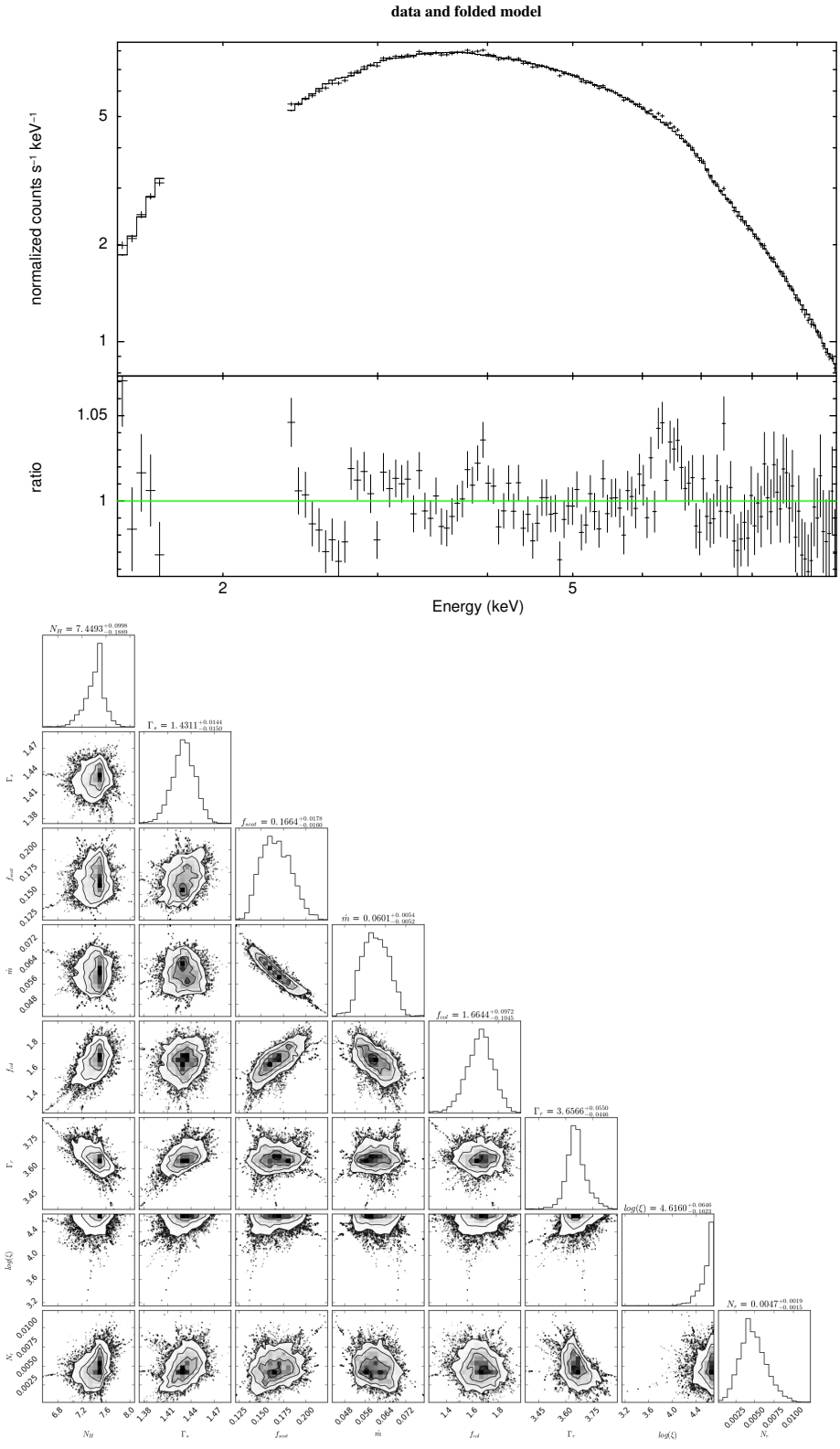

Figure B.45: XMM-Newton pn spectrum of the source IGR J17497-2821 (rev1245) and the residuals. (Hard state)

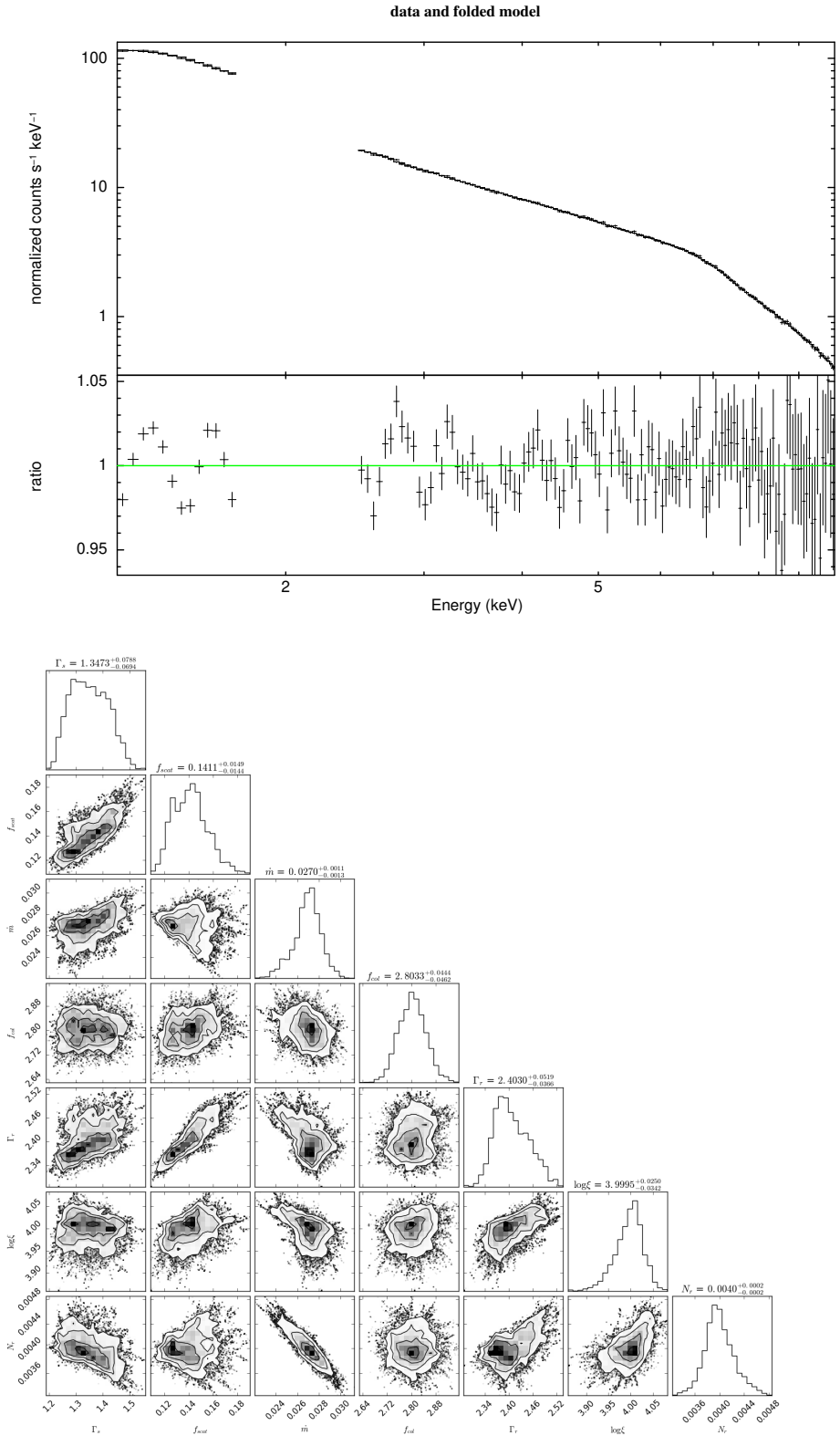

Figure B.46: XMM-Newton pn spectrum of the source XTE J1752-223 and the residuals. (Hard state)

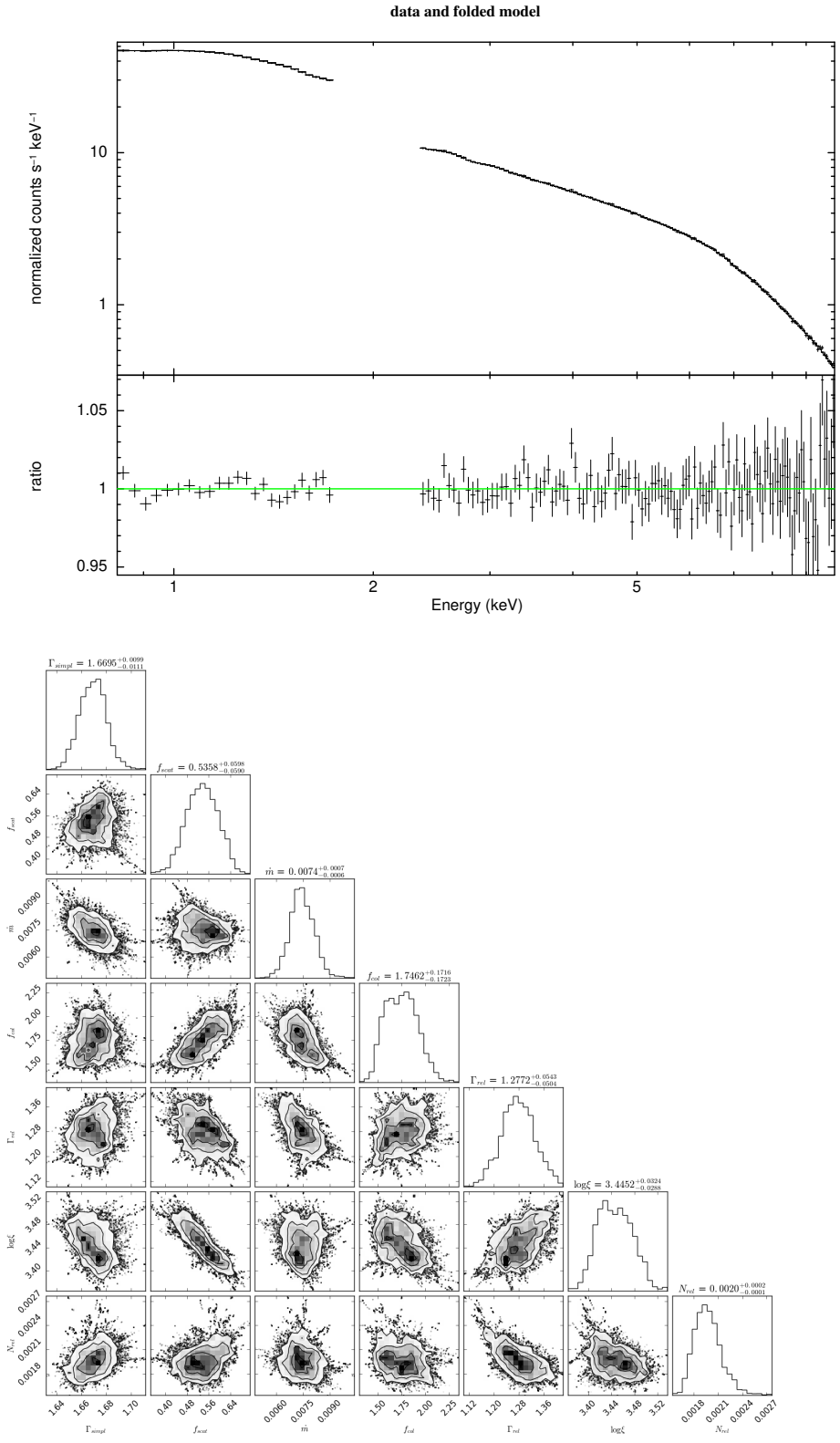

Figure B.47: XMM-Newton pn spectrum of the source Swift J1753.5-0127 (rev1152) and the residuals. (Hard state)

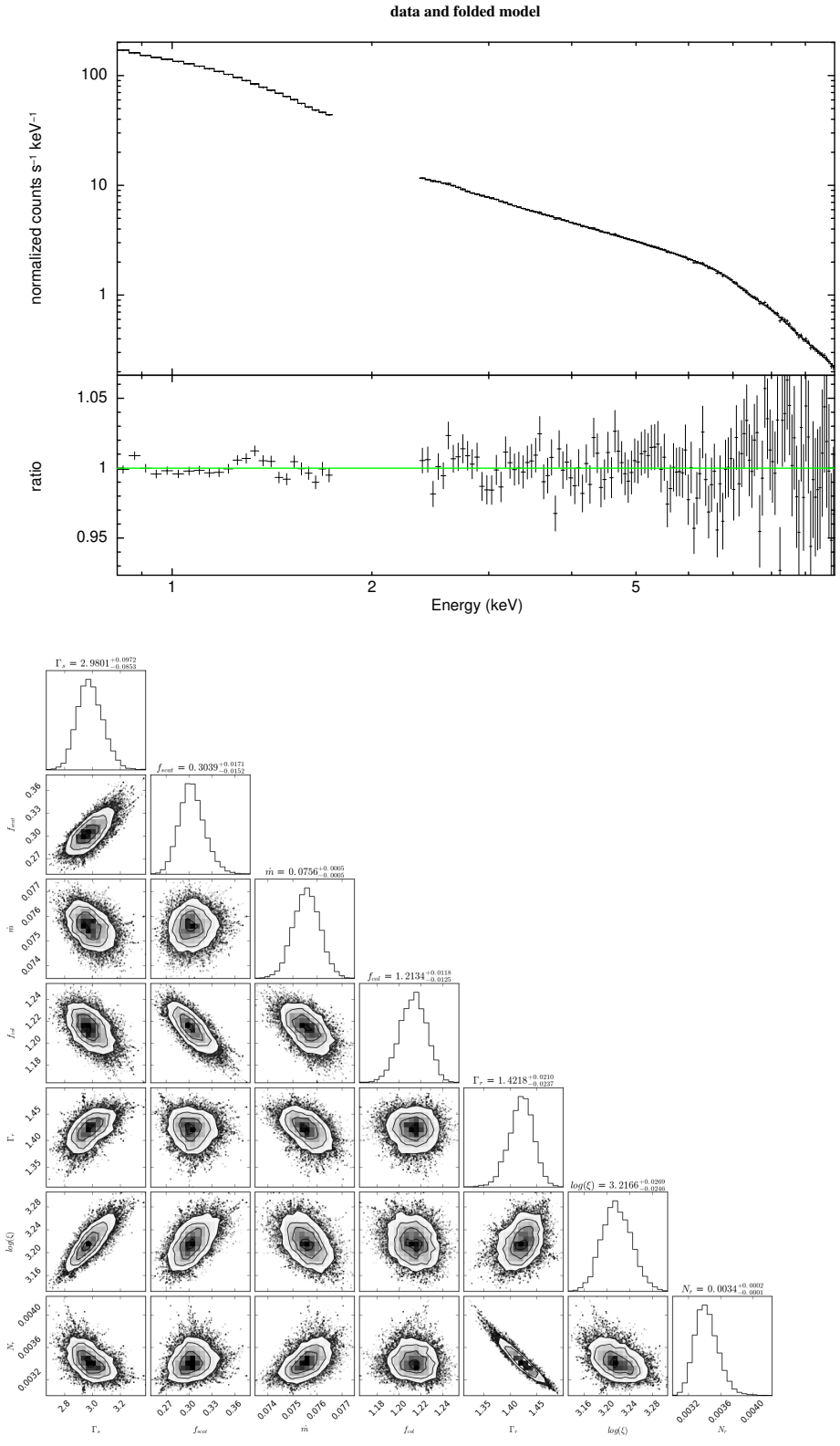

Figure B.48: XMM-Newton pn spectrum of the source Swift J1753.5-0127 (rev1716) and the residuals. (Hard state)

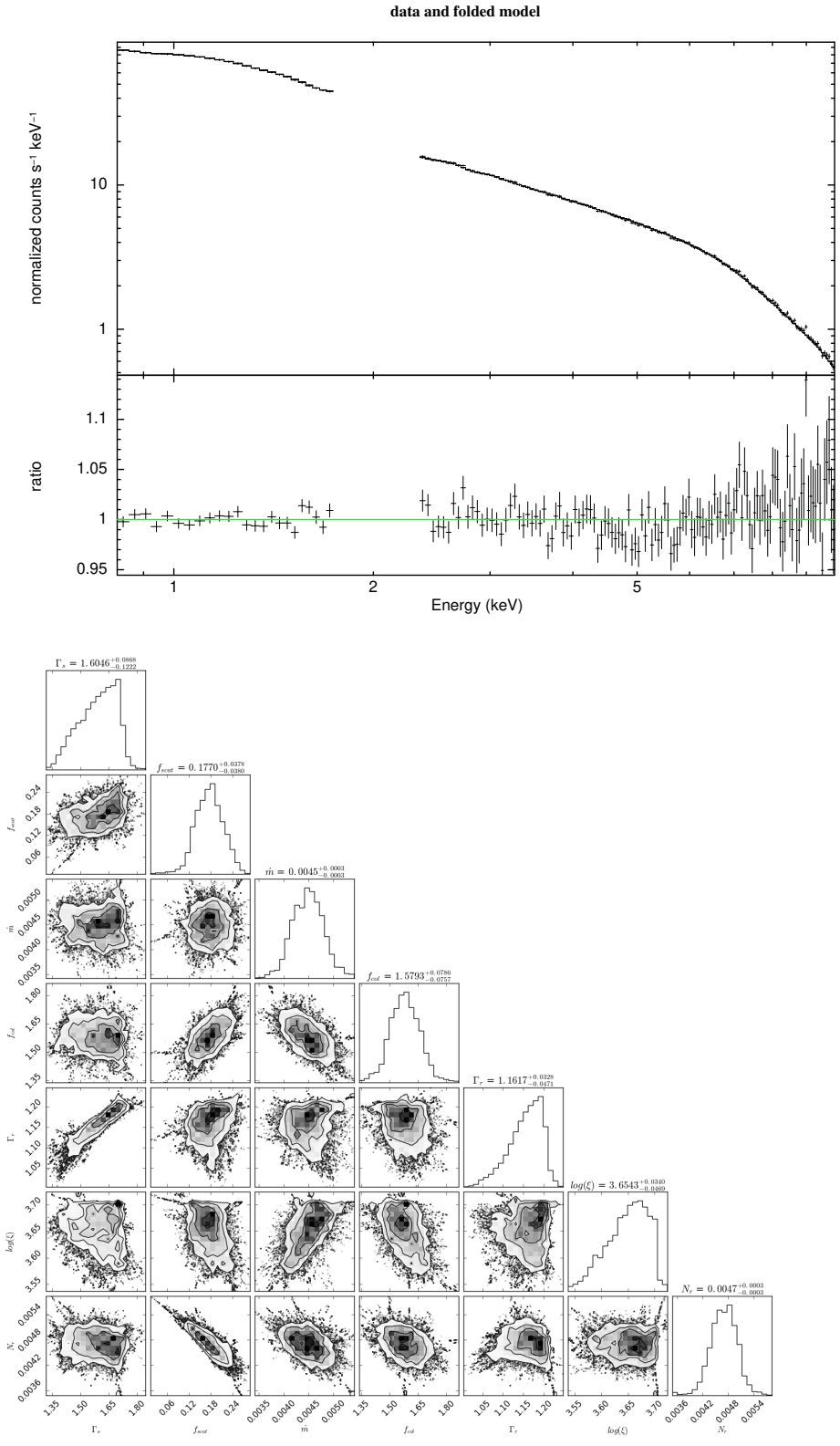

Figure B.49: XMM-Newton pn spectrum of the source Swift J1753.5-0127 (rev2336) and the residuals. (Hard state)

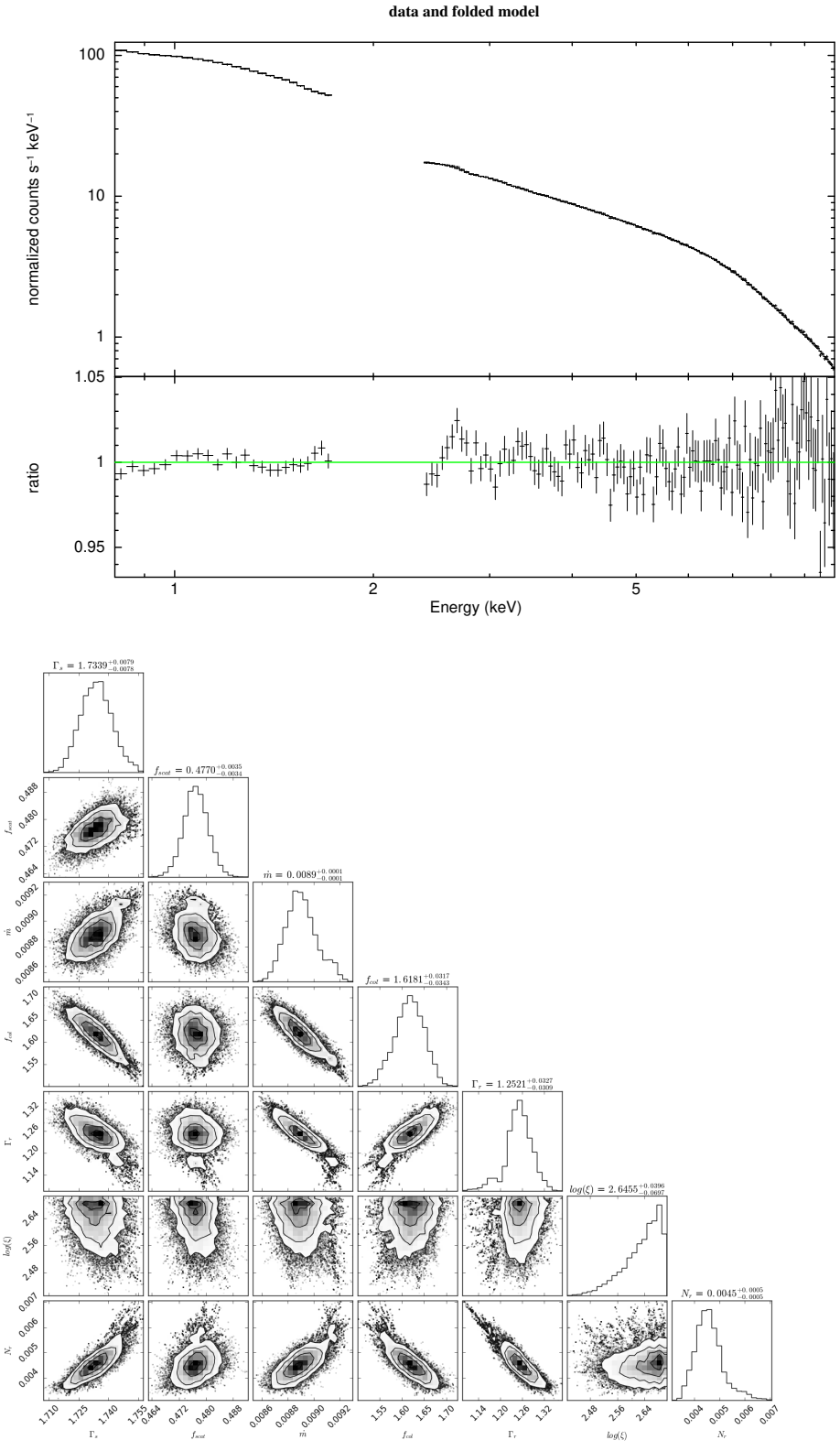

Figure B.50: XMM-Newton pn spectrum of the source Swift J1753.5-0127 (rev2350) and the residuals. (Hard state)

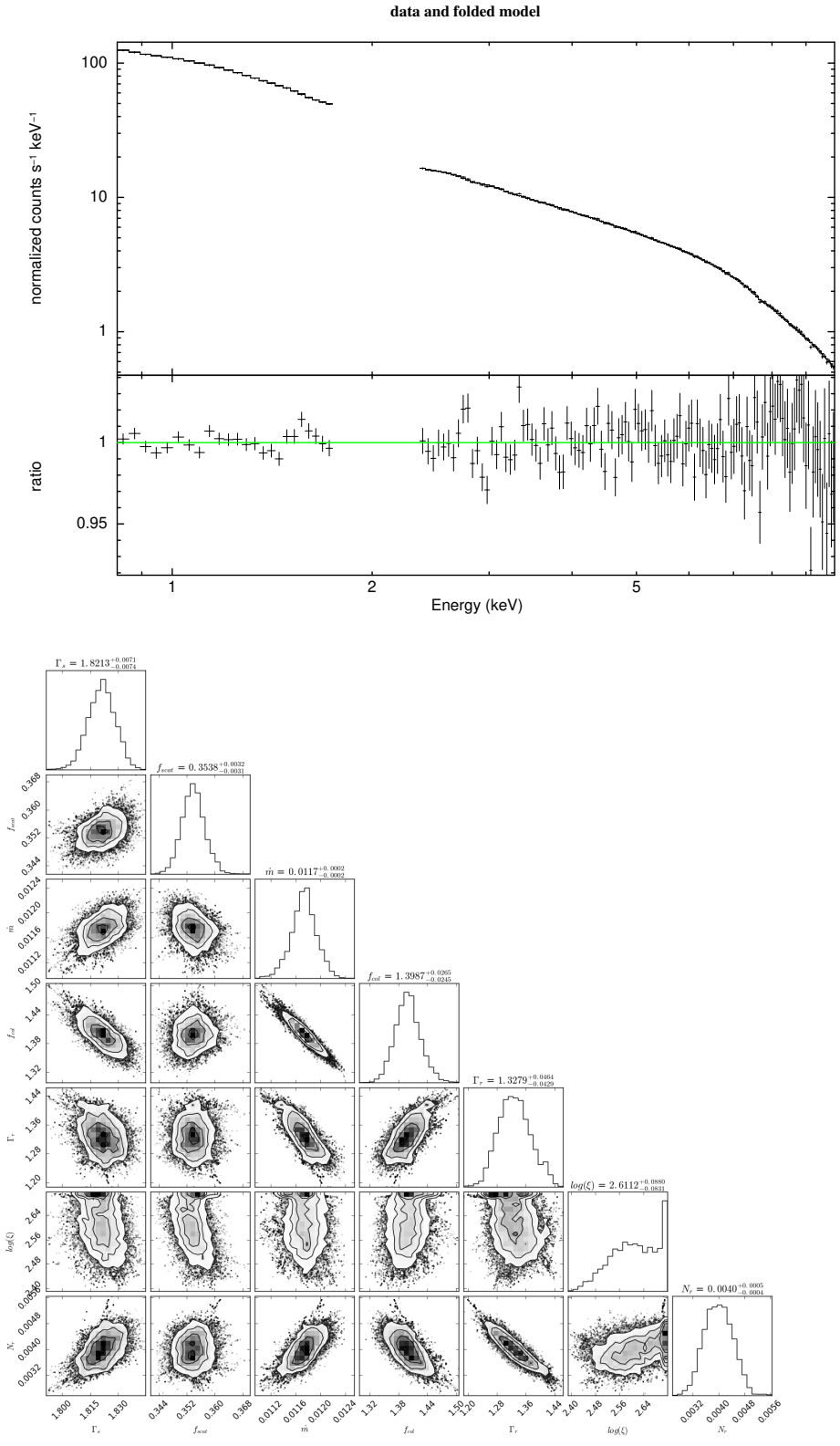

Figure B.51: XMM-Newton pn spectrum of the source Swift J1753.5-0127 (rev2704) and the residuals. (Hard state)

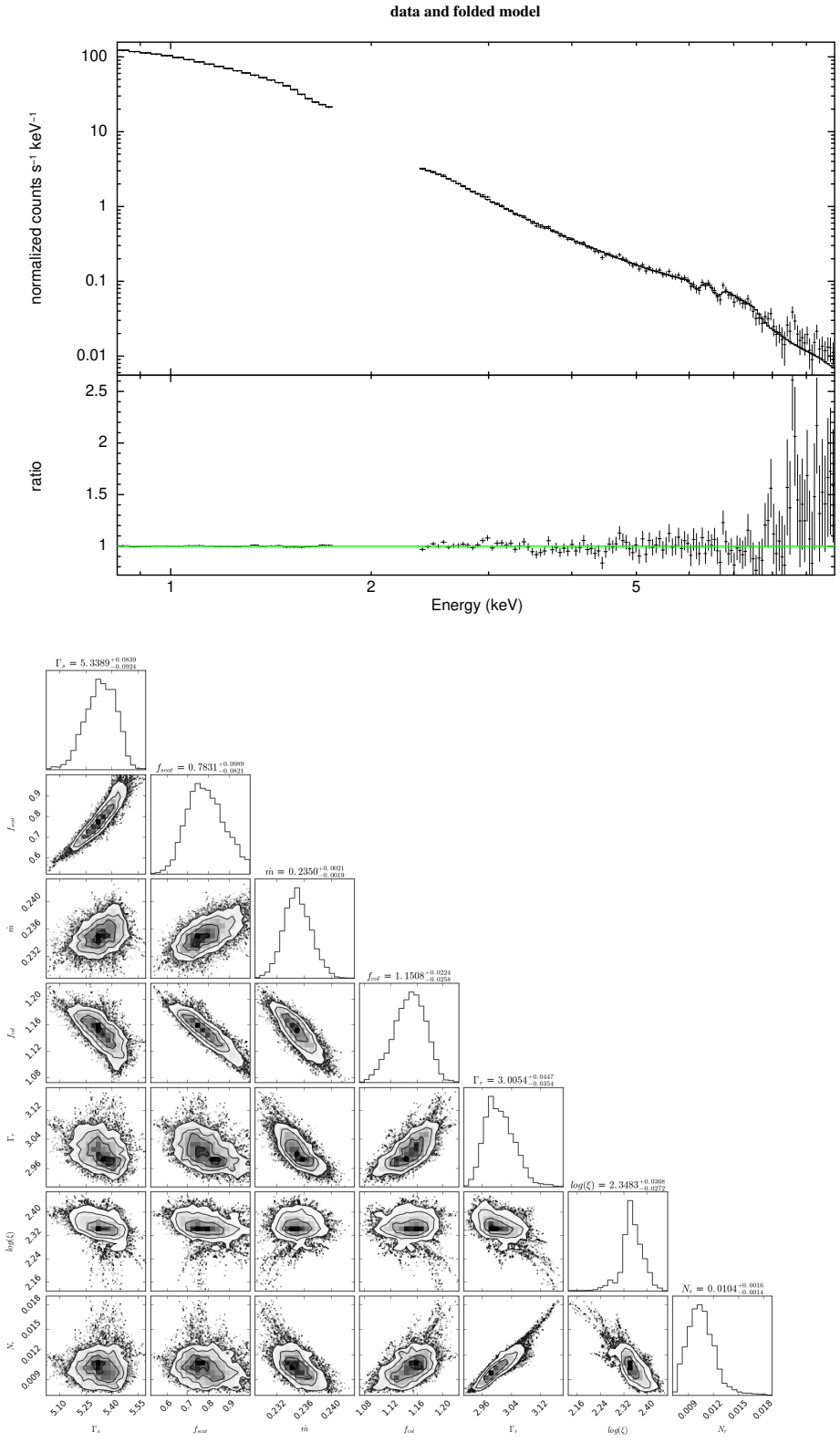

Figure B.52: XMM-Newton pn spectrum of the source Swift J1753.5-0127 (rev2724) and the residuals. (Soft state)

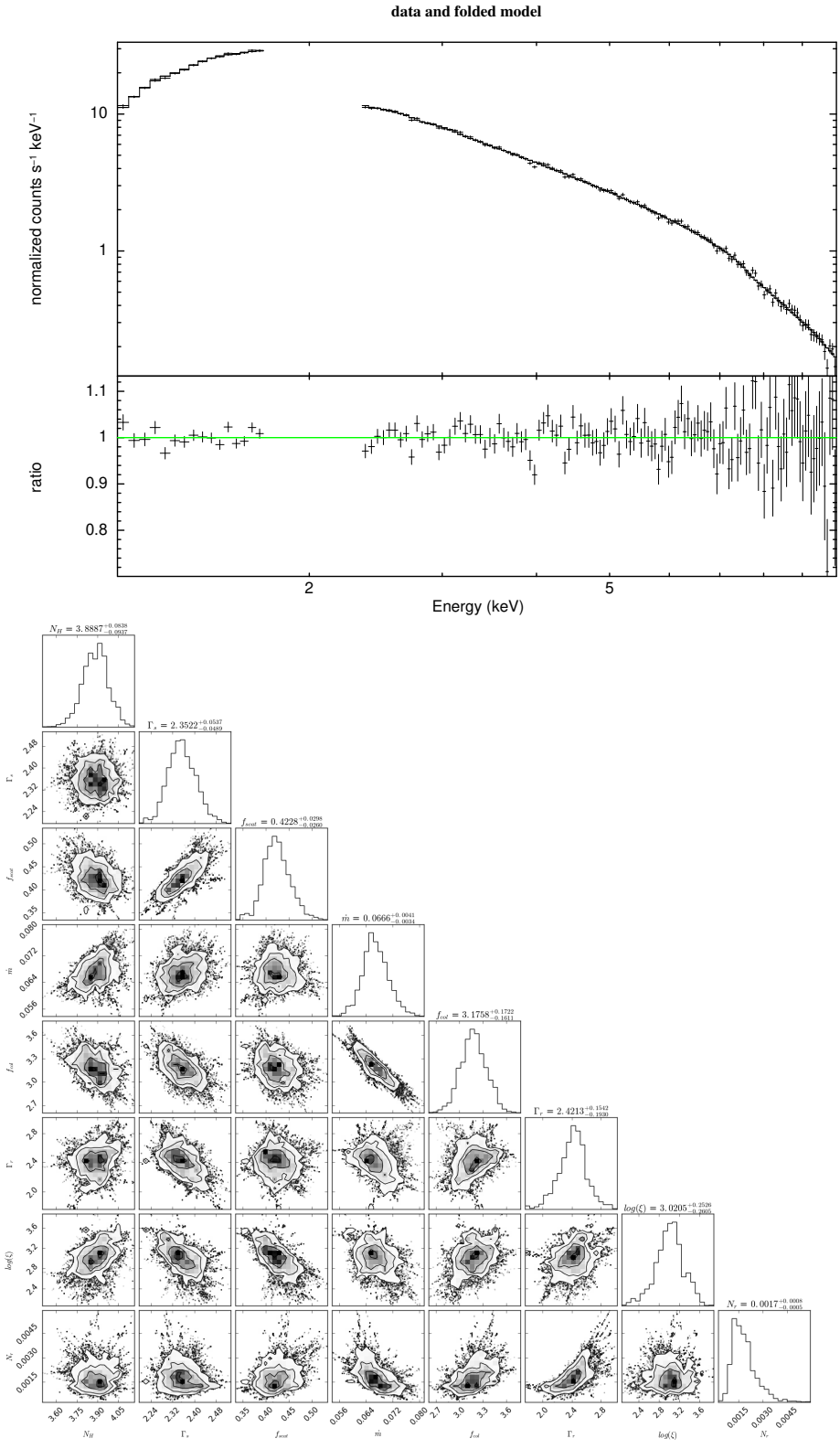

Figure B.53: XMM-Newton pn spectrum of the source GRS 1758-258 (rev143) and the residuals. (Intermediate state)

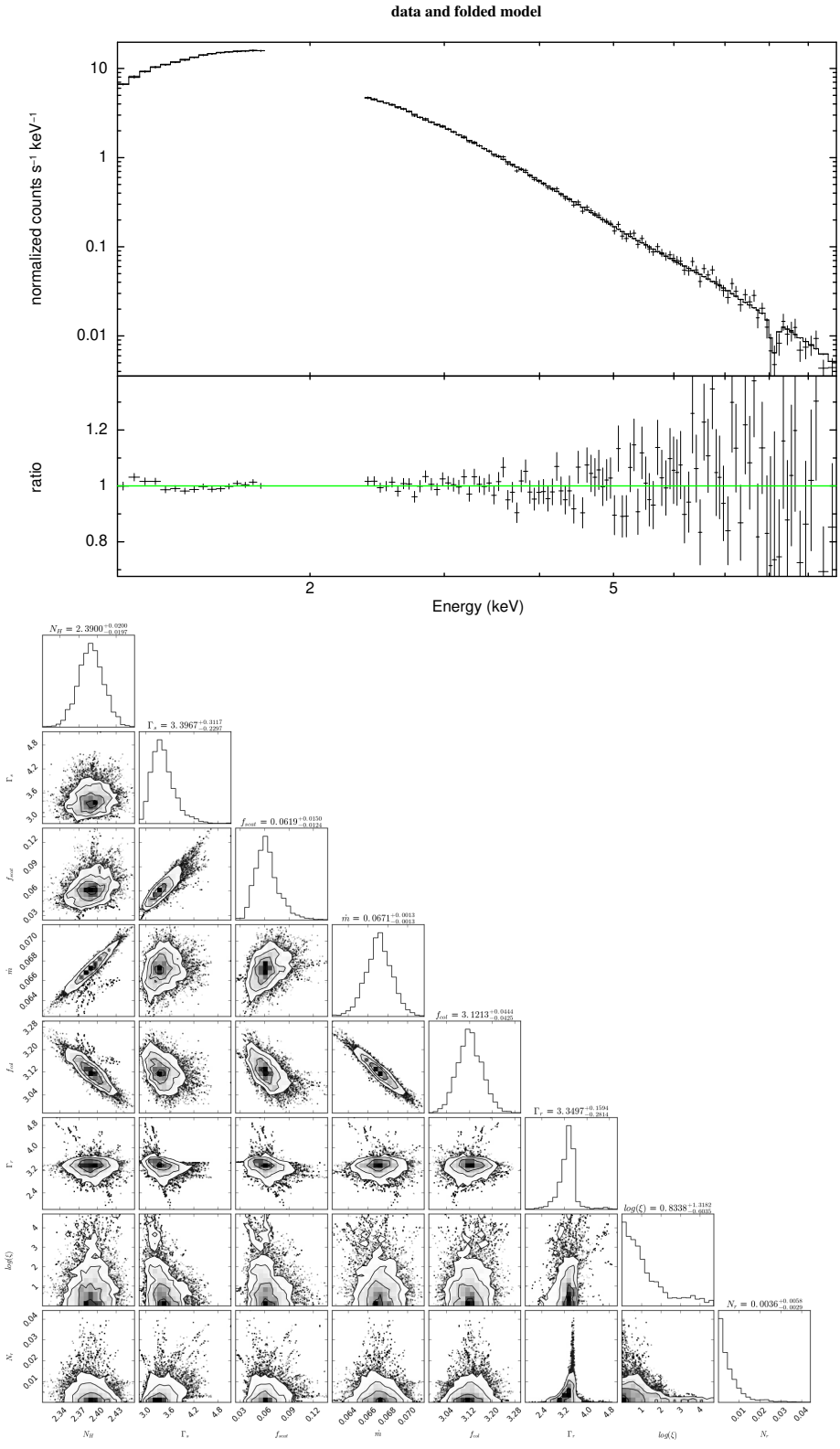

Figure B.54: XMM-Newton pn spectrum of the source GRS 1758-258 (rev235) and the residuals. (Soft state)

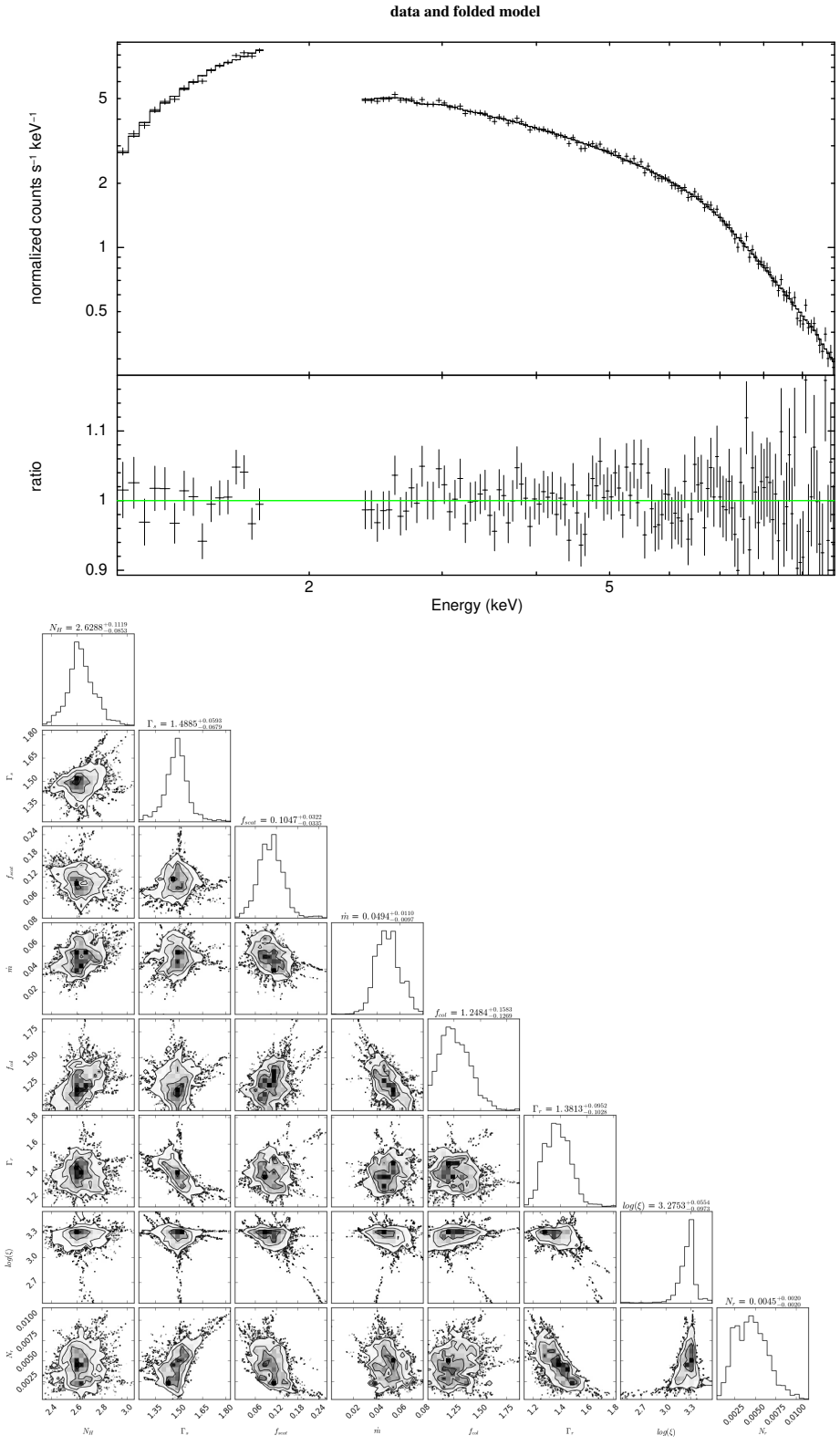

Figure B.55: XMM-Newton pn spectrum of the source GRS 1758-258 (rev513) and the residuals. (Hard state)

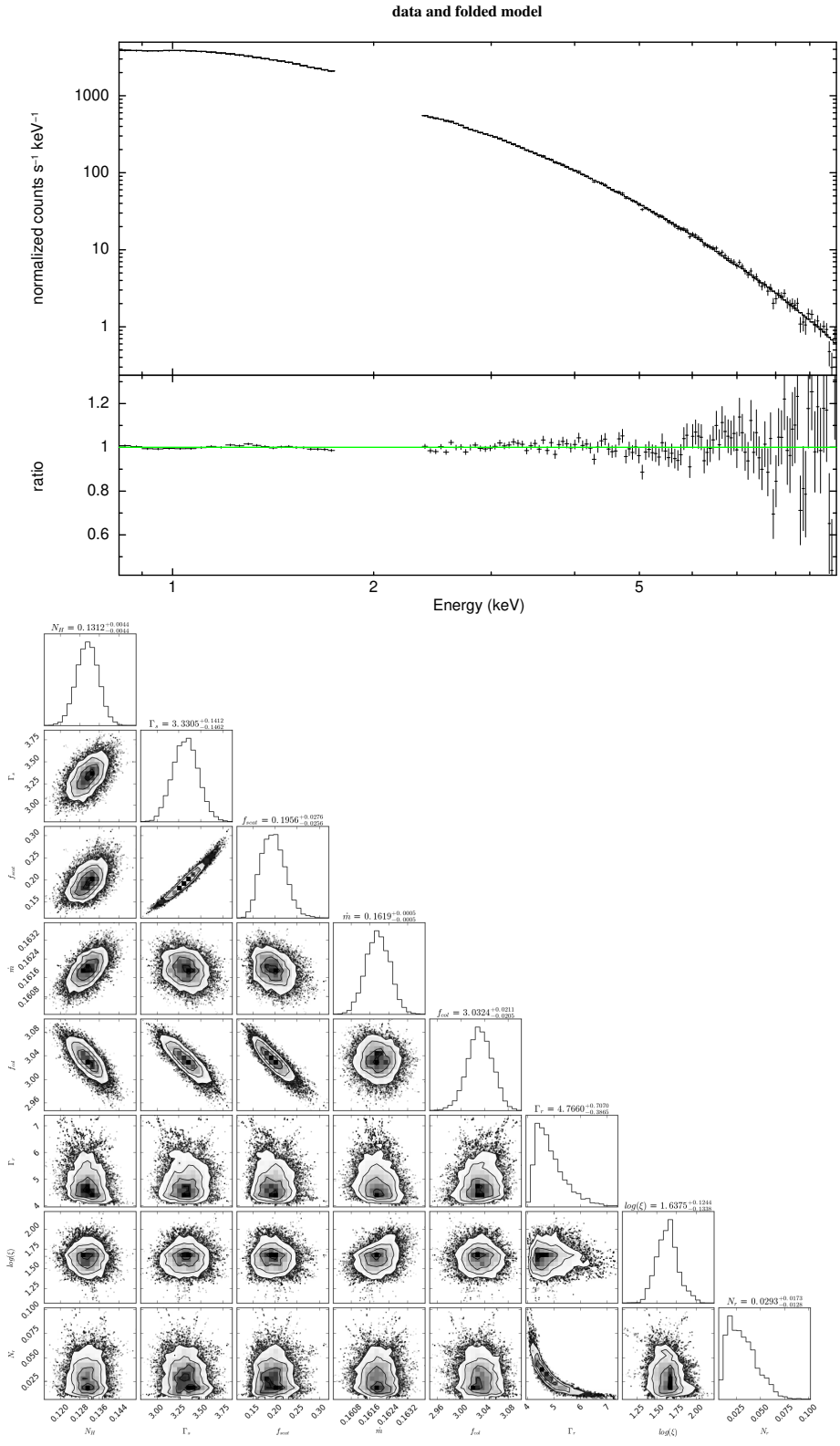

Figure B.56: XMM-Newton pn spectrum of the source XTE J1817-330 (rev1146) and the residuals. (Soft state)

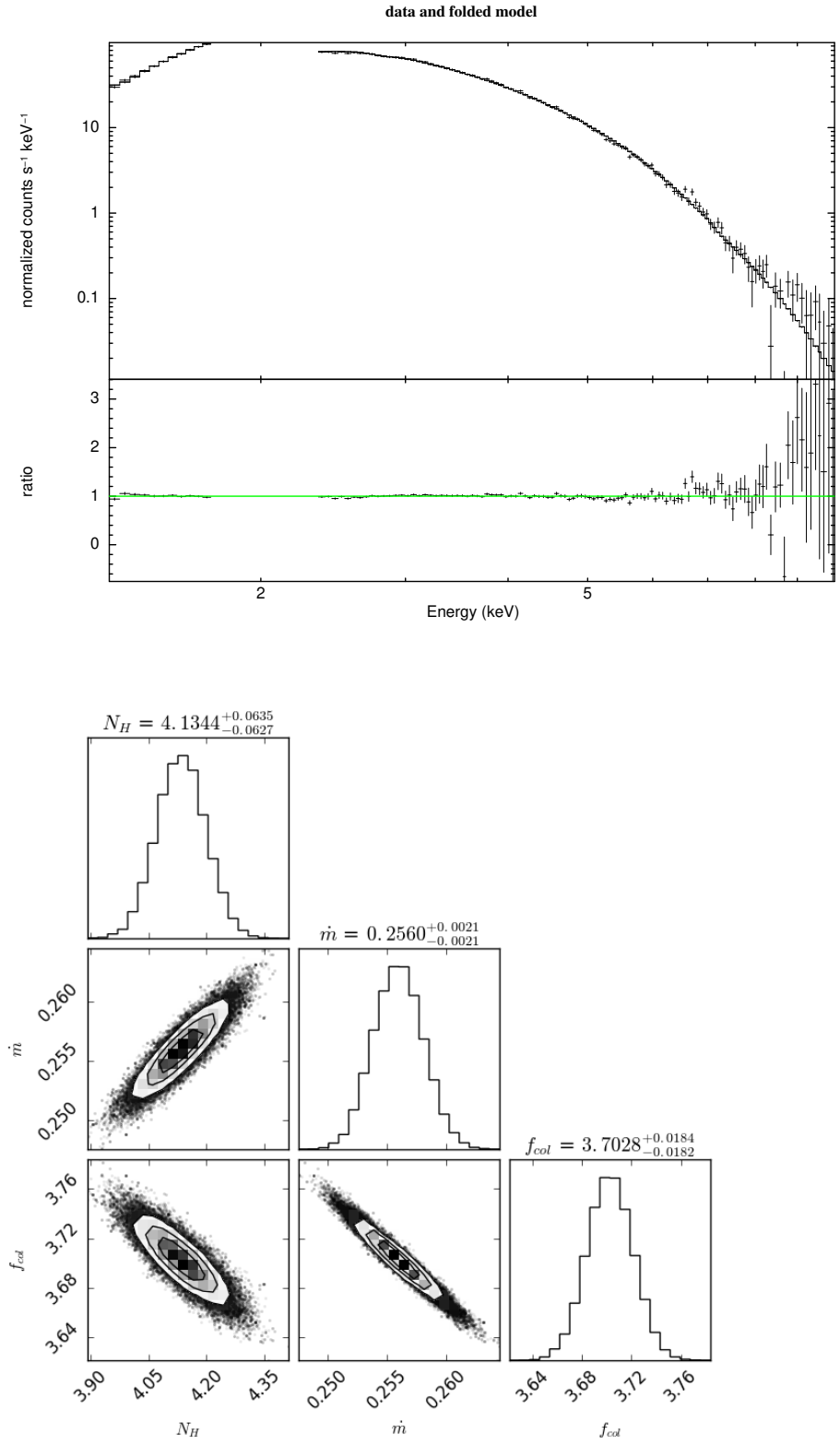

Figure B.57: XMM-Newton pn spectrum of the source XTE J1856+053 and the residuals. (Soft state)

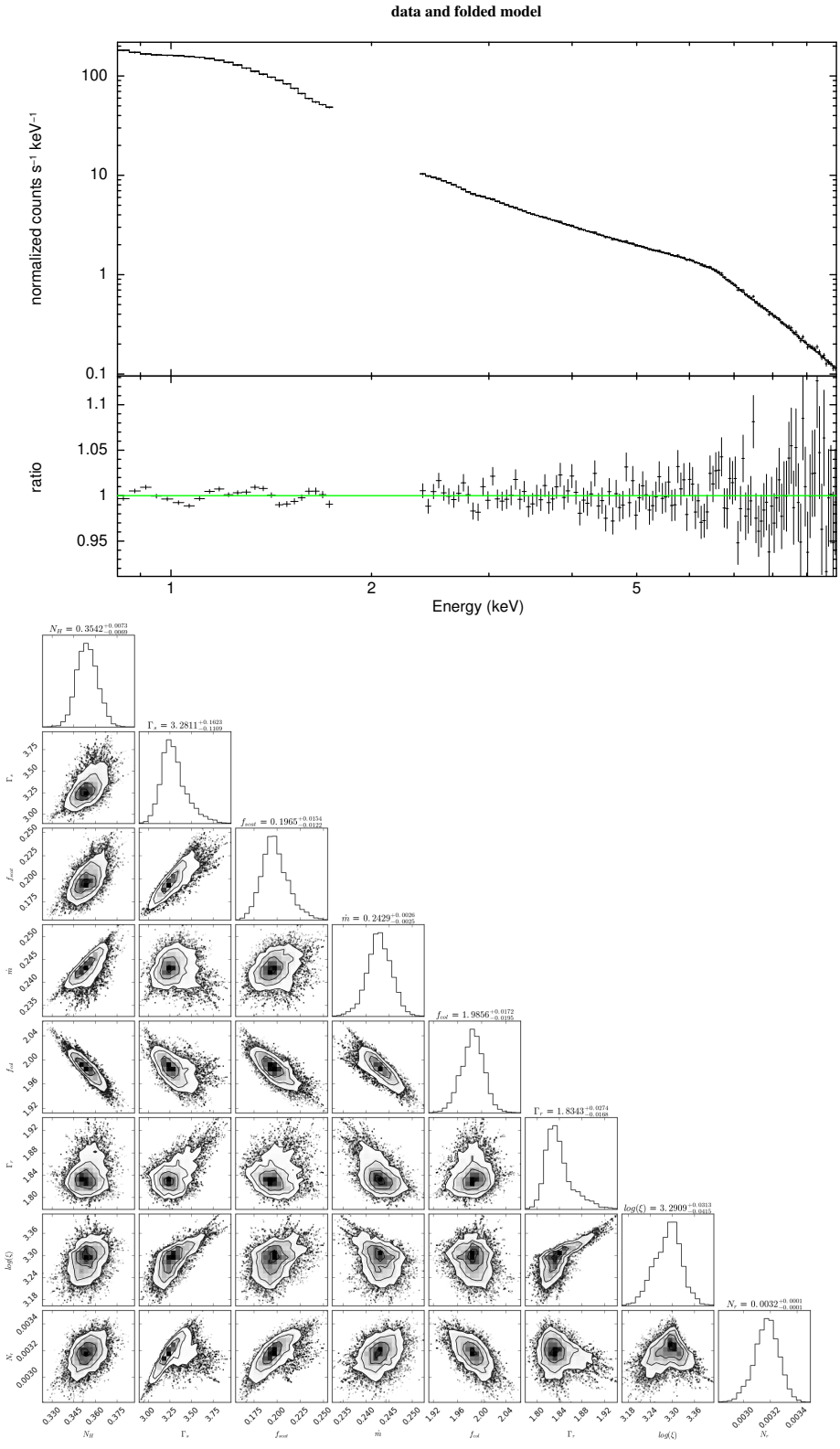

Figure B.58: XMM-Newton pn spectrum of the source Swift J1910.2-0546 (rev2335) and the residuals. (Intermediate state)

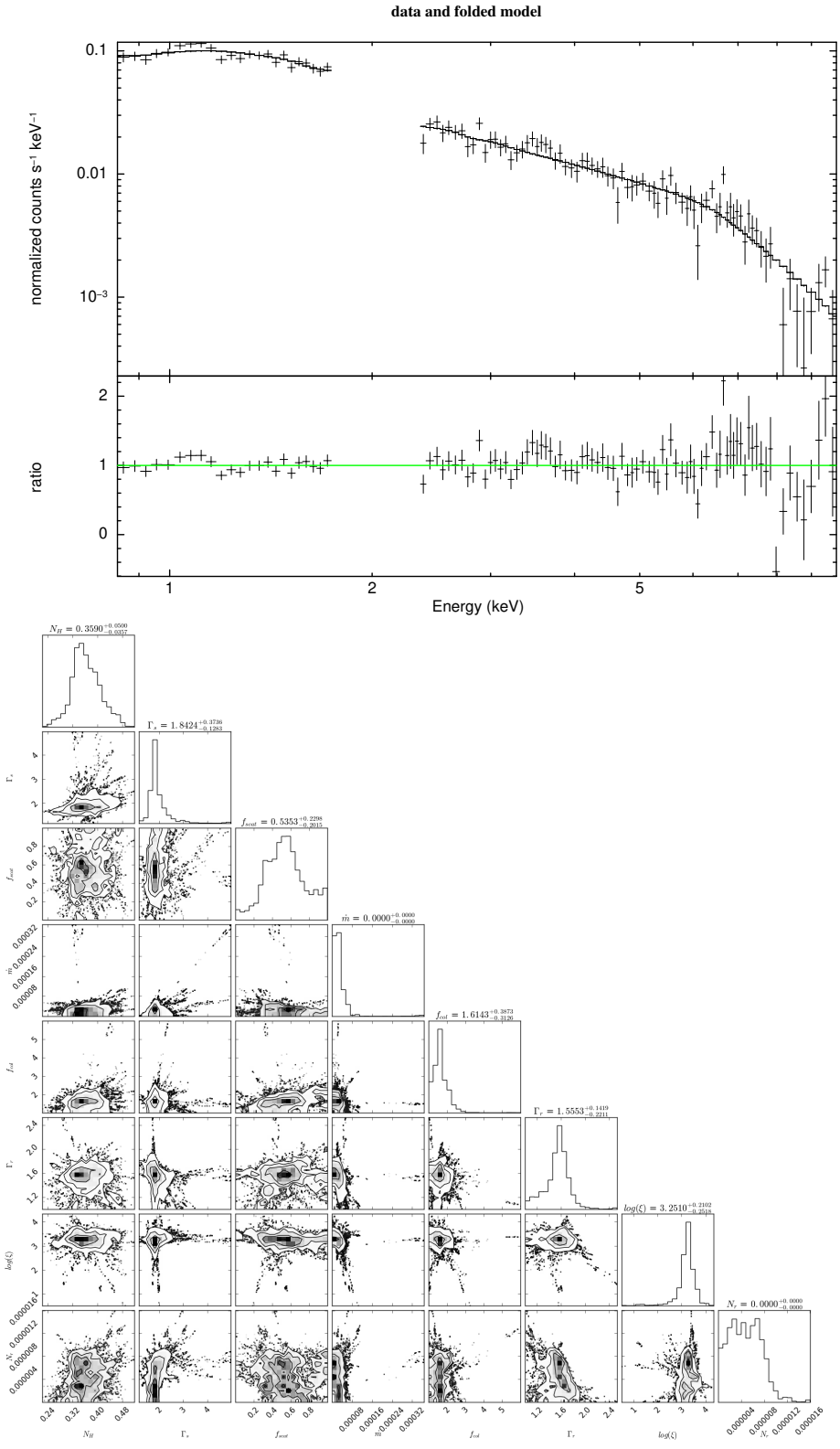

Figure B.59: XMM-Newton pn spectrum of the source Swift J1910.2-0546 (rev2715) and the residuals. (Hard state)

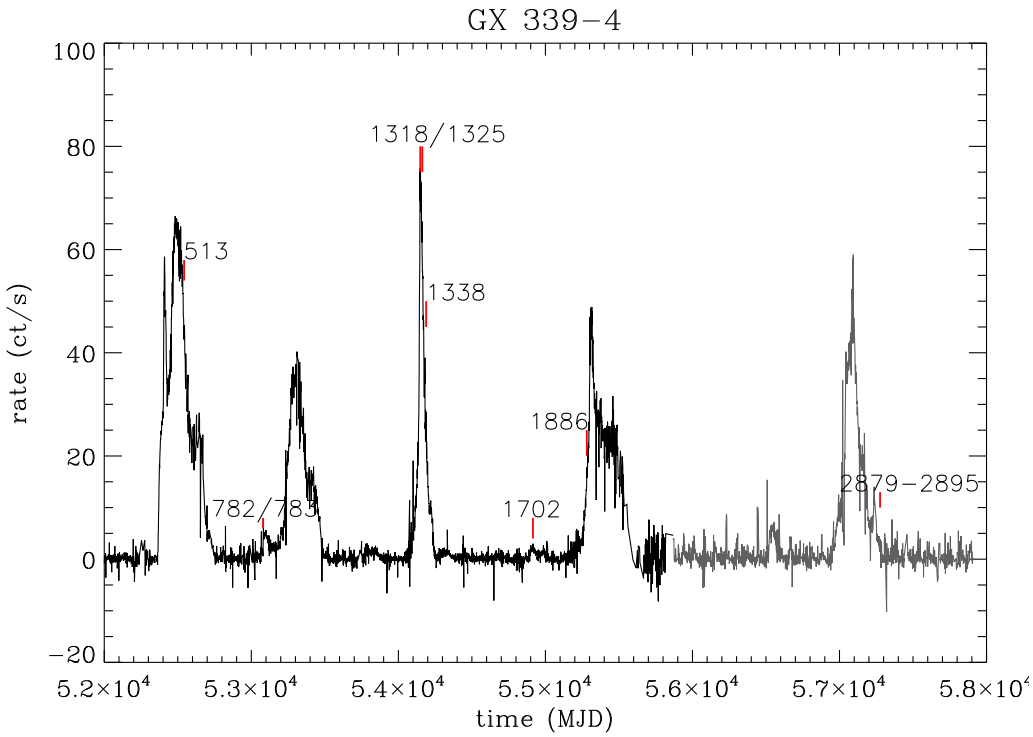

Figure B.60: RXTE/ASM and MAXI lightcurve, and the times of the *XMM-Newton* observations for GX 339-4.

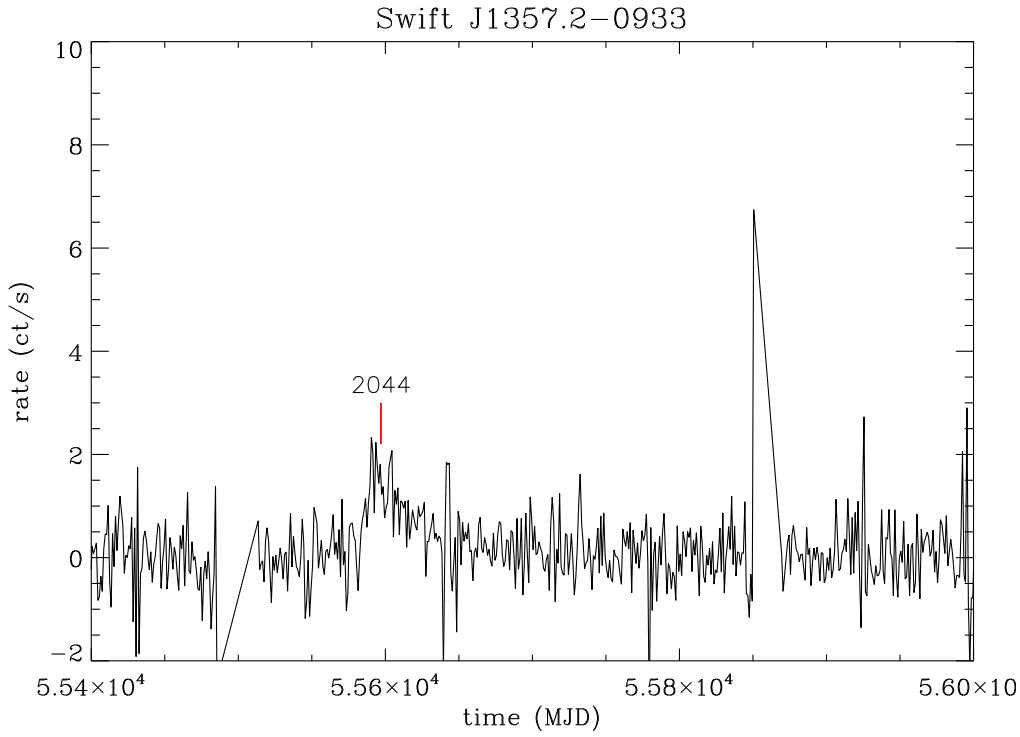

Figure B.61: MAXI lightcurve and the time of the *XMM-Newton* observation for Swift J1357.2-0933.

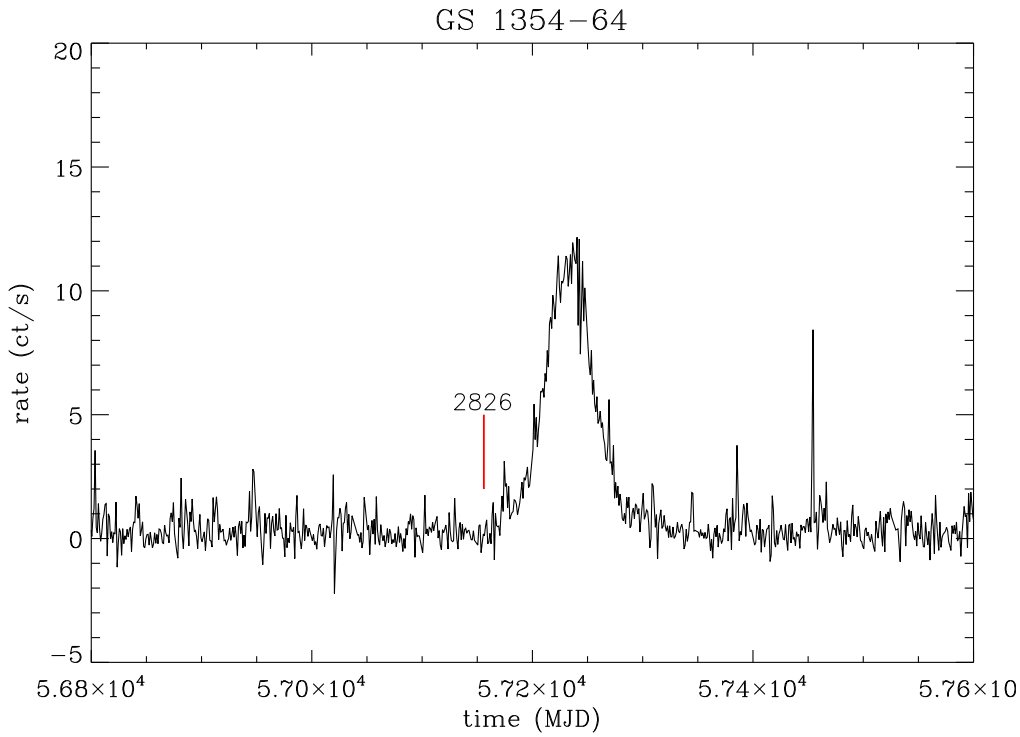

Figure B.62: MAXI lightcurve and the time of the *XMM-Newton* observation for GS 1354-64.

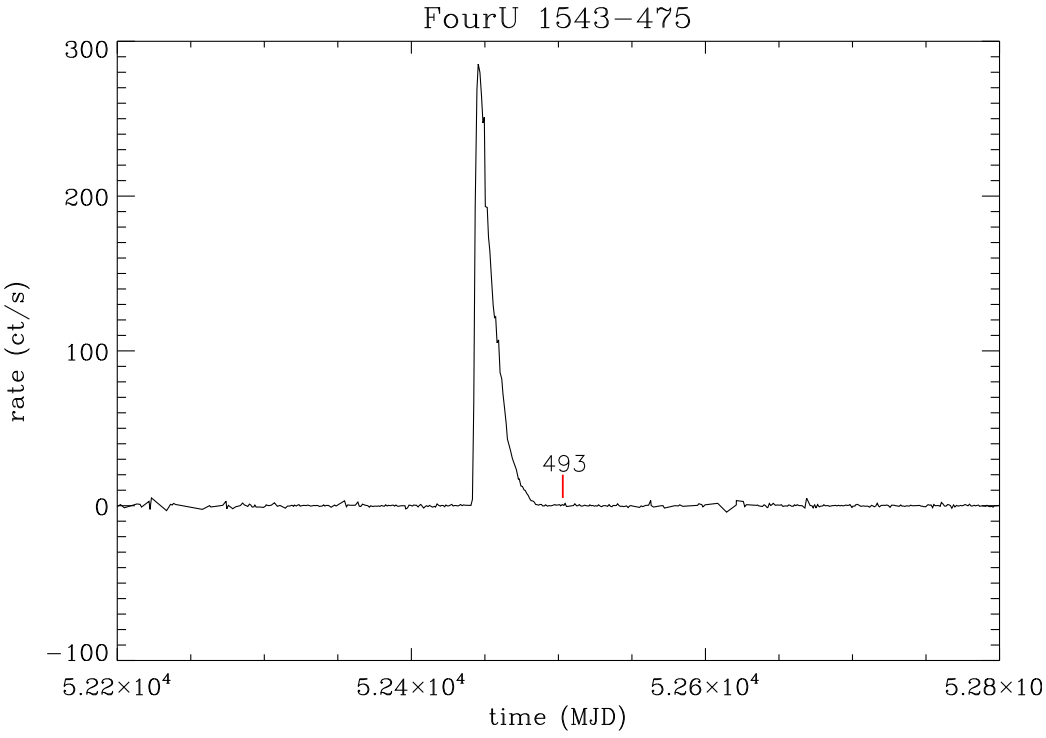

Figure B.63: RXTE/ASM lightcurve and the time of the *XMM-Newton* observation for 4U 1543-475.

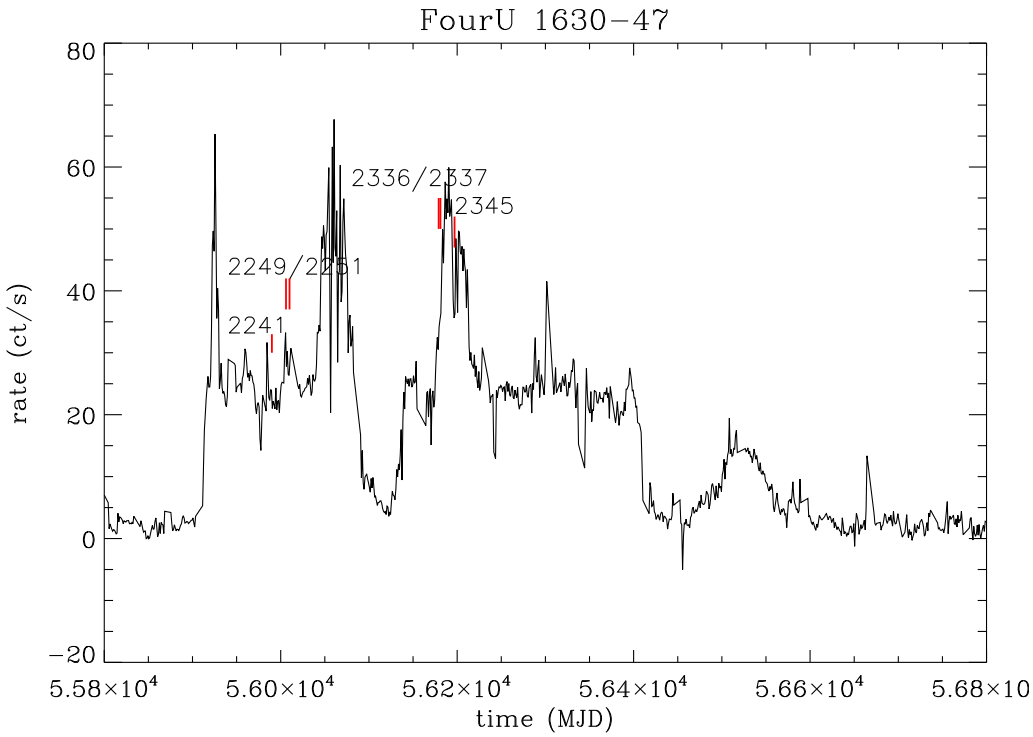

Figure B.64: MAXI lightcurve and the times of the *XMM-Newton* observations for 4U 1630-47.

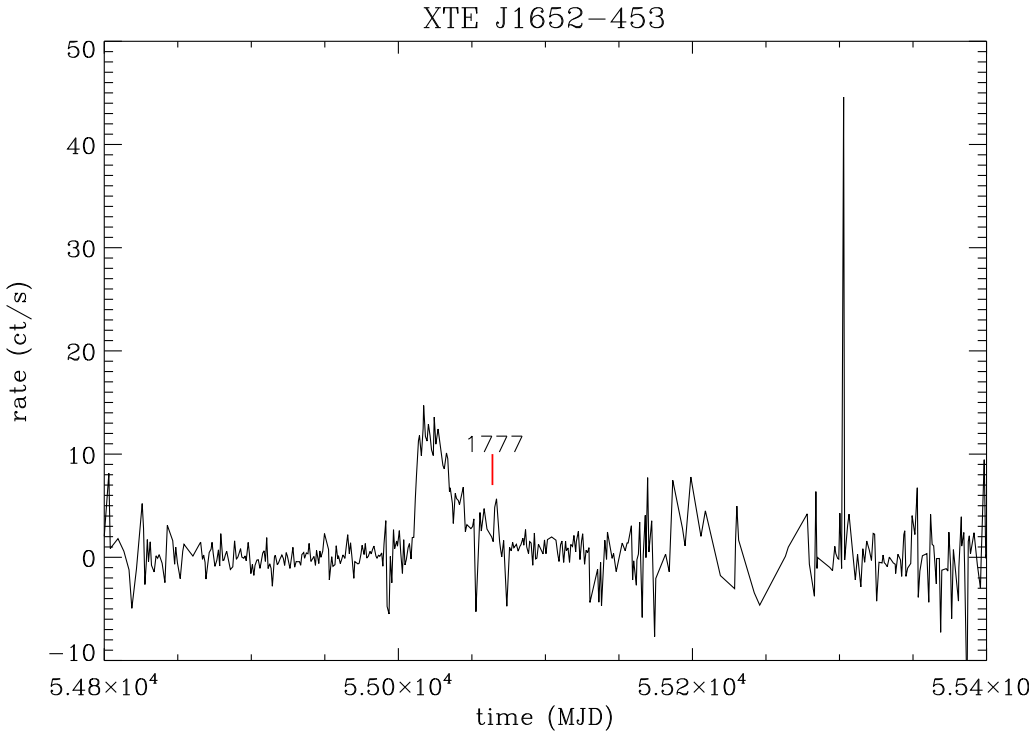

Figure B.65: RXTE/ASM lightcurve and the time of the *XMM-Newton* observation for XTE J1652-453.

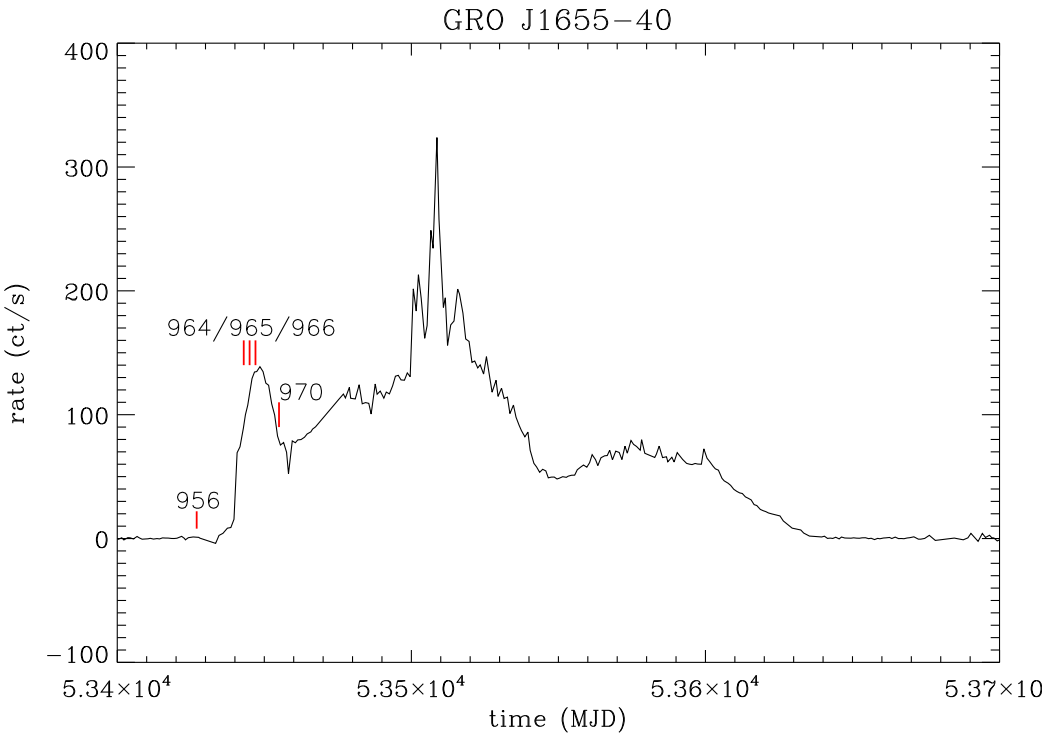

Figure B.66: RXTE/ASM lightcurve and the times of the *XMM-Newton* observations for GRO J1655-40.

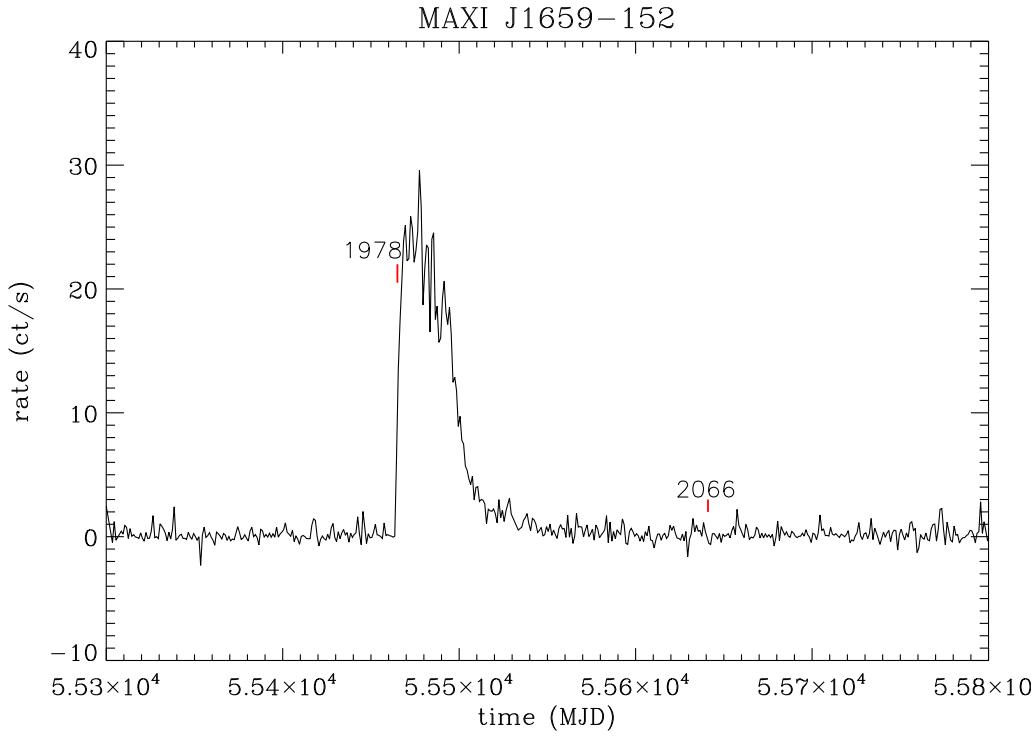

Figure B.67: MAXI lightcurve and the times of the *XMM-Newton* observations for MAXI J1659-152.

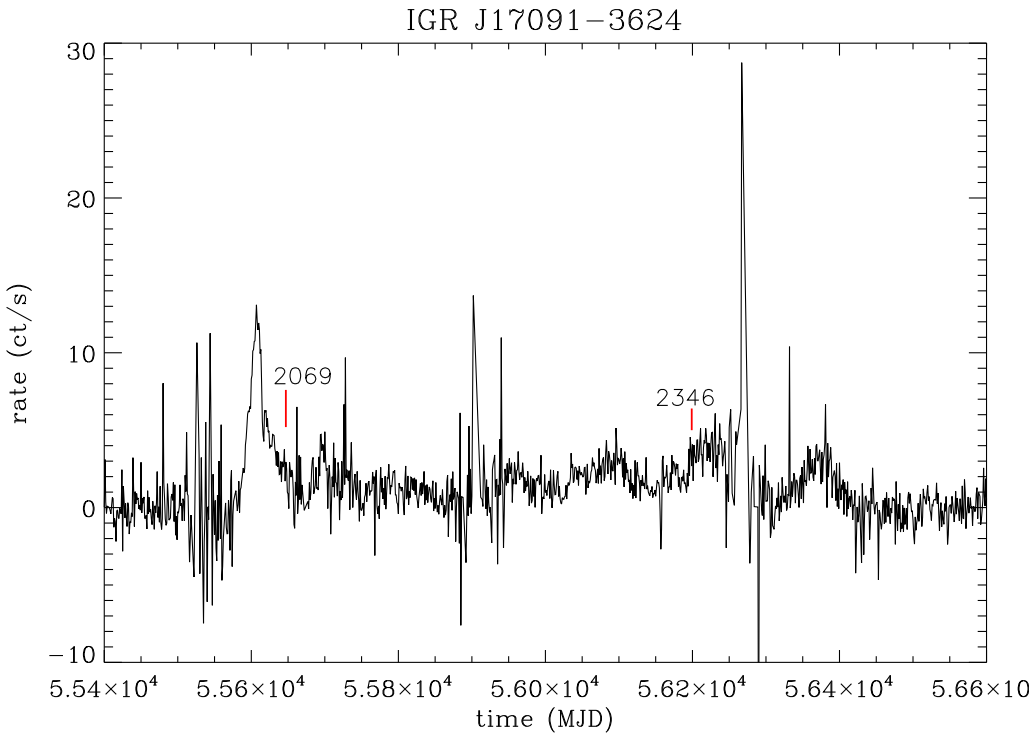

Figure B.68: Swift/BAT lightcurve and the times of the *XMM-Newton* observations for IGR J17091-3624.

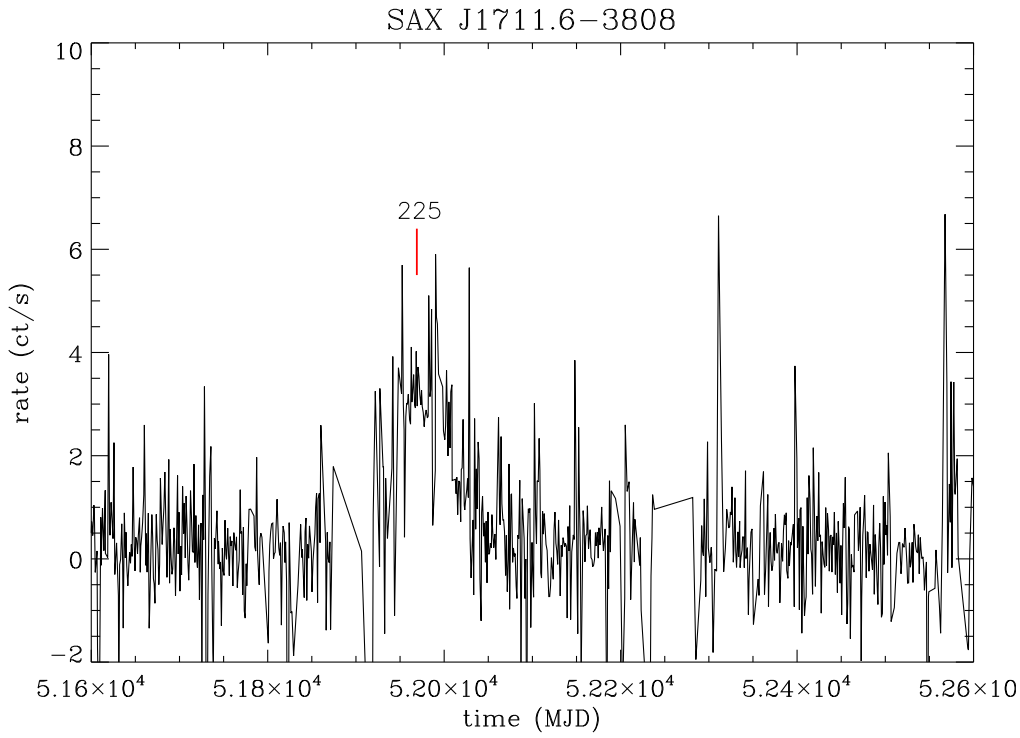

Figure B.69: RXTE/ASM lightcurve and the time of the *XMM-Newton* observation for SAX J1711.6-3808.

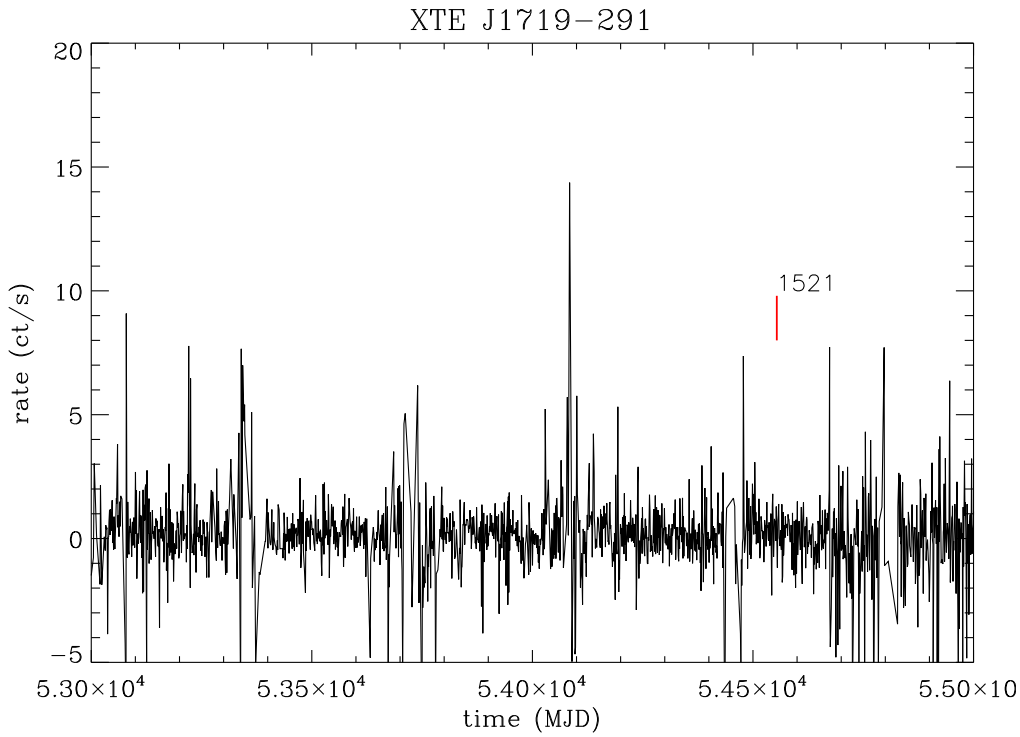

Figure B.70: RXTE/ASM lightcurve and the time of the *XMM-Newton* observation for XTE J1719-291.

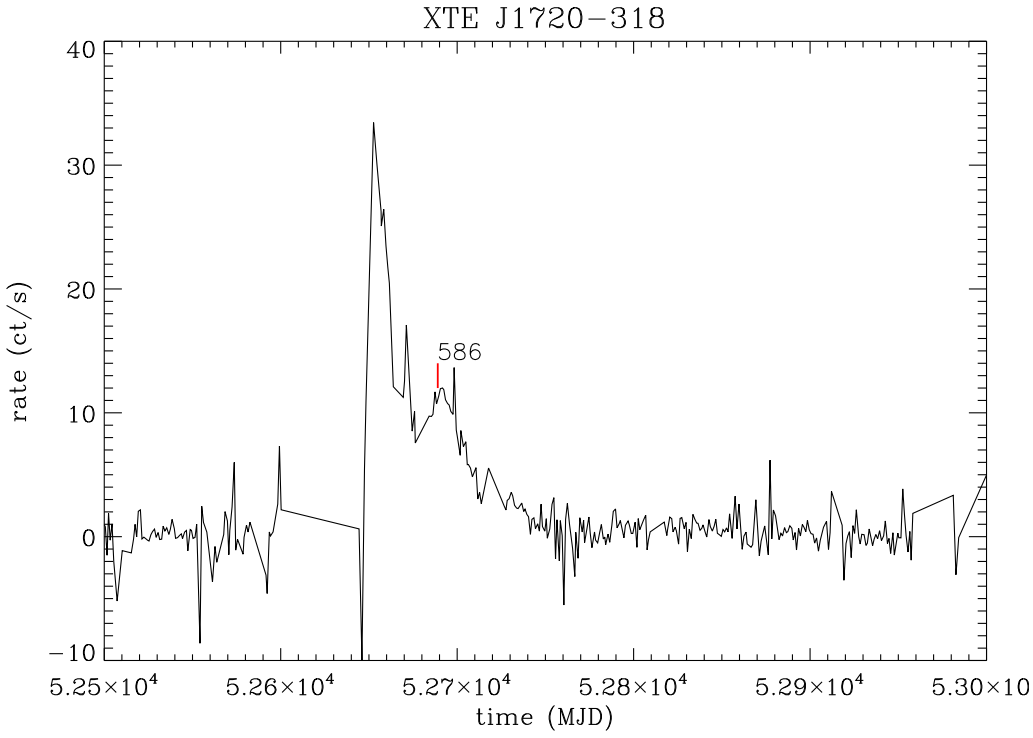

Figure B.71: RXTE/ASM lightcurve and the time of the *XMM-Newton* observation for XTE J1720-318.

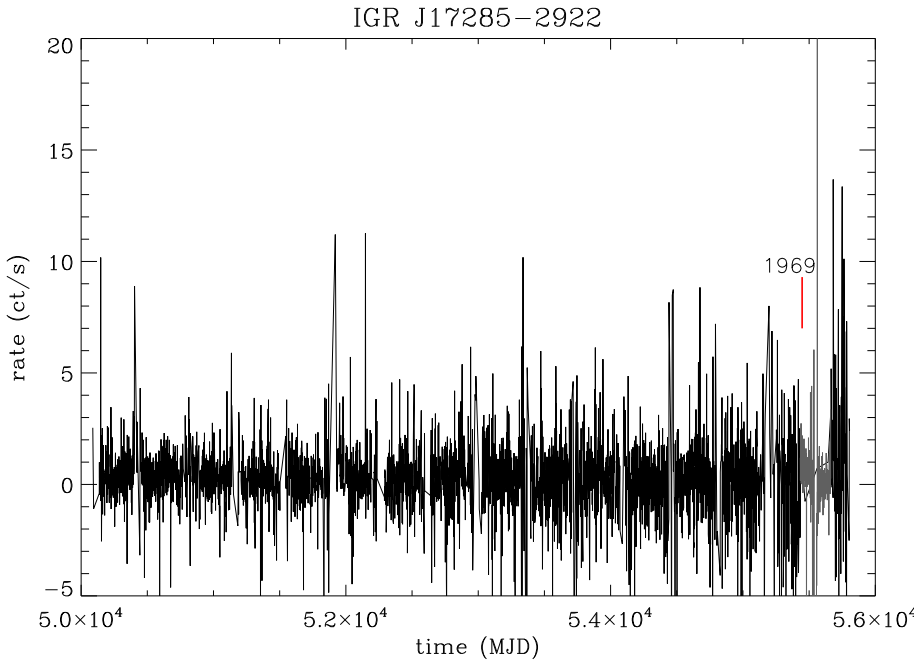

Figure B.72: RXTE/ASM and Swift/BAT lightcurve, and the time of the *XMM-Newton* observation for IGR J17285-2922.

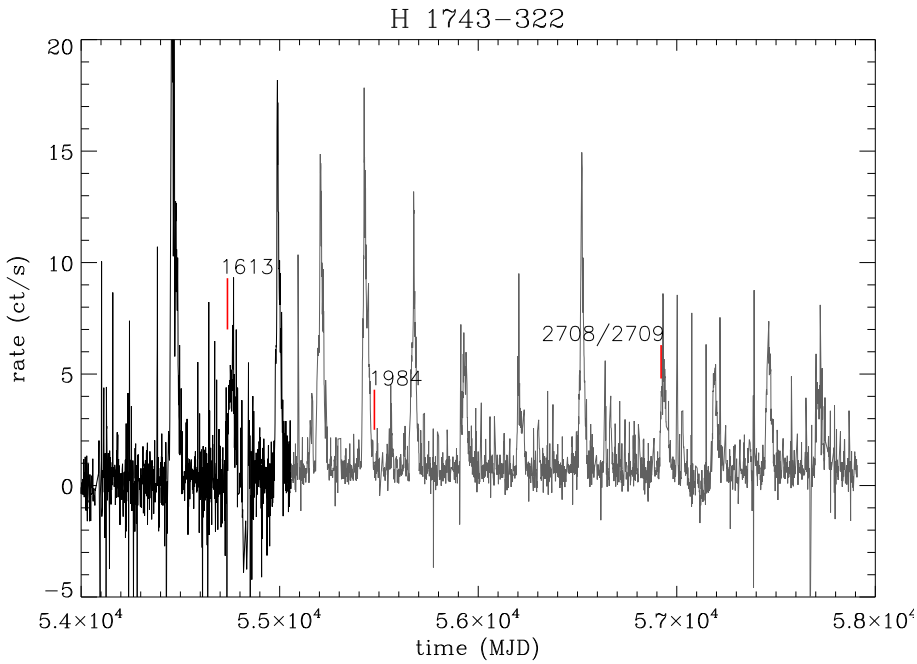

Figure B.73: RXTE/ASM and MAXI lightcurve, and the times of the *XMM-Newton* observations for H 1743-322.

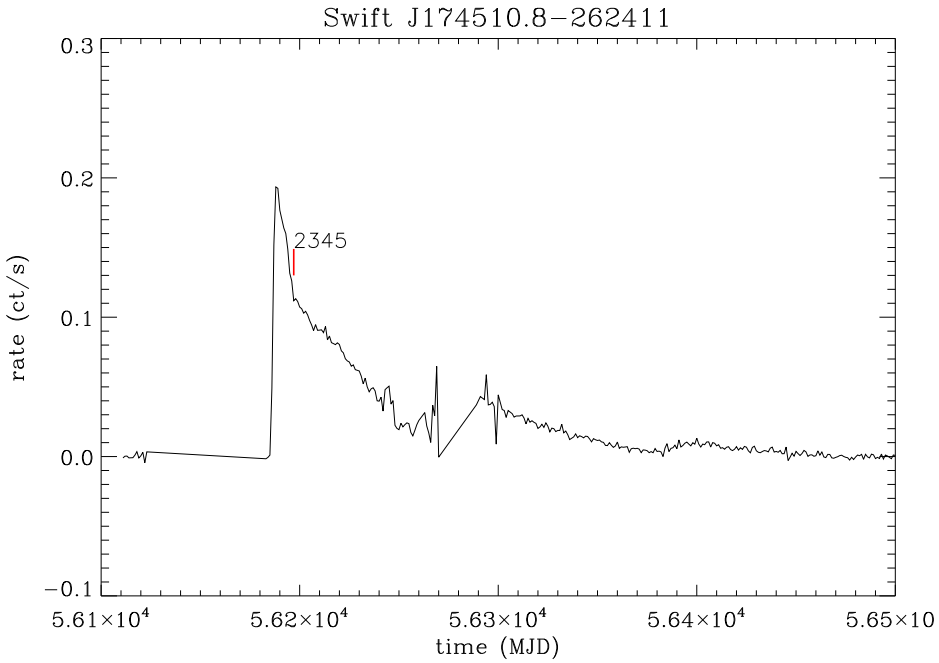

Figure B.74: Swift/BAT lightcurve and the time of the *XMM-Newton* observation for Swift J174510.8-262411.

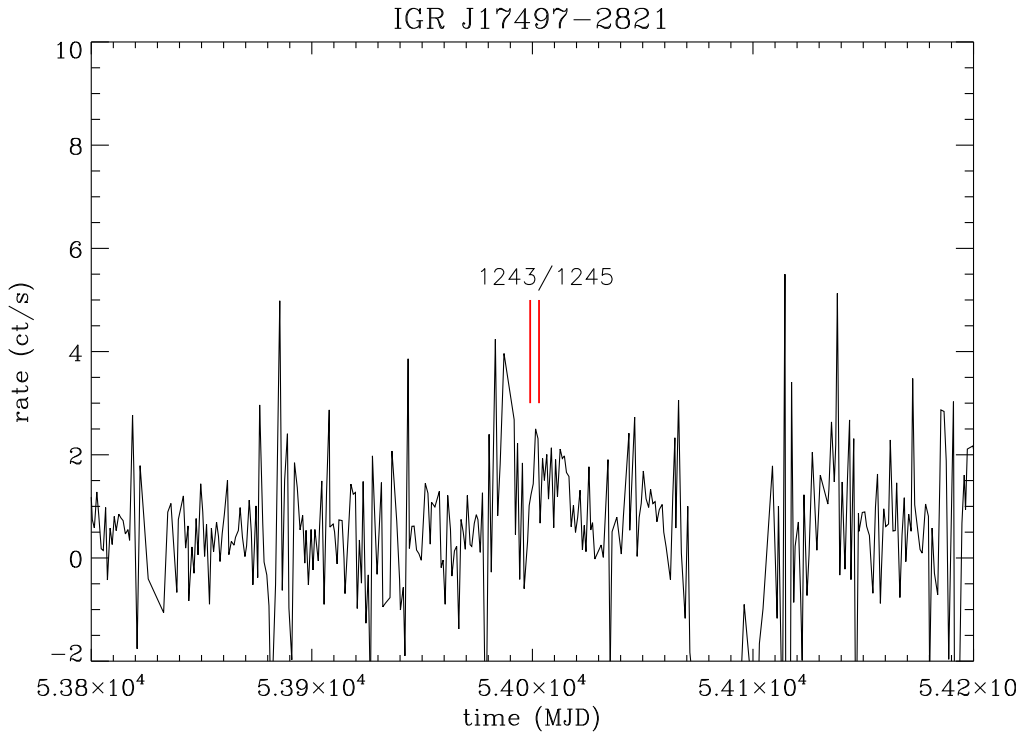

Figure B.75: RXTE/ASM lightcurve and the times of the *XMM-Newton* observations for IGR J17497-2821.

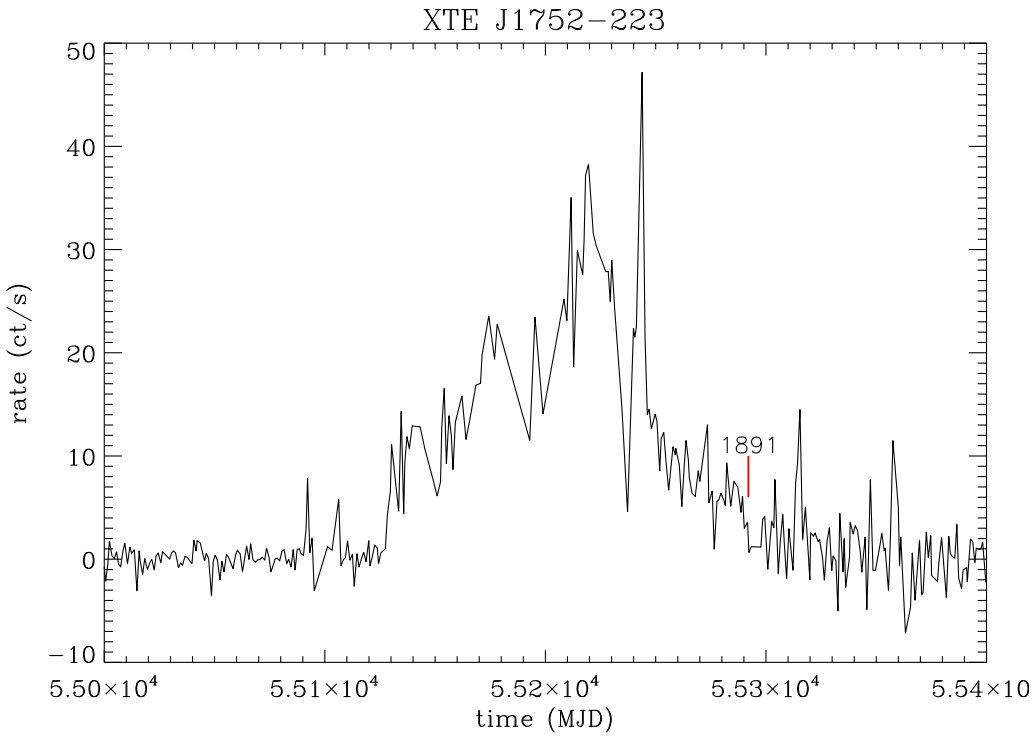

Figure B.76: RXTE/ASM lightcurve and the time of the *XMM-Newton* observation for XTE J1752-223.

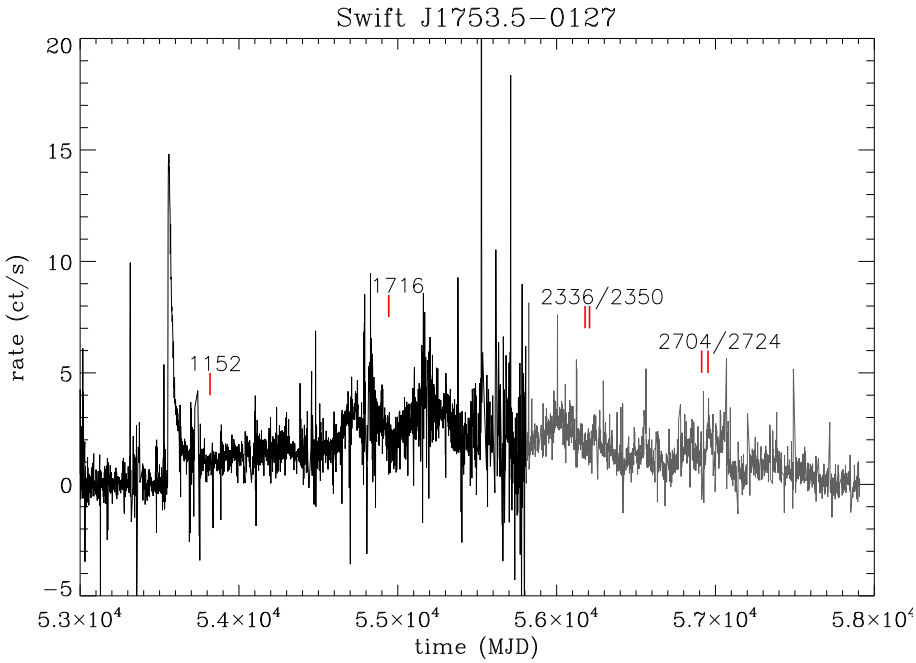

Figure B.77: RXTE/ASM and MAXI lightcurve, and the times of the *XMM-Newton* observations for Swift J1753.5-0127.

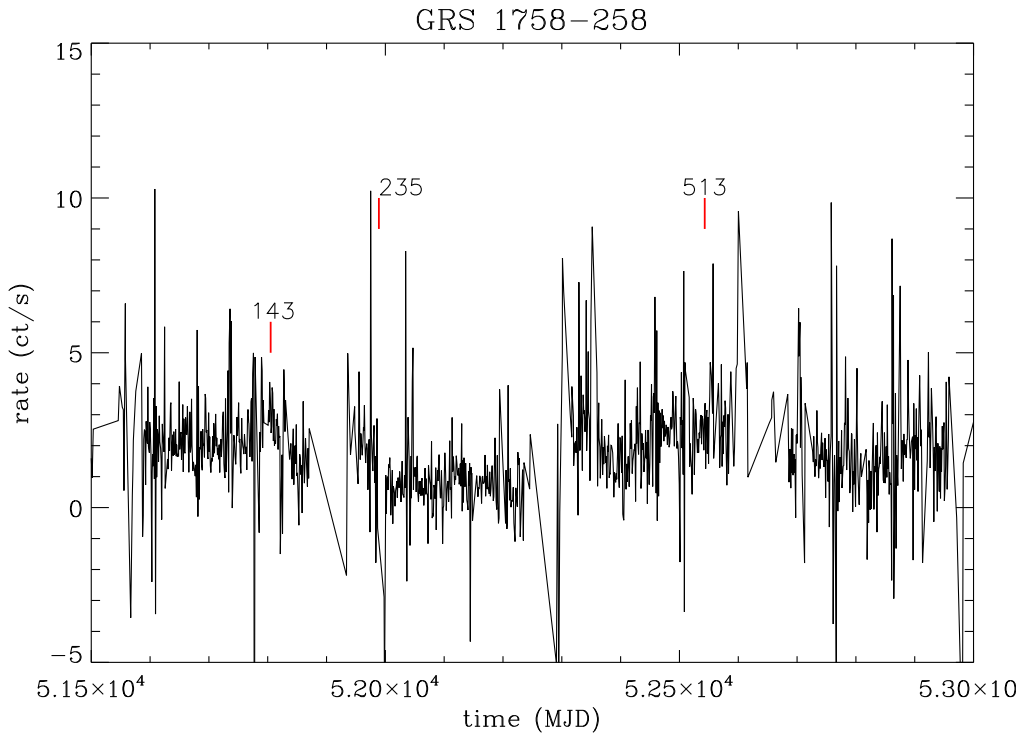

Figure B.78: RXTE/ASM lightcurve and the times of the *XMM-Newton* observations for GRS 1758-258.

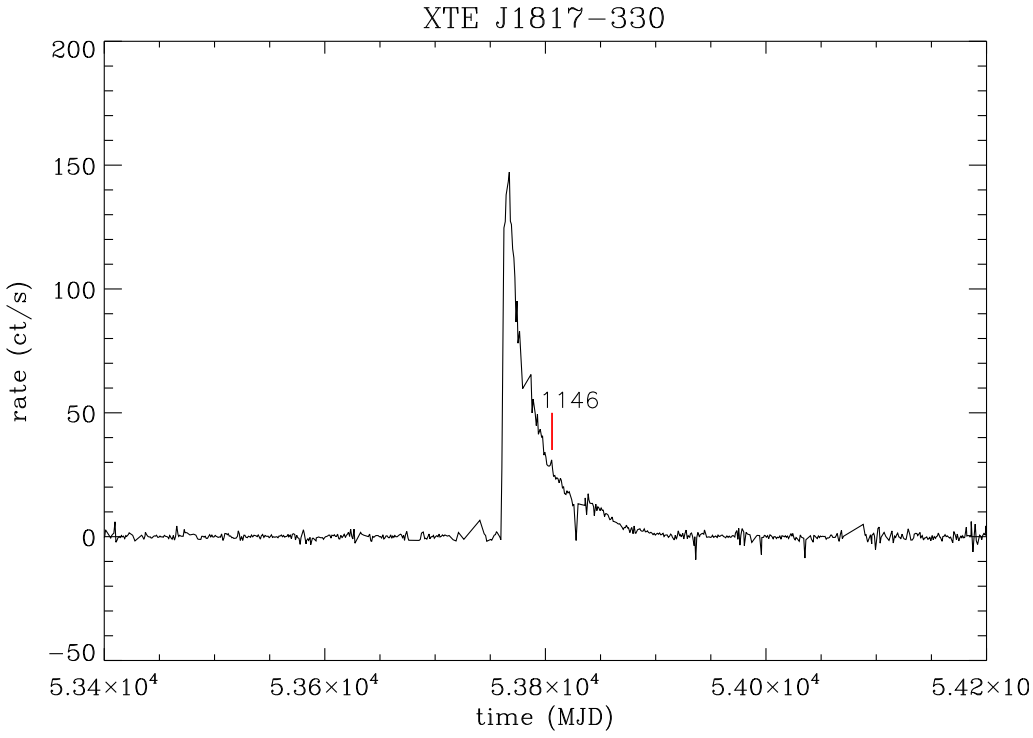

Figure B.79: RXTE/ASM lightcurve and the time of the *XMM-Newton* observation for XTE J1817-330.

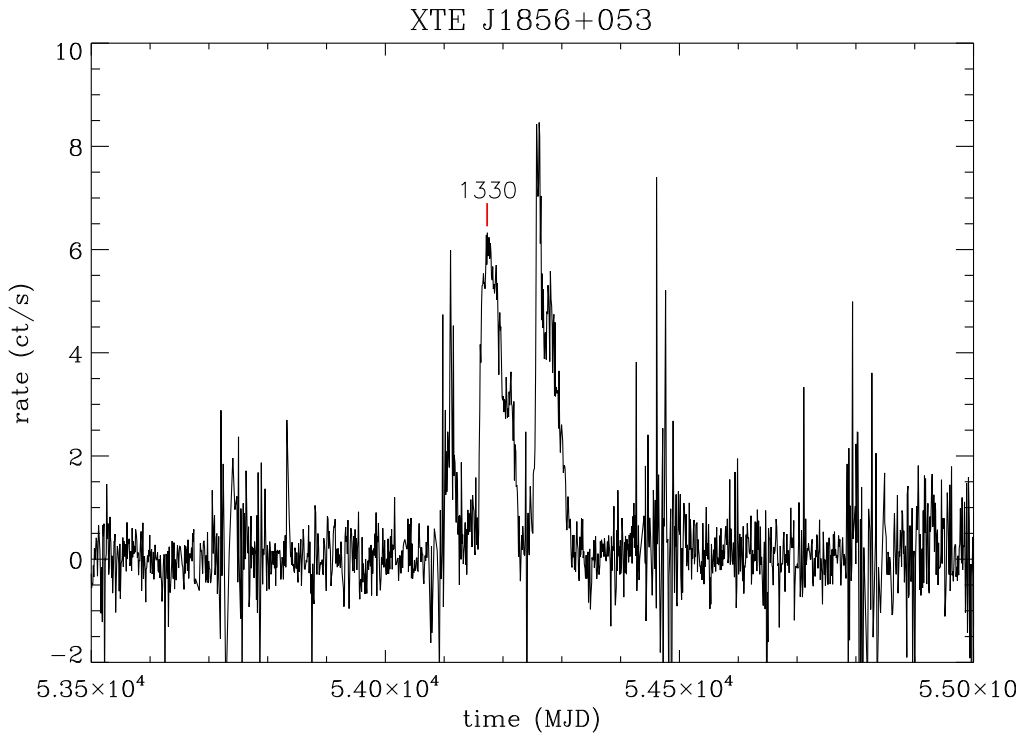

Figure B.80: RXTE/ASM lightcurve and the time of the *XMM-Newton* observation for XTE J1856+053.

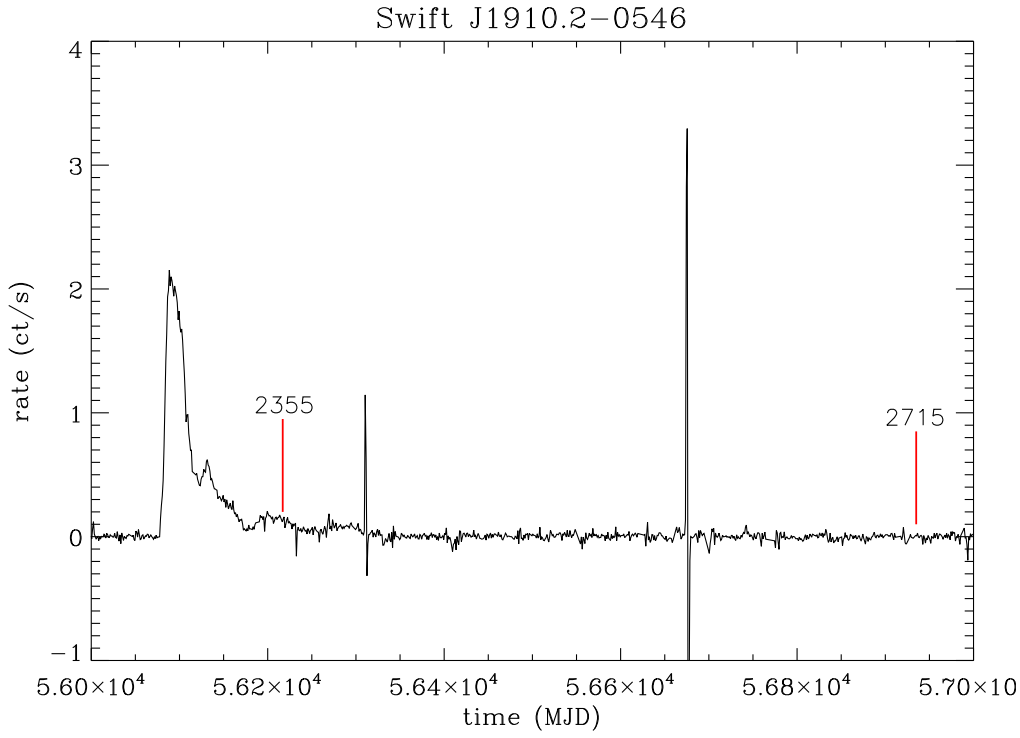

Figure B.81: MAXI lightcurve and the times of the *XMM-Newton* observations for Swift J1910.2-0546.

References

Anders E., Ebihara M., 1982, GeCoA, 46, 2363

Armas Padilla M., Degenaar N., Patruno A., Russell D. M., Linares M., Maccarone T. J., Homan J., Wijnands R., 2011, MNRAS, 417, 659

Armas Padilla M., Degenaar N., Russell D. M., Wijnands R., 2013, MNRAS, 428, 3083

Armas Padilla M., Wijnands R., Altamirano D., Méndez M., Miller J. M., Degenaar N., 2014, MNRAS, 439, 3908

Arnaud K. A., 1996, in ASP Conf. Ser., Vol. 101, Astronomical Data Analysis Software and Systems V., Jacoby G. H., Barnes J., eds., Astron. Soc. Pac., San Fransisco, p. 17

Balbus S. A., Hawley J. F., 1998, Reviews of Modern Physics, 70, 1

Balucinka M., Hasinger G., 1991, A&A, 241, 439

Balucinska-Church M., McCammon D., 1992, ApJ, 400, 699

Barr P., van der Woerd H., 1990, ApJ, 352, L41

Basak R., Zdziarski A. A., 2016, MNRAS, 458, 2199

Begelman M. C., Armitage P. J., Reynolds C. S., 2015, ApJ, 809, 118

Belloni T., Homan J., Casella P., van der Klis M., Nespoli E., Lewin W. H. G., Miller J. M., Méndez M., 2005, A&A, 440, 207

Belloni T. M., 2010, in Lecture Notes in Physics, Vol. 794, The Jet Paradigm. Springer-Verlag, Belloni T., ed., Berlin, p. 53

Belloni T. M., Sanna A., Méndez M., 2012, MNRAS, 426, 1701

Beloborodov, 1999, ApJ, 510, L123

Bildsten L. et al., 1997, ApJS, 113, L2

Boirin L., Méndez M., Díaz Trigo M., Parmar A. N., Kaastra J. M., 2005, A&A, 436, 195

Cabanac C., Fender R. P., Dunn R. J. H., Körding E. G., 2009, MNRAS, 396, 1415

Cadolla Bel M. et al., 2004, A&A, 426, 659

Carter J. A., Read A. M., 2007, A&A, 464, 1155

Casares J. et al., 2009, ApJS, 181, 238

Casella P., Belloni T., Stella L., 2005, ApJ, 629, 403

Cassatella P., Uttley P., J. M. T., 2012, MNRAS, 427, 2985

Chen W., Shrader C. R., Livio M., 1997, ApJ, 491, 312

Chiang C.-Y., Reis R. C., Walton D. J., Fabian A. C., 2012, MNRAS, 425, 2436

Chun Y. Y. et al., 2013, ApJ, 770, 10

Coppi P. S., 2000, Bulletin of the American Astronomical Society, 32, 1217

Coriat M. et al., 2011, MNRAS, 414, 677

Dauser T., García J., Wilms J., Böck M., Brenneman L. W., Falanga M., Fukumura K., Reynolds C. S., 2013, MNRAS, 430, 1694

Dauser T., Wilms J., Reynolds C. S., Brenneman L. W., 2010, MNRAS, 409, 1534

Davis S. W., Blaes, O M., Hubeny I., Turner N. J., 2005, ApJ, 621, 372

Del Santo M. et al., 2016, MNRAS, 456, 3585

den Herder J. W., et al., 2001, A&A, 365, L7

Díaz Trigo M., Migliari S., Miller-Jones J. C. A., Guainazzi M., 2014, A&A, 571, A76

Díaz Trigo M., Parmar A. N., Miller J., Kuulkers E., Caballero-García, 2007, A&A, 462, 657

Dickey J. M., Lockman F. J., 1990, ARA&A, 28, 215

Done C., Diaz Trigo M., 2010, MNRAS, 407, 2287

Done C., Gierliński M., 2006, MNRAS, 367, 659

Done C., Gierliński M., Kubota A., 2007, A&AR, 15, 1

Dove J. B., Wilms J., Begelman M. C., 1997, ApJ, 487, 747

Dubus G., Hameury J.-M., Lasota J.-P., 2001, A&A, 373, 251

Ebisawa K., Ueda Y., Inoue H., Tanaka Y., White N. E., 1996, ApJ, 467, 419

Esin A. A., McClintock J. E., Narayan R., 1997, ApJ, 489, 865

Fabian A. C., J. R. M., Stella L., White N. E., 1989, MNRAS, 238, 729

Falcke H., Körding E., Markoff S., 2004, A&A, 414, 895

Fender R., Homan J., Belloni T. M., 2009, MNRAS, 396, 1370

Fender R. P., Gallo E., Jonker P. G., 2003, MNRAS, 343, L99

Foreman-Mackey D., 2016, JOSS, 24

Foreman-Mackey D., Hogg D. W., Lang D., Goodman J., 2013, PASP, 125, 306

Froning C. S., Maccarone T. J., France K., Winter L., Robinson E. L., Hynes R. I., Lewis F., 2014, ApJ, 780, 48

Fürst F. et al., 2015, ApJ, 808, 122

García J. et al., 2014, ApJ, 782, 76

García J., Dauser T., Reynolds C. S., Kallman T. R., McClintock J. E., Wilms J., Eikmann W., 2013, ApJ, 768, 146

García J., Kallman T. R., 2010, ApJ, 718, 695

García J., Kallman T. R., Mushotzky R. F., 2011, ApJ, 731, 131

Gatuzz E., Garcia J., Kallman T. R., Mendoza C., 2016, A&A, 588, A111

Gatuzz E., Garcia J., Kallman T. R., Mendoza C., Gorczyca T. W., 2015, ApJ, 800, 29

Gatuzz E., Garcia J., Mendoza C., 2014, ApJ, 790, 131

Gatuzz E. et al., 2013a, ApJ, 778, 83

Gatuzz E. et al., 2013b, ApJ, 768, 60

Goodman J., Weare J., 2010, A&A, 391

Gregory P. C., 2005, Bayesian Logical Data Analysis for the Physical Sciences, Cambridge Univ. Press, Cambridge

Grimm H.-J., Gilfanov M., Sunyaev R., 2002, A&A, 391

Haardt F., Maraschi L., 1993, ApJ, 413, 507

Hiemstra B., Méndez M., Done C., Díaz Trigo M., Altamirano D., Casella P., 2011, MNRAS, 411, 137

Homan J., Belloni T., 2005, Ap&SS, 300, 107

Homan J., Kong A., Tomsick J., Miller J., Campana S., Wijnands R., Belloni T., Lewin W., 2005, ATel, 644

Homan J., Wijnands R., van der Klis M., Belloni T., van Paradijs J., Klien-Wolt M., Fender R., Méndez M., 2001, ApJ, 132, 377

Ingram A., Done C., Fragile P. C., 2009, MNRAS, 397, L101

Jansen F. et al., 2001, A&A, 365, L1

Jonker P. G. et al., 2010, MNRAS, 401, 1255

Kafka S., 2018, Observations from the AAVSO International Database. `https://www.aavso.org`

Kalberla P. M. W., Burton W. B., Hartmann D., Arnal E. M., Bajaja E., Morras R., Pöppel W. G. L., 2005, A&A, 440, 775

King A. R., Ritter H., 1998, MNRAS, 293, L42

Knevitt G., Wynn G. A., Vaughan S., Watson M. G., 2014, MNRAS, 437, 3087

Kolehmainen M., Done C., M. D. T., 2014, MNRAS, 437, 316

Kolijonen K. I. I., Russell D. M., Corral-Santana J. M., Armas Padilla M., Muñoz-Darias T., Lewis F., Coriat M., Bauer F. E., 2016, MNRAS, 460, 942

Körding E. G., Fender R. P., Migliari S., 2006, MNRAS, 369, 1451

Kuulkers E., 1998, New Astron. Rev., 42, 1

La Palombara N., Mereghetti S., 2005, A&A, 430, 53

Lasota J.-P., 2001, New Astron. Rev., 45, 449

Li L.-X., Zimmerman E. R., Narayan R., McClintock J. E., 2014, ApJS, 157, 335

Liu B. F., Taam R. E., Meyer-Hofmeister E., Meyer F., 2007a, ApJ, 671, 695

Liu Q. Z., van Paradijs J., van den Heuvel E. P. J., 2007b, A&A, 469, 807

Lockman F. J., Jahoda K., McCammon D., 1986, ApJ, 302, L432

Luo Y., Fang T., 2014, ApJ, 780, 170

MacKay D., 2003, Information Theory, Inference, and Learning Algorithms, Cambridge Univ. Press, Cambridge

Markoff S., Falcke H., Fender R., 2001, A&A, 372, L25

Markoff S., Nowak M. A., Wilms J., 2005, ApJ, 635, 1203

Markwardt C., Homan J., Swank J., 2005, ATel, 436

Mason K. O., et al., 2001, A&A, 365, L36

McClintock J. E., Remillard R. A., 2006, In Compact Stellar X-Ray Sources, Lewin W., van der Klis M., eds., Cambridge Univ. Press, Cambridge, p. 157

Merloni A., Fabian A. C., 2002, MNRAS, 322, 165

Merloni A., Heinz S., di Matteo T., 2003, MNRAS, 345, 1057

Miller J. M., Homan J., Miniutti G., 2006a, ApJ, 652, 113

Miller J. M., Homan J., Steeghs D., Rupen M., Hunstead R. W., Wijnands R., Charles P. A., Fabian A. C., 2006b, ApJ, 653, 525

Morrison R., McCammon D., 1983, ApJ, 270, 119

Motta, S E., Belloni T. M., Stella L., Muñoz-Darias T., Fender R., 2014, MNRAS, 437, 2554

Motta, S E., Muñoz-Darias T., Casella P., Belloni T., Homan J., 2011a, MNRAS, 418, 2292

Motta, S E., Muñoz-Darias T., Casella P., Belloni T., Homan J., 2011b, MNRAS, 437, 2554

Motta S., Homan J., Muñoz-Darias T., Casella P., Belloni T. M., Hiemstra B., Mendez M., 2012, MNRAS, 427, 595

Narayan R., E. M. J., Yi I., 1996, ApJ, 457, 821

Narayan R., Yi I., 1995, ApJ, 452, 710

Pinto C., Kaastra J. S., Constantini E., de Vries C., 2013, A&A, 551, A25

Pinto C., Kaastra J. S., Constantini E., Verbunt F., 2010, A&A, 521, A79

Plant D. S., Fender R. P., Ponti G., Muñoz-Darias T., Coriat M., 2015, A&A, 573, A120

Ponti G., Fender R. P., Begelman M. C., Dunn R. J. H., Neilsen J., Coriat M., 2012, MNRAS, 422, L11

Poutanen J., 1998, in Theory of Black Hole Accretion Disks, Abramowicz M. A., Bjornsson G., Pringle J. E., eds., Cambridge Univ. Press, Cambridge, p. 100

Poutanen J., Krolik J. H., Ryde F., 1997, MNRAS, 292, L21

Reis R. C., Fabian A. C., Miller J. M., 2010, MNRAS, 402, 836

Reis R. C. et al., 2011, MNRAS, 410, 2497

Remillard R. A., McClintock J. E., 2006, ARA&A, 44, 49

Reynolds C. S., Novak, M A., 2003, Phys. Rep., 377, 389

Reynolds S. P., 1999, ApJ, 525, 368

Reynolds S. P., Keohane J. W., 1998, ApJ, 493, 357

Ross R. R., Fabian A. C., 2005, MNRAS, 358, 211

Rykoff E. S., Miller J. M., Steeghs D., Torres M. A. P., 2007, ApJ, 666, 1129

Sala G., Greiner J., Ajello M., Bottacini E., Haberl F., 2007a, A&A, 473, 561

Sala G., Greiner J., Ajello M., Primak N., 2008, A&A, 489, 1239

Sala G., Greiner J., Vink J., Haberl F., Kendziorra E., Zhang X. L., 2007b, A&A, 461, 1049

Salvesen G., Miller J. M., Reis R. C., Begelman M. C., 2013, MNRAS, 431, 3510

Sánchez-Fernández C., Santos-Lleó M., In't Zand J. J. M., González-Riestra R., Altieri B., Saxton R., Castro-Tirado A. J., 2006, AN, 327, 1004

Seifina E., Titarchuk L., Shaposhnikov N., 2014, ApJ, 789, 57

Shakura N. I., Sunyaev R. A., 1973, A&A, 24, 337

Shaw A. W. et al., 2016, MNRAS, 458, 1636

Shidatsu M. et al., 2011, PASJ, 63, 785

Shimura T., Takahara F., 1995, ApJ, 445, 780

Sidoli L., Paizis A., Mereghetti S., Götz D., Del Santo M., 2011, MNRAS, 415, 2373

Steiner J. F., A. G. J., Eikmann W., McClintock J. E., Brenneman L. W., Dauser T., Fabian A. C., 2017, ApJ, 836, 119

Steiner J. F., Narayan R., McClintock J. E., Ebisawa K., 2009, PASP, 121, 1279

Stella L., Vietri M., 1998, ApJ, 492, L59

Stella L., Vietri M., 1999, Physical Review Letters, 82, 17

Stella L., Vietri M., Morsink S. M., 1998, ApJ, 492, L59

Stiele H., Muñoz-Darias T., Motta S., Belloni T. M., 2012, MNRAS, 422, 679

Strohmayer T. E., 2001, ApJ, 552, L49

Strohmayer T. E., Zhang W., Swank J. H., Smale A., Titarchuk L., Day C., Lee U., 1996, ApJ, 496, L9

Strüder L., et al., 2001, A&A, 365, L18

Tetarenko B. E., Sivakoff G. R., Heinke C. O., Gladstone J. C., 2016, ApJS, 222, 98

Thorne K. S., 1974, ApJ, 191, 507

Titarchuk L., 1994, ApJ, 434, 313

Tomsick J. A., Yamaoka K., Corbel S., Kaaret P., Kalemci E., Migliari S., 2009, ApJL, 707, L87

Tomsick J. A., Yamaoka K., Corbel S., Kalemci E., Migliari S., Kaaret P., 2014, ApJ, 791

van der Klis M., 2006, Rapid X-ray Variability, Lewin W. H. G., van der Klis M., eds., Cambridge Univ. Press, Cambridge

van Paradijs J., 1996, ApJL, 464, L139

Willingale R., Starling R. L. C., Beardmore A. P., Tanvir N. R., O'Brien P. T., 2013, MNRAS, 431, 394

Wilms J., Allen A., McCray R., 2000, ApJ, 542, 914

Yamada S. et al., 2009, ApJ, 707, L109

Zhang S. N., Cui W., Chen W., 1997, ApJ, 482, L155